Uniwersytet im. Adama Mickiewicza w Poznaniu

Wydział Chemii

Zakład Fizyki Chemicznej

ANNA LEWANDOWSKA

Praca doktorska

FOTOINDUKOWANE PROCESY PRZENIESIENIA ELEKTRONU, PROTONU LUB ATOMU WODORU W UKŁADACH BICHROMOFOROWYCH BENZOFENON-TYROZYNA ORAZ BENZOFENON-METIONINA

Promotor: ***Prof. dr hab. Bronisław Marciniak***

Praca przedstawiona Radzie Naukowej Wydziału Chemii

Uniwersytetu im. Adama Mickiewicza w Poznaniu

celem uzyskania stopnia doktora nauk chemicznych

Poznań, 2011

Adam Mickiewicz University, Poznan
Faculty of Chemistry
Department of Chemical Physics

ANNA LEWANDOWSKA

Ph. D. Thesis

PHOTOINDUCED ELECTRON, PROTON OR HYDROGEN-ATOM TRANSFER REACTIONS IN BENZOPHENONE-TYROSINE AND BENZOPHENONE-METHIONINE BICHROMOPHORIC SYSTEMS

Supervisor: ***Prof. dr. hab. Bronisław Marciniak***

This thesis was submitted

to the Scientific Board of the Faculty of Chemistry

at the Adam Mickiewicz University

Poznan, 2011

Adam Mickiewicz University, Poznan
Faculty of Chemistry
Department of Chemical Physics

Acknowledgements

I would like to express my deepest gratitude to **prof. dr. hab. Bronisław Marciniak,** *for the opportunity to do such interesting research under his supervision.*

I am also particularly thankful for his guidance, advice, patience and fruitful discussions and encouragements during the whole period of my Ph.D. work.

I owe my most sincere gratitude to **dr. Gordon. L. Hug** *for his support and guidance throughout this work. His wide knowledge, logical way of thinking and great efforts to explain things clearly and simply have been of great value for me. I appreciate all his contributions of time, ideas to make my Ph.D experience productive and stimulating. Although most of the time he was in USA he was always accessible via e-mail or Skype willing to help with my research, I do appreciate that.*

I also wish to thank him for revising the English of my manuscript throughout my thesis-writing period which was doubtlessly time-consuming.

I warmly thank **prof. dr. hab. Klaus-Dieter Asmus** *for his valuable advice and friendly help. I am deeply grateful for his detailed and constructive comments, stimulating scientific discussions and for his important support throughout this work.*

I also wish to thank him for helpful suggestions which increased readability and reduced ambiguity of the thesis.

Adam Mickiewicz University, Poznan
Faculty of Chemistry
Department of Chemical Physics

Acknowledgements

I am deeply indebted to **prof. Ian Carmichael** *who gave me the opportunity to work in the Radiation Laboratory, University of Notre Dame. I wish to thank him also for his guidance in the theoretical calculations which were performed during my stay in USA.*

I wish to express my warm and sincere thanks to **dr. Gerald Hörner** *who introduced me to the field of photoinduced hydrogen atom transfer. His ideas and concepts have had a remarkable influence on my work. I am grateful not only for the extensive discussions around my topic but also for listening to me whenever I was excited about new idea. I also thank for his constructive criticism and excellent advice and for providing me with the new compounds during the whole period of my Ph. D. work.*

I would like to record my gratitude to **prof. dr. hab. Jacek Koput** *for his advice and guidance regarding theoretical calculations at the early stage of my research.*

My warm thanks are due to **dr. Franciszek Kaźmierczak** *who provided me with the compounds. I also owe him a huge debt of gratitude for invaluable help in product analysis.*

Adam Mickiewicz University, Poznan
Faculty of Chemistry
Department of Chemical Physics

Acknowledgements

Furthermore I am deeply indebted to people from Department of Chemical Physics for stimulating and fun environment. I would specially like to thank my colleagues ***Małgorzata Bayda**, **Marta Ignasiak**, **Aleksandra Wójcik**, **Katarzyna Taras-Goślińska*** *for their extremely valuable experiences, support and numerous discussions, more or less related to this thesis. This is extended to* ***Piotr Filipiak*** *and* ***Tomasz Pędzinski*** *whom I would like to thank also for their technical support and help with measurements. Furthermore I would like to* ***Ms. Janina Brzezińska*** *for her sympathetic help in secretarial work.*

Their support in this effort is greatly appreciated.

I gratefully acknowledge the funding sources that made my Ph.D. work possible.

I was funded by the Ministry of Science and Higher Education (Poland) (grant N N204 143138). I got also a stipend from the Adam Mickiewicz University Foundation.

I would like to thank also Director of the Radiation Laboratory for a stipend that supported part of this work which was done during my stay in Notre Dame Radiation Laboratory.

Adam Mickiewicz University, Poznan
Faculty of Chemistry
Department of Chemical Physics

Acknowledgements

I owe my loving thanks to ***Paweł Andrałojć****. Without his encouragement, emotional support and understanding it would have been impossible for me to finish this work. Special thanks to him also for helping me with the figures of this dissertation.*

Lastly, and most importantly, I wish to thank my family, specially my parents ***Stefania*** and ***Grzegorz Lewandowscy****. They bore me, raised me, supported me, taught me, and loved me. To them I dedicate this thesis.*
Thank you for believing in me.

Serdeczne podziękowania składam również Rodzicom za cierpliwość, wsparcie i zrozumienie oraz udzieloną pomoc podczas powstawania tej pracy.

Table of Contents

1 INTRODUCTION AND LITERATURE BACKGROUND

1.1 Introduction and Aim of the work

The main aims of this thesis are (1) to characterize methionine and tyrosine chemistry of biological significance, (2) to provide basic chemical information concerning photochemical reactions that can occur in natural biological systems, e.g. in proteins, and (3) to contribute to an understanding of biological processes at the molecular level. Since methionine contains the thioether group, it plays crucial roles in many biological and cellular processes. As S-adenosine-methionine, it takes part in *trans*-methylation, *trans*-sulfurylation and *trans*-alkylation.[1] In addition the oxidation of methionine is one of the most important causes for the inactivation of some hormones (corticotrophin, human growth hormone).[2] Oxidation of the thioether side chain of methionine residues in peptides and proteins that lead to sulfur radical cations has been suspected in oxidative stress and aging.[3, 4] Moreover, in the pathogenesis of some neurodegenerative diseases (Alzheimer's, Jacob-Creutzfeld's, and Parkinson's),[5-8] oxidation of the thioether side chain of methionine seems to be strongly involved.

Tyrosine, as well as phenols, in general play fundamental roles in biology due to their, mainly, reversible redox chemistry. The propensities of phenols to act as chain-breaking agents or antioxidants in the radical-induced peroxidation of organic compounds are well established as vital roles for the tyrosine/tyrosyl radical couple in the active centers of numerous enzymes.[9-12] The chain-breaking ability of phenols is generally attributed to the ease of the donation of the phenolic hydrogen atom (H-atom) to the attacking radical. As a net effect, one hydrogen atom is transferred from the donor to the acceptor.

In the light of the roles of tyrosine and methionine presented above, it is of general importance to carry out a comprehensive study of the photoinduced reactions of hydrogen, electron and proton transfer that occur from those two amino acids. Because of the complexity of the biological systems, simple model bichromophores such as benzophenone-tyrosine and benzophenone-methionine as well as trichromophores such as carboxybenzophenone-methionine-tyrosine were employed to analyse the photochemical intramolecular reactions that occur *in vitro*. This approach can serve as a useful tool in understanding the radical processes that take place *in vivo*.

Although photoinduced hydrogen-abstraction and electron transfer reactions by triplet-excited carbonyl compounds have been central topics of photochemical research for many years, there is still much controversy about the mechanisms of these reactions. In addition, various factors associated with these photoprocesses have been considered to influence their reaction rate constants. Stereochemical control and chiral discrimination are essential features in biological systems. In this context, part of the interest in the present thesis has been focused on the effect of chiral center configurations on the diastereo-selectivity of the triplet quenching processes. This was accomplished by a comparison of the reactivity of pairs of diastereoisomers for benzophenone-tyrosine as well as for benzophenone-methionine dyads. In addition, special attention is paid to the effect of molecular geometry on the quenching rate constants. The role of the steric constraints on the overall reactivities was examined by modulation of the flexibility of the linkage between the interacting groups.

Furthermore, the impact of the reaction media on the rates and the actual transfer mechanisms is addressed. Since there are no systematic studies on the solvent dependence on the intramolecular H-atom transfer, one of the goals of this thesis is to perform detailed studies on the solvent dependence of the intramolecular H-atom transfer in order to verify whether the Ingold *et al.*'s concept of a Kinetic Solvent Effects (KSE)[13-17] of bimolecular H-atom transfer is applicable to intramolecular reactions. To clarify the respective solvent dependence on the photoinduced intramolecular reactions, studies on the dyads were augmented by results on a bimolecular system: benzophenone/anisole. It will be shown that the reactivity of an electronically excited molecule can be greatly enhanced by changes in the nature of the solvent. In particular, the efficient one-electron oxidation of anisole by triplet-excited BP in protic solvents allowed convenient access to the radical-cation chemistry of anisole.[18]

In order to describe photoinduced intramolecular reactions of hydrogen atom, electron and proton transfer, a comprehensive study was carried out by means of laser-flash photolysis and steady-state irradiations. These experimental studies were supplemented by the results from molecular-dynamics simulations and theoretical calculations. This theoretical work involved studies of the ground-state structures and conformations which established a quantitative picture of the conformer distributions of the dyads and triads and defined the molecular prerequisites of the individual quenching geometries.

These experimental and theoretical studies provided basic information on the kinetics of intramolecular reactions between tyrosine/methionine and triplet-excited benzophenone. This information opened possibilities for a discussion of the details of the transfer mechanisms in terms of the reaction media and the molecular structures. In addition, the results obtained verify whether a qualitative order of reactivity can be established. The bases for establishing this order of reactivity are geometric considerations and molecular-dynamics simulations. The latter makes use of the pair-distance distribution between the reacting groups as a function of the molecular structure. Most interestingly, as an extension to the previous knowledge, the work presented in this thesis addresses not only the question of the factors that have an impact on the overall reactivity but also of factors which characterize whether those parameters are independent or correlated with each other.

1.2 Molecules in the excited states

All photochemical and photophysical processes are initiated by the absorption of a photon of visible or ultraviolet radiation leading to the formation of an electronically-excited state. Light absorbing molecules contain groups called chromophores which are responsible for the absorption of the light. Absorption of ultraviolet and visible light by molecules results in electronic transitions in which changes in both electronic and vibrational states occur. The energy gap between electronic states is much greater than that between vibrational states.

An electronic configuration of an organic molecule is defined by listing the molecular orbitals that are occupied with electrons. The highest occupied molecular orbital is called the HOMO, and the lowest unoccupied molecular orbital is called the LUMO. Photon absorption of the appropriate energy results in excited-state configurations by the promotion of one electron from an occupied molecular orbital to a vacant molecular orbital. The electronic configurations of the ground state S_0 are generally $(HO)^2(LU)^0$ for ordinary organic molecules. An electronically excited state possesses one electron in each of the two key orbitals $(HO)^1(LU)^1$. Electrons in the half-filled orbitals can be of the same (parallel) spin or of different (opposed) spin. Such states correspond to triplet T and singlet S states, respectively. An excited triplet state generally has a lower energy than that of the corresponding excited singlet state, which is in agreement with Hund's rule. This rule states that when two unpaired electrons occupy different orbitals, there is minimum repulsion energy between the electrons when their spins are parallel. The excited states initially produced by absorption of a photon are almost always singlet states. This is because almost all organic molecules have a singlet ground state, and the selection rules for absorption strongly favor conservation of spin during an absorption process. From this aspect of molecular orbital theory, there are, in principle, six types of electronic transitions, designated: $\sigma\rightarrow\sigma^*$, $\sigma\rightarrow\pi^*$, $\pi\rightarrow\pi^*$, $\pi\rightarrow\sigma^*$, $n\rightarrow\sigma^*$, $n\rightarrow\pi^*$. If the two atomic orbitals are two s-orbitals then the resulting molecular orbitals are called σ bonding and σ^* antibonding orbitals. Molecular orbitals formed by mixing two parallel p-orbitals are called π if bonding and π^* if antibonding. Molecular orbitals, designated n, contain in the ground state a lone pair of electrons localized on just one atom.

Of the possible electronic transitions, more attention will be paid to $\pi\rightarrow\pi^*$ and $n\rightarrow\pi^*$ due to their relevance for the aromatic ketones used in this work, namely benzophenone. Absorptions due to $\pi\rightarrow\pi^*$ and $n\rightarrow\pi^*$ transitions differ from one another in several important aspects. First of all, $\pi\rightarrow\pi^*$ transitions normally occur at shorter wavelengths than do absorptions due to $n\rightarrow\pi^*$. In addition, $\pi\rightarrow\pi^*$ transitions are characterized by high values of molar absorption coefficients ε_{max} in the range of 10^3 – 10^5 M^{-1} cm^{-1} whereas $n\rightarrow\pi^*$ transitions have weak absorption with ε_{max} values of 1 – 10^2 M^{-1} cm^{-1}. In agreement with the description above, the UV-vis spectrum of benzophenone has a maximum absorption at 250 nm in acetonitrile with ε_{max} = 16000 M^{-1} cm^{-1} which can be assigned to a $\pi\rightarrow\pi^*$ transition. A weaker $n\rightarrow\pi^*$ transition appears at 340 nm in acetonitrile ($\varepsilon_{max} \approx 150$ M^{-1} cm^{-1}).[19]

1.2.1 **Dissipative pathways of excited states – Jablonski diagram**

Electronically-excited states of molecules have an excess of energy due to their being formed by photon absorption. These excited states are short-lived, losing their excess energy through a variety of deactivation processes. If the excited molecule returns to its original ground state, then the dissipative process is a physical process. However, if a new molecular species is formed, then the dissipative process is accompanied by chemical change. The properties of the excited states (relative energies, electronic configurations) and their relaxation processes are represented by Jablonski diagrams (Figure 1.2-1).

Radiative processes (blue solid arrows in Figure 1.2-1) involve the emission of electromagnetic radiation as the excited molecule relaxes to the ground state. Two processes can be distinguished:

- Fluorescence (**F**) – caused by a radiative transition between states of the same multiplicity. It usually occurs from the lowest vibrational level of the lowest excited singlet state, S_1: $S_1(v \rightarrow 0) = S_0 + h\nu_F$. Fluorescence is a rapid process with a rate constant k_F on the order of $10^6 - 10^9$ s^{-1}.[20]
- Phosporescence (**Ph**) – is the result of a spin-forbidden transition between states of different multiplicity, usually from the lowest vibrational level of the lowest excited triplet state T_1: $T_1(v \rightarrow 0) = S_0 + h\nu_{Ph}$. The process has a much smaller rate constant $k_{Ph} \sim 10^{-2} - 10^4$ s^{-1}.[20]

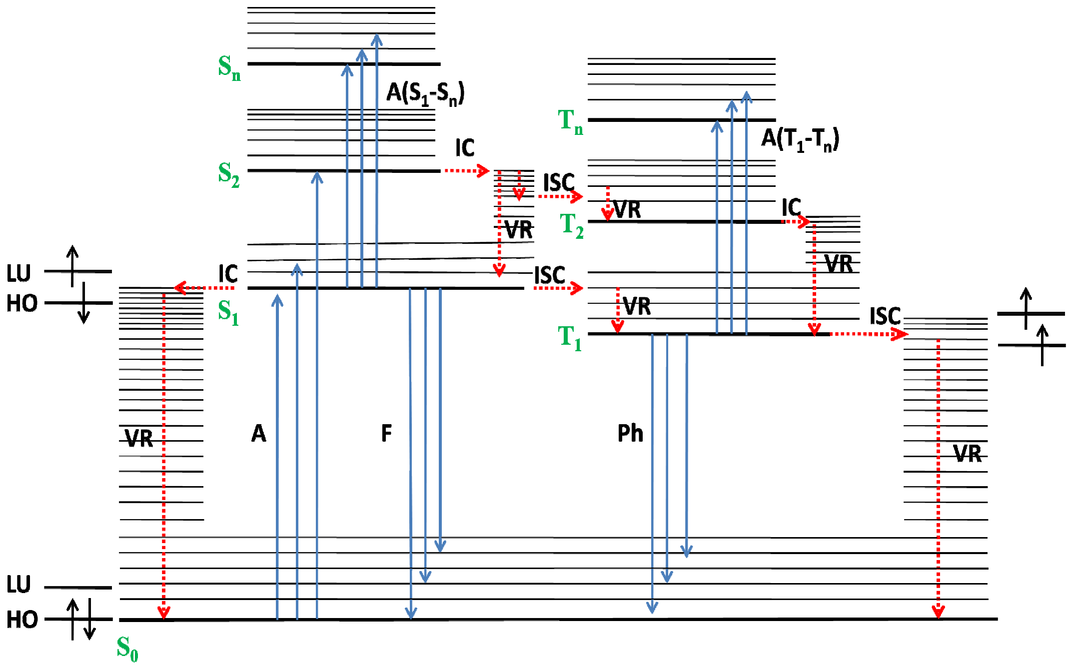

Figure 1.2-1 The Jablonski state energy diagram; blue solid arrows – radiative transitions, red dashed arrows – nonradiative transitions.

In contrast to radiative processes in radiatonless transitions (red dashed arrows in Figure 1.2-1) there is no emission of electromagnetic radiation accompanying the deactivation process. Radiationless transitions occur between isoenergetic vibrational-rotational levels of different electronic states. Among the radiationless transitions two processes can be identified:

- Internal Conversion (**IC**) – is a radiationless transition between different electronic states of the same multiplicity. Internal conversions from upper excited electronic states, e.g. $S_m \rightarrow S_n$, $T_m \rightarrow T_n$ are extremely rapid so that other radiative and nonradiative transitions do not generally occur from upper electronically-excited states as they cannot compete with these internal conversions. Internal conversion from the first excited singlet state, however, is so slow that fluorescence can compete with it. Typical rate constants for internal conversion between excited states k_{IC} are on the order of 10^{11} – 10^{14} s^{-1}.[20] It is worth noticing that the energy differences between the excited states for each multiplicity are usually less than between the ground state S_0 and the first excited states (S_1 or T_1). Thus, as a consequence of the energy gap law, irrespective of which upper excited states are initially populated, fast internal conversion and vibrational relaxation will relax an electronically excited molecule to its lowest vibrational levels of S_1 or T_1. This is the basis of Kasha's rule, which states that luminescence emission and chemical reactions of excited molecules will always originate from the lowest vibrational levels of S_1 and T_1.

- Intersystem Crossing (**ISC**) – is a spin-forbidden radiationless transition between isoenergetic states of different multiplicity, e.g. $S_1 \rightarrow T_1$. The intersystem crossing $S_1 \rightarrow T_1$ or $S_1 \rightarrow T_n$, which is competitive with fluorescence, is the process by which the triplet states can be populated. In addition, radiationless deactivations of the lowest triplet state $T_1 \rightarrow S_0$ compete with the phosphorescence from the T_1 state. The intersystem crossing usually has rate constants k_{ISC} on the order of $10^8 – 10^{11}$ s^{-1}.[20]

Vibrational relaxation (**VR**) involves transitions between vibrational states within a given electronic state. In solutions, this occurs efficiently when excited molecules collide with other species such as solvent molecules. The excess vibrational energy is dissipated as heat. Typical rate constants for the process k_{VR} are on the order of 10^9 – 10^{13} s^{-1}.[20]

The radiative and radiationless processes of excited-state deactivation described above are unimolecular processes that involve only one molecule. It is also possible to deactivate an excited state by an interaction with another molecule, in a process called quenching. Quenching processes occur by many different mechanisms and are induced by many different substances. Of these, oxygen is one of the most efficient quenchers of the excited states. Thus, in order to perform quantitative quenching studies, it is essential to limit its concentration.

Quenching of electronically excited states can occur by photophysical processes or by photochemical reactions, e.g photoaddition or photoreduction *via* hydrogen abstraction. Photophysical processes, which do not lead to new ground state products, can be divided into charge transfer, energy transfer and heavy atom effect. Photoinduced hydrogen abstraction and electron transfer are directly related with aspects of this thesis, and that will be described in detail in Chapter 1.3.1.1 and Chapter 1.3.1.2, respectively.

In order to determine what processes are most likely to occur from S_1 or T_1, information is required on the rate constants for all of the possible photochemical and photophysical processes that can compete for deactivation of these states. The relative rates of the transitions from a given state determine the probability of the various processes that can occur from that state.

Since the investigated compounds are all derivatives of benzophenone, its energy state diagram will be considered (Figure 1.2-2). This molecule is nearly nonfluorescent (quantum yield $\Phi_F < 10^{-4}$), and the lifetime of its singlet state S_1 is very short ($\tau_S \sim 10^{-11}$ s). At 77 K, benzophenone exhibits intense phosphorescence with a quantum yield $\Phi_{Ph} = 0.9$ and a lifetime of 6×10^{-3} s.[19] Almost every benzophenone molecule undergoes intersystem crossing to T_1 with a very high rate constant $k_{ISC} \sim 2 \times 10^{-11}$ s^{-1}.[21] This feature is common for a carbonyl compound having a $S_1(n,\pi^*)$ state with a closely-lying $T(\pi,\pi^*)$.

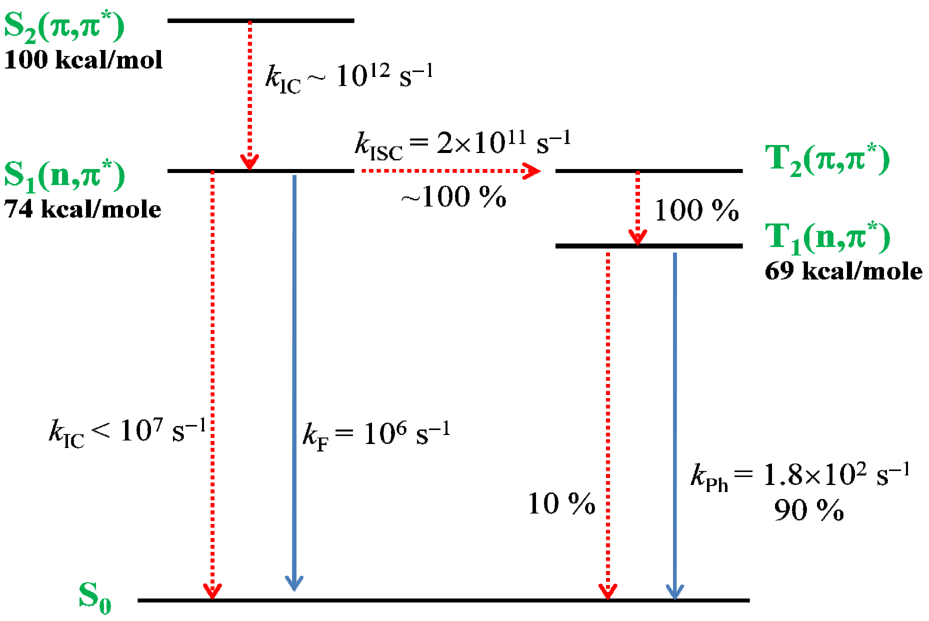

Figure 1.2-2 State diagram for benzophenone at 77 K.[19]

1.3 Selected aspects of the photochemistry of carbonyl compounds

Compounds containing the carbonyl C=O chromophore are widely and intensely investigated in photochemistry. The overall photoreaction of ketones and aldehydes is composed of two stages:

- the primary photochemical process which is typically initiated by $S_1(n,\pi^*)$ or $T_1(n,\pi^*)$ states and produces intermediates, e.g. radical pairs, biradicals, radical ion pairs;
- secondary thermal processes that lead to products.

All of the compounds investigated in the thesis were benzophenone derivatives. So, the following description of the photochemistry of carbonyl compounds will be limited to aromatic ketones.

1.3.1 Primary processes of carbonyl compounds and molecular orbital description of their excited states

The reactive state of aromatic ketones is generally the triplet state due to very efficient intersystem crossing (Figure 1.2-2). The description of the $T_1(n,\pi^*)$ excited state assumes that the n-orbital is localized on the O atom of the C=O group and that the π^* is delocalized over both atoms of the C=O group. In some molecules, e.g. benzophenone, the π^* molecular orbital is not only delocalized onto the C=O atoms but also to some extent onto other atoms which are conjugated with the C=O group. In addition, there is the possibility of mixing π,π^* states with n,π^* state. This can influence the photochemistry of the compound. For example, an n,π^* state that possesses some π,π^* character can undergo the same processes as a pure n,π^* state but with different rate constants.

An analysis of the orbital interactions of n,π^* states with HOMO and LUMO states of other molecules or with intramolecular groups gives a description of the possible kinds of photochemical primary processes. A molecule in an n,π^* state will interact *via* its n-orbital with a HOMO of another molecule, and *via* its π^* orbital with the LUMO of another molecule. Taking into account that orbitals of the HOMOs of organic molecules can be defined as σ, π and n orbitals, there are three possible types of interaction between the n-orbital of an n,π^* state with the HOMOs of another molecule: $n \leftarrow \sigma^2$, $n \leftarrow \pi^2$, $n \leftarrow n^2$. By analogy, there are only two categories for the LUMOs of organic molecules: π^*, σ^*; so, as a result, there are only two possible types of $\pi^*\rightarrow$ LUMO interactions: $\pi^*\rightarrow\pi^*$, $\pi^*\rightarrow\sigma^*$. A summary of all the fundamentally different types of orbital interactions involved with a typical primary photochemical processes are presented in Figure 1.3-1.

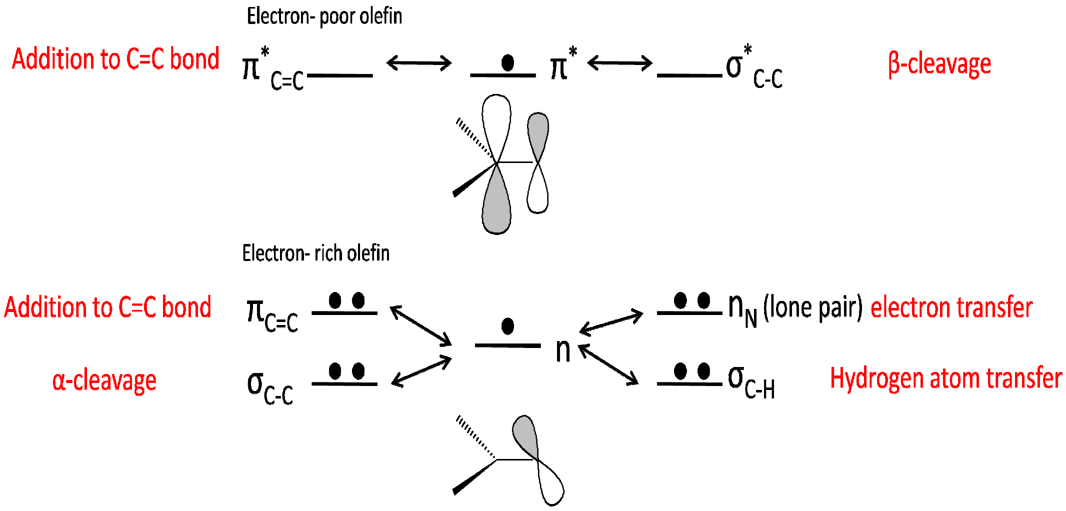

Figure 1.3-1 Possible primary reactions of the n,π^* state based on the orbital interactions.[19]

Electron transfer and hydrogen atom abstraction relevant to the work presented in this thesis will be discussed separately in Chapters 1.3.1.1 and Chapter 1.3.1.2, respectively.

1.3.1.1 **Photoinduced hydrogen atom transfer**

Photoinduced hydrogen-abstraction reactions by triplet-excited carbonyl compounds have been a central topic of photochemical research for many years.[19, 22, 23] The mechanisms involve transfer of a hydrogen atom to the oxygen atom of the carbonyl excited state from a donor moiety which may be a solvent molecule, an added reagent or an intramolecular hydrogen-atom donor. As a consequence, possible reactions of the investigated compounds with the solvent molecule have to be taken into account in such experiments. Abstraction of a hydrogen atom by the triplet excited state of a carbonyl compound from a hydrogen donor XH leads to a geminate radical pair $^3I(RP)_{gem}$ that consists of a ketyl radical and an X radical:

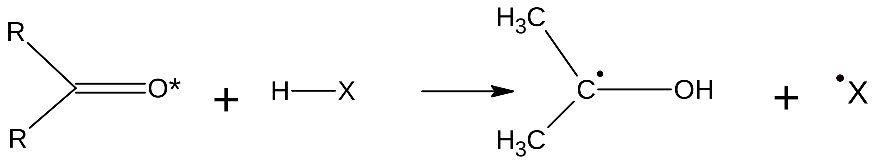

The ${}^{3}I(RP)_{gem}$, before undergoing combinations or disproportionation, needs to undergo intersystem crossing. However, this process takes ~ 10^{-8} s and is slower than the escape of the geminate radical pair from a solvent cage in non-viscous solvents. The favored route for secondary reactions depends on the structure of the radical intermediates, on the concentrations of the reagent, on the hydrogen-donor power of the reducing agent and on the temperature. The most common reaction involving alcohol as H-donor leads to the corresponding pinacol with high yields.

The nature of the lowest excited triplet state and hence the electron distribution in this state of the carbonyl compound is of decisive importance in the process of hydrogen atom transfer. As an example, there is an almost three orders of magnitude difference in the rate constant of H-abstraction from 2-propanol by benzophenone in a $T_1(n,\pi^*)$ state ($k_q = 1 \times 10^6\ M^{-1}\ s^{-1}$) and 4-phenylbenzophenone in a $T_1(\pi,\pi^*)$ state ($k_q = 5 \times 10^3\ M^{-1}\ s^{-1}$).[19] The smaller reactivity of the $T(\pi,\pi^*)$ state toward hydrogen abstraction might be a very good way to observe switching between $T_1(n,\pi^*)$ and $T_1(\pi,\pi^*)$ states with a change in the solvent. For example, the rate constant for triplet acetophenone to abstract hydrogen from 2-propanol decreases by three orders of magnitude in going from benzene to acetonitrile which indicates that the triplet state has π,π^* character in acetonitrile. The rate constant for hydrogen abstraction can be increased by using better hydrogen donors with weaker H-X bonds.

The reactivity of n,π^*excited triplet aromatic ketones, mostly benzophenone, with alkanes,[24] alcohols,[25] hydrides,[26] alkylbenzenes,[27, 28] and amines[29, 30] has been investigated to establish the role of the donor in the hydrogen abstraction process. These works revealed that hydrogen abstraction can occur by a variety of mechanisms depending on the identity of the hydrogen atom donor. These mechanisms include (1) “pure” alkoxy radical like abstraction,[31, 32] (2) a reaction initiated by charge or electron transfer to the excited carbonyl compound from the hydrogen atom donor, followed by proton transfer,[28, 33-35] and (3) a mechanism involving an intermediate hydrogen-bonded triplet exciplex.[36, 37] The configuration of the lowest triplet state is believed to be less important in electron transfer-mediated reactions. Thus for most amine donors, for example, the rate constants are determined primarily by the thermodynamics of electron transfer.[38] The mechanism for charge transfer (CT) assisted hydrogen abstraction from alkylbenzenes is believed to involve the initial formation of an exciplex, held together by interactions between the electron-deficient n-orbital of the ketone and a π-MO of the H-donor. This results in a slight increase in the acidity of the transferring hydrogen which, in fact, facilitates its transfer. Rate constants for ketone triplet quenching *via* this mechanism correlate with both the arene ionization potential and the triplet reduction potential of the ketone.[28]

1.3.1.1.1 **Hydrogen atom abstraction by phenols**

Among all of the photoinduced hydrogen atom transfer reactions, special attention has been given to reactions between remote phenol and triplet-excited ketone moieties since hydrogen-atom abstraction from phenols is certainly one of the most important oxidation processes in biochemical systems. Starting with the seminal study by Das and Scaiano in 1981,[36] reactions of phenols with triplet-excited carbonyl compounds have stimulated recurrent interest.[27, 37, 39-60] There is much interest and controversy in the mechanism of the H-atom transfer quenching of aromatic triplet states by phenols. Three main mechanisms of the phenols' action as a hydrogen-atom donor are generally discussed: 1) hydrogen-atom transfer (HAT) with the electron and proton being transferred in one kinetic step; this notation includes proton-coupled electron transfer (PCET); 2) sequential proton loss and electron transfer (SPLET), which was put forward only recently by Litwinienko and Foti;[15, 61] and 3) electron-transfer followed by proton transfer (ET-PT).[62, 63]

Das and Scaiano presented, for the first time, data on absolute rate constants for the reactions of aromatic carbonyl triplets with phenols. They used 18 different phenols to quench the triplet state of benzophenone, having its lowest triplet state being of n,π^* character, and p-methoxypropiophenone, with its lowest triplet state of π,π^* character. Representative rate constants for benzophenone triplets in benzene were measured to be 1.3×10^9 M^{-1} s^{-1} (phenol) and 8.1×10^8 M^{-1} s^{-1} (m-fluorophenol) while for p-methoxypropiophenone the respective values were 4.9×10^9 M^{-1} s^{-1} and 5×10^9 M^{-1} s^{-1}. Irrespective of the electronic nature of the lowest excited triplet state (n,π^* *vs.* π,π^*), H-atom transfer from phenols occurred with high efficiencies (usually close to unity), in particular much higher rates than were observed for aliphatic alcohols. The high efficiency of radical intermediate formation was contrasted by a very inefficient product formation.[36] The excited-state energy thus is dissipated *via* consecutive H-atom transfer steps, which regenerate the starting materials in their electronic ground state. Aromatic ketones abstract hydrogen from phenols at rates that are substantially faster than those from substituted toluenes, which is what might be expected on the basis of the lower ionization potential and bond dissociation energy of phenol compared to those of toluene.[36] However, the lack of a significant difference in n,π^* and π,π^* triplet ketone reactivity with phenols and the generally small kinetic isotope effects for H-transfer in these reactions both tend to argue against a simple H-atom abstraction mechanism. Kinetic isotope effect measured by Das and Scaiano for the benzophenone triplet state quenched by phenol in an acetonitrile-water (9:1 v/v) mixture was only k_H/k_D = 1.2.[36] Those researchers also showed that protic solvents have a rate retarding effect for benzophenone and p-methoxypropiophenone, which has been suggested to be the result of hydrogen bonding between the solvent and both the phenol[37] and the excited ketone.[64]

Recently, evidence has been presented for the formation of encounter complexes prior to H-atom transfer between phenol and the excited ketone benzoylthiophene, with a π,π^* lowest triplet, based on laser flash photolysis results and DFT calculations.[52, 53] Perez-Prieto *et al.*[52, 53] demonstrated that photoreduction of benzoylthiophene (BT) in the presence of phenol or indole generates ketyl radicals with high rate constants and quantum yields close to 1. However, long irradiation times were needed (mainly in the case of indole) to achieve important conversions in the steady-state irradiation experiments. These data confirmed that ketyl and phenoxyl or indolyl radicals largely react to regenerate the starting materials, which was also observed for the photoreactions of benzophenones with phenols and amines. Based on the different trends observed for the solvent-dependence of the quenching rate constants, together with DFT theoretical studies, they proposed fundamental differences between the mechanisms of the reaction of the BT triplet with phenol and indole. Specifically, they proposed that the reaction for the BT/phenol pair involves a hydrogen-bonded exciplex, where concerted electron and proton transfer leads to a radical pair. Conversely, in the case of indole, electron-transfer precedes proton transfer. Pereze-Prieto *et al.* suggested that this marked reactivity difference arises from the lower ionization potential and acidity of indole, together with the lower acidity of the indole radical cation, when compared to the corresponding values for phenol and its radical cation.

Leigh *et al.* in 1996 have also proposed that the alkoxyacetophenones' (π,π^*) mechanism of hydrogen abstraction from phenol involves hydrogen bonding between the excited triplet ketone and the phenol, in which net hydrogen atom transfer occurs in the form of a coupled electron/proton transfer. The hydrogen bonding interaction was proposed to adjust the reduction and oxidation potentials of the reactants to the extent where electron transfer becomes thermodynamically favorable.[37] Such a process is expected to be more favorable for ketones with the lowest state being the π,π^* triplet state because of the increased basicity in this type of triplet configuration in comparison to ketones with n,π^* as their lowest triplet state. Detailed study of the quenching of fluorenone (π,π^*) triplets by phenol in aprotic solvents led Linschitz and co-workers to the same mechanism.[39] In 2006 Leigh and co-workers reported extensive results for rate constants of reactions involving the lowest triplet states of 37 aromatic ketones with p-methylphenol in acetonitrile. The list of investigated ketones included substituted benzophenones, acetophenones and several bicyclic and tricyclic compounds with different configurations of the lowest triplet state. Based on the plots of log k_q *vs.* the triplet reduction potential, they suggested that phenolic quenching of ketones with a lowest n,π^* state proceeds *via* two mechanisms, depending on the triplet state reduction potential and the proximity of the higher lying π,π^* triplet state. Electron-acceptor-substituted benzophenone derivatives were proposed to be quenched by the charge transfer exciplex mechanism where the charge flows from the aromatic ring of the donor into the half-filled n-orbital of the ketone. The quenching rate constant for this mechanism depends both on the oxidation potential of the hydrogen donor and reduction potential of the acceptor. Quenching of electron-donor-substituted derivatives, on the other hand, was proposed to proceed, as with the π,π^* triplet state, *via* the hydrogen-bonded exciplex mechanism involving the higher-lying, relatively basic π,π^* triplet states. The quenching situation for the π,π^* triplet state is expected to be different in protic solvents, in which the solvent dominates as a hydrogen bond agent and thus the hydrogen-bonded exciplex mechanism cannot operate. The mechanisms of the phenolic quenching of the π,π^* triplet state and the n,π^* triplet state merge into the electron-transfer mechanism when the triplet reduction potential is reduced to the level at which the free energy of electron transfer becomes negative. Clear evidence for a two-step process, initiated by electron transfer, ET, is limited to aqueous media.[41, 59] Recent work by Sultimowa and co-workers showed that the quenching process of the triplet state of 4-carboxybenzophenone (CB) by phenol in water proceeds, at any pH, *via* an electron transfer. By direct observation, they observed the radical anion $CB^{\bullet-}$ which at pH = 8 is protonated, producing a ketyl radical $CBH^{\bullet}$.

1.3.1.1.1.1 Intramolecular H-atom transfer

The biochemical applications of H-atom transfer naturally generate special interest in the intramolecular version of triplet carbonyl-phenol quenching of covalently bound dyads. Various aspects of this photoprocess can be considered. Although intramolecular H-atom transfer is expected to be affected by the molecular structure, the effects of steric constraints on monomolecular reaction rates have been the subject of only a few studies.[46, 55, 65] The chemical nature of the linker between the chromophores, that is, the flexibility and the directionality of the linker, has been reported to be a major source of kinetic diversity. Remarkable variations in the reaction rates of isomeric ketone/phenol dyads have been attributed to modulations of the distance distributions and relative orientations of the reacting moieties. Moreover chiral center configurations have been reported to influence the monomolecular quenching of ketone triplets by phenols covalently linked by flexible spacers.[51, 54] In addition, the intramolecular reactivity of the phenol with the triplet-excited ketone is expected to be substantially dependent on the H-bonding properties of the medium. However, the solvent dependence of intramolecular H-atom transfer reactions in ketone/phenol dyads, in contrast to intermolecular H-atom transfer, has not been addressed in detail.

Issues such as stereoelectronics, steric hindrance effects and the influence of the chemical surroundings will be discussed in detail in the following chapters since they seem to be the most important factors that may influence the kinetics and mechanism of hydrogen abstraction.

1.3.1.1.1.1.1 Chiral discrimination

Chiral recognition is a subject of increasing interest in photochemistry. In principle, the use of chiral compounds can enable examination of pure chiral discriminations by a comparison of their quenching rates, since diastereoisomers have the same electronic nature and are of the same size. However, the diastereodifferentiating interactions in the intramolecular hydrogen abstraction by excited triplet aromatic ketones from different donors have been rarely reported.[51, 54, 66-68]

Aside from abstracting hydrogen atoms from the phenols, it is noteworthy to mention briefly chiral discriminations in intramolecular abstractions from other hydrogen donors. Bosca and co-workers undertook a study in order to detect a possible chiral discrimination in the intramolecular abstraction of allylic hydrogens (S- or R- 1,2-dimethylcyclohexa-2-5-diene-1-methanol) by benzophenone triplets (S-ketoprofen).[67] Intramolecular quenching of the triplet aromatic ketones with allylic systems occurs by hydrogen abstraction and by physical quenching with the allylic π system. The results presented by Bosca indicated that there is a chiral discrimination in all the photophysical and photochemical processes involved in intramolecular hydrogen abstraction. The stereoselectivity factor, expressed as the ratio of the rate constants for a pair of diastereoisomers involved in the hydrogen abstraction process, was equal to 2.3. Abad and co-workers investigated a series of diastereomeric compounds combining (S)-ketoprofen and tetrahydrofuran or isopropylbenzene moieties as hydrogen donors.[66] The highest stereoselectivity found in that work was 1.8. The authors stated that the observed stereodifferentiation was the result of three factors: 1) the strain introduced in the cyclic transition state for hydrogen abstraction, 2) the steric hindrance related to the close approach between the two active moieties and 3) the degree of freedom associated with conformation equilibra.

Enantioselective discrimination in the intramolecular quenching of the excited aromatic ketone by a phenol in diasteromeric dyads was reported by Miranda *et al.* in 1999.[51] They have investigated the four enantiomerically pure bichromophoric compounds obtained from the thiaprofenic (TPA) acid or suprofen (SUP), with the methyl ester of the naturally occurring amino acid (S)-tyrosine. Remarkable stereodifferentiation was found for the triplet lifetimes of the bichromophores. The largest difference of the triplet lifetimes was reported for the pair of diastereoisomers (S,S)-SUP-Tyr and (R,S)-SUP-Tyr in MeOH. The values measured were 312 ns and 45 ns, respectively. Inversion of the configuration in one stereocenter produced a marked variation in the triplet lifetimes, which indicated that there are specific structural requirements for the intramolecular quenching of the aromatic ketones. The authors related the reactivity of the systems with the ability of the compound to form a parallel, sandwich type arrangement of the aromatic rings connected through the aliphatic chain. Even small deviations from parallel were associated with the observed decrease in the reactivity. The extended analysis of the stereodifferentiations of those systems was presented in 2004.[54] In addition to previous work, considerable stereodifferentiation was also observed for the biradical lifetimes, which was connected with the ease of the system to undergo intersystem crossing. The results of the stereodifferentiation in the intramolecular quenching could have important biological consequences. Thiaprofenic acid and suprofen have been shown to be potent photoallergens. This is thought to depend on the binding of the drugs to proteins, probably to tyrosine residues. In this regard, Perez-Prieto and co-workers[54] found, in the remarkable configuration-dependent photobehavior of the bichromophoric compounds, the possibility of a different photoallergenic potential for the drug enantiomers.

1.3.1.1.1.1.2 **Geometric effects**

In the current section the role of geometric factors in intramolecular phenolic hydrogen abstraction by aromatic ketone triplets will be reviewed. Leigh and co-workers showed that rate constants of H-atom transfer varied strongly with the position of the attachment of oxyethyl spacers to the carbonyl and phenol moieties.[46, 48] This research group has studied bichromophoric compounds having a para- or meta- phenolic moiety attached *via* meta- or para- three-atom (oxyethyl) spacers to acetophenones, indanones, and benzophenones. The effect of the different positions of the attachment of the oxyethyl linker on the triplet lifetimes of the phenolic ketones were reported to be significant. The reaction of the meta,meta’ analogue of the phenolic acetophenone toward intramolecular H-atom transfer was found to be 500 times slower than the reactions of the para,para’ analogue although the rate constants for the bimolecular quenching of p- and m-methoxyacetophenone by p- and m-cresol were similar. The differences between para and meta positional isomers for benzophenone and indanone derivatives follow the same trends, but the ratio of the triplet lifetimes between meta,meta’ and para,para’ isomers were less pronounced and equal to 18 and 2.5 for the benzophenone and indanone derivatives, respectively. Lathioor *et al.*[46] concluded that the origin of the variation of the triplet lifetimes in the phenolic ketones must be connected with structural factors that affect the ease with which the molecules can adopt a conformation that allows for fast hydrogen atom transfer. They have proposed, based on molecular mechanics calculations, that the much longer triplet lifetime for the meta,meta’ phenolic acetophenone derivative is due to its ability to adopt conformations in which the phenolic hydrogen is within abstracting distance of the carbonyl oxygen, but in which there were no overlaps between the aryl rings. In contrast, the very reactive para,para’ analogue can form a sandwich-like geometry with nearly perfect orbital overlap between all six carbons of the two aromatic rings, which were thought by

Lathioor *et al.* to be required for fast H-atom transfer. Based on all the experimental and theoretical data, they proposed that the almost three-orders of magnitude difference between the triplet lifetimes of the above discussed acetophenones is a characteristic of the intramolecular hydrogen abstraction by the ketones connected *via* meta,meta' – *vs.* para,para' – oxyethyl linkages when the lowest triplet states are of the π,π^* configuration and possess moderate charge transfer character.

The relative reactivity factor of 18, measured for the meta,meta'-linkage compared to para,para' of the phenolic benzophenones, was one order of magnitude smaller than the analogous relative reactivity of 500 measured in the acetophenone series. The proposed reason for this constrasting behavior is related to the electron-withdrawing character of the meta-alkoxy substituent which facilitates the formation of conformers in which the n-orbital of the carbonyl oxygen is directed into the π-system of the remote phenolic group. The additional quenching path *via* an n-type exciplex for meta,meta' phenolic benzophenone, which is geometrically impossible in the para,para'-analogue, resulted in smaller differences in relative reactivity between the para,para' and meta,meta' benzophenone derivatives. The work presented by Lathioor *et al.* [46] has further shown that the geometric constraints on intramolecular motions, tuned by different positions of the attachment of oxyethyl spacers within the phenolic ketones, have observable consequences for their intramolecular reactions.

Perez-Prieto and co-workers also took up the subject of the geometric effects on intramolecular H-atom transfer.[55] They have investigated the process of model bichromophoric compounds where the linker between the donor group (phenol, indole) and the 2-benzoylthiophene chromophore is attached either to the thienyl's 5-position or the benzoyl's para position. This structural difference caused a marked influence on the photoreactivity of the compounds. In general, for all 12 investigated compounds, quenching rate constants were higher for the 5-alkyl-2-benzoylthiophenes than for their corresponding regioisomers, 2-(p-alkylbenzoyl)thiophenes. Interestingly, the time-resolved studies have shown that the rate constants for the bimolecular quenching of 2-benzoyl-thiophene substituted at the thienyl's 5-position were lower than those for the 2-benzoylthiophene substituted at the benzoyl's para position. Thus the trend for this intermolecular triplet quenching is opposite to the analogous intramolecular reaction. It shows that predicting the influence of geometric factors on intramolecular hydrogen abstraction is not trivial. Based on DFT calculations, Perez-Prieto *et al.*[55] suggested that possible overlapping of the molecular orbitals is the origin of the variation of the reactivity of the bichromophoric compounds with different positions of the substituent. The 5-alkyl-2-benzoylthiophenes showed a more favorable orbital interaction of the approaching atoms in the exciplex and were found to be the more reactive isomer.

Work by Hörner and co-workers has presented another point of view of the geometry being an important factor in controlling the intramolecular reactivity toward hydrogen.[65] They addressed the question of how the intramolecular reactivity of ketone/phenol dyads could be modulated by tuning the flexibility of the linkage between the interacting groups. The study addressed the effects of molecular geometry on the intramolecular triplet quenching in four benzophenone-tyrosine dyads, synthesized from three benzophenone carboxylic acids and (*S*)- and (*R*)-tyrosine methylester, Tyr-OMe. It was found that the rate constants for the H-atom transfer depended markedly on the dyad geometries with values varying by three orders of magnitude in acetonitrile solution. Hörner *et al.* interpreted the reactivity order of the four dyads in terms of molecular geometry. Discussion was based on the results of ground-state NMR and molecular modelling. Within a series of three meta-substituted dyads that differed only in the nature of the amide-linking group between the phenol and the triplet-excited ketone, the reactivity could be correlated with the probability of close contacts and the extent of electronic overlap.

Substantially smaller H-atom-transfer rates were found for the dyad whose chromophores were connected *via* a rigid amide bond, compared to the rates found in two more flexible alkylamide dyads. This was true even though similar distance distributions of the reacting moieties prevailed in all three cases. This was interpreted as due to insignificant aromatic–aromatic interaction, found in NMR. A lack of intramolecular reactivity was observed for the compounds that had a rigid amide bond in the para-position. Based on the results of simulations, it was concluded that the presence of a rigid amide bond linked in the para-position confines the accessible space of the remote groups in a way such that close contacts between the ketone and the phenol are completely inhibited. The directionality of the benzamide linker between the two chromophores effectively excludes reactive intramolecular contacts and thereby inhibits the concerted HAT pathway. Lack of the reactivity of the dyad linked by a rigid amide bond in the para position is in agreement with the work of Wagner,[32] who found an upper limit of 3.1 Å for the distance between the carbonyl oxygen and the H-atom of the donor RH to allow an intramolecular HAT quenching. In summary, in cited work of Hörner *et al.* the observed order of reactivity correlated with both the probability of close contacts and the extent of the electronic overlap between the π systems of the donor and acceptor moieties.

Studies of the intramolecular HAT of several phenolic ketones have provided evidence that the chemical nature of the linker between the chromophores, that is, the flexibility and the directionality of the linker, is one major source of kinetic diversity. Based on literature reports, it can be stated that remarkable variations in the reaction rates of isomeric phenolic ketone dyads can be attributed to modulations of the distance distributions and relative orientations of the reacting moieties.

1.3.1.1.1.2 **Kinetic solvent effect**

The concept of a Kinetic Solvent Effect (KSE) on the rate of H-atom transfer reactions by specific solvation of the H-atom donor has been elaborated mainly by Ingold and Lusztyk within the past two decades.[13-17, 69-71] Systematic studies of the solvent dependence on the rate constants of hydrogen abstraction were made on various H-donors: tert-butyl hydroperoxide, numerous phenols, aniline, cyclohexane and different radicals such as diphenylpicrylhydrazyl and cumyloxyl radicals. The model on which the KSE was derived is based on an H-bond equilibrium (XH---solvent) in a simple kinetic scheme (Scheme 1.3-1)

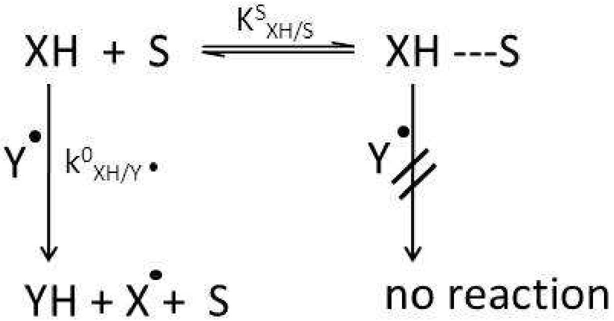

Scheme 1.3-1

This simple kinetic model assumes that each substrate molecule, XH, can act as a hydrogen-bond donor to only a single hydrogen-bond acceptor solvent molecule, S, at any time. Moreover for steric reasons, the H-atom in the XH-S complex cannot be directly abstracted by the radical $Y^{\bullet}$. It means that only a small fraction of the XH molecules can react with $Y^{\bullet}$, in particular, the ones that are not hydrogen bonded to a solvent molecule, S.

Based on this model and the analysis of the experimental results for intermolecular H-atom abstraction, the Kinetic Solvent Effect was quantified in one single empirical equation (Eq 1.3-1) which predicts reaction rates, if the HB-acceptor ability, $\Sigma\beta_2^{H}$, of the solvent is known[13-17, 70]

$$log\left(k_H^S/M^{-1}s^{-1}\right) = log(k_H^0/M^{-1}s^{-1}) - 8.3\Sigma\alpha_2^H\Sigma\beta_2^H \qquad \text{Eq 1.3-1}$$

In this equation, k_H^S and k_H^0 denote the bimolecular rate constant for H-atom abstraction from a H-atom donor by a radical in the solvent S under study and in a reference solvent that has negligible HB-acceptor ability (usually a hydrocarbon), respectively. The parameters $\Sigma\alpha_2^{H}$ are the solutes' HB-donor abilities given by the constants of Abraham *et al.*.[72] Values of $\Sigma\alpha_2^{H}$ range from 0.00 in alkanes to nearly 1.00 for strong acids. The relative hydrogen-bond acceptor (HBA) properties of solvents are given by the $\Sigma\beta_2^{H}$ constants of Abraham *et al.*[73] These $\Sigma\beta_2^{H}$ values represent a general, thermodynamically related scale of solute hydrogen-bond basicites in CCl_4 and vary in magnitude from 0.00 for a non-HBA solvent such as an alkane to 1.00 for hexamethylphosphortriamide, the strongest organic base. The scale contains values of $\Sigma\beta_2^{H}$ for at least 400 organic compounds. The monotonic decrease of rate constants with increasing $\Sigma\beta_2^{H}$ of the solvents, as implied in Eq 1.3-1, is interpreted as being due to a reduction in the concentration of free phenol by hydrogen bonding to the solvent. It is based on the assumption that only the fraction of phenol that is not H-bonded to the solvent is active towards H-atom transfer. An important implication of this model is that the nature of the attacking radical, which implies also its solvation properties, has no impact on the KSE.

Triplet states are commonly taken to be radical-like in nature,[74] so it is reasonable to expect that the KSE concept should hold when applied to a description of H-atom transfer in the quenching of a triplet-excited ketone by phenols. The KSE model with its argument of a solvent-dependent "masking" of the phenol was used to interpret the solvent dependence of rate constants for intermolecular triplet quenching by phenols, qualitatively[39, 45] and quantitatively.[44] In the latter study the rate constants for H-atom transfer from phenol to the triplet state of 2-benzoylthiophene were analyzed in terms of Eq 1.3-1. This equation predicts a slope of −4.9 for a linear fit of log (k_H^S / $M^{-1}s^{-1}$) *vs.* $\Sigma\beta_2^H$ in describing H-atom transfer reactions with phenol ($\Sigma\alpha_2^H$ = 0.59), independent of the hydrogen acceptor.[72] Experimentally a significantly smaller slope of −3.9 was found for the bimolecular quenching. The deviation was associated with increasing contributions of an electron-transfer-initiated mechanism in strongly HB-accepting solvents.[44]

Solvent effects have also been commonly observed on the rates of intramolecular H-atom transfer in ketone-phenol dyads.[37, 46, 51, 54, 65] The relative order of the rates has been tentatively ascribed to the H-bond acceptor properties of the surrounding medium but was based on data in only 2-3 solvents.[54, 65] There are no systematic studies on the solvent dependence of intramolecular H-atom transfer except for two works by Hörner and co-workers.[75, 76] Thus, one of the goals of this thesis was to perform detailed studies on the solvent dependence of intramolecular H-atom transfer and to verify whether the Ingold *et al.*'s concept of a KSE towards H-atom transfer could also be applied to intramolecular reactions.

1.3.1.2 **Photoinduced electron transfer**

Photoinduced electron transfer (PET) is one of the most important chemical processes in nature, and it plays a central role in many biological, physical and chemical (both organic and inorganic) systems. Photosynthesis involves a chain of electron-transfer reactions, which result in effective charge separation and lead to a proton gradient across a biological membrane. As a result, sunlight energy is stored and can be used for the formation of energy-rich adenosine triphosphate. In proteins and other macromolecules, such as DNA, the transfer of electrons occurs over distances that are significantly larger than the sum of the van der Waals radii of the electron donor and the acceptor. Moreover PET plays a role in semiconductor photocatalysis, silver halide photography and xerography. Studying PET processes in well-defined model systems may lead to further insight into the early events of the biological processes that are responsible for a major part of the energy cycle on earth.

Light induced electron transfer is a process in which an electron is transferred from an electron donating species to an electron accepting species. Prior to electron transfer one of the components is excited with light. In PET, the excited state, R^*, can be either an electron donor or an electron acceptor when reacting with another molecule, M (Figure 1.3-2 and Figure 1.3-3).

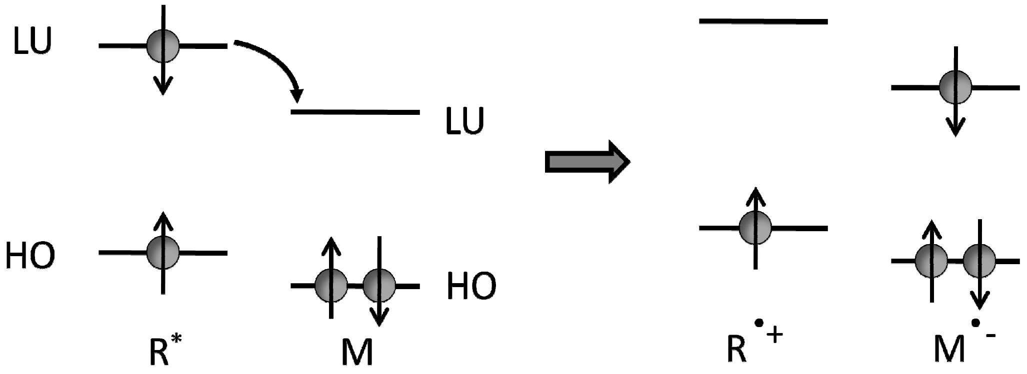

Figure 1.3-2 Molecular orbital representation of oxidative electron transfer.

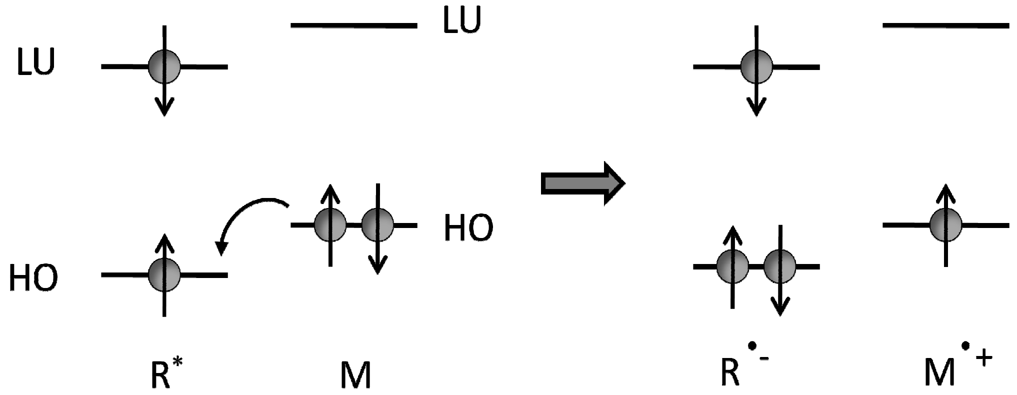

Figure 1.3-3 Molecular orbital representation of reductive electron transfer.

Subsequent to an electron transfer in which both the donor and acceptor are neutral species, a charge transfer state is created consisting of the radical cation of the donor and the radical anion of the acceptor.

An important parameter of photoinduced electron transfer is the rate constant k_{ET} of the primary process. The rate constant k_{ET} has been found to depend on several factors.[77-84] These factors include the separation distance of R^* and M, the relative orientation of the electron donor and acceptor (that determines the effective orbital overlap), solvent polarity, excitation energy of R^* and the redox potentials of R^* and M that influence the Gibbs free energy change. During the past decades, there have been numerous studies on photoinduced intramolecular electron transfer in covalently linked donor-bridge-acceptor compounds that incorporate hydrocarbon bridges e.g. steroids,[81] cyclohexyls,[77] or norbornylogous[80] types, to link two chromophores. Based on these studies much information has been obtained about this process, regarding distance dependence, symmetry effects, influence of the bridge configuration (rigid spacer, flexible spacer) and the energetics.

Oevering *et al.*[80] studied a series of molecules containing a 1,4-dimethoxynaphthalene as an excited state electron donor and a 1,1-dicyanoethylene moiety as an electron acceptor connected by 5 different, rigid and nonconjugated bridges. The length of the bridges varied to provide donor-acceptor center-to-center separations ranging from 7.0 – 14.9 Å. One of the main aims of the work was to obtain experimental insight into the manner in which the rate of PET is modulated by the bridge linking the donor and acceptor groups. Indeed, the rate constant k_{ET} showed only a small dependence on the solvent polarity but decreased significantly with increasing separation distance, ranging from $> 10^{11}$ s^{-1} for a four-bond separation to 4×10^{8} s^{-1} for a 12-bond separation. One of the most remarkable features of this work was the observation that a saturated hydrocarbon bridge can be highly effective in mediating electron transport. Electron transfer based on Fermi’s golden rule requires electronic coupling between the donor and acceptor. The magnitude of the electronic coupling depends on the overlap of the wave functions of the donor and the acceptor. Electronic wave functions of the donor and acceptor cannot overlap significantly when they are separated by a distance of 10 Å. However, very large values of k_{ET} were nonetheless found for compounds with such a large distance separation. In that case, a second mechanism was proposed for the electronic coupling of the donor and acceptor that uses the wavefunctions of the σ and σ^{*} orbitals of the spacer in assisting the propagation of the electronic coupling interaction between the donor and acceptor. This mechanism is called electron superexchange or through-bond electronic coupling.

1.3.1.2.1 **Energetics of photoinduced electron transfer**

Photoinduced electron transfer can be regarded as the process where light energy is converted into electrochemical energy. However, successful electron transfer depends on thermodynamic factors. At heart of electron transfer photochemistry lies the fundamental thermodynamic condition which states that spontaneous electron transfer reactions require a negative overall free energy (Gibbs energy) change. The reactants must not only meet this exothermic condition for electron transfer, but the lifetime of the excited sensitizer (electron donor or acceptor) must be long enough to make quenching by electron transfer possible.

The excited state R^* is always both a better oxidizing and a better reducing species than the ground state R. Electron affinity (*EA*) is the energy released when an electron is moved from a non-interacting environment at infinity into a vacant orbital near the nucleus. The *EA* for the excited state R^* is larger than for the ground state (Figure 1.3-4), since more energy is released in going from the ionization limit to the half-filled bonding HOMO than in going from the ionization limit to the antibonding LUMO of any molecule. On the other hand, the ionization potential is lower for the excited state R^* than for the ground state because it requires less energy to remove an antibonding electron from the LUMO since electrons are not as strongly bound as core electrons from the HOMO of the ground state, R. All this is schematically summarized in Figure 1.3-4.

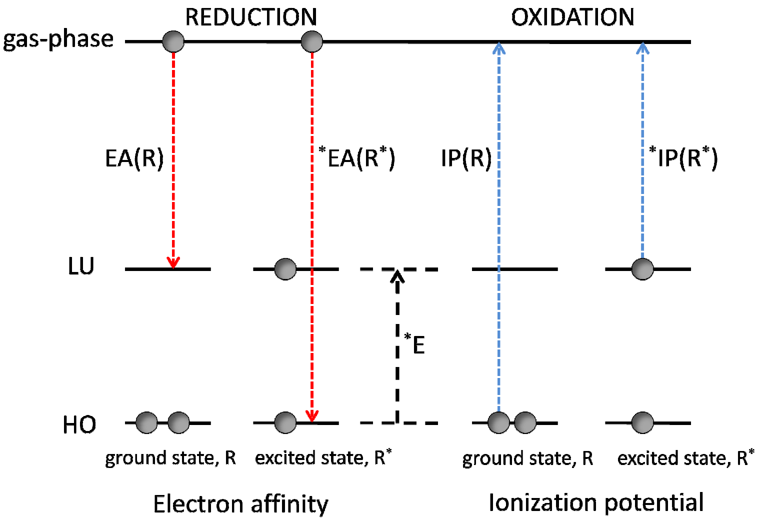

Figure 1.3-4 The ionization potential (*IP*) and electron affinity (*EA*) of an excited state are decreased and increased, respectively, as compared with the ground state.

The free energy change in the gas phase for ground state electron transfer is equal to the difference in the ionization potential of the donor (IP_D) and the electron affinity of the electron acceptor (EA_A). For an excited donor, the free energy change for excited state electron transfer differs from the free energy of ground state electron transfer by the amount of the electronic excitation energy ($E_{o,o}$) (Eq 1.3-2).

$$\Delta_{ET}G^o = IP_D - EA_A - E_{o,o} \qquad \text{Eq 1.3-2}$$

The more negative the free energy change, the more exothermic the reaction is. Based on Eq 1.3-2, it should be noted that excitation energy provides a negative contribution to the free energy change which makes the excited state more favorable for electron transfer compared to the ground state. Ionization potentials and electron affinities are electronic properties obtained in the gas phase, and so they cannot describe properly electron transfer processes in solution. Solvation of the charged species produced by electron transfer causes a significant modification in the gas-phase free energy change $\Delta_{ET}G^{o}$. Adjustment of the free energy change of electron transfer from the gas phase to solution is performed by employing electrochemical techniques, e.g. cyclic voltammetry, which allow to measure reversible potentials for oxidations $E_{ox} = E^{O}_{(D^{+}/D)}$ and reductions $E_{red} = E^{O}_{(A/A^{-})}$. The free energy for an electron transfer reaction from the excited state in solution is given by Eq 1.3-3.

$$\Delta_{ET}G^{o} = FE^{o}_{(D^{+}/D)} - FE^{o}_{(A/A^{-})} - E_{o,o} - N_{A}\frac{e^{2}}{4\pi\varepsilon_{o}\varepsilon r} \qquad \text{Eq 1.3-3}$$

where:

F – Faraday constant, used to convert redox potentials to appropriate units, 9.65×10^{4} C mol^{-1};

N_{A} – Avogadro's number, 6.023×10^{23};

e – charge of the electron, 1.6×10^{-19} C;

ε_{o} – permittivity of the vacuum, 8.85×10^{-12} C^{2} N^{-1} m^{-1};

ε – dielectric constant of the solvent;

r – distance between the two charges.

The last term in Eq 1.3-3 is called the Coulombic term and will be discussed in the next paragraph for the case of neutral reactants. Redox potentials always refer to the reduction process, so that one has to be careful concerning the signs of redox potential values when computing the overall value of $\Delta_{ET}G^{o}$. In addition, redox potentials are reported *vs.* a reference electrode. So, comparing the redox potentials or calculating free-energy changes requires converting the redox potentials to the same reference electrode. Calculating of the overall free energy by neglecting the Coulombic term requires only three experimental parameters: 1) the excited state energy of the photoexcited molecule, 2) the reduction potential of the electron acceptor and 3) the oxidation potential of the electron donor.

The Coulombic term in Eq 1.3-3 is an expression of the energy connected with bringing two particles of opposite charge closer together. The Coulombic correction is proportional to $\frac{e^2}{\varepsilon r}$, where r, as a first approximation, can be taken as the sum of the radii of the two ions. This term shows that small separation distances and solvents with low dielectric constants should favor PET. As the solvent polarity increases the Coulombic term decreases and may become negligible even for small values of r. For example, in water, the Coulombic term is less than 1 kcal/mol at separations of ~ 2 Å. For comparison, in nonpolar solvents like benzene, the Coulombic term is already 10 kcal/mol at a separation of ~ 2 Å and may become sufficiently large to favor ionic association. Coulombic forces draw the initially formed ions into close proximity. These ions are called contact ion pairs. Due to close proximity of the ions, back electron to the donor can occur very rapidly, resulting in no net chemical change. However, in polar environments, the solvent molecules can stabilize the charge on the contact ion pairs. Solvent molecules can surround the ions and also penetrate the space between the ions which can then lead to the formation of solvent-separated ion pairs. Polar conditions facilitate escape from the solvent cage and block electron return. Escape of ions from the solvent cage is a desired feature of PET in solution because it allows the ion pairs to react with other molecules.

The dependence of the electron transfer rate constants k_{ET} on the free-energy change $\Delta_{ET}G^{o}$ has been investigated by Rehm and Weller who plotted the log k_{ET} for electron-transfer fluorescence quenching in acetonitrile by a variety of quenchers *vs*. the free energy change $\Delta_{ET}G^{o}$.[82] The measured values of k_{ET} ranged from ~ 10^{6} to ~ 2×10^{10} $\mathrm{M^{-1}s^{-1}}$ whereas the free energy change for the investigated electron transfer varied from ~ 5 to –60 kcal/mol. The Rehm-Weller plot is characterized by a steep decrease of the rate constants for endothermic reactions. Moreover, the value of k_{ET} reached a plateau when the free energy change $\Delta_{ET}G^{o}$ was about –10 kcal/mol and remained at the diffusion controlled rate constant up to the highest negative values of $\Delta_{ET}G^{o}$. It was concluded that electron transfer is not the rate-determining step in the plateau region but that diffusion becomes the rate-limiting process.

1.3.1.2.1.1 **Marcus Theory of electron transfer**

The theory of electron transfer was developed by Rudolph A. Marcus, who received the Nobel Prize in 1992 for this work.[78, 85-87] It was originally formulated to address outer-sphere electron-transfer reactions, in which the two reacting chemical species are not directly bonded to each other. Marcus was the first to appreciate that the activation barrier to electron transfer results from differences in the nuclear configurations of the reactants and products. For weakly coupled donor-acceptor systems, the activated state for electron-transfer is characterized by those nuclear configurations for which the energies of the donor (reactant) and acceptor (product) states are equal (point TS in Figure 1.3-5). Thus, in terms of Marcus theory, the rate determining factor in elementary electron transfer processes involves nuclear reorganization. Once the reorganization of the molecular and solvent structures have taken place and the nuclear-reaction coordinate is at the crossing point of the two potential-energy surfaces for the reactants and products, weak electronic interaction can initiate the electron-transfer event from the donor (D) to the acceptor (A). Factors that determine the nature of the transition state in electron transfer include the bond and angle changes that take place during the formation of the transition state (TS) as well as changes in the orientations of the solvent molecules occurring prior to electron transfer.

A profile of the potential energy surfaces for reactants and products are given in Figure 1.3-5. The vertical axis is the free-energy change, and the horizontal axis represents a generalized reaction coordinate which is a function of all the nuclei of the reacting species and the surrounding solvent. The black parabola represents the potential-energy surface for the nuclear motion of the reactants/solvent, along the reaction coordinate, in the initial state, and the red parabola represents the potential-energy surface for the nuclear motion of the products/solvent, along the reaction coordinate, in the final state. Based on Figure 1.3-5, the coupling parameters required for the quantitative computation of k_{ET} in terms of the Marcus theory can be defined:

- the reorganization energy, λ – is the energy difference (in an overall isoenergetic transfer) between having the electron on the initial site with the nuclei relaxed and the electron on the final site, but with the nuclei still in their original configurations. The total reorganization energy can be separated into two terms: $\lambda = \lambda_v + \lambda_s$, where λ_v is the inner-sphere reorganization energy that refers to the energy changes accompanying changes in bond lengths and bond angles and λ_{s} is the outer-sphere energy whose contributions come from the reorganization of the solvent around the reactants and products;

- the thermodynamic free energy of reaction, $\Delta_{ET}G^{o}$ – is the difference between the minima of the reactants' and products' free-energy curves;
- the free-energy of activation, $\Delta G^{\neq}$ – represents the free energy required to reach the transition-state configuration (TS) starting from the minimum of the reactants' potential-energy curve.

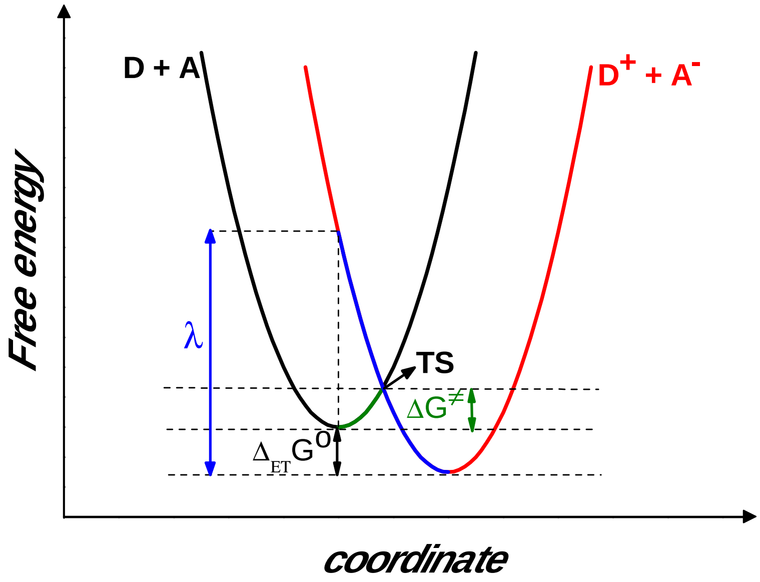

Figure 1.3-5 Representation of the potential energy curves used in electron transfer theory; $\Delta_{ET}G^{0}$ – overall Gibbs free energy change, λ –total reorganization energy, $\Delta G^{\neq}$ – Gibbs free energy of activation.

If entropy changes are ignored, the free energy becomes an energy or a potential-energy. Using Marcus's approximation of parabolic potential energy surfaces for the reaction coordinate, the free energy of activation $\Delta G^{\neq}$ for the crossing of two adiabatic curves in terms of the overall free energy of reaction $\Delta_{ET}G^{o}$ and the reorganization energy, λ, can be derived (Eq 1.3-4).

$$\Delta G^{\neq} = \frac{(\Delta_{ET}G^{o} + \lambda)^{2}}{4\lambda} \qquad \text{Eq 1.3-4}$$

Eq 1.3-5 (of the Arrhenius type) gives the usual transition-state theory expression between the experimental rate constant and an activation energy.

$$k_{ET} = A\, exp\left(-\frac{\Delta G^{\neq}}{k_{B}T}\right) \qquad \text{Eq 1.3-5}$$

where:

T – temperature;

k_B – Boltzmann constant, 1.38×10^{-23} J K^{-1};

A – pre-exponential factor that represents the probability that the representative point will jump from the reactants curve to the products curve when it is in the vicinity of the transition state for electron transfer.

The Marcus expression for the activation energy, itself, is remarkable in that it directly connects the kinetics of the reaction with its overall thermodynamics. Furthermore, it shows that even in an isoenergetic electron transfer, the nuclear reorganization provides a purely nuclear barrier to electron transfer. These expressions hold when the electronic coupling between donor and acceptor is weak.

Based on the general relationship of the free energy of activation as a function of the overall free-energy change and the reorganization energy, the Marcus theory identifies three different regions for electron transfer:

- the "normal" region – it is the region from $\Delta_{ET}G^{o} = 0$ to negative values that meet the condition $-\Delta_{ET}G^{o} < \lambda$. From Eq 1.3-4 it can be concluded that the free energy of activation $\Delta G^{\neq}$ in the normal region decreases as long as the reaction exothermicity increases and, at the same time, based on Eq 1.3-5, the electron-transfer rate constant increases;
- the "optimal" region – it is the barrierless region which is reached when $-\Delta_{ET}G^{o} = \lambda$. Mathematical analysis of Eq 1.3-5 for the $\Delta G^{\neq} = 0$ leads to the conclusion that the rate of electron transfer is then at a maximum;
- the "inverted" region – it is the region from $-\Delta_{ET}G^{o} = \lambda$ to any value of $-\Delta_{ET}G^{0} > \lambda$. Marcus' theory predicts that for $-\Delta_{ET}G^{o} > \lambda$ the activation free energy increases as $\Delta_{ET}G^{o}$ becomes more negative. If the absolute value of $\Delta_{ET}G^{o}$ is larger than λ, then the term $(\Delta_{ET}G^{o} + \lambda)$ in Eq 1.3-4 is more negative. However, the free energy of activation is proportional to the square of that term and, thus, the free energy of activation increases even though the reaction is more exothermic. Moreover, the rate of electron transfer slows down as the reaction becomes more exothermic beyond the point for which $-\Delta_{ET}G^{o} = \lambda$.

The experimental evidence for the inverted region required avoiding the diffusion controlled limiting electron transfer reaction. Closs and Miller were the first to show evidence for such an inverted region in intramolecular electron transfer by using a series of covalent donor-bridge-acceptor compounds.[88] Later, Guldi and Asmus documented an inverted region even for an intermolecular process, namely, the electron transfer between C_{76} and C_{78} fullerenes and arene radical cations.[89]

The classical Marcus equation works well in the normal and optimal regions, but in the inverted region, the measured rates are higher than expected from the theory.

1.3.1.2.2 **Photooxidation of methionine containing compounds**

The thioether side chain of methionine in peptides and proteins is susceptible to oxidation. Indeed methionine is one of the most easily oxidized amino acid residues by reactive oxygen species.[90, 91] Such oxidation is of great interest because of its relevance to the inactivation of protein pharmaceuticals,[92] aging,[93, 94] and neurodegenerative diseases such as Parkinson's[95] and Alzheimer's.[96] The important role of methionine containing compounds in biological processes has stimulated numerous studies on simpler systems in order to understand the oxidation of the thioether group in biologically relevant compounds.[97-105] These efforts have involved both the characterization of the reactive species in these oxidations and the detailed reaction mechanisms in which these species participate.

Marciniak and co-workers have studied one electron photooxidations of methionine derivatives by 4-carboxybenzophenone.[2, 99, 100, 103] The quenching event involving the deactivation of triplet CB by dipeptides (Met-Gly, Gly-Met) and tripeptides (Met-Gly-Gly, Gly-Met-Gly, Gly-Gly-Met) was probed in detail for aqueous solutions and reported in 1995.[103] The primary photochemical step in these reactions was proposed to involve an electron transfer from the sulfur atom to the triplet state of the carbonyl. This conclusion was supported by the observation of large rate constants for quenching which were determined to be in the range $(1.8–2.3) \times 10^9\ M^{-1}\ s^{-1}$ for neutral and alkaline solutions. In addition, the presence of the various electron-transfer intermediates accompanying the CB triplet quenching event was identified.

The detected electron-transfer intermediates included the CB radical anion, the CB ketyl radical, intermolecularly bonded $(S\therefore S)^+$ and intramolecularly bonded $(S\therefore N)^+$ radical cations. The characteristic electronic feature of these latter species is that the respective bonds contain two bonding σ-electrons and one antibonding σ^*-electron resulting in an overall bond order of ½.[90] The $(S\therefore N)^+$ two-center, three-electron-bonded species was observed only when there were N-terminal methionines because, then, a relatively stable five-membered ring can be formed. Although $(S\therefore N)^+$ was expected to form only when an N-terminal methionine residue had an unprotonated amino group with a lone pair of electrons (which occurs at high pH), it was also detected at low pH, but with a lower efficiency (Scheme 1.3-2). Formation of the $(S\therefore N)^+$ at low pH was explained by deprotonation from the amino group of the methionine derivatives that temporarily frees a lone pair on the amino group while the proton neutralizes the $CB^{\bullet-}$ to the $CBH^{\bullet}$ ketyl radical.

It was shown that the radical-ion complex decays competitively by 1) a back electron-transfer process to form the ground state of the reactants, 2) proton transfer within the complex, with diffusion apart of the CB ketyl radical and an α-thio-alkyl radical, and 3) escape of the radical ions into the bulk solution (Scheme 1.3-2). The ratio between these three decay channels varied, depending on the quencher and molecular structures. Secondary reactions of the electron-transfer products were also affected. Possible reactions that may accompany the quenching process of CB by methionine-containing compounds are presented in Scheme 1.3-2. The types of intermediates and their quantum yields were found to depend on the pH of the solution and also on the structure of the methionine-containing compounds e.g. on the location of the methionine unit with respect to the terminal functions.

One prominent reaction that was observed was decarboxylation. The products of this reaction were α-amino-alkyl radicals (αN) which are good reducing agents and were observed to reduce, for example, the ground state of CB (Scheme 1.3-2). As a result, a secondary growth of the CB radical anion was observed.[2] In contrast to the studies on the quenching of the CB triplet by methionine where efficient decarboxylation was observed,[2] only very low yields of CO_2 were measured in the work on dipeptides and tripeptides, which led to the conclusion that the α-amido-alkyl radicals (αN) were not formed. In 1996, Hug *et al.* stated that the resonance structure of the $>S^{\bullet+}$ radical with the radical cation site on the nitrogen atom was the precursor to the observed decarboxylation.[102] Moreover, they noticed that the electron-withdrawing substituents on the analogous nitrogen in the C-terminal of methionine-containing peptides affect the stability of the resonance structure leading to a complete lack of decarboxylation in those peptides.[102]

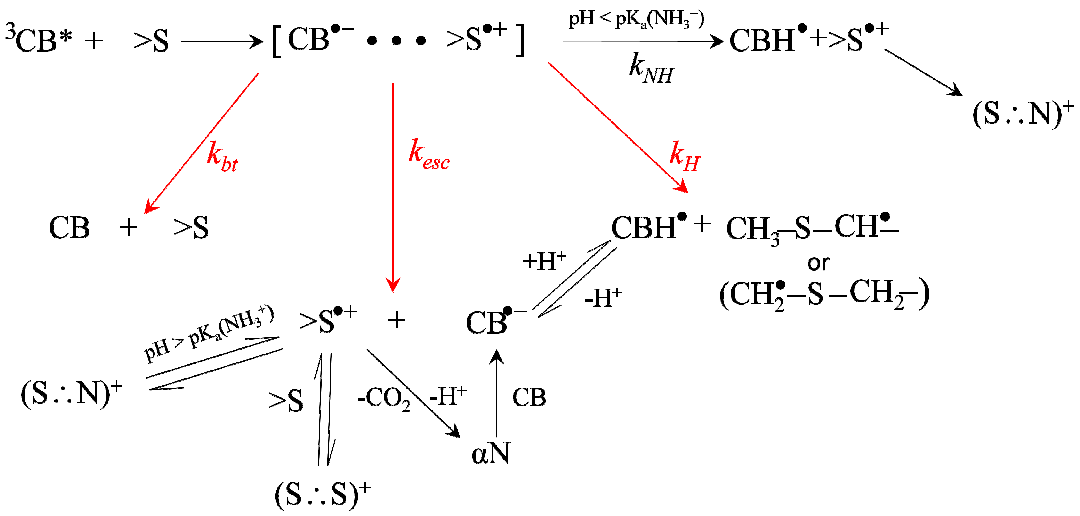

Scheme 1.3-2 Possible electron-transfer processes accompanying the CB triplet quenching by methionine containing compounds.

A continuation of the work on the photooxidation of dipeptides and tripeptides, containing one methionine residue, was a study on N-methionyl oligopeptides with differing numbers and positions of the methionine groups. One of the aims of that work was to investigate the competition between the two intramolecular two-centered, three-electron bonded species $(S\therefore S)^+$ and $(S\therefore N)^+$ that play roles in the secondary kinetics of these chemical systems.[100] This was accomplished by measuring the primary photochemical quantum yields in the CB-sensitized photooxidation of these oligopeptides and determining the extent of decarboxylation. The main conclusions of this work were as follows: 1) back electron transfer was efficient for all the investigated peptides; 2) significant yields of the $(S\therefore N)^+$ species were observed even at low pH where there were no lone electron pairs on the amino groups that could directly participate in forming intramolecular three-electron $S\therefore N$ bonds. As in the example above, it was concluded that the $(S\therefore N)^+$ formation at low pH was preceded by a proton transfer within the charge-transfer complex from the protonated amino group of the radical cation to the CB radical anion (Scheme 1.3-2). The relatively high quantum yields of $(S\therefore N)^+$ at both low and high pH further showed that $(S\therefore N)^+$ formation was a competitive process to intramolecular formation of $(S\therefore S)^+$ in these multi-methionine containing oligopeptides.

The electron lone pairs on the heteroatoms in peptide bonds until recently were thought to be delocalized and, as a result, to be unable to participate in the stabilization of sulfur radical cations. Stabilization of sulfur radical cations in peptides was, nevertheless, found to involve lone pairs of electrons on the C-terminal and N-terminal moieties of the peptides. is known that the sulfur radical cation $>S^{\bullet+}$ can be stabilized by complexation with nucleophilic heteroatoms, in general, and especially through neighboring group effects.[90, 97, 98, 101, 106] This effect on the intramolecular stabilization of sulfur radical cations was studied, in particular, for two cyclic dipeptides cyclo-L-Met-L-Met and cyclo-D-Met-L-Met as models for proteins with no terminal groups.[97, 101] One-electron oxidation of cyclo-L-Met-L-Met by $^{\bullet}OH$ radicals, for example, led to efficient formation of the intramolecular $(S\therefore N)$ radical. This process was competitive with the formation of intramolecular $(S\therefore S)^+$ radical cations. Moreover, it was shown that formation of $(S\therefore N)$ radicals involved the hydrogen atom of the peptide bond.[97] In contrast, similar oxidations of the isomer cyclo-D-Met-L-Met did not lead to the intramolecular $(S\therefore S)^+$ radical cations. This contrasting behavior between the two cyclic Met–Met dipeptide isomers was attributed to the structural differences between the two isomers that were computed by molecular modelling.[101]

1.3.1.2.3 Reactions of methoxybenzenes with benzophenone

The mechanism of BP-triplet quenching by methoxybenzenes in non-protic solvents has previously been studied in some detail. A number of workers[107-109] associated the decay rates with the extent of charge-transfer interactions between the BP triplet and the quencher, with the former being the acceptor and the latter being the donor. Quenching of benzophenone by anisole and its derivatives (ADs) has been studied in non-protic solvents like benzene, dichloromethane, acetonitrile (ACN) and in an ACN-H_2O (4:1 v/v) mixture.[107-109] Das *et al.* carried out a detailed study of the charge-transfer interaction of different carbonyl triplets with a number of methoxybenzenes. By means of nanosecond flash photolysis, the rate constants for benzophenone quenching by the ADs were determined in acetonitrile and benzene. The values in ACN varied from $3.9 \times 10^6\ M^{-1}\ s^{-1}$ for anisole to $3.9 \times 10^9\ M^{-1}\ s^{-1}$ for 1,2,4-trimethoxybenzene. What is more important was the observation that there was only a two-fold increase in the quenching rate constants on changing the solvent from benzene to acetonitrile.[107, 109] This observation speaks in favor of the formation of intermediates with only partial charge-transfer character. An involvement of a charge-transfer interaction in a reaction requires that a good correlation exists between the reaction rate constants and thermodynamic factors such as ionization potentials or oxidation-reduction potentials of the participating species. Correlations of the rate constants of benzophenone triplet quenching with the oxidation potentials of the substituted methoxybenzenes in acetonitrile gave slopes of -6.6 eV^{-1} [107] and -5.5 eV^{-1}.[110] With a view to the experimental uncertainties, the slopes were in good agreement and point to charge-transfer quenching. Formally one third of a full charge was being transferred during the quenching processes, whereas a full electron transfer requires a significantly higher slope of ca. 17.9 eV^{-1}.[28, 82]

Okada *et al.* considered two competing mechanisms of quenching of triplet-excited benzophenone by the ADs: electron transfer (ET) and induced quenching (IQ).[108] Both of these mechanisms are preceded by the formation of a triplet exciplex with charge-transfer character. In benzene, the formation of transient photoproducts for the ADs has not been observed. However, in an ACN-H_2O (4:1 v/v) mixture for the anisole derivatives excluding anisole itself, the radical cation has been produced as a consequence of the separation of the charge-transfer complexes. The induced quenching appeared to be very efficient for anisole since no transient products of the BP-triplet quenching by the anisole have ever been observed, even in the very polar ACN-H_2O (4:1 v/v) mixture. Similar conclusions also hold for the quenching of other triplet sensitizers like biacetyl[74] and flavin derivatives,[111, 112] by anisole.

Due to the relative low rate constants (~10^6 M^{-1} s^{-1}) and the lack of transient intermediates in the quenching of carbonyl triplets by anisole, O-methylated phenolic derivatives could provide information on the intrinsic triplet-state properties of bichromophoric compounds containing ketone and phenol. So, the methoxy analogues of the phenolic dyads were often employed as the reference compounds to account for non-HAT triplet-decay pathways.[46, 48, 51, 54]

2 METHODOLOGY AND METHODS

The aim of this chapter is the introduction of the experimental and theoretical methods that were used to derive the results presented in this work.

2.1 Investigated compounds and solvents used

The investigated compounds have been synthesized at the Department of Chemical Physics in Adam Mickiewicz University by Franciszek Kazmierczak (benzophenone-tyrosine dyads, rigid benzophenone-methionine dyads and reference compounds) and by Gerald Hörner (flexible benzophenone-methionine dyads, triads and 4-carboxybenzophenone-*N*-methylamide) at the “Institut für Chemie, Technische Universität Berlin“. The schematic drawing of the type of compounds studied in this thesis is presented in Chart 2.1–1.

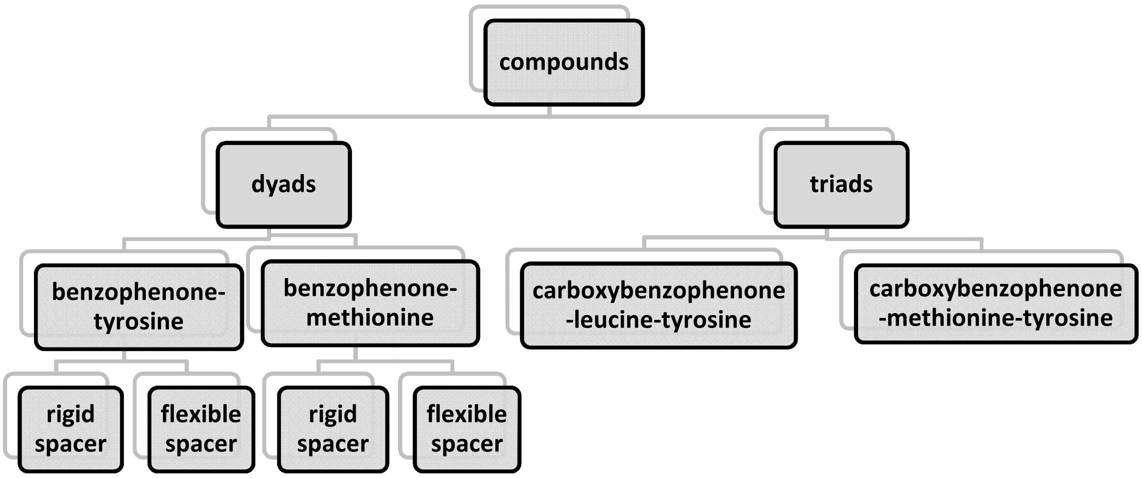

Chart 2.1–1 Schematic drawing of the types of compounds investigated.

The detailed list of the investigated compounds can be found in Table 2.1-1.

Table 2.1-1 List of the investigated compounds.

Symbol	Structure	Molecular formula	M [g/mol]	Additional notes[a]
(S,S)-BP-Tyr	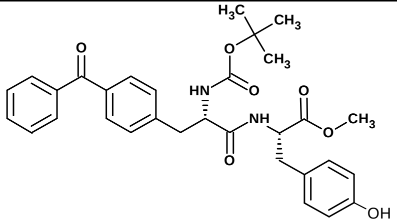	$C_{31}H_{34}N_2O_7$	546.6	pale yellowish micro crystals, good solubility
(R,S)-BP-Tyr	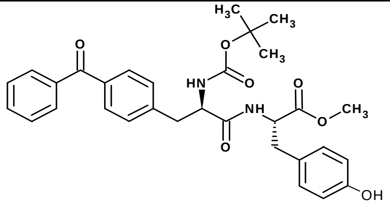	$C_{31}H_{34}N_2O_7$	546.6	white crystalline foam, good solubility
(S,S)-BP-DKP-Tyr	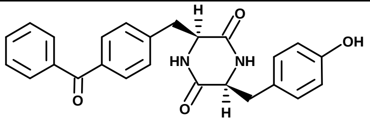	$C_{25}H_{22}N_2O_4$	414.5	white powder, moderate solubility
(S,R)-BP-DKP-Tyr	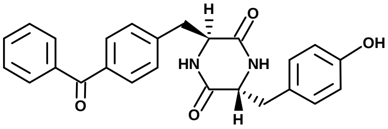	$C_{25}H_{22}N_2O_4$	414.5	white powder, moderate solubility
(S,S)-BP-Met	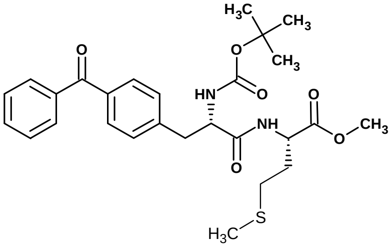	$C_{27}H_{34}N_2O_6S$	514.6	pale yellowish micro crystals, good solubility
(R,S)-BP-Met	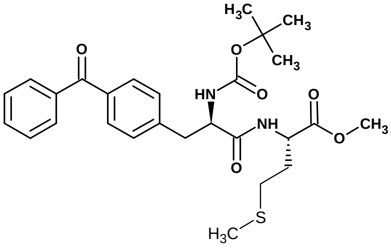	$C_{27}H_{34}N_2O_6S$	514.6	pale yellowish powder, good solubility

(S,R)-BP-DKP-Met	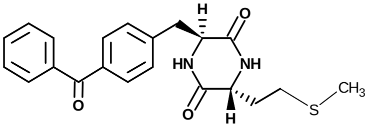	$C_{21}H_{22}N_2O_3S$	382.5	white powder, good solubility
(S,S)-BP-DKP-Met	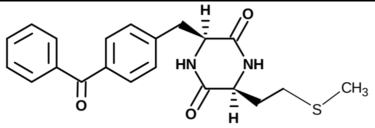	$C_{21}H_{22}N_2O_3S$	382.5	white powder, weak solubility
CB-Leu-Tyr	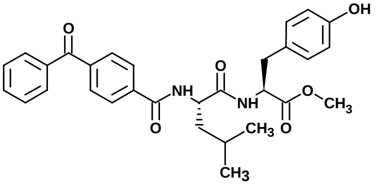	$C_{30}H_{32}N_2O_6$	516.5	white powder, good solubility
CB-Met-Tyr	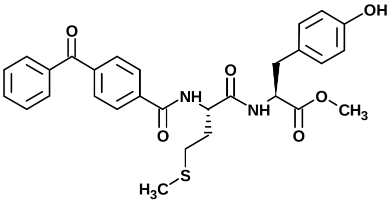	$C_{29}H_{30}N_2O_6S$	534.6	white powder, good solubility
BP-DKP	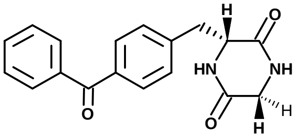	$C_{18}H_{16}N_2O_3$	308	white powder, good solubility
(S,R)-BP-DKP-TyrOMe	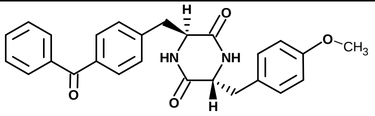	$C_{26}H_{24}N_2O_4$	428.5	white powder, moderate solubility
(R,R)-BP-DKP-TyrOMe	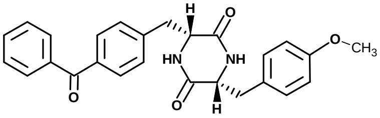	$C_{26}H_{24}N_2O_4$	428.5	white powder, moderate solubility
(R,S)-BP-TyrOMe	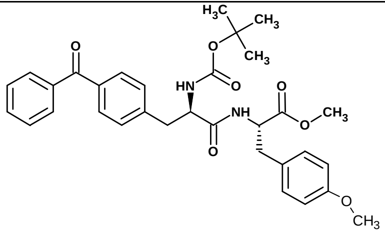	$C_{32}H_{36}N_2O_7$	560.6	white powder, good solubility
CBCONHMe	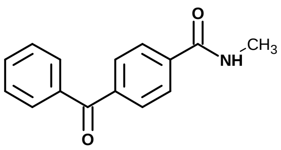	$C_{15}H_{13}NO_2$	239.3	white powder, good solubility

[a] solubility refers to solvents used.

Commercially available compounds used in the experiments are listed in Table 2.1-2.

Table 2.1-2 List of commercially available compounds used.

Substance	Abbreviation	Structure	Source of supply and purity
benzophenone	BP	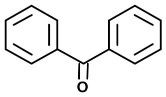	Sigma-Aldrich, ReagentPlus®, 99 %
4-carboxybenzophenone	CB	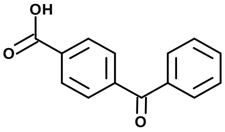	Sigma-Aldrich 99 %
4,4'-dimethoxybenzophenone	DMBP	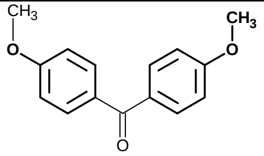	Sigma-Aldrich 99 %
4-methylbenzophenone	MBP	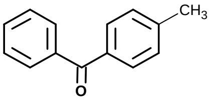	Sigma-Aldrich 99 %
4-trifluoromethylbenzophenone	TMBP	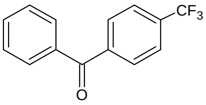	Sigma-Aldrich 97 %
decafluorobenzophenone	DFBP	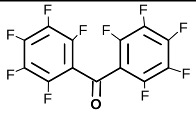	Sigma-Aldrich 99 %
anisole	AN	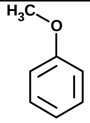	Sigma-Aldrich ≥ 99.9 % (GC)

Solvents used for preparation of the solutions were of the highest available analytical grade and were used without further purification (Table 2.1-3). Deionized water used throughout this study was obtained from a Millipore (Simplicity™) purification system. The pH of the solutions was adjusted with HCl and NaOH depending on the experiments. It was controlled with a pH-meter METLER TOLEDO FE20/EL20.

Table 2.1-3 Solvents used in experiments.

Solvent	**Abbreviation**	**Source of supply and purity**
acetonitrile	ACN	Merck, gradient grade for liquid chromatography LiChrosolv®
methanol	MeOH	Merck, for spectroscopy Uvasol®
dichloromethane	DCM	Merck, for spectroscopy Uvasol®
chloroform	$CHCl_3$	Merck, for spectroscopy Uvasol®
1,2-dichloroethane	DCE	Sigma-Aldrich, ≥ 99.8 %, HPLC grade
acetic acid	HAc	Sigma-Aldrich, ReagentPlus®, 99 %
2,2,2-trifluoroethanol	TFE	Sigma-Aldrich, ≥ 99.0 % (GC)
1,1,1,3,3,3-hexafluoro-2-propanol	HFIP	Sigma-Aldrich, ≥ 99.0 %
ethyl acetate	EtOAc	Sigma-Aldrich, ≥ 99.8 %, HPLC grade
tert-butanol	tert-ButOH	Sigma-Aldrich, ≥ 99.7 % (GC)
benzonitrile	C_6H_5CN	Sigma-Aldrich, CHROMASOLV®, for HPLC, 99.9 %

2.2 Methods of measurement

2.2.1 UV spectroscopy

UV spectroscopy is a useful technique for the investigation of organic compounds containing chromophores such as aromatic rings and carbonyl groups. For those organic molecules the energy required to excite an electron from an occupied valence orbital to an unoccupied antibonding orbital corresponds to electromagnetic wavelengths in the range of 180 nm to 400 nm. An absorption spectrum is a characteristic feature of a particular chromophore and can be used to identify it. For a complete description of a spectrum, the wavelengths at the maximum absorptions (λ_{max}) for each band and the values of the molar absorption coefficients at these wavelengths (ε_{max}) have to be given. The determination of the molar absorption coefficient requires application of a quantitative analysis based on the Beer - Lambert law. This law states that the absorbance A of a dissolved substance is a linear function of its concentration. The length of the light path and the molar absorption coefficient determine the slope of the linear plot (Eq 2.2-1).

$$A_{\lambda} = log\frac{I_o}{I} = \varepsilon_{\lambda}cl \qquad \text{Eq 2.2-1}$$

where:

A – absorbance at wavelength λ;

I_{o} – intensity of the incident light [Einstein $\text{dm}^{-3}\ \text{s}^{-1}$];

Einstein – one mole of photons

I – intensity of the transmitted light [Einstein $\text{dm}^{-3}\ \text{s}^{-1}$];

ε – molar absorption coefficient at wavelength λ [$\text{M}^{-1}\ \text{cm}^{-1}$];

c – concentration of the sample $\left[\text{M} = \frac{\text{mol}}{\text{dm}^3}\right]$;

l – optical path length [cm].

Detailed analysis of the absorption spectra including evaluation of λ_{max} and ε_{max} has been performed to check possible effects of the substitution on the electronic properties of the BP moiety. Additionally, UV spectra have always been taken before performing the nanosecond flash photolysis in order to set an appropriate optical density at the excitation wavelength in the range of 0.2–0.5. The UV absorption technique has also been used as a supportive method to the HPLC method to detect changes of the substrate concentration during irradiation of the compounds.

UV spectra were measured at room temperature using a Cary 300 Bio Varian spectrophotometer or a Hewlett-Packard 8452A diode array spectrophotometer. Spectra were recorded in a range of 200–400 nm using 1 cm × 1 cm rectangular cells.

2.2.2 **Phosphorescence spectroscopy**

Phosphorescence spectroscopy in conjunction with absorption spectroscopy can be used to verify substituent effects on the properties of the BP moiety, which exhibits a characteristic emission-band structure. The emission spectra were measured using a Perkin-Elmer MPF3 spectrofluorimeter. Phosphorescence spectra were measured at 77 K in mixtures of the solvents: DCM–MeOH (1:1 v/v). The phosphorescence spectra were recorded at λ_{exc} = 270 nm in the 380-600 nm range. The triplet energies of all of the tested compounds were calculated from the wavelength corresponding to the 0-0 band of the emission.

2.2.3 **HPLC chromatography**

High-performance liquid chromatography (HPLC) is a very powerful chromatographic tool. The technique is employed in a broad range of qualitative and quantitative analyses of chemical reactions and their products. It allows the separation of the components in mixtures, and it can be used to identify, quantify and purify the individual components of the solutions. HPLC instruments consist of a reservoir of a mobile phase, a pump, an injector, a separation column, and a detector. Compounds are separated by injecting a generally small, defined volume of the sample mixture onto the column. The different components in the mixture pass through the column at different rates due to differences in their partitioning behavior between the mobile liquid phase and the stationary phase.

The HPLC technique has been applied to investigate the decomposition of the substrates and the formation of the products of the reactions, which were induced during steady-state irradiations of the investigated compounds. The progress of the reactions was followed by HPLC using a Waters 600E Multisolvent Delivery System Pump. The detection system consisted of a Waters 996 Photodiode Array UV-Vis Detector. Analytical HPLC analyses were carried out on a Waters XTerra RP_{18} reverse phase column (4.6 × 250 mm, 5 μm particle size). Two different eluents were employed; by applying different ratios of the eluents, better separation of the components could be achieved. The mobile phases were mixtures of solutions of ACN and 20 mM KH_2PO_4 : ACN (95:5 v/v), with a flow rate of 1 ml min^{-1}. The volume of the injected sample was 50 μl or 5 μl depending on the concentration of the sample.

2.2.4 **GC-MS chromatography**

Gas-chromatography – mass spectroscopy (GC-MS) is a technique that combines both gas – chromatography and mass spectroscopy to identify different substances in the analyzed samples. GC can separate volatile and semivolatile compounds with great resolution, while MS can provide detailed structural information on most compounds. GC-MS analyses were performed in order to identify the stable products of the steady-state irradiations of TFE solutions of BP and anisole. The analyses have been carried out with a gas chromatograph CP3800 connected to a mass spectrometer (4000MS, ion trap) by Mrs Izabela Banczyk from the Advanced Chemical and Equipment and Instrumentation Facility, UAM, Poznan. The ionization technique employed was the most standard type, namely electron ionization. The electron energy used was 70 eV. The GC was carried out on a VF-5ms Varian column (30 m × 0.25 mm × 0.39 mm). Mass spectra were detected in the mass range 40 – 800 m/z.

2.2.5 **Flash photolysis**

Flash photolysis equipment is commonly used to investigate fast photochemical reactions. The laser flash photolysis (LFP) technique provides effective methods for studying the reactions of transient species such as radicals, excited states or ions, in chemical and biological systems by direct measurement. LFP setups were used in this work to investigate the intramolecular H-atom and electron-transfer reactions involving the triplet state of aromatic carbonyls. The same technique was applied to study the photochemical oxidation of anisole in protic solvents.

The flash-photolysis technique concept allows one to measure both transient absorption spectra at various delay times after the initial laser pulse and absorbance changes with time (kinetic traces) at particular wavelengths. As a result, this method enables one to identify the presence of the transients in solutions and to determine rate constants of formation and decay of the intermediates.

Nanosecond laser flash photolysis experiments were carried out with three different experimental setups: a) at the facility of the Department of Chemical Physics at Adam Mickiewicz University, b) at the facility of the Notre Dame Radiation Laboratory at the University of Notre Dame, IN, USA and c) at the facility of the Department of Photochemistry and Spectroscopy at the Institute of Physical Chemistry of the Polish Academy of Sciences in Warsaw. The nanosecond LFP experiments employed pulsed N_2 lasers and Nd:YAG lasers for excitation. Data acquisition systems are described in detail in Chapter 2.2.5.1 and Chapter 2.2.5.2. Transient decays were recorded at individual wavelengths by the step-scan method with a step distance of 10 nm in the range of 320 to 800 nm as the mean of 10 to 15 pulses.

Femtosecond flash photolysis was used to monitor the triplet state of the trichromophores in protic solvents. In this particular case, the triplet state decay was too fast to permit its detection in analogous experiments employing nanosecond flash photolysis systems.

2.2.5.1 **Nd-YAG laser system**

Nanosecond laser flash photolysis experiments employing a pulsed Nd-YAG laser were carried out with two different experimental setups. The setup at the Department of Chemical Physics at Adam Mickiewicz University is presented in Figure 2.2-1. The fundamental Nd-YAG emission wavelength is 1064 nm. Starting with that wavelength, outputs at 532, 355 and 266 nm can be generated by frequency doubling, frequency tripling and frequency quadrupling, respectively. The latter two wavelengths are very convenient for studying benzophenones since they correspond to excitation of the strong $\pi\rightarrow\pi^*$ transition but also the much weaker $n\rightarrow\pi^*$ transition of the benzophenone chromophore with 266 nm or 355 nm pulses, respectively. In the case of the 266 nm photolysis of benzophenone-tyrosine and trichromophores dyads, simultaneous excitation of both chromophores (BP and Tyr) cannot be avoided. However, an analysis of the molar absorption coefficients measured for BP and Tyr[113] shows that excitation of the tyrosine moiety amounts to less than 10 % (see Figure 3.1-9). There were no such complications for the benzophenone-methionine dyads. The advantage of using 266 nm excitation is the possibility of avoiding self-quenching processes since lower concentrations can be used (10^{-5} M) due to the high molar absorption coefficient of benzophenone at this wavelength. Additionally, 266 nm excitation has been employed when the solubility of the compound in particular solvent was limited and the millimolar concentration necessary for the 355 nm excitation could not be reached.

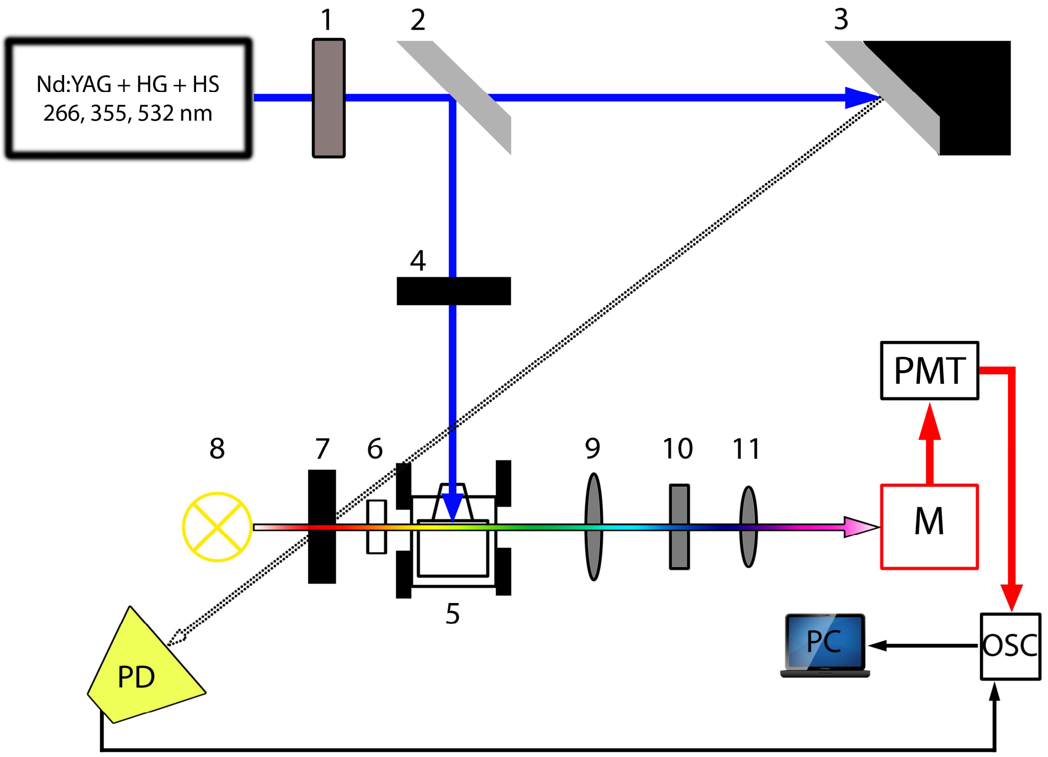

Figure 2.2-1The experimental setup for Nd-YAG nanosecond laser flash photolysis (see text for details).

In more detail, the Nd-YAG flash photolysis consists of the following components:[114]

- an Nd-YAG laser from Spectra Physics (Mountain View, CA, USA), model INDI 40-10, equipped with a harmonic generation module to achieve 266, 355 and 532 nm excitation wavelengths at 10 Hz repetition rate, pulse duration 6-8 ns, maximal pulse energy 450 mJ at 1064 nm and 155 mJ at 355 nm;
- 150 W pulsed Xe lamp system with the lamp pulser (**8**) from Applied Photophysics (Surrey, UK);
- a two-turret, grating monochromator (**M**) from Acton (MA, USA), model Spectra Pro SP-2155;
- a photomultiplier (**PMT**) from Hamamatsu (Japan), model R955 working with 5 dynodes amplification;
- a real-time digital oscilloscope (**OSC**) from LeCroy, model Wave Runner 6100A, 1 Gz, 10 GS/s;

- a computer (**PC**) equipped with an analog-to-digital converter (DAQ) and timer PCI-cards from National Instruments, software based on LabView 8.0, and a computer program providing synchronization of the laser excitation of the sample with the monitoring light;
- a pyroelectric joulemeter (Molectron);
- a variety of electronics, optics and mechanics (Standa)
    - filter (**1**) – lowers the energy of the laser pulse;
    - dielectric mirror (**2**) – the majority of the photons from the beam is reflected from it and hits the sample in the cuvette kept in the cell holder, the rest of the photons is transmitted and reach the delay generator (**3**);
    - photodiode (**PD**) – the 10 ms delayed signal from the delay generator acts as the zero time trigger for the oscilloscope;
    - laser shutter (**4**) – repetition time 0.5 Hz, only when it opens can photons reach the sample;
    - lamp shutter (**7**) – repetition time 1 Hz, opening time 40 ms, together with the 10 ms delay sets the laser pulse to the beginning of the plateau region of the probing 150 W Xe arc lamp pulse;
    - sample holder (**5**);
    - cut-off filter (**6**) (< 300 nm);
    - cut-off filter (**10**) (< 500 nm);
    - optical lenses (**9**), (**11**) – focus the light in order to enter the slit of the monochromator.

Additional computer program regulated parameters of the measurement were applied:

- number of points collected for each wavelength – 1000 points;
- timebase – time per one division (whole time window is divided into 10 divisions) – it varied, depending on the process investigated, from 2×10^{-8} s to 2×10^{-5} s.

2.2.5.2 **Nitrogen laser system**

Nanosecond laser flash photolysis experiments employing a pulsed nitrogen laser were carried out with the setup of the Radiation Laboratory at Notre Dame. The nitrogen laser system is presented in Figure 2.2-2. The principle of operation of this device is the same as for the LFP based on the Nd-YAG laser. Laser excitation at 337.1 nm from a Laser Photonics PRA/Model UV-24 nitrogen laser (operated at about 3 mJ, pulse width ≈ 8 ns) was at a right angle with respect to the monitoring light beam. The detection system consisted of a pulsed xenon lamp (**7**) (1 kW) as the monitoring light source and a SPEX 270 M monochromator (**M**) coupled with a Hamamatsu R955 photomultiplier (**PMT**). The signal from the photomultiplier was processed by a LeCroy LC574A digital storage oscilloscope (**OSC**) and a PC-AT compatible computer (**PC**). Cut-off filters (**13**) were used to avoid spurious response from second-order scattering of the monochromator gratings. Additional units of this equipment are:

- dielectric mirrors (**1**), (**3**);
- laser shutter (**5**);
- lamp shutter (**9**);
- lenses (**2**), (**6**), (**11**), (**12**);
- quartz plate (**4**);
- optical trigger for scope (**T**).

Experiments were performed in rectangular quartz cells (0.5 × 1 cm) with an optical path length of 0.5 cm for the monitoring beam.

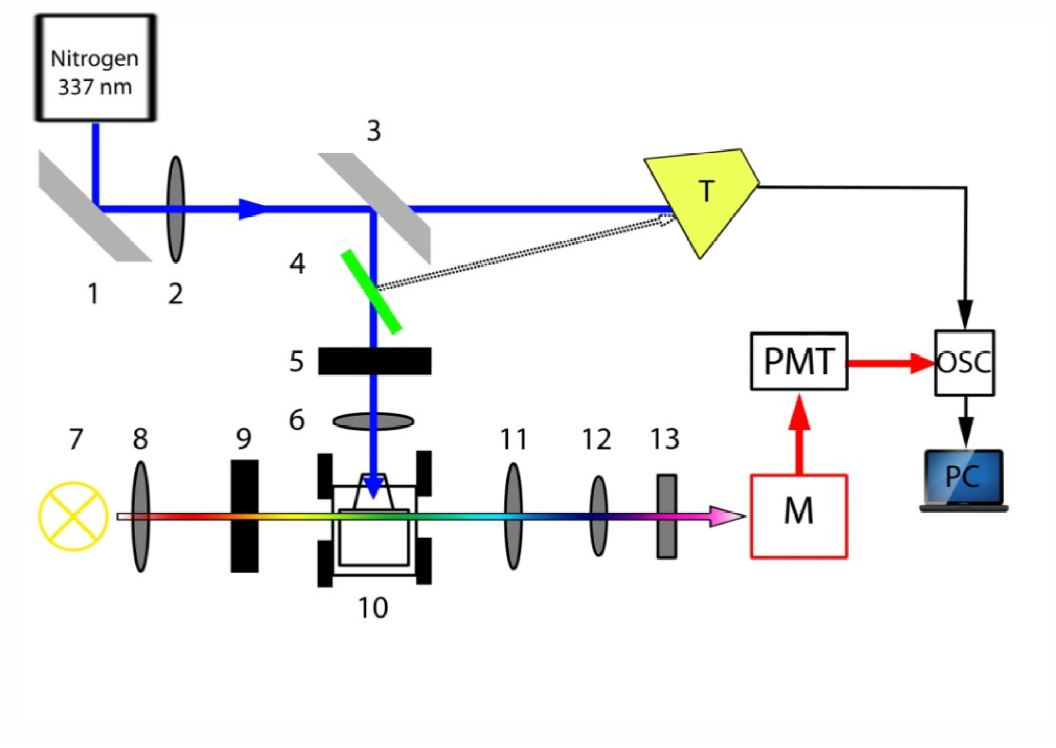

Figure 2.2-2 The experimental setup for the N_2 nanosecond laser flash photolysis (see text for details).

In contrast to the Nd-YAG system in the Department of Chemical Physics at AMU, multiple time scales were generated for a single kinetic trace. Each of the 10 kinetic traces consisted of 200 points. Additionally, in the Notre Dame Radiation Laboratory setup, there is a routine that automatically kept the voltage of the PMT in a range where its response was linear. Another feature was the automatic spectral scan. Through the graphical user interface, initial and final wavelengths and the wavelength interval could be chosen at the start of the experiment.

Triplet-state decay for the open-chain BP-Tyr dyads in dichloromethane was measured at the Department of Photochemistry and Spectroscopy in the Institute of Physical Chemistry of the Polish Academy of Sciences in Warsaw under supervision of dr hab. Jerzy Karpiuk. In this particular case, the triplet-state decay was so fast that the signal was convoluted with the laser pulse when standard nanosecond flash photolysis systems were employed. A unique transient-absorption spectrometer, working in the whole visible range, being an example of the so-called pump-probe technique, has been custom-designed and built by Prof. J. Jasny. A nitrogen laser (excitation wavelength 337 nm, pulse energy 1 mJ, temporal pulse width 1 ns) was used both to excite the sample and to pump a tuneable dye laser used as the source of the monitoring light. The apparatus was used in one of two basic operational modes: kinetic measurement at a fixed wavelength of the monitoring light or temporal evolution of the transient absorption. Spectra could be recorded within the time range from 2 ns before the excitation to 100 ns after the excitation with 1 ns time-resolution due to the unique optical delay line concept employed in the spectrophotometer.

2.2.5.3 **Femtosecond flash photolysis**

Femtosecond transient absorbance measurements were conducted at the Radiation Laboratory of the University of Notre Dame using a Clark 6MXR 2010 laser system and an optical detection system provided by Ultrafast Systems (Helios). The source for the pump and probe pulses was the fundamental emission at 775 nm (1 mJ/pulse, fwhm = 130 fs, 1 kHz repetition rate). A third harmonic generator provided laser pump pulses at 258 nm (3.50 eV, 130 fs, 2 mm diameter beam). Five percent of the fundamental laser output was diverted through a sapphire crystal to create a white light continuum (450−750 nm) for monitoring the transient absorbance at times after the pump pulse, determined by an optical delay. Measurements were carried out in a magnetically stirred sample cell (2 mm light path). A time window of 1.6 ns with a maximum step resolution of 7 fs was used for transient observation.

2.2.6 **Lamps used in steady-state irradiation**

Steady-state irradiation was used to determine the quantum yields of substrate disappearance and, in a further step, to identify the stable products. Three different setups were employed: a high pressure mercury lamp, a low pressure mercury lamp and an Argon ion laser.

2.2.6.1 **High pressure mercury lamp**

A high-pressure mercury lamp (HBO 200, Narva) works at 200 W and contains mercury vapor at a pressure of about 10 MPa. Due to its high luminescence efficacy, the UV radiation which it emits, and the high-pressure within the lamp, the lamp must be operated within an enclosed, protective metal casing. Additionally, due to its emission of large amounts of heat, cooling is required. High-pressure mercury lamps emit many wavelengths including visible light. To select the desirable irradiation wavelength appropriate filters have to be used. Irradiations at 313 nm were performed using a BC-4 filter in conjunction with interference filters from Zeiss. The solution in the cuvette was stirred during irradiation by a magnetic stirrer.

2.2.6.2 **Low pressure mercury lamp**

Irradiation with a low-pressure mercury lamp (λ_{irr} = 254 nm) was chosen when it was necessary to work with low concentrations in order to avoid side reactions such as self-quenching. Specifically, a low-pressure mercury lamp TNN 15/32 from Original-Hanau was employed. The lamp contains mercury vapour at a pressure of about 0.1 Pa. Quite unlike the high-pressure mercury lamp, the low-pressure mercury lamp emits mainly monochromatic radiation. The main light emission is at 253.7 nm (greater than 80 % of the radiant power) and 184.9 nm. Therefore, filters were not required. The low-pressure mercury lamp operates near ambient temperature and thus does not require cooling. For quantum-yield determinations, irradiations were performed in rectangular quartz cells (1 cm × 1 cm). Disappearance of the substrate was monitored by HPLC. However, in the case of **(S,S)-BP-DKP-Met** larger quantities of the irradiated solutions was required in order to identify stable products. Irradiations on a preparative scale with concentrations 4.75 × 10^{-5} M were carried out in a photoreactor. This procedure allows for irradiating 50 ml of solution at one time. When needed, the irradiations were repeated several times with the same volume and same time of irradiation. The scheme of the photoreactor used is presented in Figure 2.2-3.

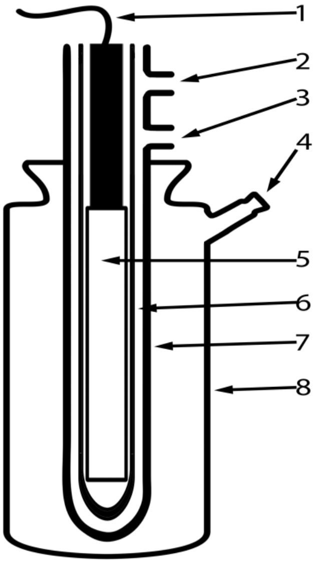

Figure 2.2-3 Photochemical reactor for irradiations on preparative scale (see details in text).

The reactor consists of a low-pressure mercury lamp (**5**) ((**1**) – power supply) which is put into a quartz tube (**6**). Outside there is another quartz tube (**7**), where water for cooling can flow between the internal and external casings (**2**) and (**3**). The irradiated solution was placed between the external tube (**7**) and glass tube (**8**). Samples for irradiation were deoxygenated by purging (**4**) with high-purity argon for 30 minutes prior to the measurements. The time of the irradiation was chosen so as not to decompose the entire substrate. After the irradiations the solutions were concentrated by evaporating the solvent, prior to actual analysis.

2.2.6.3 **Argon ion laser**

An argon ion laser uses, as its name implies, high purity argon gas as the lasing medium. A multi-line argon ion laser can generate up to 18 discrete laser lines (wavelengths) ranging from the UV (275.4 nm) to the visible, green (528.7 nm), with the majority of the power being developed at the 488 nm and 514.5 nm lines. Argon lasers may be configured to produce a single laser line only, which is highly desired in selective irradiation and quantitative analysis by placing a dispersing prism between the active medium and the output mirror. The setup in the Department of Chemical Physics at AMU consists of (see Figure 2.2-4):

- an argon ion laser (Coherent INNOVA 400, equipped with a special UV grade tube and UV resonator optics) – the laser plasma tube (**3**) is sealed by Brewster-angle-oriented windows (**2**) and (**5**); the laser is, moreover, equipped with a water cooling system (**6**) and (**4**);
- a double Pellin-Broca prism-line separator (**11**) – to select narrow band irradiation wavelengths (351.1 and 351.4 nm);
- a Newport 1918-C laser-power meter with an 818P-010-12 thermopile head (**14**);
- a home-built beam expander (**12**) - the beam profile was expanded (5x);
- a temperature-controlled cell holder (**13**) (Quantum Northwest, model TC 125), placed on a micrometer, one-axis translation stage;
- a CCD spectrometer (Edmund Optics, model BRC111A-USB) – a small portion (< 1 %) of the laser beam was reflected by a beam splitter to monitor the wavelength;
- a series of optics: highly reflective mirrors (**1**), output coupler mirrors (**2**); lenses (**9**), (**10**);
- a filter – to lower the power of the laser (**15**).

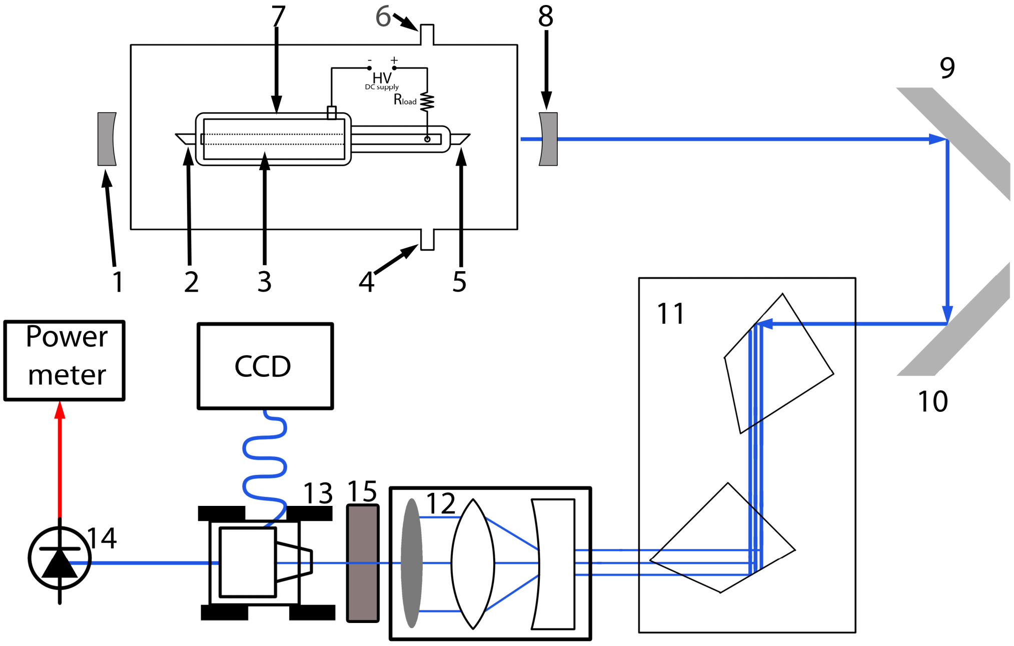

Figure 2.2-4 Argon ion laser setup (see details in text).

The intensity of the incident light (351 nm) for the quantum-yield determinations was measured using a Reinecke’s salt actinometer.

The superiority of the irradiation using an argon ion laser over traditional lamps arises from the availability of a much higher intensity of the incident light that may significantly reduce the time of irradiations. On the other hand, one must be aware of the fact that using too much laser power may cause additional side reactions e.g. two-photonic processes. To avoid that possibility, a filter that transmittes only 20 % was used. This arrangement allows the laser to operate at higher power where it is more stable and at the same time only 20 % of the output beam reaches the sample.

2.3 Methods of Theoretical Calculations

Computational chemistry is a branch of chemistry that assists in solving chemical problems. Experimental studies on the possibility of intramolecular reactions involving the investigated compounds were, therefore, supported by a series of computational calculations. The structural demand on the dyads and triads to achieve a suitable geometry for the intramolecular reactions (HAT, electron transfer) was addressed by Density-functional theory (DFT) methods and molecular dynamics (MD). The calculations were performed at the Poznan Supercomputer Center PCSS or at Notre Dame Radiation Laboratory cluster.

2.3.1 Density functional theory

DFT is one of the most popular and successful quantum-mechanical approaches to many-electron systems. The principle aim of these calculations is to identify optimized structures, i.e. the energetically most favorable structures and geometries of stable species of interest as well as to quantify their molecular parameters such as charge distributions, spin densities etc.

Key features of DFT are two Hohenberg-Kohn (H-K) theorems:[115, 116]

- **the Hohenberg-Kohn theorem (I).** The external potential V_{ext} and thus the total energy uniquely determines functional of the electron density ρ_{o}. Thus the ground state electron density is sufficient to describe any ground state property of the system without the knowledge of the many-electron wavefunction. This theorem states that the electron density for the ground states is equivalent to the wavefunction for the ground state and contains exactly the same information.
- **the Hohenberg-Kohn variational principle (II).** The functional $\mathrm{E}[\rho]$ for the ground state energy is minimized by the ground state electron density ρ_{o}: $\mathrm{E}[\rho] \geq \mathrm{E}[\rho_{\mathrm{o}}] = \mathrm{E}_{\mathrm{o}}$ for every trial electron density. The second H-K theorem proves that the correct ground state electron density minimizes the energy functional.

Although the Hohenberg-Kohn theorems are extremely powerful, they do not offer a way of computing the ground-state density of a system in practice. The energy as given in the Kohn-Sham formulation of the density functional theory, has the form:[117]

$$E = T_o + \int v(r)\rho(r)dr + J[\rho] + E_{xc}[\rho] \qquad \text{Eq 2.3-1}$$

where:

T_o – the kinetic energy of the non- interacting electrons;

$\int v(r)\rho(r)dr$ – potential energy of the interaction of the electrons with nuclei;

$J[\rho]$ – the classical coulomb repulsion of the electrons:

$$J[\rho] = \frac{1}{2}\iint \frac{\rho(\boldsymbol{r_1}) \cdot \rho(\boldsymbol{r_2})}{|\boldsymbol{r_1} - \boldsymbol{r_2}|} d\boldsymbol{r_1} d\boldsymbol{r_2} \qquad \text{Eq 2.3-2}$$

$E_{xc}[\rho]$ – exchange-correlation functional.

The major problem with DFT is that the exact functionals for exchange and correlation are not known except for the free electron gas. However, approximations exist which permit the calculation of certain physical quantities quite accurately. The development of the functionals that precisely describe nature is one of the most important areas in the research of quantum chemistry. The functionals normally used in density functional theory are integrals of some function of the density and possibly the density gradient. Many forms of such functionals have been suggested, and names for the various pure DFT models are given by combining the names for the exchange and correlation functional. Some of the most important are listed below:

- **Local Density Approximation** (LDA)[115] – the local exchange-correlation energy per particle depends only on the local density and is equal to the local exchange-correlation energy per particle of a homogeneous electron gas of the same density. This approach is highly successful and is considered in DFT as the basis for most of the developments of other functionals.
- **Local Spin Density Approximation** (LSDA) – an improvement of the LDA which is motivated by the fact that the exchange–correlation hole is very different for electrons with parallel and with antiparallel spins.
- **Generalized Gradient Approximation** (GGA) – the next step of sophistication in functional forms; it is still local but also takes into account the gradient of the density at the same coordinate.
- **The hybrid functional of Becke**[118, 119] – The Becke functional was the first example of a hybrid theory, a theory which is a mixture of a Hartree-Fock

functional of orbitals and a DFT functional of density. A hybrid exchange-correlation functional is usually constructed as a linear combination of the Hartree-Fock exact exchange functional (E_x^{HF}) and any number of exchange and correlation density functionals. The parameters determining the weight of each individual functional are typically specified by fitting the functional's predictions to experimental or accurately calculated thermochemical data. An example is the popular B3LYP (Becke, three-parameter, Lee-Yang-Parr) exchange-correlation functional which contains 3 parameters:

$$E_{xc} = E_{xc}^{LSDA} + a_o\left(E_x^{HF} - E_x^{LSDA}\right) + a_x E_x^{B88} + a_c E_c^{LYP} \qquad \text{Eq 2.3-3}$$

where:

E_{xc}^{LSDA} – LSDA exchange-correlation functional;
E_x^{HF} – Hartree-Fock exchange functional;
E_x^{LSDA} – LSDA exchange functional;
E_x^{B88} – Becke gradient corrections to exchange functional from 1988;
E_c^{LYP} – correlation functional of Lee, Yang and Parr;
$a_o = 0.20$, $a_x = 0.72$, $a_c = 0.81$ – are the three empirical parameters determined by fitting the predicted values to a set of atomization energies, ionization potentials, proton affinities, and total atomic energies.

Fitting parameters to some set of experimental data are common approaches to developing new functionals.

- **PBE1PBE (PBE0) functional** – the functional contains no parameters fitted to experimental data. PBE0 generally provides results which are at least comparable to those obtained with more empirical functionals. Perdew and co-workers have also proposed that, based on fourth order perturbation theory, the optimum value of the mixing coefficient should be set to ¼.[120] This functional uses 25 % exchange and 75 % correlation weighting. It is known in the literature as PBE0. The keyword for this functional in Gaussian03 is PBE1PBE. The resulting exchange-correlation functional can be expressed as:

$$E_{xc} = E_{xc}^{GGA} + \frac{1}{4}\left(E_x^{HF} - E_x^{GGA}\right) \qquad \text{Eq 2.3-4}$$

where:

E_{xc}^{GGA} – GGA exchange-correlation functional;
E_{x}^{HF} – Hartree-Fock exchange functional;
E_{x}^{GGA} – GGA exchange functional.

All actual quantum chemical calculations were performed using Gaussian 03 suites of programs.[121] Optimizations of the ground-state and triplet-state geometries of molecules were obtained using density functional theory (DFT). In order to obtain the global minimum, different starting geometries were used in the optimizations. The optimized structures were verified as corresponding to real minima by establishing the absence of imaginary frequencies. The hybrid functional of Perdew, Burke and Ernzerhof PBE1PBE was used.[122, 123] Geometry optimization and energy calculations were carried out using the standard 6-31+G(d) or 6-31G basis set. These bases sets offer a reasonable compromise between the proper description of the species and good performance at a modest computational cost.

In the calculations in this thesis, special attention was paid to rigid benzophenone-tyrosine dyads since that pair of diasteroisomers exhibits significant solvent-dependent stereoselectivity toward intramolecular HAT. In addition to gas-phase calculations for those dyads, solvent effects were evaluated using the self-consistent reaction field (SCRF) method with the “integral equation formalism polarizable continuum model” (IEFPCM). The same level of theory was used to calculate the energy of optimized structures in the presence of ACN. The gas-phase geometries were reoptimized in this model.[124, 125] The notation for the rotamers of the diketopiperazine-based cyclic dyads will be described in detail in Chapter 3.2.2.2.1. The structures of the conformations with the lowest energies for each compound were compared to the highest populated conformations obtained *via* molecular dynamics simulations.

Additionally, theoretical calculations were carried out to characterize the hydrogen-bond complexes between solvent molecules and benzophenone, both in its ground state and excited triplet state. The relationship between hydrogen-bond length and strength was studied by systematically lengthening the distance between the hydrogen-bond donor (molecule of TFE solvent) and the hydrogen-bond acceptor (carbonyl oxygen of BP), recalculating the hydrogen-bond energy (E_{HB}) at each step. E_{HB} was calculated as the difference in energy between the complex and the infinitely separated monomers, benzophenone and TFE. For each constrained O–H distance, the rest of the molecular complex was allowed to optimize completely. O–H distances between 1.2 and 3.0 Å were studied. The same procedure was used for the ground state S_0 and the excited triplet state T_1 of benzophenone.

Furthermore DFT calculations were employed to confirm the importance of specific solvent-solute interactions in electron-transfer quenching of the benzophenone triplet by anisole. Experimental data, in conjunction with theoretical calculations, were used to quantify the solvent effects on the activation free energy of ET reactions in terms of the Marcus theory of adiabatic electron transfer (see details in Chapter 3.6.5).

2.3.2 **Molecular Dynamics**

Molecular dynamics (MD) is a computer simulation technique where the time evolution of a set of interacting atoms is followed by integrating their classical mechanical equations of motion. The main justification of the MD method is that statistical ensemble averages are equal to time averages of the system, known as the ergodic hypothesis.

Because molecular systems, in general, consist of a large number of particles, it is impossible to find the properties of such complex systems analytically. Molecular-dynamics simulation circumvents this problem by using numerical, step-by-step, solutions of the classical equations of motion. A molecular-dynamics simulation requires the characterization of a potential energy which describes the terms by which the particles in the simulation will interact. Most force-fields in chemistry are empirical and consist of a summation of bonded forces associated with chemical bonds, bond angles, bond dihedrals, and non-bonded forces associated with van der Waals forces and electrostatic charge (see Eq 2.3-5). Molecular-dynamics simulations performed for the investigated compounds were used with the general AMBER force field (GAFF) which well describes small organic molecules.[126] It applies additive harmonic energy functions and nonbonded interactions between pairs of atoms (*i*, *j*) which are represented by the last two terms:

$$E_{pair} = \sum_{bonds} K_r\left(r - r_{eq}\right)^2 + \sum_{angles} K_\theta\left(\theta - \theta_{eq}\right)^2 + \sum_{dihedrals} \frac{V_n}{2}\left[1 + \cos(n\phi - \gamma)\right] + \sum_{i<j}\left[\frac{A_{ij}}{R_{ij}^{12}} - \frac{B_{ij}}{R_{ij}^{6}} + \frac{q_i q_j}{\varepsilon R_{ij}}\right] \qquad \text{Eq 2.3-5}$$

where:

K_r, K_θ, V_n – the force constants for bond length stretching, bond angle bending and torsional angle twisting, respectively;

r, θ – bond length and bond angle, respectively;

r_{eq}, θ_{eq} – the equilibrium bond length and bond angle, respectively;

n – the multiplicity of the function;

ϕ – dihedral angle;

γ – the phase angles of the Fourier series in the dihedral terms;

A_{ij}, B_{ij} – the parameters of Lennard–Jones 12-6 potentials;

q_i, q_j – the point charges of atoms i and j, respectively;

ε – dielectric constant of the space;

R_{ij} – distance between atoms i and j.

For the MD simulations version 10 of the AMBER molecular-modelling package was applied which is implemented on the Notre Dame Radiation Laboratory cluster. [127] The AMBER package consists of the variety of programs. The programs and their applications used during the work are listed below:

- **The preparatory programs:**
  - **Antechamber** – The Antechamber software package contains procedures and algorithms by which the parameters from Eq 2.3-5 can be automatically assigned to arbitrary molecules, given only a three-dimensional structure as input. That algorithm requires solving the following problems before the MD calculations: (1) recognizing the atom type; (2) recognizing the bond type; (3) judging the atomic equivalence; (4) generating a residue topology file; (5) finding missing force field parameters and supplying reasonable and similar substitutes. Gaussian output files, from the previously performed DFT optimization, are one of the acceptable formats for the Antechamber program; so, those files were

    used for conversion into appropriate files which could then be read into LEAP.
  - **LEAP –** the program takes into consideration the force field, topology and coordinate information, and it was used to produce the files necessary for production calculations: one file containing a description of the molecular topology and the necessary force field parameters (*prmtop* file) and a second file containing a description of the atom coordinates and velocities (*inpcrd* file).
- **The simulation program:**
  - **SANDER –** it is the basic energy minimizer and molecular-dynamics program that requires an input file (*mdin*) consisting of a series of namelists and control variables that determine the options and type of simulation to be run.
- **The analysis program:**
  - **PTRAJ –** has been used for the initial analysis of the trajectories from MD simulations and for the calculation of root mean square deviation (RMSd) as a function of time.

Design of a molecular-dynamics simulation should account for the available computational power. The number of particles, time step and total time duration must be selected so that the calculation can finish within a reasonable time period. However, the simulations should be long enough to be relevant to the time scales of the natural processes being studied. Thus instead of performing simulations with explicit solvation, which are time consuming, the Born solvation model was used. In order to achieve reliable statistical distributions for the conformers of the compounds in this work, the free MD simulations were done with a 2 fs time step and 100 ns propagation time, preceded by 20 ps of heating from 0 K to 300 K and 60 ps of equilibration.

Visual Molecular Dynamics (VMD) was used for visualising and analysing results produced by the Sander module of the AMBER software suite. VMD is a freely available molecular visualization program designed by the Theoretical Biophysics Group at the University of Illinois and Beckman Institute. VMD was applied in the quantitative analysis of the desired properties of the simulated systems: distances between reactive moieties (see an example of such an analysis in Figure 2.3-1), and dihedral angles which define the orientation of the side-chain rotamers. The example data show a dominating d(O-O) distance of about 8-9 Å, but reveal also, although with much lower probability, the possibility of a close contact at around 4 Å.

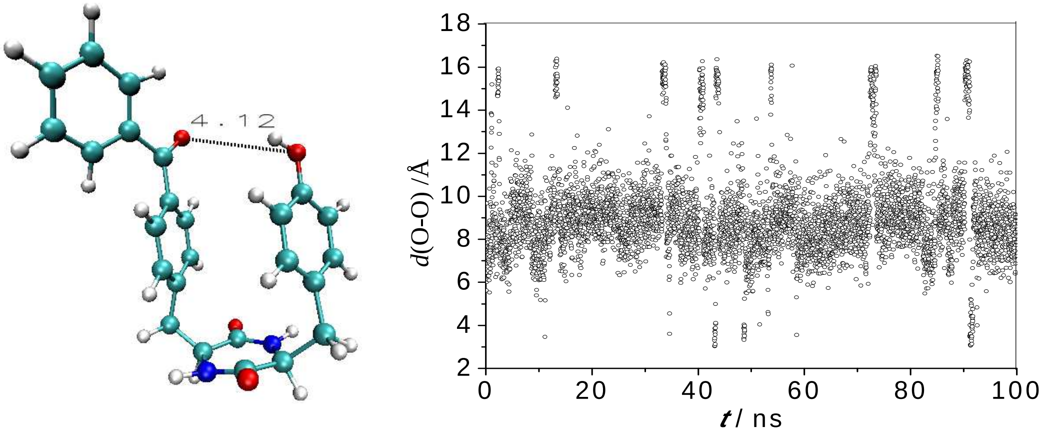

Figure 2.3-1. Sample application of the VMD program for the analysis of the long-time molecular-dynamics simulations for dyad **(S,S)-BP-DKP-Tyr**: time variation of the inter-side-chain distance d(O–O) between the Tyr hydroxylic oxygen atom and the BP carbonyl oxygen atom.

Additionally the VMD program can calculate the spherical atomic radial distribution function $g(r)$ between two atoms coordinates over a given trajectory. Function $g(r)$ is defined so that the probability $p(r)$ of r being between r_1 and r_2 is the integral between r_1 and r_1 of $4\,\pi\,r^2\,g(r)$ (Eq 2.3-6).

$$p(r) = \int_{r_1}^{r_2} 4\pi g(r) r^2 \, dr \tag{Eq 2.3-6}$$

The radial distribution function $g(r)$ is a fundamental quantity for verifying the possibility for the compound to achieve suitable geometries for intramolecular reactions.

2.4 Sample preparation

Samples for determining the spectroscopic properties were prepared as follows:

- **UV spectra** – for the detection of the $\pi\rightarrow\pi^*$ and $n\rightarrow\pi^*$ bands the sample concentrations were around 6×10^{-5} M and 1×10^{-3} M, respectively. If the solubility of the compound was too small to dissolve it in millimolar concentration, only the absorption spectra for the $\pi\rightarrow\pi^*$ band were measured. The exact masses of the compounds were estimated using an analytical balance, a Mettler-Toledo UMT2 with an accuracy of 10^{-7} g. The UV spectra for each of the investigated compounds were measured in three different solvents. For acetonitrile, the molar absorption coefficient was obtained and compared with pure benzophenone. The molar absorption coefficients were determined as the averages of three trials on the basis of the Beer-Lambert law (Eq 2.2-1).
- **Phosphorescence spectra** – were measured at 77 K in a mixture of solvents: DCM–MeOH (1:1 v/v). This solvent mixture was chosen because it forms a transparent glass.[128] The glass was formed by cooling the solutions in a special cuvette to liquid nitrogen temperature. To avoid moisture condensing on the cuvette during the experiments, nitrogen was blown around the cuvette. The phosphorescence spectra were recorded with solutions having an absorbance at the excitation wavelength of $A_{\lambda_{exc}} \sim 0.5$.

Samples for the investigation of intramolecular and intermolecular reactions were prepared as follows:

- **Steady-state irradiation –** solutions of the investigated compounds used for the determination of the quantum yields of substrate disappearance had concentrations of 2×10^{-3} M when the excitation wavelength was 313 nm (high-pressure mercury lamp, irradiated volume 2.2 cm^3) or 351 nm (argon ion laser, irradiated volume 2.5 cm^3), or 4.75×10^{-5} M when the excitation wavelength was 254 nm (low-pressure mercury lamp, irradiated volume 2.2 cm^3). The reaction progress was monitored by HPLC. To avoid errors caused by changing the volume of solutions and from dissolving oxygen inside the cuvette after piercing the septum, each irradiation was performed with a fresh solution. Experiments were performed in a 1 cm × 1 cm rectangular UV cell except for irradiations on a preparative scale. All samples for irradiation were deoxygenated with high-purity argon for 15 minutes prior to the measurements.

- **Nanosecond flash photolysis** – samples for LFP were deoxygenated with high-purity argon for 15 minutes prior to the measurements and kept under argon during the measurements. The laser interaction with the sample often results in irreversible changes, and this necessitates sample replacement for each individual measurement. Concentrations in the range of 4 to 8 × 10^{-5} M and 1 to 3 × 10^{-3} M were used at 266 and 355 nm, respectively. Different orders of magnitude of the concentrations used are connected with exciting the strong $\pi\rightarrow\pi^*$ transition (λ = 250 nm; ε = 16000 M^{-1} cm^{-1}) or the much weaker $n\rightarrow\pi^*$ transition (λ = 340 nm; ε = 100-200 M^{-1} cm^{-1}). Possible irreversibility of the reaction was taken into account when concentrations of the solutions were in the range 10^{-5} M. In such cases, a flow-system procedure was applied. This was accomplished by putting a volume of 100 ml of the investigated solution inside a reservoir and then deoxygenating it. The flow (by gravity) of the solution (from the reservoir into the cell) was adjusted to 1 drop per 1-2 seconds. The waste solution was gathered in the beaker, and it was not recycled. When reversible reactions were investigated and/or when millimolar concentrations were used, which is three orders of magnitude higher than the initial concentration of formed transients, then the flow system was not used. In such cases, experiments were performed in rectangular quartz cells (1 cm × 1 cm) or (1 cm × 0.5 cm), with a solution volume of 3 cm^3 and 2 cm^3, respectively. The LFP were performed with solutions having an absorbance at the excitation wavelength in the range $0.1 < A_{\lambda_{exc}} < 0.4$. All experiments were performed with freshly prepared solutions at room temperature (295 ± 1 K). A solution of benzophenone in ACN, whose absorbance matched the absorbance of each of the investigated solutions at the excitation wavelength, was used as an actinometer. In order to determine the bimolecular quenching rate constants, k_q, for the triplet quenching of BP and its derivative by anisole, the decay of the triplet state of benzophenone was monitored in the presence of increasing concentrations of anisole. It was carried out by adding increasing amounts of the quencher (μl) from a stock solution to 5-6 flasks of 5 cm^3 volume containing the same solution of benzophenone or its derivative.

2.5 Methodology of Measurements

2.5.1 Determination of the initial intensity of the light using uranyl oxalate actinometry

Uranyl oxalate actinometer was used to determine the intensity of the incident light (I_o) used in quantitative analysis in steady-state irradiations. The actinometer consisted of the mixture (1:1 v/v) of 0.02 M of $UO_2SO_4 \times 3H_2O$ and 0.1 M of $H_2C_2O_4 \times 2H_2O$. The photochemical reaction of the transformation of the oxalic acid is:

$$H_2C_2O_4 \xrightarrow{h\upsilon, UO_2^{2+}} CO_2 + CO + H_2O$$

where the UO_2^{2+} acts as a photosensitizer.

The quantum yields of this reaction (Φ_λ) for the excitation wavelengths λ_{irr} = 254 nm and λ_{irr} = 313 nm are 0.602 and 0.561, respectively. The number of oxalate ions in solution, before and after the irradiation, was determined by titration with 0.004 M potassium permanganate:

$$5H_2C_2O_4 + 2KMnO_4 + 3H_2SO_4 \rightarrow 10CO_2 + K_2SO_4 + 2MnSO_4 + 8H_2O$$

The photolysis of the oxylic acid should be performed only up to until 50 % conversion at most. A 2.2 cm^3 volume of the actinometer was irradiated, and the same volume of irradiated samples was used in the steady-state irradiations of the compounds. The intensity of the incident light is given by:

$$I_o = \frac{5}{2}\frac{\Delta V_{KMnO_4} \cdot c_{KMnO_4}}{\Phi_\lambda \cdot V \cdot t_{irr}} \qquad \text{Eq 2.5-1}$$

where:

I_o – intensity of the incident light [Einstein dm^{-3} s^{-1}];

ΔV_{KMnO_4} – the difference of the $KMnO_4$ volume used in titration of the sample before and after irradiation, the difference of volume was taken as an average of three independent titrations done before and after irradiation [cm^3];

c_{KMnO_4} – concentration of the $KMnO_4$ used for titration [M];

Φ_λ – quantum yield of the photolysis of the oxylic acid at λ excitation wavelength;

V – volume of the actinometer taken for titration [cm^3];

t_{irr} – irradiation time [s].

The factor of 5/2 comes from the stoichiometry of the redox reaction.

2.5.2 **Determination of the initial intensity of the light using Reinecke's salt**

Reinecke's actinometer is based on the $K[Cr(NH_3)_2(SCN)_4]$ (potassium diaminetetrakis(thiocyanato-N) chromate) salt diluted in acidic solution. This actinometer was used to determine the incident intensity of the light emitted by the argon ion laser at the 351 nm wavelength. The quantum yield of the reaction in the Reinecke actinometer is 0.39 at 351 nm.[128] Irradiation by UV-vis light caused the substitution of a SCN^- ligand by a water molecule:

$$[Cr(NH_3)_2(SCN)_4]^- + H_2O \xrightarrow{h\nu} [Cr(NH_3)_2(SCN)_3(H_2O)] + SCN^-$$

The concentration of free SCN^- ions was determined spectrophotometrically *via* complexation with ferric nitrate:

$$Fe^{3+} + SCN^- \rightarrow Fe(SCN)^{2+}$$

At the end of the irradiation period (90 s), 0.2 cm^3 of the to-be-analyzed solution was accurately diluted with 2 cm^3 of reagent solution consisting of 0.02 M $Fe(NO_3)_3$ and 0.35 M of $HClO_4$. The resulting red complex has a maximum absorption at $\lambda_{\mathrm{max}} = 430$ nm ($\varepsilon = 3200\ \mathrm{M}^{-1}\ \mathrm{cm}^{-1}$). Spectrophotometric measurements were performed both for the irradiated sample and a sample kept in the dark. This procedure was done in order to make corrections for any thermal aquation reaction. The intensity of the incident light was calculated from the formula:

$$\mathrm{I}_0 = \frac{K \cdot \Delta A}{\Phi_\lambda \cdot \varepsilon \cdot \mathrm{t}_{\mathrm{irr}} \cdot \mathrm{l}} \qquad \text{Eq 2.5-2}$$

where:

I_o – intensity of the incident light [$\mathrm{Einstein\ dm^{-3}\ s^{-1}}$];

K – conversion factor connected with dilution equal 11;

ΔA – difference in absorbance of the irradiated and non-irradiated sample at 430 nm;

Φ_λ – quantum yields of the photoaquation reaction at λ_{exc} =351 nm;

ε – molar absorption coefficient of the complex at λ_{max} [M^{-1} cm^{-1}];

t_{irr} – the irradiation time [s];

l – optical pathlength [cm].

2.5.3 Determination of the quantum yield of substrate disappearance

The quantum yield is a value of how efficiently the absorbed photons are utilized. After photon absorption there are different paths in which the excited state might be deactivated. So, not every excited molecule will form a primary product. The overall quantum yield can be expressed as the ratio of the number of reactant molecules, R, that disappear to the number of photons of light absorbed:

$$\Phi = \frac{number\ of\ molecules\ of\ R\ consumed}{number\ of\ photons\ absorbed\ by\ R} \qquad \text{Eq 2.5-3}$$

An alternative way of defining this quantum yield is through a differential quantum yield. This is expressed as the ratio of the velocity of the process (disappearance of the substrate or product formation) to the intensity of the light absorbed by the substrate:

$$\Phi_S = -\frac{\frac{d[S]}{dt}}{I_a^s} \qquad \text{Eq 2.5-4}$$

$$\Phi_P = \frac{\frac{d[P]}{dt}}{I_a^s} \qquad \text{Eq 2.5-5}$$

where:

Φ_S – differential quantum yield of substrate disappearance;

Φ_P – differential quantum yields of product formation;

$-\frac{d[S]}{dt}$ – loss of the substrate concentration in time dt, [$\mathrm{M\ s^{-1}}$];

$\frac{d[P]}{dt}$ – growth of the product concentration in time dt, [$\mathrm{M\ s^{-1}}$];

I_a^S – intensity of the light absorbed by the substrate, [$\mathrm{Einstein\ dm^{-3}\ s^{-1}}$].

Practically, the quantum yields of substrate disappearance were calculated from the simplified equation:

$$\Phi_s = \frac{\Delta c}{I_a^s \cdot t} \qquad \text{Eq 2.5-6}$$

where:

Δc – change in the concentration, of the sample before and after irradiation, [M].

The loss of concentration was monitored with the HPLC method by calculating the area under the peak corresponding to the substrate after time *t* of irradiation and comparing that to the area under the peak of the substrate without irradiating. The values of the quantum yields at time t of irradiation were extrapolated to time *t* = 0.

The intensity of the light absorbed by the sample was calculated on the basis of the formula:

$$I_a^s = I_o(1 - 10^{-A_\lambda}) \qquad \text{Eq 2.5-7}$$

where:

I_o – intensity of the incident light [Einstein $\mathrm{dm^{-3}\ s^{-1}}$];

I_a^S – intensity of the light absorbed by the substrate, [Einstein $\mathrm{dm^{-3}\ s^{-1}}$];

A_λ – absorbance of the sample at the irradiation wavelength λ.

2.5.4 **Determination of the quenching rate constant**

The quenching rate constants k_q were determined for the quenching of the triplet states of benzophenones by methoxybenzene (anisole) on the basis of the Stern-Volmer equation:

$$k_{obs} = \frac{1}{\tau_T} = \frac{1}{\tau_T^o} + k_q[Q] \qquad \text{Eq 2.5-8}$$

where:

k_{obs} – observed rate constant [$\mathrm{s^{-1}}$];

τ_T – triplet lifetime of the benzophenone or its derivative in a presence of a quencher [s];

τ_T^o – triplet lifetime of the benzophenone or its derivative without a quencher [s];

k_q – quenching rate constant $[\mathrm{M\ s^{-1}}]$;

$[Q]$ – concentration of the quencher $[\mathrm{M}]$.

The Stern-Volmer equation describes the observed rate constant as a linear function of the quencher concentration (k_{obs} *vs*. $[Q]$ should be a straight line), and hence it allows for a very easy experimental determination of the quenching rate constant. Triplet lifetimes were measured in the absence of quencher and then in the presence of incremental amounts of quencher. The resulting observed rate constant k_{obs} is plotted as a function of quencher concentration $[Q]$ (see typical plot in Figure 2.5-1). The quenching rate constants k_q have been obtained from the slope of the linear Stern-Volmer plot.

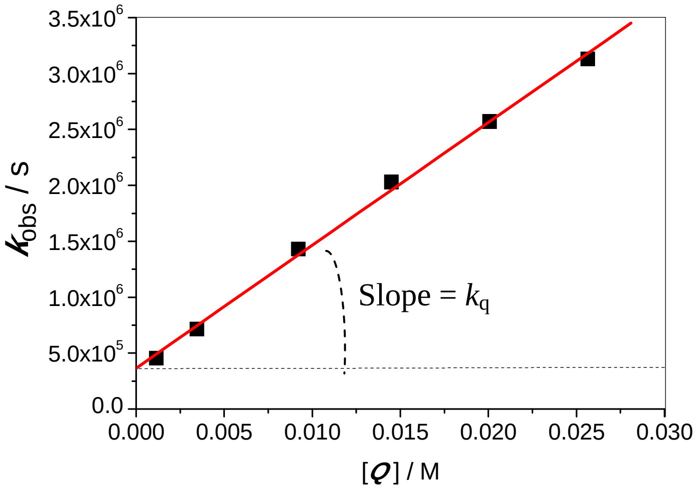

Figure 2.5-1 Graphic representation of Stern-Volmer type kinetic analysis.

2.5.5 **Determination of the intramolecular H-atom transfer rate constant**

In order to study the solvent effects on the intramolecular HAT pathway for benzophenone-tyrosine dyads, the corresponding rate constants, k_H, had to be isolated from the observed gross triplet-decay rate constants, k_{obs}. The rate constants of the triplet decay, k_{obs}, were obtained by a monoexponential fit to the experimental decay profiles at 630 nm. At this wavelength only the triplet state has significant absorption since formation of the benzophenone radical anion, with a strong absorption at 630 nm, was insignificant throughout the study (except in ACN–H_2O mixtures for the dyad **(S,R)-BP-DKP-Tyr**). The values obtained have been cross-checked by biexponential fits to the profiles at 520 nm, where the observed second decay component is attributed to the biradical decay with k_{BR}. Finally, in selected solvents, spectral-resolution techniques were used to resolve the convoluted profiles into separate concentration-time profiles. The rate constant then was obtained by a monoexponential fit to the triplet concentrations. Agreement between all of the methods was generally within ± 5 %.

The decay-rate constant of the triplet-excited state of the dyads, k_{obs}, is the result of several competing pathways (see Scheme 2.5-1).

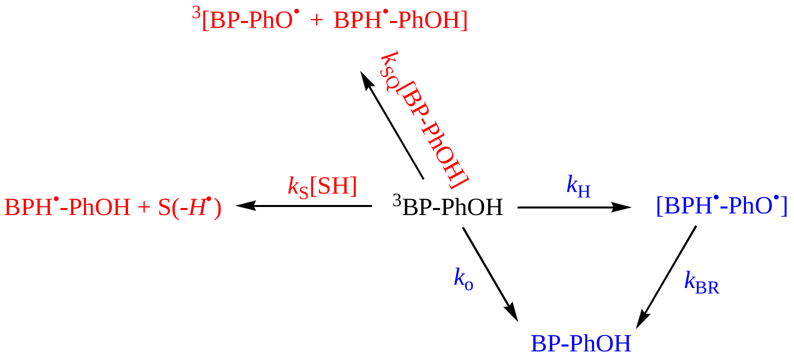

Scheme 2.5-1 Deactivation paths (red: bimolecular; blue: unimolecular) of the triplet-excited state of the dyads benzophenone-tyrosine.

At constant light intensity and dyad concentration, the intrinsic decay constant (k_o), the self-quenching constant ($k_{SQ}[BP-PhOH]$), the solvent reaction rate ($k_S[SH]$) and the intramolecular HAT transfer rate constant (k_H) can be summed to give k_{obs} (Eq 2.5-9).

$$k_{obs} = k_o + k_H + k_{SQ}[BP-PhOH] + k_s[SH] \qquad \text{Eq 2.5-9}$$

The small contribution from the triplet-triplet annihilation rate is assumed to be negligible at low laser power. The contributions from solvent abstraction, ($k_S[SH]$) were accounted for by employing reference compounds (see Chapter 3.5.2) to estimate ($k_S[SH]$) in the respective solvents. The sum of the intrinsic decay constant k_0 and the solvent reaction rate ($k_S[SH]$) is equal to the triplet decay rate constant k_T for the reference compound. Under the experimental conditions of 266 nm excitation, the contributions from self quenching, k_{SQ}, were negligible, so that the rate constant for the hydrogen-atom transfer (HAT) step, k_H, is given by Eq 2.5-10.

$$k_H = k_{obs} - k_0 - k_S[SH] = k_{obs} - k_T \qquad \text{Eq 2.5-10}$$

When solubility allowed for the use of 337 nm or 355 nm excitation, the self-quenching was taken into account with $k_{SQ}[BP - PhOH]$ (Eq 2.5-11).

$$k_H = k_{obs} - k_T - k_{SQ}[BP - PhOH] \qquad \text{Eq 2.5-11}$$

It is noted that the poor solubility of the some of the dyads interfered with accurate measurements of some self-quenching rate constants. For calculations, the rate constant for self-quenching was taken from a structurally related, but open-chain benzophenone/phenol dyad.[76]

2.5.6 **Resolution of the transient absorption spectra**

Resolution of the transient spectra into spectral components was used to study the selectivity of the quenching reaction for dyads and to determine the quantum yields for the formation of the *i*-th transient. In most cases of convoluted spectra, a multi-regression analysis has to be done on the optical transient spectra resulting from pulsed irradiation in order to extract the individual transient concentrations c_i. In any time window, following the excitation pulse, the absorbance of the signal is related to the concentrations and molar absorption coefficients of the transients *via* Beers's Law:

$$\Delta A(\lambda_{j,}t) = \sum_{i=1}^{n} c_i(t) \cdot \varepsilon_i\,(\lambda_j) \cdot l, \qquad j = 1 \dots r \qquad \text{Eq 2.5-12}$$

where $\Delta A(\lambda j,t)$ is the observed absorbance change of the composite spectrum at the *j*th wavelength, $\varepsilon_i(\lambda j)$ is the molar absorption coefficient of the *i*th species at the *j*th wavelength of the observation, $c_i(t)$ is the concentration of the *i*th transient, and *l* is the optical path length.[129] When molar absorption coefficients of all possible transients present in the system are known at different wavelengths, a set of equations can be solved, in a least-squares fashion, to give the unknown concentrations of the intermediates, $c_i(t)$.[130, 131] Eq 2.5-12 corresponds to r linear equations, one for each wavelength, and n unknowns $c_i(t)$. If $n < r$, there are more equations than unknowns, i.e., an overdetermined set of equations. In such a case, the unknowns $c_i(t)$ can be determined by a least-squares regression. This is the strategy for spectral resolutions. The uncertainties for the $c_i(t)$ are computed from the square roots of the diagonal matrix elements of the covariance matrix for each linear regression. Such a spectral resolution requires isolated reference spectra of all likely transients, together with their molar absorption coefficients $\varepsilon_i(\lambda j)$.

As an numerical example, reference spectra will be analyzed in the following for the excited triplet states of the benzophenone-tyrosine dyads, obtained by LFP of benzophenone in an ACN-H_2O (1:1 v/v) mixture. The spectra were normalized to the extinction coefficients that were measured by Baral-Tosh et.al (green symbols in Figure 2.5-2).[132] Spectra of radical species relevant to this study: the ketyl radical $BPH^{\bullet}$ and the radical anion $BP^{\bullet-}$ were obtained by bimolecular quenching of the triplet state of BP with 2-propanol (1 M) at pH = 6 and pH = 11, respectively. Spectra of the resulting ketyl radicals were corrected by scaling with known molar absorption coefficients (Figure 2.5-2).[132, 133]

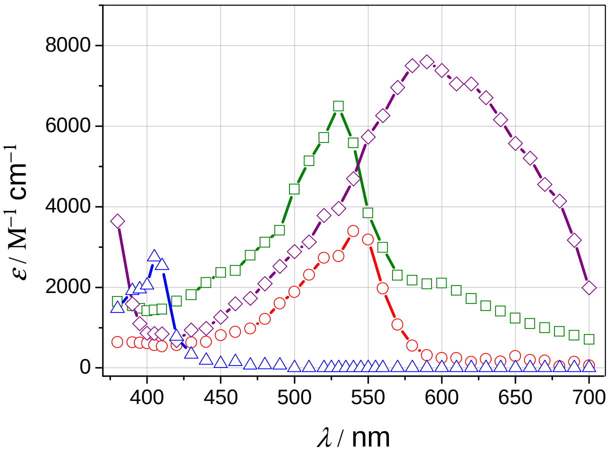

Figure 2.5-2 Reference transient absorption spectra of the BP triplet state, ketyl radical $BPH^{\bullet}$, radical anion $BP^{\bullet-}$ obtained during laser flash photolysis at 355 nm of deoxygenated solutions in ACN-H_2O (1:1 v/v) and transient absorption spectra of Tyr($O^{\bullet}$) obtained in pulse radiolysis. The symbols represent: □ for the triplet state ^3BP, ○ for the ketyl radical $BPH^{\bullet}$, ◊ for the BP radical anion $BP^{\bullet-}$ and ▵ for the tyrosyl radical Tyr($O^{\bullet}$), Detailed description in text.

Spectra of the tyrosyl radical Tyr($O^{\bullet}$) came from pulse radiolysis experiments and were provided by K. Bobrowski from the Institute of Nuclear Chemistry and Technology, Warsaw, Poland. Tyrosyl radicals were generated by pulse-irradiating N_2O-saturated neutral aqueous solutions of 2×10^{-3} M tyrosine containing 0.1 M NaN_3. Tyrosyl radicals exhibit a sharp optical absorption band at 405–410 nm with a relatively low molar absorption coefficient (blue symbols in Figure 2.5-2). The reference spectrum of the tyrosyl radical was normalized to a molar absorption coefficient of 2750 M^{-1} cm^{-1},[134, 135] which was considered to be the most reliable value.

Reference spectra for the 4-carboxybenzophenone intermediates: ^{3}CB, CBH$^\bullet$, and CB$^{\bullet-}$, were obtained by P. Filipiak from the Department of Chemical Physics at Adam Mickiewicz University. The reference spectrum for the CB triplet, used in the spectral resolutions was generated by laser flash photolysis of an aqueous solution at pH = 6.8. The radical anion CB$^{\bullet-}$ and ketyl radical CBH$^\bullet$ spectra were obtained by LFP with a 2 mM CB solution at pH = 10 and pH = 6.8, respectively, in the presence of 2-propanol (1 M). The reference spectra of ^{3}CB, CBH$^\bullet$, CB$^{\bullet-}$ were normalized to the molar absorption coefficients used earlier by Marciniak *et al.* (Figure 2.5-3).[136]

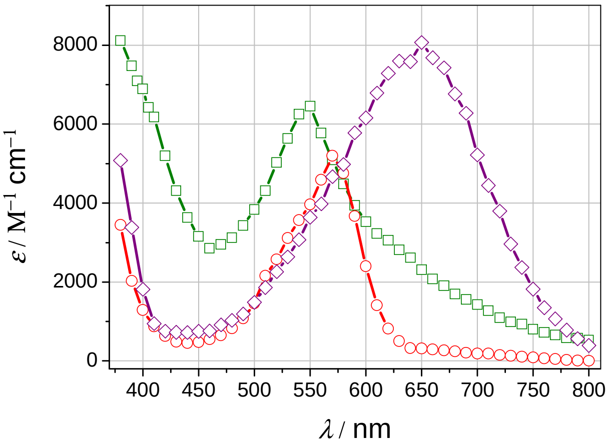

Figure 2.5-3 Reference transient absorption spectra of the CB triplet state, ketyl radical CBH$^\bullet$, and radical anion CB$^{\bullet-}$ obtained during laser flash photolysis at 355 nm in deoxygenated aqueous solutions. The symbols represent: □ for the triplet state ^{3}CB, ○ for the ketyl radical CBH$^\bullet$, ◊ for the CB radical anion CB$^{\bullet-}$. Detailed description in text.

2.5.7 **Determination of the quantum yield of the radical formation**

Quantitative information regarding the yields of the photoproducts as a result of the primary interactions between the triplet and the quencher (tyrosine, methionine, anisole) is as important a mechanistic detail as is the magnitude of the quenching rate constants. Quantum yields were determined either from concentration profiles (for benzophenone-tyrosine dyads) or directly from isolated absorbances at characteristic wavelengths for single transients in regions where there were no spectral overlaps (Eq 2.5-13). Quantum yields of the radicals’ formation, namely of the ketyl radical and tyrosyl radical from benzophenone-tyrosine dyads were extracted from the concentration profiles obtained *via* resolution of the transient absorption spectra by extrapolation back to the end of the excitation pulse.

The quenching of triplet-excited BP derivatives by anisole in protic solvents (TFE, ACN–H_2O mixture) was accompanied by significant formation of free radicals. The quantum yields of free-radical formation were derived by relative actinometry with optically matched solutions of BP in ACN. The absorbances at the respective spectral maxima of the transient photoproducts were measured (see a typical plot in Figure 2.5-4) and compared with the end-of-pulse absorbance at 520 nm of the benzophenone triplet.

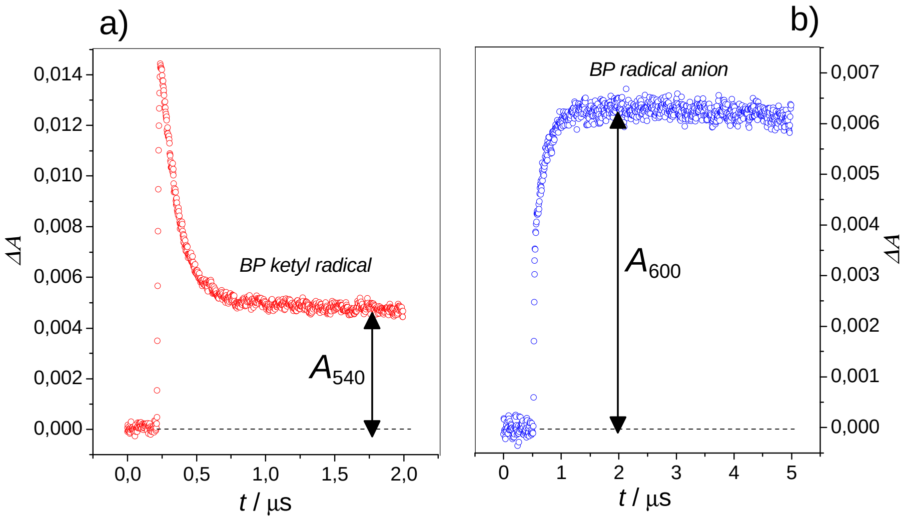

Figure 2.5-4 Decay profiles of the transient absorption monitored at a) 540 nm for the quenching of BP (1.2×10^{-3} M) by anisole (0.138M) in ACN-TFE (1:4 v/v) b) 600 nm for the quenching of BP (1.2×10^{-3} M) by anisole (0.0057 M) in ACN-H_2O (1:9 v/v).

The concentration of anisole was sufficiently high to quench the triplet almost totally (>90 %). The yields Φ_P were calculated according to the formula:

$$\Phi_P = \frac{\Phi_T^{BP} \cdot A_\lambda \cdot \varepsilon_{520}^{BP}}{A_{520} \cdot \varepsilon_\lambda^P} \qquad \text{Eq 2.5-13}$$

where:

A_λ – the observed absorbance of the transient under study at λ;

ε_λ^P – molar absorption coefficient of the transient at the wavelength λ;

A_{520} – the transient absorbance of the BP triplet at 520 nm in the actinometer solution measured under conditions of no quenching;

$\varepsilon_{520}{}^{\mathrm{BP}}$ – molar absorption coefficient of the BP at 520 nm in ACN, $\varepsilon_{520}^{BP} = 6500$ M^{-1} cm$^{-1;}$

$\Phi_{\mathrm{T}}{}^{\mathrm{BP}}$ – triplet quantum yield of the BP, $\Phi_{\mathrm{T}}{}^{\mathrm{BP}} = 1.0$.

For the following transient intermediates, the molar absorption coefficients werederived from pulse radiolysis or flash photolysis in aqueous solutions:

- BP ketyl radical BPH$^{\bullet}$: $\varepsilon_{540} = 3400$ M^{-1} cm^{-1};
- BP radical anion BP$^{\bullet-}$: $\varepsilon_{600} = 7600$ M^{-1} cm^{-1};
- Anisole radical cation: $\varepsilon_{430} = 3800$ M^{-1} cm^{-1};
- CB ketyl radical (CBH$^{\bullet}$): $\varepsilon_{570} = 5200$ M^{-1} cm^{-1};
- CB radical anion (CB$^{\bullet-}$): $\varepsilon_{650} = 8100$ M^{-1} cm^{-1}.

It is noted that the approach rests on the assumption that the absorption properties of the transients do not vary significantly with the nature of the solvent. As a consequence, the derived quantum yields carry a relatively high intrinsic uncertainty.

3 RESULTS AND DISCUSSION

3.1 Spectroscopic properties of the investigated compounds

The photophysical properties of the investigated compounds were studied in order to trace possible effects of the substitutions on the electronic properties of the BP chromophore in the investigated BP-Tyr, BP-Met dyads and triads. The examination included measuring of the absorption and phosphorescence spectra, and subsequent comparisons with unsubstituted benzophenone.

3.1.1 Absorption spectra

3.1.1.1 Bichromophores: benzophenone–tyrosine

The UV spectra of the benzophenone-tyrosine dyads were recorded in three solvents: ACN, TFE and MeOH at ca. 6.2 × 10^{-5} molar concentrations. Millimolar concentrations (ca. 1.0 × 10^{-3} M) were employed for the determination of the $n\rightarrow\pi^*$ transition of the benzophenone chromophore at around 340 nm. The UV spectra measured for **(S,S)-BP-Tyr** and **(S,S)-BP-DKP-Tyr** are presented in Figure 3.1-1 and Figure 3.1-2, respectively.

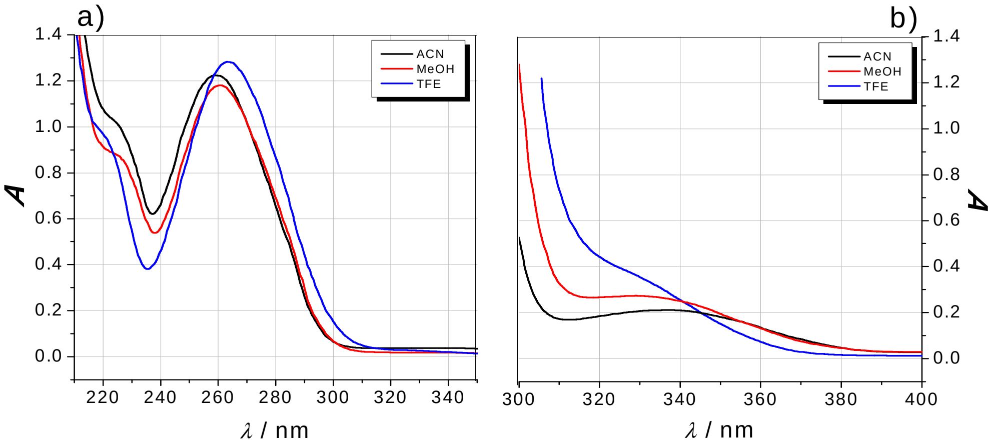

Figure 3.1-1 Absorption spectra of **(S,S)-BP-Tyr** in different solvents: a) $\pi\rightarrow\pi^*$ band, concentrations: ACN – 6.2 × 10^{-5} M, MeOH – 6.3 × 10^{-5} M, TFE – 6 × 10^{-5} M, b) $n\rightarrow\pi^*$ band, concentrations: ACN – 9.2 × 10^{-4} M, MeOH – 9.7 × 10^{-4} M, TFE – 9.8 × 10^{-4} M.

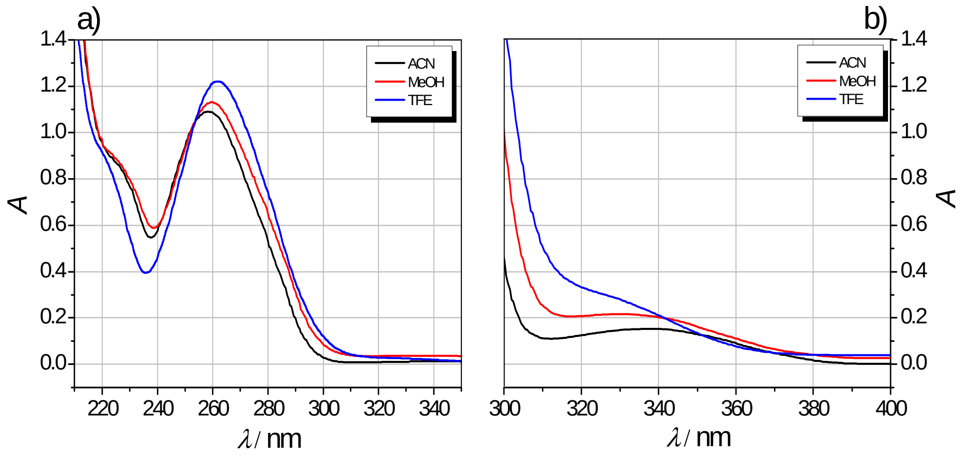

Figure 3.1-2 Absorption spectra of **(S,S)-BP-DKP-Tyr** in different solvents: a) π→π^* band, concentrations: ACN – 5.9 × 10^{-5} M, MeOH – 5.9 × 10^{-5} M, TFE – 6 × 10^{-5} M, b) n→π^* band, concentrations: ACN – 8.9 × 10^{-4} M, MeOH – 8.9 × 10^{-4} M, TFE – 9 × 10^{-4} M.

The UV spectra of **(R,S)-BP-Tyr** and **(S,R)-BP-DKP-Tyr** are very similar, and they are not presented here graphically. A summary of the absorption properties of the benzophenone-tyrosine dyads is, however, collected in Table 3.1-1. It includes the wavelengths of the maximum absorptions (λ_{max}) for each band obtained in three solvents and the values of the molar absorption coefficients at these wavelengths ($\varepsilon_{\mathrm{max}}$) measured in ACN. As can be seen from Table 3.1-1, there are only small differences between the compounds in regard to both λ_{max} and $\varepsilon_{\mathrm{max}}$. The absorption of the π→π^* band for each compound showed a continuously increasing red shift with an increase of the HB-donating abilities of the solvents in going from ACN to TFE. On the other hand, the n→π^* band showed a blue shift with an increase of the HB-donating abilities of the solvents.

Table 3.1-1 Absorption properties of benzophenone-tyrosine dyads in different solvents.

Dyad	**λ_{max} (ACN)** / [nm]		**$\varepsilon_{\mathrm{max}}$ (ACN)** / [M^{-1} cm^{-1}]		**λ_{max} (MeOH)** / [nm]		**λ_{max} (TFE)** / [nm]	
	π→π^*	n→π^*	π→π^*	n→π^*	π→π^*	n→π^*	π→π^*	n→π^{*a}
(S,S)-BP-Tyr	259	337	19200	230	260	329	263	-
(R,S)-BP-Tyr	259	337	18700	215	260	329	263	-
(S,S)-BP-DKP-Tyr	258.5	337	18100	170	259.5	330.5	262	-
(S,R)-BP-DKP-Tyr	258	337	18900	200	259.5	331	262	-

[a] not determined due to the lack of a well-defined maximum of absorption.

3.1.1.2 Bichromophores: benzophenone–methionine

The UV spectra for open-chain BP-Met dyads were measured in the two solvents: ACN and TFE, and in one solvent mixture: ACN-H_2O (1:1 v/v). In the flash photolysis studies, the same solvents were used. In the case of the DKP-based BP-Met dyads, the UV spectra were recorded in ACN, MeOH, and DCM. The concentration of the compounds used for the study of the $\pi\rightarrow\pi^*$ and the $n\rightarrow\pi^*$ transitions of the benzophenone chromophore were 6×10^{-5} M and 1×10^{-3} M, respectively. Absorption spectra of the $\pi\rightarrow\pi^*$ and $n\rightarrow\pi^*$ bands of **(S,S)-BP-Met** in different solvents are presented in Figure 3.1-3. Due to the similarity of the UV spectra of **(S,S)-BP-Met** and **(R,S)-BP-Met**, the spectrum of latter is not shown.

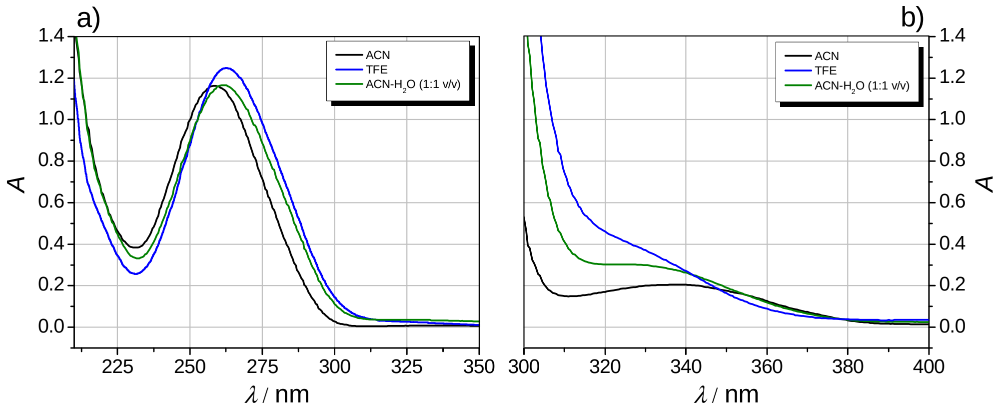

Figure 3.1-3 Absorption spectra of **(S,S)-BP-Met** in different solvents: a) $\pi\rightarrow\pi^*$ band, concentrations: ACN – 5.9 × 10^{-5} M, ACN-H_2O (1:1 v/v) – 6.0 × 10^{-5} M, TFE – 6.4 × 10^{-5} M, b) $n\rightarrow\pi^*$ band, concentrations: ACN – 1 × 10^{-3} M, ACN-H_2O (1:1 v/v) – 1 × 10^{-3} M, TFE – 1 × 10^{-3} M.

The wavelengths at the maximum absorptions (λ_{max}) for each band obtained for the three solvents and the values of the molar absorption coefficients at these wavelengths (ε_{max}) for **(S,S)-BP-Met** and **(R,S)-BP-Met** measured in ACN are summarized in Table 3.1-2. As in the case of the BP-Tyr dyads, no difference was observed in the absorption properties of **(S,S)-BP-Met** and **(R,S)-BP-Met**.

Table 3.1-2 Absorption properties of **(S,S)-BP-Met** and **(R,S)-BP-Met** in different solvents.

Dyad	**λ_{max} (ACN) / [nm]**		**ε_{max} (ACN) / [M^{-1} cm^{-1}]**		**λ_{max} (ACN/H_2O) / [nm]**		**λ_{max} (TFE) / [nm]**	
	$\pi\rightarrow\pi^*$	$n\rightarrow\pi^*$	$\pi\rightarrow\pi^*$	$n\rightarrow\pi^*$	$\pi\rightarrow\pi^*$	$n\rightarrow\pi^{*a}$	$\pi\rightarrow\pi^*$	$n\rightarrow\pi^{*a}$
(S,S)-BP-Met	258.5	338	19200	215	262	-	262.5	-
(R,S)-BP-Met	259.5	338	19100	201	261.5	-	262.5	-

[a] not determined due to the lack of a well-defined maximum of absorption.

The UV spectra obtained for **(S,R)-BP-DKP-Met** are presented in Figure 3.1-4. UV spectra for the second diastereoisomer, **(S,S)-BP-DKP-Met**, were measured only for the $\pi\rightarrow\pi^*$ band and at a concentration of 4×10^{-5} M. This limitation of the concentration range was the result of the low solubility of the compound **(S,S)-BP-DKP-Met** in the solvents used.

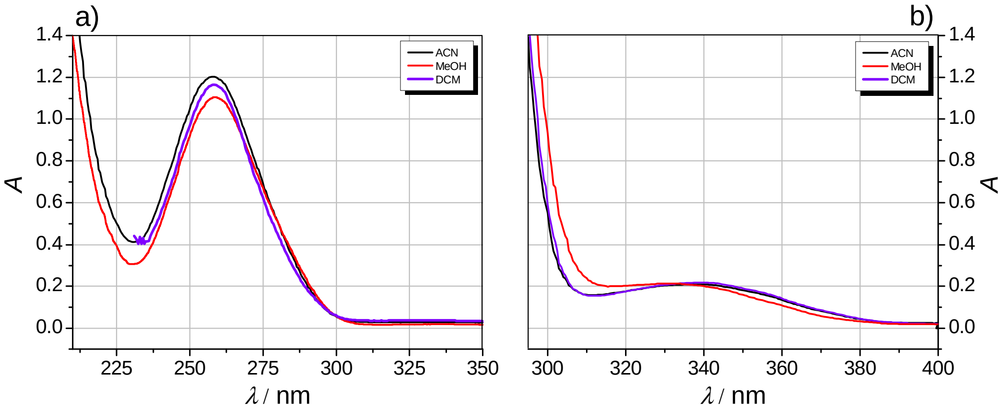

Figure 3.1-4 Absorption spectra of **BP-DKP-Met-(S,R)** in different solvents: a) $\pi\rightarrow\pi^*$ band concentrations: ACN – 6.2×10^{-5} M, MeOH - 6.0×10^{-5} M, DCM – 6.2×10^{-5} M, b) $n\rightarrow\pi^*$ band, concentrations: ACN – 1.0×10^{-3} M, MeOH – 9.7×10^{-4} M, DCM – 1×10^{-3} M.

The observed similarity in the absorption properties of the **(S,S)-BP-Met** / **(R,S)-BP-Met** pair of diastereoisomers holds also for the DKP-based BP-Met dyads (Table 3.1-3). Only the molar absorption coefficient at the maximum wavelength of the $\pi\rightarrow\pi^*$ band for **(S,S)-BP-DKP-Met** is slightly smaller than the analogous value for **(S,R)-BP-DKP-Met**.

Table 3.1-3 Spectroscopic properties of **(S,S)-BP-DKP-Met** and **(S,R)-BP-DKP-Met** in different solvents.

Dyad	**λ_{max} (ACN)** / [nm]		**ε_{max} (ACN)** / [M^{-1} cm^{-1}]		**λ_{max} (MeOH)** / [nm]		**λ_{max} (DCM)** / [nm]	
	$\pi\rightarrow\pi^*$	$n\rightarrow\pi^*$	$\pi\rightarrow\pi^*$	$n\rightarrow\pi^*$	$\pi\rightarrow\pi^*$	$n\rightarrow\pi^*$	$\pi\rightarrow\pi^*$	$n\rightarrow\pi^*$
(S,S)-BP-DKP-Met	258	–[a]	16500	–[a]	258.5	–[a]	258.5	–[a]
(S,R)-BP-DKP-Met	257.5	338	19200	205	258.5	331.5	258.5	339.5

[a] not determined due to low solubility.

3.1.1.3 **Trichromophores**

The UV spectra of the triads: **CB-Met-Tyr** and **CB-Leu-Tyr** were measured in two solvents: ACN and TFE, and in one solvent mixture: ACN-H_2O (1:1 v/v). The respective spectra obtained for **CB-Met-Tyr** are plotted in Figure 3.1-5.

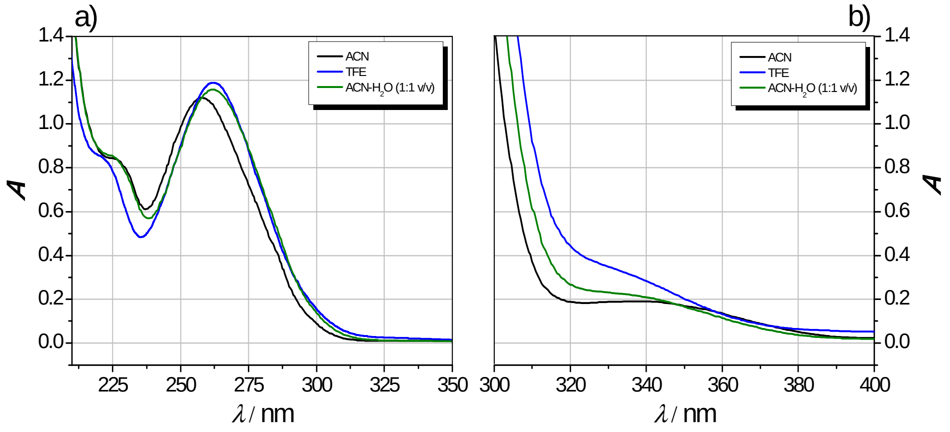

Figure 3.1-5 Absorption spectra of **CB-Met-Tyr** in different solvents: a) $\pi\rightarrow\pi^*$ band, concentrations: ACN – 6.0 × 10^{-5} M, ACN-H_2O (1:1 v/v) – 6.2 × 10^{-5} M, TFE – 6.1 × 10^{-5} M, b) $n\rightarrow\pi^*$ band, concentrations: ACN – 1.1 × 10^{-3} M, ACN-H_2O (1:1 v/v) – 9.9 × 10^{-4} M, TFE – 1 × 10^{-3} M.

Based on the data collected in Table 3.1-4, it can be concluded that both triads have the same absorption properties.

Table 3.1-4 Spectroscopic properties of **CB-Met-Tyr** and **CB-Leu-Tyr** in different solvents.

Triad	**λ_{max} (ACN)** / [nm]		**ε_{max} (ACN)** / [M^{-1} cm^{-1}]		**λ_{max} (ACN/H_2O)** / [nm]		**λ_{max} (TFE)** / [nm]	
	$\pi\rightarrow\pi^*$	$n\rightarrow\pi^*$	$\pi\rightarrow\pi^*$	$n\rightarrow\pi^*$	$\pi\rightarrow\pi^*$	$n\rightarrow\pi^{*a}$	$\pi\rightarrow\pi^*$	$n\rightarrow\pi^{*a}$
CB-Met-Tyr	257.5	338	18900	190	262	-	262.5	-
CB-Leu-Tyr	257.5	338	21500	201	262	-	262.5	-

[a] not determined due to the lack of a well-defined maximum of absorption.

3.1.1.4 Benzophenone–diketopiperazine

The UV spectra of the reference **BP-DKP** compound were measured in three solvents: ACN, MeOH, and TFE for two ranges of concentrations: 6×10^{-5} M and 1×10^{-3} M depending on the transition of interest (Figure 3.1-6).

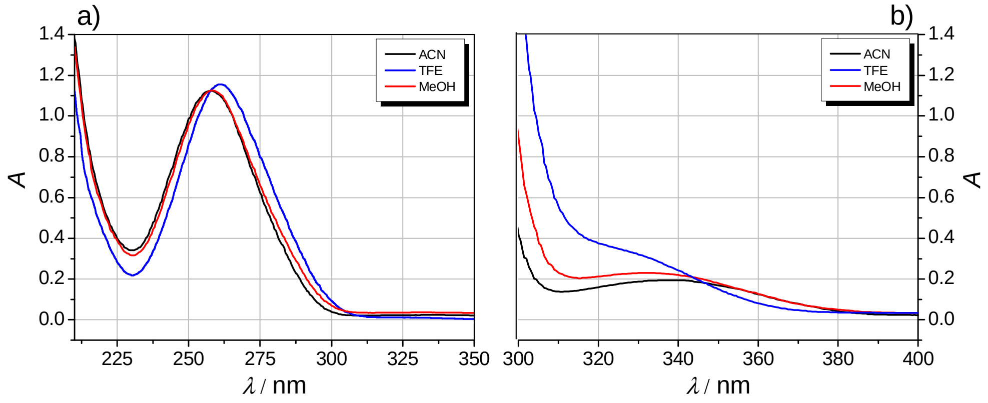

Figure 3.1-6 Absorption spectra of **BP-DKP** in different solvents: a) $\pi\rightarrow\pi^*$ band, concentrations: ACN – 5.9×10^{-5} M, MeOH – 5.9×10^{-5} M, TFE – 5.9×10^{-5} M, b) $n\rightarrow\pi^*$ band, concentrations: ACN – 1×10^{-3} M, MeOH – 1×10^{-3} M, TFE – 1×10^{-3} M.

Analogous UV spectra were recorded for the unsubstituted benzophenone. Table 3.1-5 summarizes the absorption properties of **BP-DKP** and **BP**.

Table 3.1-5 Absorption properties of **BP-DKP** and **BP** in different solvents.

Compound	**λ_{max} (ACN) / [nm]**		**ε_{max} (ACN) / [M^{-1} cm^{-1}]**		**λ_{max} (MeOH) / [nm]**		**λ_{max} (TFE) / [nm]**	
	$\pi\rightarrow\pi^*$	$n\rightarrow\pi^*$	$\pi\rightarrow\pi^*$	$n\rightarrow\pi^*$	$\pi\rightarrow\pi^*$	$n\rightarrow\pi^*$	$\pi\rightarrow\pi^*$	$n\rightarrow\pi^{*a}$
BP-DKP	257.5	338	18700	198	258.5	331.5	261	-
BP	251.5	338.5	17700	159	253.5	331.5	258	-

[a] not determined due to the lack of a well-defined maximum of absorption.

3.1.2 Phosphorescence spectra

The phosphorescence emission spectra of the compounds were recorded in DCM-MeOH (1:1 v/v) glass at 77 K with BP and CB as spectral references for dyads and triads, respectively. All the compounds exhibited the typical emission-band structure of benzophenone. Normalized phosphorescence emission spectra for BP-Tyr and BP-Met dyads were almost indistinguishable from the unsubstituted benzophenone (Figure 3.1-7).

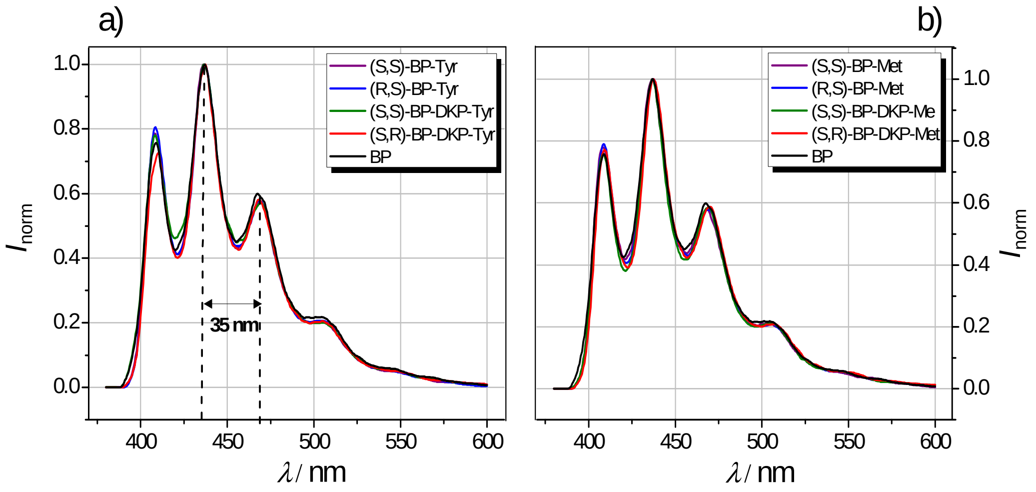

Figure 3.1-7 Phosphorescence spectra of a) BP-Tyr b) BP-Met dyads measured in DCM-MeOH (1:1 v/v) at 77 K with 2.5×10^{-5} M, λ_{exc} = 270 nm.

The phosphorescence spectra have well-defined vibrational progressions with a period of ca. 1700 cm^{-1} (ca. 35 nm) (Figure 3.1-7a) which indicates the participation of the >C=O vibration in the radiative process.

Since these triads are the derivatives of the carboxybenzophenone moiety, CB was used as the spectral reference for **CB-Met-Tyr** and **CB-Leu-Tyr**. The phosphorescence spectra of the triads coincide with the respective phosphorescence spectra of CB (Figure 3.1-8). It can be noted that the phosphorescence spectra of the triads are red shifted by ca. 8 nm in comparison to BP (see black plot in Figure 3.1-8 and Table 3.1-6). This emission characteristic is in accord with literature data for BP-derivatives.[65, 137]

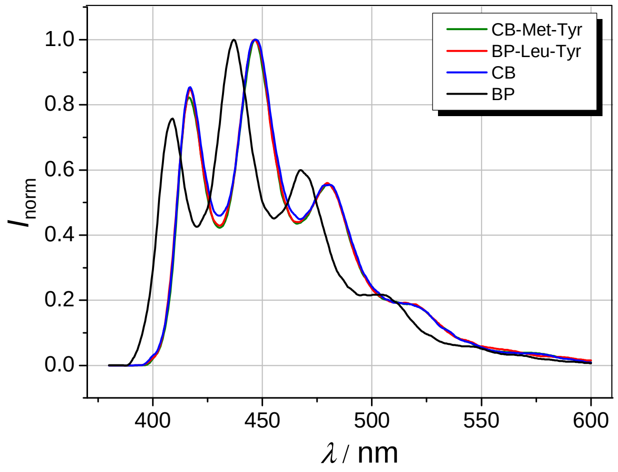

Figure 3.1-8 Phosphorescence spectra of triads and CB, BP measured in DCM-MeOH (1:1 v/v) at 77 K with 2.5 × 10^{-5} M, λ_{exc} = 270 nm.

Triplet energies, E_T, were estimated for all the tested compounds from the wavelength corresponding to the 0-0 emission band (Table 3.1-6). Triplet energies fall into a narrow range between 68.4 and 69.9 kcal/mol, to be compared with an E_T of 69.8 kcal/mol found for benzophenone.

Table 3.1-6 Summary of low-temperature phosphorescence data of the investigated compounds.

Compound	**λ ($T_1 \rightarrow S_o$) / [nm]**	**E_T / [kcal/mol]**
(S,S)-BP-Tyr	408	69.9
(R,S)-BP-Tyr	408.5	69.9
(S,S)-BP-DKP-Tyr	408.5	69.9
(S,R)-BP-DKP-Tyr	410	69.6
(S,S)-BP-Met	408	69.9
(R,S)-BP-Met	408.5	69.9
(S,S)-BP-DKP-Met	408	69.9
(S,R)-BP-DKP-Met	409	69.8
BP-DKP	409	69.8
CB-Met-Tyr	416.5	68.5
CB-Leu-Tyr	417	68.4
CB	417	68.4
BP	409	69.8

3.1.3 **Discussion**

The ultraviolet absorption spectra of the investigated compounds were dominated by the intense resonances of the aromatic chromophores. The UV spectra of all the compounds are typical for benzophenone with a maximum absorption at ca. 258 nm assigned to a $\pi \rightarrow \pi^*$ transition, and a characteristic $S_0 \rightarrow S_1$ transition of $n \rightarrow \pi^*$ character at ca. 340 nm which is only weakly allowed with extinction coefficients in the range of 10^2 M^{-1} cm^{-1}. It is noted that the $\pi \rightarrow \pi^*$ band of the investigated compounds is red shifted by ca. 7-8 nm in comparison to unsubstituted benzophenone. The wavelength of the maximum absorption of the $n \rightarrow \pi^*$ band and the molar absorption coefficients of the investigated compounds are well in accord with the data obtained for BP.

The tyrosine chromophore also absorbs light in the UV region. Specifically, in addition to the absorption spectral features described above, compounds which contain the tyrosine moiety (BP-Tyr dyads and triads) exhibit a band with a maximum at 225 nm and a small shoulder at 280 nm (Figure 3.1-1, Figure 3.1-2, Figure 3.1-5). That absorption is assigned to the Tyr moiety (blue line in Figure 3.1-9).[138, 139] The spectra of the BP-Tyr dyads and triads display absorption bands due to both chromophores, but overall the absorption spectra were a sum of the two independent chromophores present in the molecules, indicating no ground state interaction between the moieties. It is noted that the absorption spectra of the compounds containing the tyrosine residue are dominated by the absorption of the benzophenone chromophore due to its much higher molar absorption coefficients, compared to the tyrosine moiety (Figure 3.1-9).

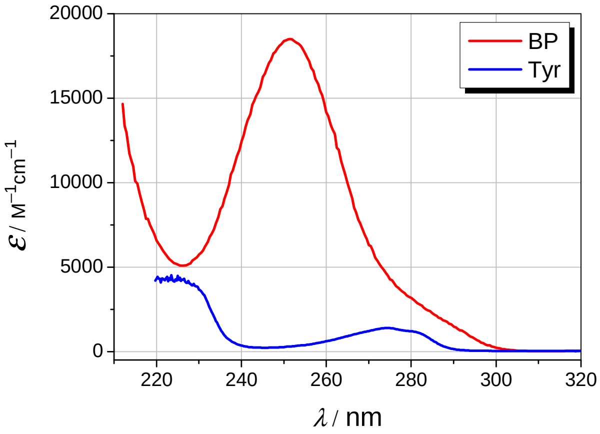

Figure 3.1-9 Absorption spectra of the **BP** in ACN (6.2×10^{-5} M) (this study) and tyrosine taken from reference.[139]

Both the $\pi \rightarrow \pi^*$ transition at 258 nm and the weaker $n \rightarrow \pi^*$ transition at 340 nm exhibited no significant differences between the compounds in different solvents, e.g., ACN, MeOH, or TFE. The most important contribution to the observed solvatochromic effect is due to effects of electrostatic and hydrogen bonding interactions on the solute molecule. During the process of excitation, one n-electron is promoted from a nonbonding orbital on the oxygen atom to an antibonding π^* orbital which is delocalized onto the aromatic group. Removal of an electron from the oxygen atom implies a decrease of the dipole moment in the excited state. As a result, the n,π^* state is not stabilized by solvents with high polarity as much as the ground state is stabilized. In addition, protic solvents are capable of hydrogen-bond formation with oxygen lone pairs, which lowers the energy of the ground state further, relative to the n,π^* state. Thus the observed the hypsochromic shift of the $n \rightarrow \pi^*$ transition can be interpreted as the result of cooperating effects originating from both electrostatatic and specific solute-solvent interactions. These specific solute-solvent effects are the result of the formation of hydrogen bonding between the solute molecule and the protic solvent (TFE, MeOH, ACN-H_2O (1:1 v/v)). On the other hand, the $\pi \rightarrow \pi^*$ transition showed a bathochromic shift on changing the solvent from one of lower to another of higher polarity and H-bond donor abilities. This phenomena of the solvatochromic effect of $\pi \rightarrow \pi^*$ transition is fully in accord with the literature data. It is attributed to the hydrogen-bond formation between the solute and solvent molecules. The red-shift in the $\pi \rightarrow \pi^*$ transition is due to (relatively weaker) electrostatic effects and (relatively stronger) effects of hydrogen-bonding to the solvent.[140-142] Both unspecific and specific solvation decrease the energy of the π,π^* state more than that of the ground state. Both of these observed solvent effects (bathochromic and hypsochromic shifts) are useful tools in characterizing the nature of electronic transitions.

The phosphorescence emission spectra of the compounds exhibit the characteristic emission-band structure of benzophenone. The shape of the phosphorescence emission spectra and calculated triplet energies are in accord with literature data for BP-derivatives.[137] Based on the collected data, it can be concluded that the electronic structure of the benzophenone unit is not affected by substitution with tyrosine/methionine moieties; i.e., the lowest-lying triplet states possess n,π^* character.

3.2 **Benzophenone–tyrosine bichromophore systems**

In this and the following sections, results are presented of laser-flash photolysis and theoretical investigations of specific systems which contain two chromophoric constituents separated from each other by different linkages.

The first systems to be presented and discussed are benzophenone-tyrosine dyads with BP and Tyr as the chromophoric centers. The investigation addresses quantitatively the effects which influence intramolecular H-atom transfer reactions in these dyads. Special attention was paid to issues such as: the effect of molecular geometry on the quenching rate constants and the effect of chiral center configurations on the diastereo-selectivity of the quenching process. Additionally, a comprehensive study of the solvent dependence on intramolecular hydrogen-atom transfer will be presented. These experimental studies are supplemented by the results from molecular-dynamics simulations and theoretical calculations involving studies on the ground-state structures and conformations which establish a quantitative picture of the conformer distributions of the dyads and define the molecular prerequisites of the individual quenching geometries.

In the first part of the study, the two chromophores were connected *via* open-chain peptide structures (see Scheme 3.2-1). However, since the high intrinsic flexibility of these linkers blurs any stereoselectivity, limitation of the flexibility of the peptide linker should allow deeper insights into any relationships between the kinetic phenomenology and the molecular structure. Therefore, in the second part of this work, more rigid linkers were used. The diketopiperazine (DKP) ring system provides such a peptide environment with reduced flexibility. First the DKP ring imposes distinct orientations between the reacting chromophores for epimeric dyads (see low part of the Scheme 3.2-1; from left to right, the structures denote the (S,S) and (S,R) epimers).

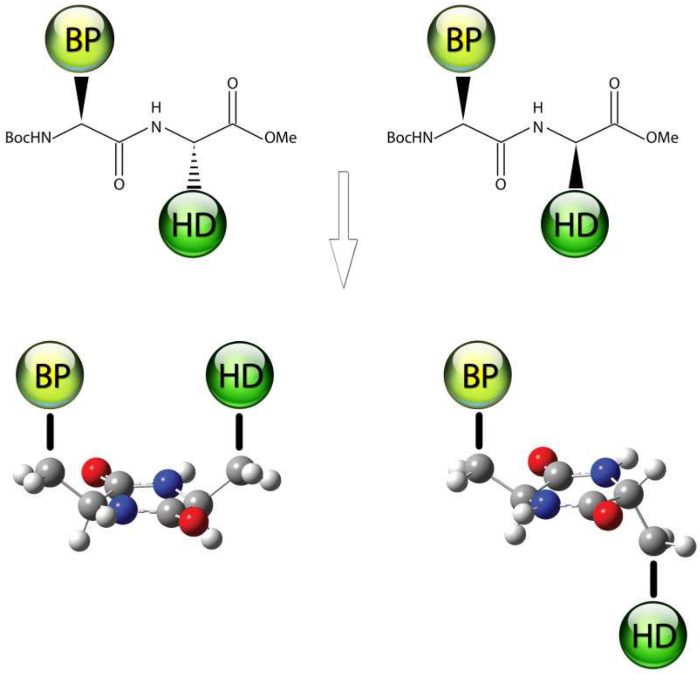

Scheme 3.2-1 Schematic view of the structural constraints on the intramolecular HAT between an H-donor (HD) and an acceptor (BP) within linear and cyclic dipeptides.

In addition, the presence of the DKP ring exerts unique control over the conformations of the respective side chains of the attached amino acids. For short, these DKP-linked dyads will, in the following, in general be ascribed to “cyclic” dyads.

3.2.1 Open chain diastereoisomers

3.2.1.1 Nanosecond flash photolysis: spectral and kinetic analysis

The excited-state dynamics of the **(S,S)-BP-Tyr** and **(R,S)-BP-Tyr** dyads were studied by means of nanosecond-laser photolysis in 15 different solvents and solvent mixtures.[75] Transient products were identified, and the efficiency of their formation was quantified by means of transient-absorption spectroscopy and spectral resolutions. The solvents were selected in order to establish a wide range in H-bonding properties and viscosities. In part of the work, performed by Hörner, it had been shown that the viscosity, η, of the solvent is an important factor.[75] In the work described in the following, 6 different protic and non-protic solvents were examined (ACN, DCM, $CHCl_3$, DCA, MeOH, TFE).

For the bichromophores **(S,S)-BP-Tyr** and **(R,S)-BP-Tyr**, in any solvent, the transient decays of the initial signals were very rapid, i.e., shorter than the triplet decay of the monochromophoric reference compound (see Chapter 3.5.2.1) by a factor of greater than 100. Triplet lifetimes were obtained from mono- or biexponential fits to the transient decays at 630 and 520 nm, respectively. Triplet lifetimes were found to be between 10 ns and 80 ns for **(S,S)-BP-Tyr** and from less than 10 ns and up to 40 ns for **(R,S)-BP-Tyr**, depending on the nature of the solvent. In all cases the triplet state was identified as the dominate intermediate in the early transient spectra through its characteristic absorption maxima at 325 nm (not shown) and 525 nm, in addition to a long-wavelength absorption above 600 nm. The spectra obtained at short times after the laser pulse matched those previously reported for the BP triplet state.[37] The triplet decays of the dyads were generally followed by spectral shifts from 325 to 335 nm (not shown), and from 525 to 540 nm, as well as by growths at 405 nm (Figure 3.2-1a, Figure 3.2-2a). This spectral evolution is in accord with the interpretation that the fast triplet quenching leads to ketyl radical BPH$^\bullet$ formation. Concomitant formation of a transient, identified as the tyrosyl radical Tyr(O$^\bullet$) based on its characteristic absorption peak at 405 nm, clearly suggests an H-atom transfer between a tyrosine moiety and the excited triplet for both diastereomers. The short intrinsic triplet lifetimes of the dyads prevented a direct study of the self-quenching for these compounds but gave evidence for the intramolecular nature of the quenching process.

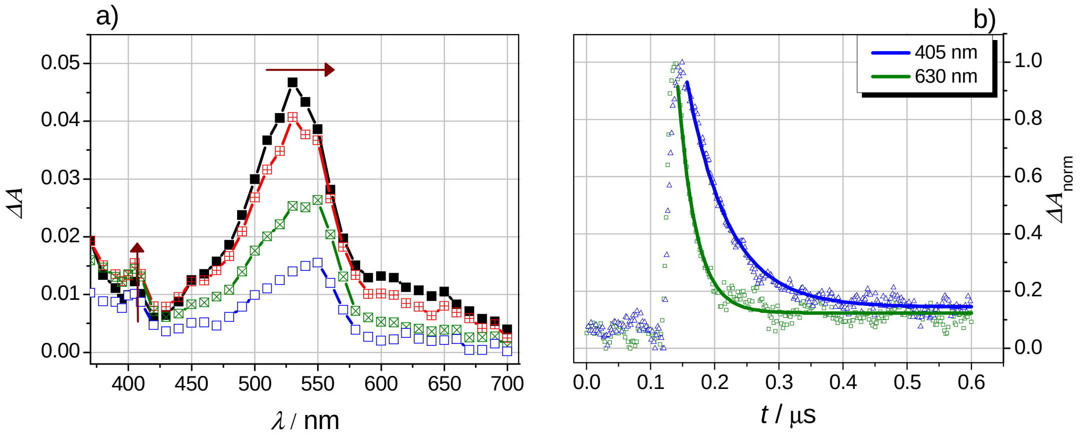

Figure 3.2-1 Summary of the results obtained during laser flash photolysis at 355 nm of a deoxygenated solution of **(R,S)-BP-Tyr** in dry ACN; a) transient absorption spectra: time delays after flash (from top to bottom): 27, 35, 55, 85 ns; b) normalized decay profiles of the transient absorption monitored at 630 nm (^{3}BP – green) and 405 nm (Tyr(O$^\bullet$) – blue).

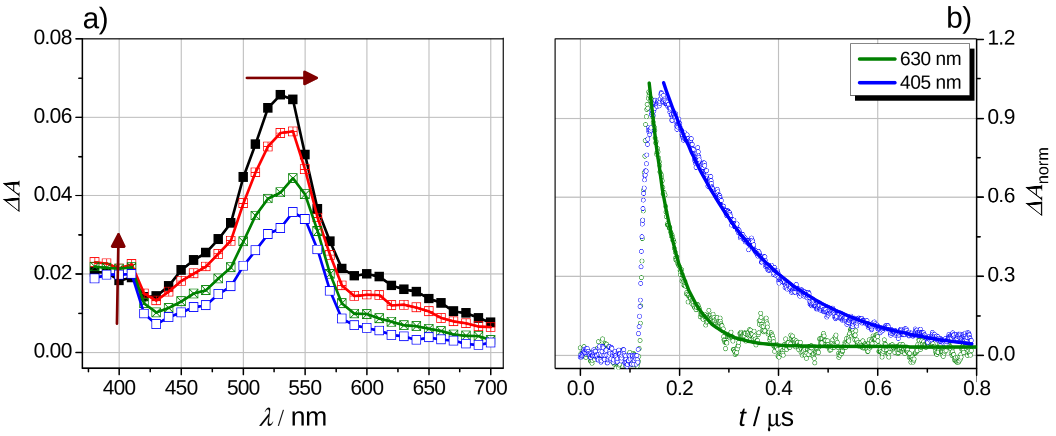

Figure 3.2-2 Summary of the results obtained during laser flash photolysis at 355 nm of a deoxygenated solution of **(S,S)-BP-Tyr** in dry ACN; a) transient absorption spectra: time delays after flash (from top to bottom): 23, 40, 65, 95 ns; b) normalized decay profiles of the transient absorption monitored at 630 nm (^{3}BP – green) and 405 nm (Tyr(O$^\bullet$) – blue).

Spectral-resolution techniques were applied, in order to unravel the nature of the intermediates and the stoichiometry of the excited-state processes for **(S,S)-BP-Tyr** and **(R,S)-BP-Tyr** in ACN. In addition, comparisons were made between the triplet-decay rate constants, obtained from monoexponential fits to the experimental decay profiles at 630 nm, and the rate constants obtained from mono-exponential fits to triplet concentration-time profiles resulting from the spectral resolutions. Agreement between these rate constants for particular experiments provides additional evidence for the accuracy of the measured triplet-decay rate constants from these two independent methods. Over the complete time scale of the transient decay only the spectral components for ^{3}BP, BPH$^\bullet$, and Tyr(O$^\bullet$) were needed to simulate the experimental data quantitatively (Figure 3.2-3a, Figure 3.2-4a). Concentration-time profiles were constructed from spectral resolutions for reaction of the dyads in ACN (Figure 3.2-3b, Figure 3.2-4b). It is noted, based on the kinetic decay profiles at 630 nm in ACN (green lines in Figure 3.2-1 and Figure 3.2-2) as well as from the concentration profiles for the triplet (green lines in Figure 3.2-3 and Figure 3.2-4) that triplet decay for **(R,S)-BP-Tyr** is faster than the triplet decay for **(S,S)-BP-Tyr**. This observation is valid for all the investigated solvents. The rate of triplet decay obtained from the fit to the concentration-time profile is, within experimental error, identical with the triplet-decay rate obtained from the kinetic decays at 630 nm. It validates that the concentration profiles were constructed accurately and, in addition, that no other intermediates, except the triplet state, were contributing to the kinetic decay profile at 630 nm.

The triplet decays were followed by the formation of equimolar amounts of BPH$^\bullet$ and Tyr(O$^\bullet$). The formation and decay of both radicals appeared to follow the same time-law, which is in accord with an intramolecular-reaction mechanism. The formation of the biradical (BPH$^\bullet$–Tyr(O$^\bullet$)) is analogous to intermediates which were reported for a number of related dyads.[37, 43, 47, 48, 52, 54, 55, 57] The biradicals, BR, decayed exponentially but on a longer timescale than the triplets. It is noted that the rate constants for triplet quenching (k_{obs}**(R,S)**/k_{obs}**(S,S)**) ≈ 1.9) (green lines in Figure 3.2-1 and Figure 3.2-2) and biradical decay (k_{BR}**(R,S)**/k_{BR}**(S,S)**) ≈ 3.0) (blue lines in Figure 3.2-1and Figure 3.2-2) exhibited some diastereo-selectivity. Decay of the biradical (monitored at 405 nm) of **(R,S)-BP-Tyr** was not only faster than the decay of the biradical of **(S,S)-BP-Tyr**, but it was also faster, relative to its corresponding triplet decay (monitored at 630 nm) (Figure 3.2-1b and Figure 3.2-2b), than was the biradical of **(S,S)-BP-Tyr**.

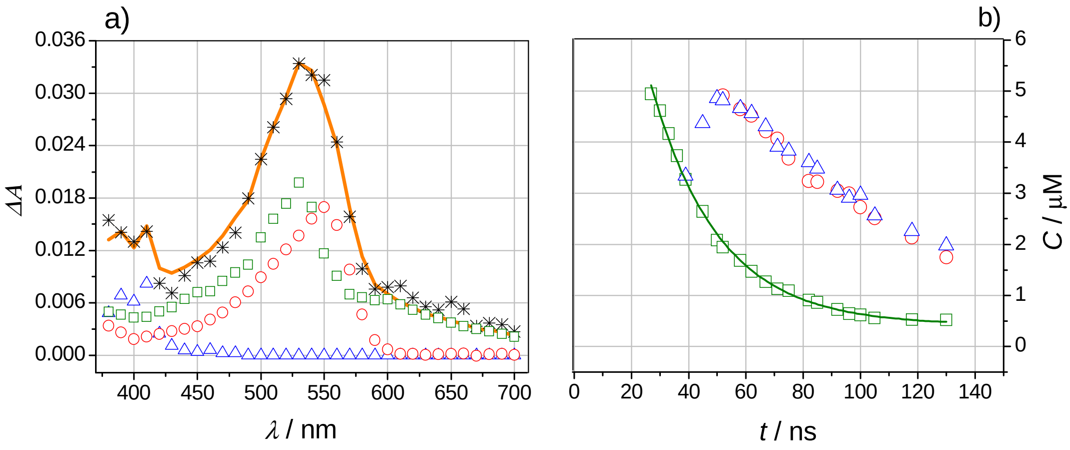

Figure 3.2-3 Resolutions of transient absorption spectra taken 41 ns after 355 nm laser pulsing (5 mJ) of a solution of **(R,S)-BP-Tyr** in dry ACN; b) concentration profiles for the transients obtained from the resolution of transient absorption spectra of **(R,S)-BP-Tyr** in ACN. The symbols represent □ for the triplet state ^{3}BP, ○ for the ketyl radical BPH$^\bullet$, ∆ for the tyrosyl radical Tyr(O$^\bullet$), and * for the experimental data; solid curves in a) and b) are the resulting fits from the regression analyses.

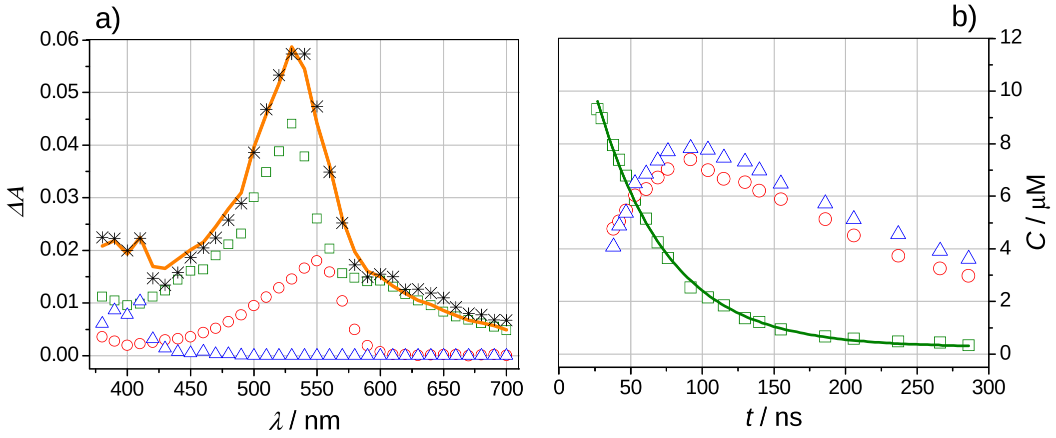

Figure 3.2-4 Resolutions of transient absorption spectra taken 42 ns after 355 nm laser pulsing (5 mJ) of a solution of **(S,S)-BP-Tyr** in dry ACN; b) concentration profiles for the transients obtained from the resolution of transient absorption spectra of **(S,S)-BP-Tyr** in ACN. The symbols represent □ for the triplet state ^{3}BP, ○ for the ketyl radical BPH$^{\bullet}$, △ for the tyrosyl radical Tyr(O$^{\bullet}$), and * for the experimental data; solid curves in a) and b) are the resulting fits from the regression analyses.

Quantum yields for BPH$^{\bullet}$ and Tyr(O$^{\bullet}$) formation were extracted from the concentration profiles in Figure 3.2-3b and Figure 3.2-4b by extrapolation back to the end of the excitation pulse. These quantum yields for **(S,S)-BP-Tyr** and **(R,S)-BP-Tyr** in ACN are practially 1.0 if account is taken for the experimental error which is estimated not to exceed ± 0.05. It can be seen that the formation of biradicals (BPH$^{\bullet}$–Tyr(O$^{\bullet}$)) from **(S,S)-BP-Tyr** and **(R,S)-BP-Tyr** are both very efficient.

The photochemistry of both dyads was also studied in other solvents, e.g in dichloromethane as an example of a nonpolar environment. The triplet lifetimes were close to the resolution limit of the Nd-YAG laser set-up (because of the laser pulse width ≈ 8 ns), and, thus, the experiments were performed at the Department of Photochemistry and Spectroscopy in the Institute of Physical Chemistry of the Polish Academy of Sciences in Warsaw. At this Institute an innovative laser photolysis system with a laser pulse width of 1 ns was employed to measure accurately the triplet lifetime of the dyads. Interestingly, in DCM, the rate constants of the triplet decays of the dyads were larger than in ACN. DCM is known to have a much weaker hydrogen-bond accepting ability than ACN. Therefore, in DCM, a diminished hindrance of the phenol group by H-bonding to the solvent and, concomitantly, an increase in the rate constant was suggested to account for this result.[15-17] The viscosities of the investigated solvents, DCM and ACN, are similar (0.537 cp *vs*. 0.369 cp), so that no significant effects on the HAT rates would be expected on the basic of viscosity alone.

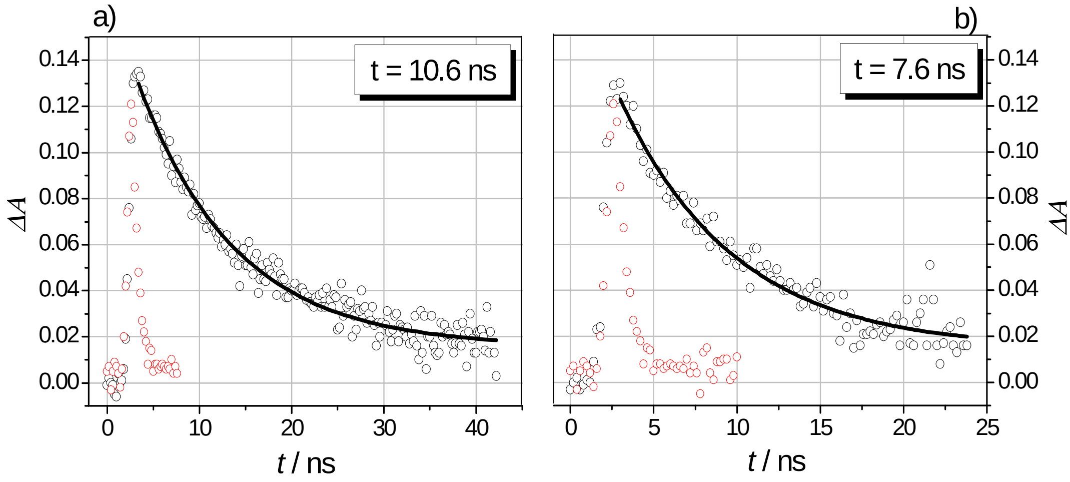

Figure 3.2-5 Decay profiles observed at 520 nm (black) and monoexponential fits to the decays for solutions of dyads a) **(S,S)-BP-Tyr** and b) **(R,S)-BP-Tyr** in DCM after 337 nm laser pulsing (red symbols laser pulse profile); numbers represent the values obtained from the fit. Note different timescales.

Solvents effects on H-atom transfer

In order to study the solvent effects on the intramolecular HAT pathway in a pair of diastereoisomers BP-Tyr, the corresponding rate constants, k_H, were isolated from the observed gross triplet-decay rate constants, k_{obs}. The procedure was outlined already in Chapter 2.5.5. The obtained kinetic data for the decay of **(S,S)-BP-Tyr** and **(R,S)-BP-Tyr** in six solvents are summarized in Table 3.2-1.

Table 3.2-1 Summary of solvent parameters and the kinetic data of the dyads **(S,S)-BP-Tyr** and **(R,S)-BP-Tyr**.

	solvent	**solvent parameters**			**rate constants**		**stereoselectivity**
		$\Sigma\alpha_2^{H}$ [b]	$\Sigma\beta_2^{H}$ [b]	η [a]	k_H **(S,S)**[c]	k_H **(R,S)**[c]	S[d]
1	chloroform	0.15	0.02	0.537	*7.8*	*9.8*	1.2
2	dichloromethane	0.1	0.05	0.437	*9.4*	*13.2*	1.4
3	acetonitrile	0.07	0.32	0.37	2.1	3.9	1.9
4	benzonitrile	0	0.33	1.2	1.6	3.1	2.0
5	trifluoroethanol	0.57	0.25	1.8[e]	2.3	5	2.1
6	methanol	0.43	0.47	0.544	0.7	2.6	3.5

[a] at 25°C; CRC Handbook of Chemistry and Physics. CRC Press. Boca Raton. 76th Ed. **1995**; [b] taken from ref. [72]; [c] results from 355 nm or 337 nm LFP, in 10^7 s^{-1}; experimental error ± 10 %, data in italics: experimental error ± 20 %; [d] $S = k_H(R,S)/k_H(S,S)$; [e] taken from: Sierra, P. S.; Tejuca, C. C.; Garcia-Blanca, F. *Helv. Chim. Acta* **2005**, *88*, 312–324.

The rate constants for the intramolecular HAT, k_H, as calculated for the dyad **(S,S)-BP-Tyr**, covered a range from 7×10^6 s^{-1} in MeOH to 9.4×10^7 s^{-1} in DCM (see Table 3.2-1). At the same time the rate constants for the intramolecular HAT for the dyad **(R,S)-BP-Tyr** varied from 2.6×10^7 s^{-1} in MeOH to 1.3×10^8 s^{-1} in DCM. The stereoselectivity, $S = k_H(\boldsymbol{R,S})/k_H(\boldsymbol{S,S})$, (measured in the same solvent) found in this work, varied from 1.2 to 3.5 (Table 3.2-1). Strikingly, stereoselection between the dyads seems to be insignificant in chlorohydrocarbon solutions ($S < 1.4 \pm 0.3$), whereas methanol gave rise to significant selectivity ($S = 3.5 \pm 0.3$). Data obtained by Hörner *et al.*[75] for that pair of diastereoisomers for another chlorohydrocarbon (1,2-dichloroethane) and three alcohols (1-pentanol, 2-propanol, ethanol) confirm the observation of the diminishing stereoselection in chlorohydrocarbons and the increase of the stereoselection in alcohols.

3.2.1.2 Steady-state irradiation

Mechanistic information could also be obtained from steady-state irradiations and product analyses. Steady-state consumption during irradiation of solutions of **(S,S)-BP-Tyr** and **(R,S)-BP-Tyr** at 313 nm in ACN, was quantified by HPLC with UV-detection. Quantum yields of substrate disappearance (Φ_{irr}), based on the uranyl oxalate actinometer, were less than < 0.005. Also no stable products were detected with HPLC. Although quantum yields for biradical formation were close to unity, the dyads **(S,S)-BP-Tyr** and **(R,S)-BP-Tyr** were very inert upon steady-state irradiation as inferred from the negligible quantum yields for dyad consumption in this inert solvent. It appears therefore that both triplet quenching and biradical decay are basically intramolecular reactions. Due to its complete reversibility in the dyads, intramolecular H-atom transfer presents an efficient path for energy dissipation in the triplet-excited BP moiety.

3.2.1.3 Theoretical calculations

In order to interpret the high reactivity of **(S,S)-BP-Tyr** and **(R,S)-BP-Tyr** with respect to intramolecular HAT, it is desirable to know the structural details of the respective quenching geometries. In addition, it is desirable to know the qualitative interrelation between the inter-side-chain reactivity and the structural preferences that are reflected by the non-bonding distances of the side chains. To provide insight into these aspects theoretical calculations were performed, and the relevant results will be presented in the following.

3.2.1.3.1 **DFT calculations**

The molecular conformations of **(S,S)-BP-Tyr** and **(R,S)-BP-Tyr** were addressed by DFT calculations in the gas-phase. The conformations of the peptide molecules can be characterized by two dihedral angles χ_1 and χ_2 describing the rotation of each of the side chains about the C^α–C^β and C^β–C^γ bonds, respectively, in the tyrosine residue.[143] The allowed conformations about the χ_1 angle are usually described by the three rotational isomers: **g+**, **g–** and **t**. Conformations **g–**, **t**, and **g+** correspond to χ_1 = –60º, 180º, +60º, respectively (Figure 3.2-6). Accordingly, DFT calculations were performed for each of the nine combinations of the side-chain χ_1 conformations of the Tyr and BP residues for both **(S,S)-BP-Tyr** and **(R,S)-BP-Tyr**. In the rotamer notation the first symbol always correspond to the tyrosine side.

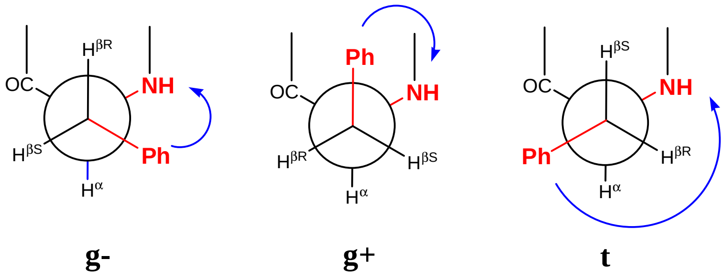

Figure 3.2-6 Newman projections of the Tyr side chain along the C^α – C^β bond; the three possible rotamers are assigned as the two gauche **(g–** with χ_1 = –60° and **g+** with χ_1 = +60°) and one anti-periplanar (**t** with χ_1 = 180°).

It is well established, that hydrogen-atom transfer reactions, initiated by triplet-excited ketones demand the close contact between the H-atom donor and the accepting carbonyl moiety.[144] The results clearly revealed that conformations with a favorable quenching geometry (close contact of the reactive moieties) were available for each dyad. The structures of the four lowest-energy conformations calculated for both dyads are depicted in Figure 3.2-7 and Figure 3.2-8. The dotted arrow-lines indicate the distance O–O between the two centers involved in the intramolecular HAT.

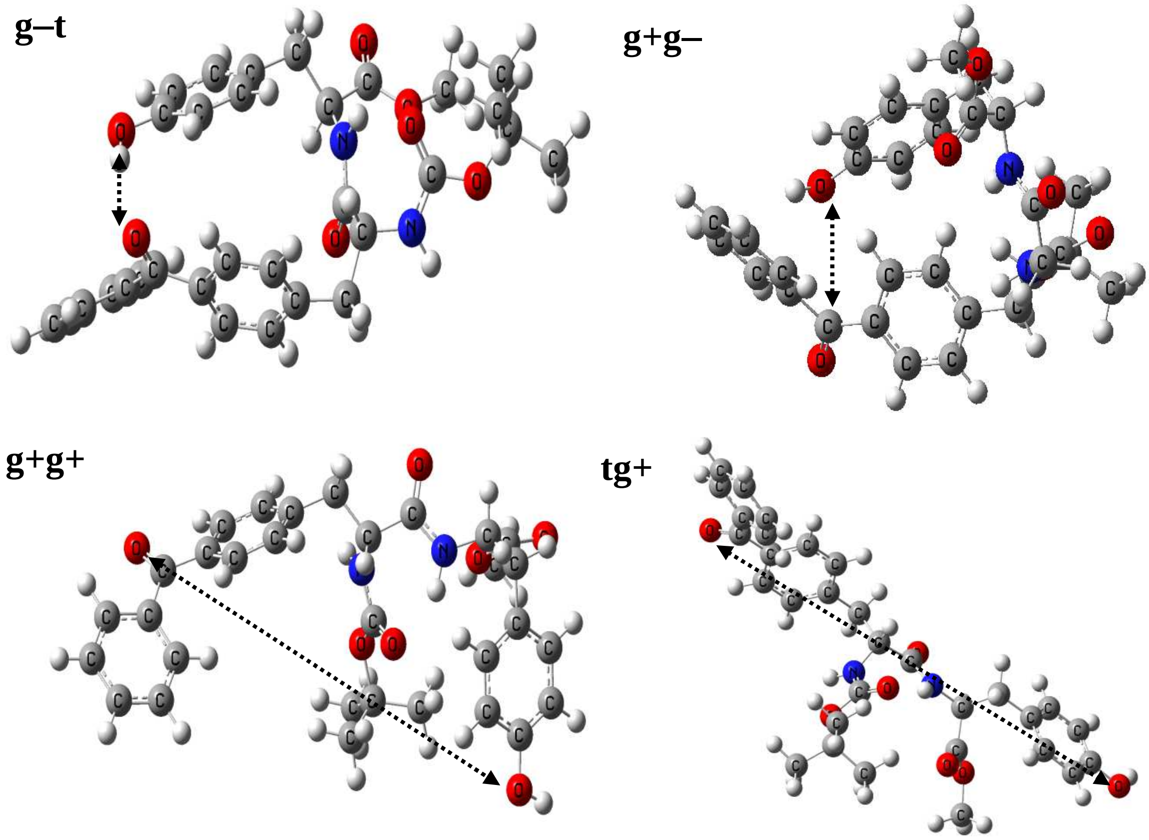

Figure 3.2-7 PBE1PBE/6-31G-optimized geometries in the gas phase of the four lowest energy structures for ground state of **(R,S)-BP-Tyr**. The dotted arrow lines denote the O–O distances between the benzophenone carbonyl and the phenol oxygen.

The energies of the four lowest-energy structures for **(R,S)-BP-Tyr** were found to be in close proximity (ΔE < 2.5 kcal/mol) (Table 3.2-2). With view to the intrinsic uncertainties of the DFT method, the energy differences were taken to be insignificant.[145] The energetic order of the rotamers in the gas phase for **(S,S)-BP-Tyr** showed that there were only two structures having similar low energy (Table 3.2-2). In Table 3.2-2 are summarized the relative energies and the O–O distances between the BP carbonyl and the Tyr for the rotamer minima of **(S,S)-BP-Tyr** and **(R,S)-BP-Tyr**, in the gas phase.

Table 3.2-2 Results of the four lowest-energy structures of gas-phase DFT calculations (PBE1PBE; 6-31G basis set) of the dyads **(R,S)-BP-Tyr** and **(S,S)-BP-Tyr**.

Parameter	**(R,S)-BP-Tyr**[a]				**(S,S)-BP-Tyr**[a]			
	g–t	**g+g–**	**g+g+**	**tg+**	**g+t**	**tt**	**g–t**	**g+g+**
Distance d(O–O)[b] / [Å]	2.8	4.4	13.1	17.6	2.7	10.7	5.7	7.0
Relative energy / [kcal/mol]	0.0	0.5	0.5	2.3	2	6	5.1	0.0

[a] in rotamer notation first symbol refers to Tyr side; [b] d(O–O) denotes the O–O distances between the benzophenone carbonyl and the phenol oxygen.

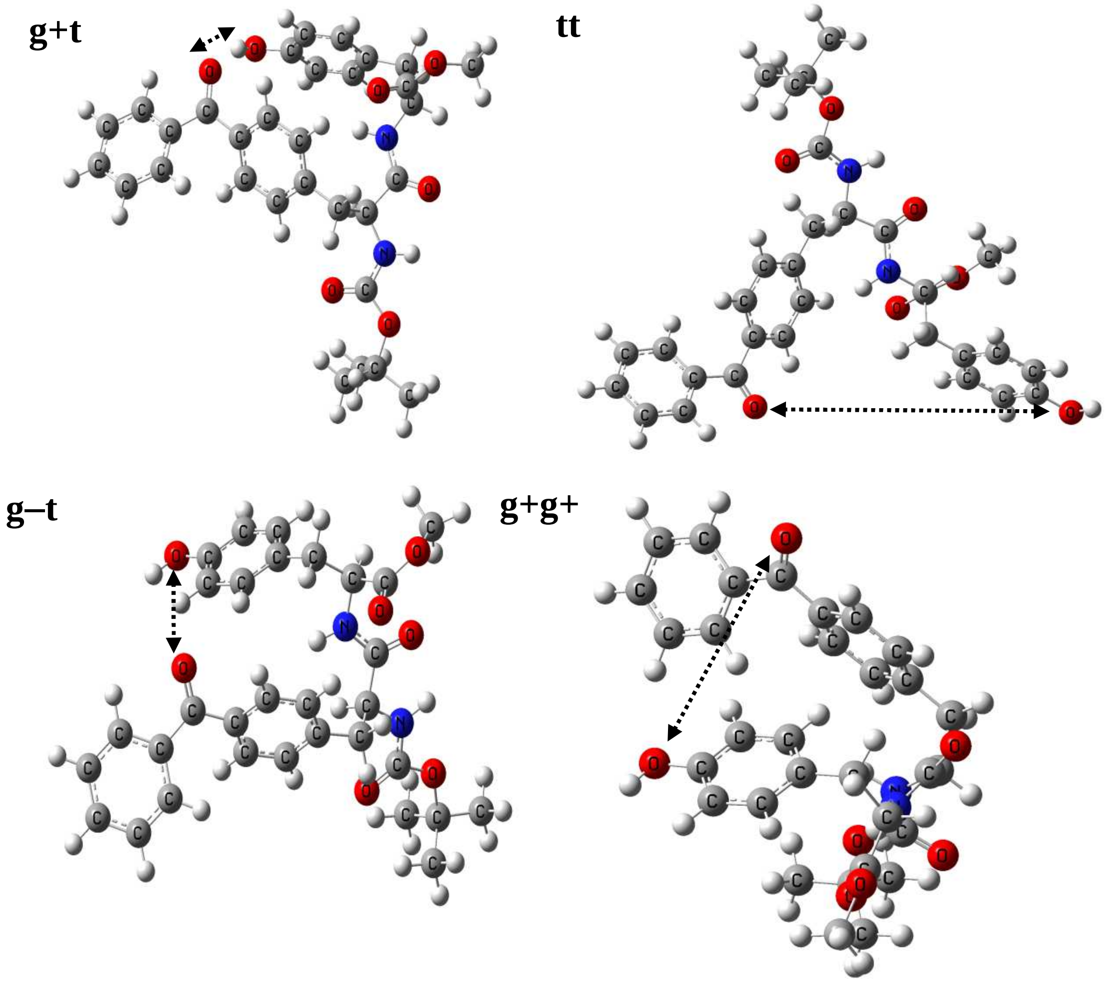

Figure 3.2-8 PBE1PBE/6-31G-optimized geometries in the gas phase of the four lowest energy structures for ground state of **(S,S)-BP-Tyr**. The dotted arrow lines denote the O–O distances between the benzophenone carbonyl and the phenol oxygen.

Importantly, the low-energy structures were accessible for various side-chain conformers. This is in full agreement with Molecular-Dynamics simulations (see below). Notably, among the four low-energy structures for each dyad there was indeed one conformer showing an oxygen-oxygen distance within the quenching limit of 3.1 Å.[144] The significantly large intramolecular reactivity of the dyads in any solvent thus seems to reflect a high flexibility of the linkage between the BP and the Tyr and indicates the possibility of the formation of conformations with close contact between the reactive moieties.

3.2.1.3.2 Molecular Dynamics

The above DFT calculations showed that a variety of structures, differing in their relative side-chain orientations, should be energetically accessible in solution. Therefore, it was of interest to obtain quantitative information about the populations of the side-chain rotamers in the dyads' ground states. Here, the results of the molecular-dynamics simulations for an implicit ACN solvent model will be presented. The interconversion between different molecular conformations was studied by means of long-time molecular-dynamics simulations (100 ns duration; implicit-solvent model for ACN). Figure 3.2-9 and Figure 3.2-10 summarize the time variation of three molecular parameters (side-chain dihedral angles; characteristic inter-side chain distance) within a 100-ns simulation for dyad **(R,S)-BP-Tyr** and **(S,S)-BP-Tyr**, respectively. Definition of the side-chain dihedral angles can be found in Chapter 3.2.1.3.1.

Figure 3.2-9a and Figure 3.2-10a show the changes of the distance *d*(O–O) between the Tyr hydroxylic oxygen atom and the BP carbonyl oxygen atom. It appears that dyad **(R,S)-BP-Tyr** adopted the conformations with the *d*(O–O) distance < 10.0 Å less frequently than did the dyad **(S,S)-BP-Tyr**. In agreement with the DFT results, mainly three rotamers (**g+**, **g–**, **t**) of each side chain were populated during the simulation of both compounds, although with different probability (see below). The distribution of the points in Figure 3.2-9b,c and Figure 3.2-10b,c basically reflects the percentage of the existence of the given conformations. For example, for the Tyr side chains in both dyads, the probability of the population of all three rotamers **g+** (~ 60°), **g–** (~ –60°), **t** (~ +/– 180°) were almost equal (Figure 3.2-9b and Figure 3.2-10b). This means that there was no one favorable conformation and that there were no constraints which limited the motions on the Tyr side chain. In contrast, MD simulations revealed that there were clear conformational preferences for the BP side-chain. For **(R,S)-BP-Tyr** the BP side-chain preferably populated the rotamer **g–** (~ –60°), whereas the rotamer **t** (~ +/– 180°) was strongly disfavored (Figure 3.2-9c). The conformational preferences for the BP side-chain of **(S,S)-BP-Tyr** showed that the highest populated conformation was the **g+** (~ 60°) rotamer, and again the **t** (~ +/– 180°) rotamer was disfavored (Figure 3.2-10c).

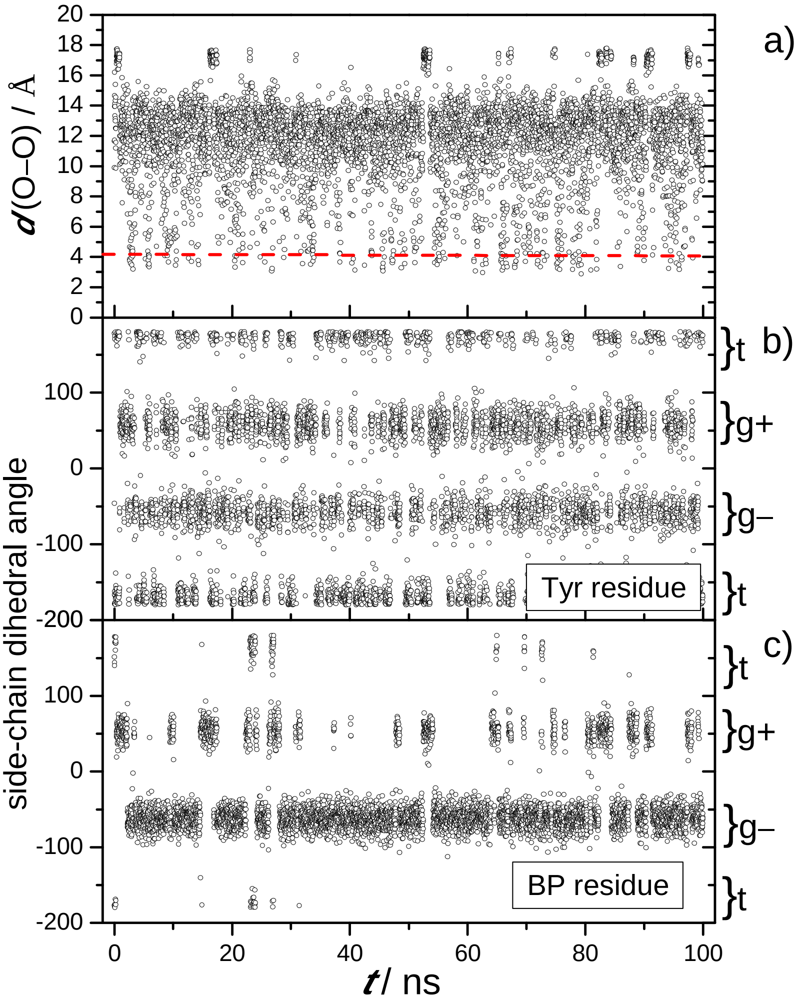

Figure 3.2-9 Long-term molecular-dynamics simulations for **(R,S)-BP-Tyr** (implicit-solvent model for ACN); a) time variation of the inter-side-chain distance *d*(O–O) between the Tyr hydroxylic oxygen atom and the BP carbonyl oxygen atom; b) time variation of the Tyr side-chain dihedral angle; c) time variation of the BP side-chain dihedral angle.

Of particular interest were the probabilities associated with conformations which would allow for close contacts < 4.0 Å (red dashed line on Figure 3.2-9a and Figure 3.2-10a) between the reacting moieties. Such close contacts should resemble the quenching geometry of these two dyads. The results clearly show that conformations which allow for close contacts are available in both dyads. However, the probabilities for the populations of these conformations were low for this pair of diastereoisomers.

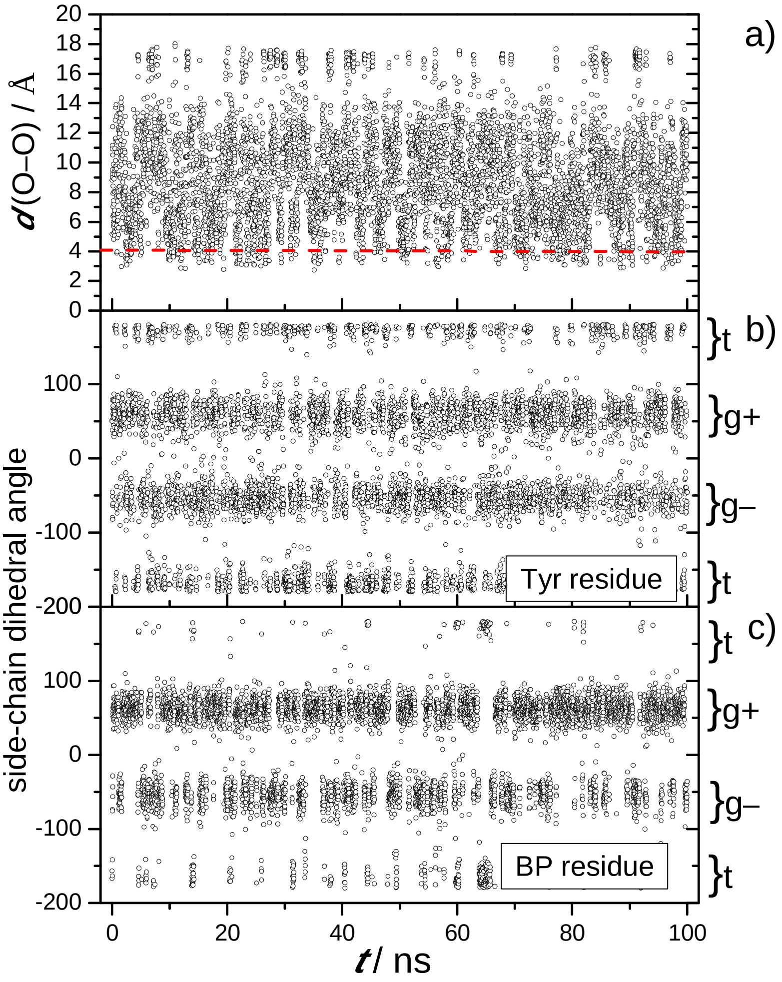

Figure 3.2-10 Long-time molecular-dynamics simulations for **(S,S)-BP-Tyr** (implicit-solvent model for ACN); a) time variation of the inter-side-chain distance *d*(O–O) between the Tyr hydroxylic oxygen atom and the BP carbonyl oxygen atom; b) time variation of the Tyr side-chain dihedral angle; c) time variation of the BP side-chain dihedral angle.

Pair-distribution functions of the carbonyl/hydroxylic group distance *d*(O–O) in Figure 3.2-11 were calculated based on the data from the MD simulations. These pair-distribution functions provide a statistical summary of the MD simulated time variation of the inter-side-chain distance *d*(O–O) presented above. They show that there is no one distinct preferable conformation and that close contact between the reacting moieties occur for both compounds. Additionally, in agreement with the DFT calculations (see Table 3.2-2), the pair-distribution functions show that **(S,S)-BP-Tyr** more frequently adopt conformations with distance *d*(O–O) between 6 Å to 10 Å, whereas **(R,S)-BP-Tyr** greatly enhances conformations with distance *d*(O–O) > 11 Å and displays, in fact, two distinct maxima (near 4.5 Å and 13 Å, respectively).

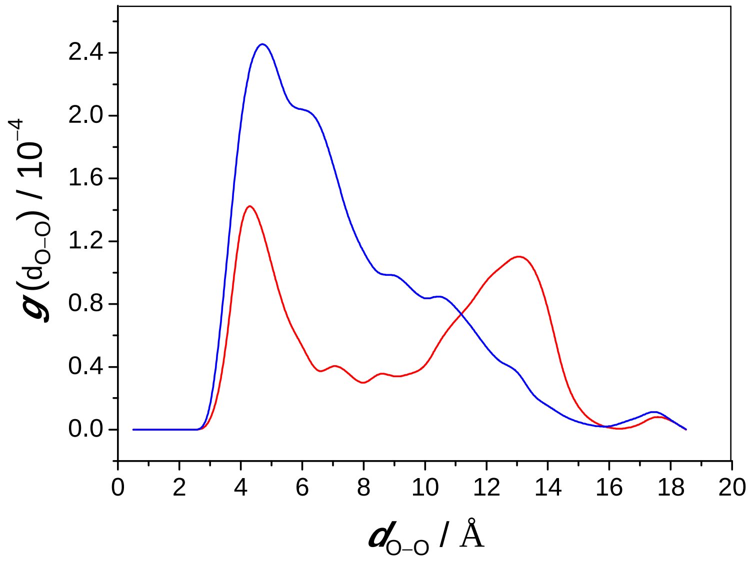

Figure 3.2-11 Pair-distribution functions of carbonyl/hydroxylic group distance *d*(O–O), obtained from molecular-dynamics simulation for **(S,S)-BP-Tyr** – (blue), **(R,S)-BP-Tyr** – (red).

3.2.1.4 **Discussion**

In this experimental study the excited-state dynamics of **(R,S)-BP-Tyr** and **(S,S)-BP-Tyr** were taken as probes of the solvent dependence on the efficiencies and rates of intramolecular hydrogen-atom transfer reactions. Both of the investigated compounds showed high reactivity toward intramolecular HAT. Depending on the molecular structure and the solvent, the intramolecular HAT rate constants k_H of the dyads ranged from ca. 7 × 10^6 s^{-1} to 1.3 × 10^8 s^{-1}. The high intramolecular reactivity of the dyads in any solvent can be readily attributed to the high flexibility of the linkage between BP and Tyr. Additionally, DFT calculations in the gas-phase and MD simulations for an implicit solvent provided evidence that the close contacts of the reactive moieties, that are needed for intramolecular HAT, can occur in both dyads.

In the following sections, it will be shown that the solvent dependence can be attributed to solute-solvent interactions of the tyrosine moiety.[75] Previous work on the solvent dependence of bimolecular HAT reactions of phenols has revealed that the rate constants are correlated with the H-bonding properties of the solvent.[13-17, 69-71] Linear-free energy relationships of the logarithmic rate constants depended solely on Abraham's H-bond acceptor ability, $\Sigma\beta_2^H$,[73] and corresponding plots were found to be linear.[70] As can be inferred from inspection of Table 3.2-1, the rate constants for intramolecular H-atom transfer, k_H, of the dyads were strongly dependent on the reaction medium. Generally, the highest rates were observed in non-polar solvents like DCM.

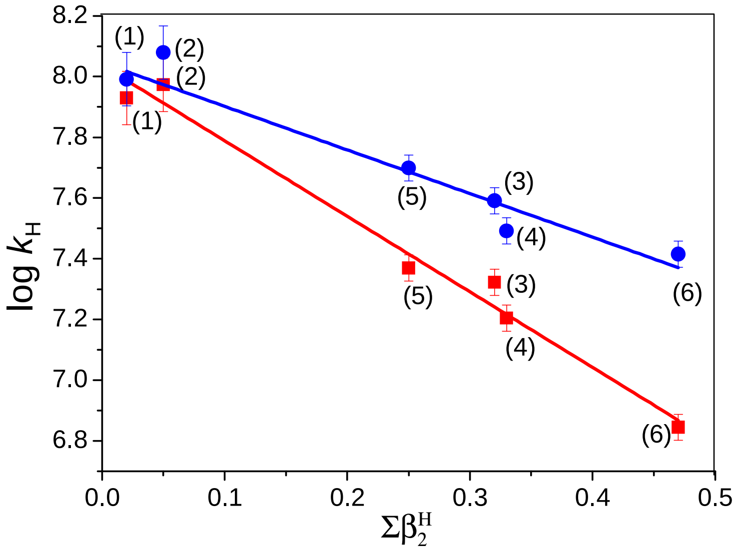

Figure 3.2-12 Plot of the H-atom transfer rate constants, log k_H against Abraham's *et al.* effective H-bond acceptor ability, $\Sigma\beta_2^H$, red symbols: data for **(S,S)-BP-Tyr**, blue symbols: data for **(R,S)-BP-Tyr**; solvent code as in Table 3.2-1.

A plot of the kinetic data for dyads **(R,S)-BP-Tyr** and **(S,S)-BP-Tyr** from Table 3.2-1 against the effective Abraham's H-bond acceptor ability, $\Sigma\beta_2^H$, of the solvents (Figure 3.2-12) are actually found to follow a linear dependence on $\Sigma\beta_2^H$ with a slope b = – 2.5 (r^2 = 0.979) and an intercept of 8.0, and a slope b = – 1.5 (r^2 = 0.935) and an intercept of 8.1 for **(S,S)-BP-Tyr** and **(R,S)-BP-Tyr**, respectively. The agreement between these two intercepts essentially predicts identical HAT rate constants k_H in the absence of solvent effects for both dyads. Interestingly, the dependence on the solvents' H-bond acceptor ability is significantly smaller for the **(R,S)-BP-Tyr** diastereomer. As an important result, the stereoselectivity of the HAT process was linearly dependent on the H-bond acceptor ability parameter, irrespective of the protic or non-protic character of the solvents.[75] The loss of reactivity in strongly H-bonding environments is in agreement with earlier observations on the bimolecular HAT from phenols.[17, 69, 70] The monotonic decrease of rate constants with the increasing $\Sigma\beta_2^H$ of the solvents is interpreted as being due to a reduction in the concentration of free phenol by hydrogen bonding to the solvent.[14-17, 70, 146] It is assumed that only the fraction of phenol that is not H-bonded to the solvent is active towards H-atom transfer. Detailed analysis of the kinetic data including derivation of the equation that predicts a linear relationship between reciprocal HAT rate constants and the equilibrium constant for the H-bonding of the phenol to the solvent can be found in Ref [75].

3.2.2 Rigidly linked “cyclic” diastereoisomers

3.2.2.1 Nanosecond flash photolysis: spectral and kinetic analysis

In the following, the results of laser-flash photolysis studies of **(S,S)-BP-DKP-Tyr** and **(S,R)-BP-DKP-Tyr** will be presented. They address, in particular, the medium dependence of the excited-state dynamics. As outlined in Chapter 3, in these dyads the BP and Tyr moieties are separated by a diketopiperazine heterocycle, i.e., a linker which is more rigid than the more flexible linker in the above “open chain” example. The excited-state dynamics of the dyads were studied in 12 different solvents and solvent mixtures.[147]

Excitation of the BP chromophore of the dyads yielded the excited triplet state with unit quantum yield within the duration of the laser flash. The transient spectrum of the triplet state was readily identified as the dominate intermediate in the early transient spectra by its characteristic absorption maxima at 325 nm and 525 nm, and a long-wavelength absorption tailing towards the NIR region. Very similar transient spectra were obtained for the reference compound that carries just the BP moiety linked to the diketopiperazine ring (see Chapter 3.5.2.1).

The triplet-state transient spectra of both DKP-dyads were indistinguishable from each other and showed only little variation with a change in the solvent. Exceptional behavior was noted only during LFP of the dyads in hexafluoro-2-propanol (HFIP) solutions, where an additional absorption band became evident at 400 nm.

A significant spectral evolution with a spectral shift from 525 to 540 nm and a growth at 405 nm would be indicative of the formation of ketyl and tyrosyl radicals, respectively. Interestingly, the triplet decay of the dyad **(S,S)-BP-DKP-Tyr** in ACN is not accompanied by a distinct spectral evolution although small changes are noticeable (Figure 3.2-13a). This finding is in contrast to the majority of studies on the triplet decay of BP in the presence of phenols (inter and intramolecularly[48, 51, 55, 65, 75]), where spectral evolutions were more obvious.

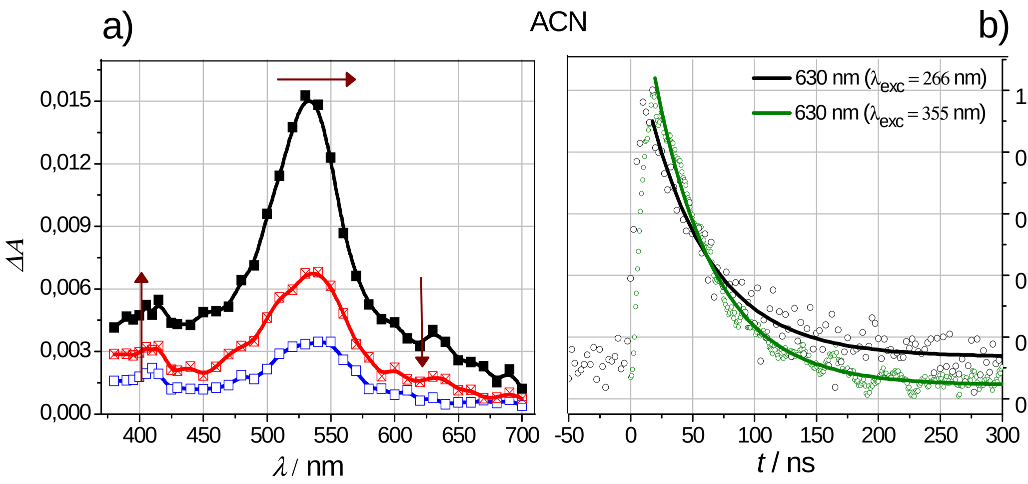

Figure 3.2-13 Summary of the results obtained during 355 nm laser flash photolysis of a deoxygentated solution of **(S,S)-BP-DKP-Tyr** in dry ACN; a) transient absorption spectra: time delays after flash (from top to bottom): 30, 100, 150 ns; b) normalized decay profiles of the transient absorption monitored at 630 nm (black) after 266 nm laser pulsing and (green) 355 nm laser pulsing; the solid lines represent monoexponential fits to the decay curves.

Resolution of the transient spectra obtained for that compound in ACN into spectral components and the construction of concentration-time profiles revealed that the triplet decay of **(S,S)-BP-DKP-Tyr** can actually be attributed to an efficient H-atom transfer reaction. To simulate the experimental data quantitatively, only three components were needed: the triplet state ^{3}BP, HAT based ketyl radicals (BPH$^•$) and tyrosyl radicals (Tyr(O$^•$)) (see Figure 3.2-14a).

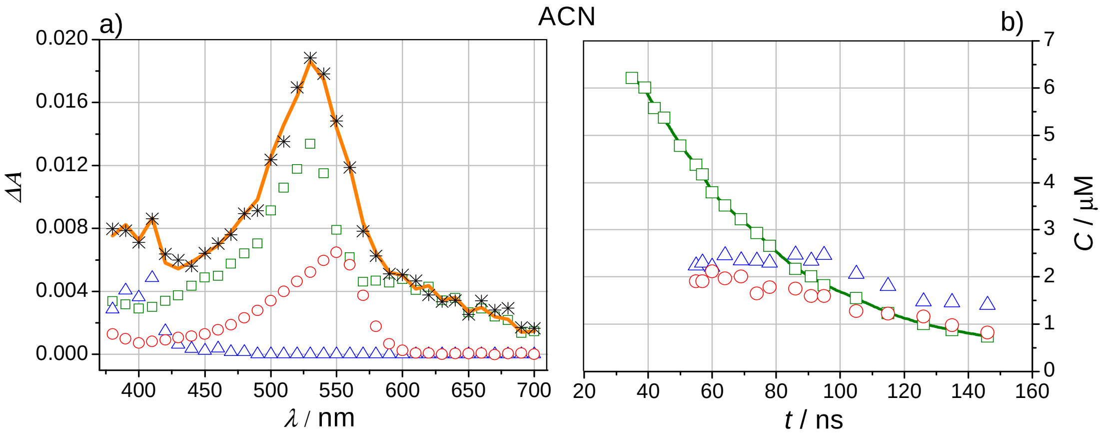

Figure 3.2-14 a) Resolutions of the transient absorption spectra taken 86 ns after 355 nm laser pulsing (5 mJ) of a solution of **(S,S)-BP-DKP-Tyr** in dry ACN; b) concentration profiles for the transients obtained from the resolution of the transient absorption spectra of **(S,S)-BP-DKP-Tyr** in ACN. The symbols represent: □ for the triplet state ^{3}BP, ○ for the ketyl radical BPH$^•$, ∆ for the tyrosyl radical Tyr(O$^•$), and * for the experimental data; the solid curves in a) and b) are the resulting fits from the regression analyses.

The concentrations of BPH$^•$ and Tyr(O$^•$) were found to be equal within the error estimation (Figure 3.2-14b). The low transient concentrations of the intermediates were found to be caused by their very fast decay which does not allow for a sufficient steady-state accumulation of these species. However, their decay on the same timescale of their formation is contrary to the general observation that biradicals decay on a much longer timescale than do their parent triplets.[54, 55, 65] This is also in contrast to the observations made on the open-chain analogues in Chapter 3.2.1.1. As is shown in Figure 3.2-15b, a change in the solvent from ACN to ACN-H_2O (2:1 v/v) did not significantly affect the transient absorption spectra of the dyad **(S,S)-BP-DKP-Tyr**. This is an observation that holds for all solvents in this study. Accordingly, resolution of the transient absorption spectra for **(S,S)-BP-DKP-Tyr** in an ACN-H_2O (2:1 v/v) mixture gave the same results as for pure ACN. The quenching was found to proceed intramolecularly with a high efficiency. This finding is in accord with the lack of a concentration dependence of the triplet decay rate constants (Figure 3.2-13b).

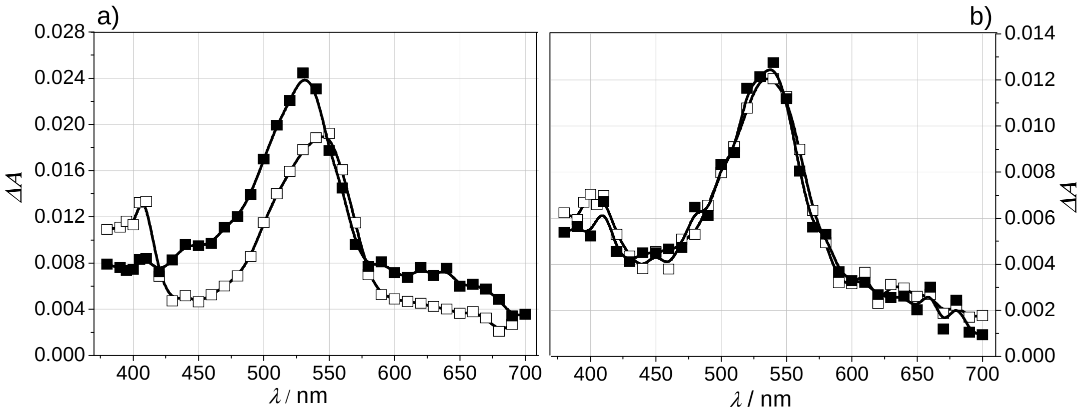

Figure 3.2-15 Transient absorption spectra obtained during laser flash photolysis at 355 nm of deoxygenated solutions (9 × 10^{-4} M) of (a) compound **(S,R)-BP-DKP-Tyr** with a time delay of 200 ns and (b) compound **(S,S)-BP-DKP-Tyr** with a time delay of 100 ns; measurements in ACN (filled symbols) and in ACN-H_2O (2:1 v/v) (open symbols).

The effect of the structure on the reactivity is illustrated by comparison of the transient spectra observed for both dyads in ACN. While the spectrum obtained for **(S,R)-BP-DKP-Tyr** in pure ACN after 200 ns still largely resembles the original triplet spectrum with its distinctive 525 nm absorption (Figure 3.2-15a, black filled symbols), the spectrum obtained for **(S,S)-BP-DKP-Tyr** carries significant contributions from a tyrosyl radical and a ketyl radical already after 100 ns (Figure 3.2-15b, black filled symbols).

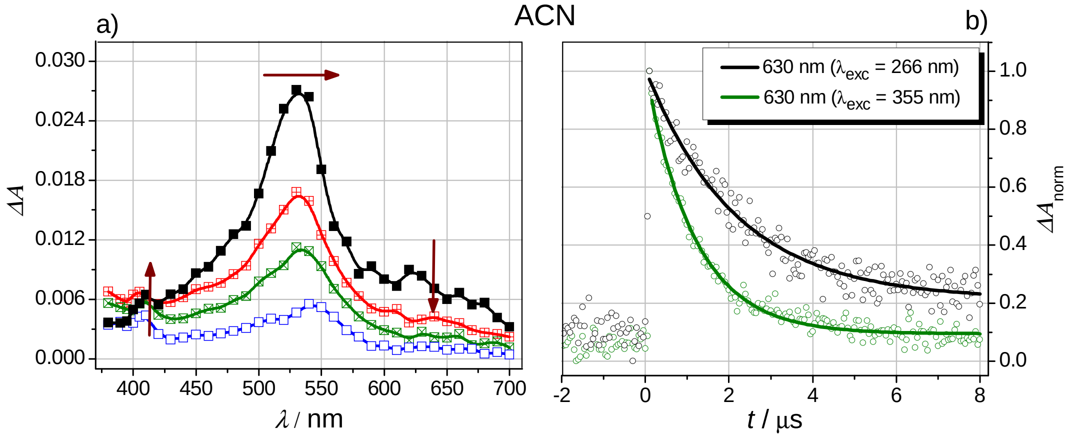

Figure 3.2-16 Summary of the results obtained during laser flash photolysis at 355 nm of a deoxygenated solution of **(S,R)-BP-DKP-Tyr** in dry ACN; a) transient absorption spectra: time delays after flash (from top to bottom): 85, 650, 1300, 3250 ns; b) normalized decay profiles of the transient absorption monitored at 630 nm (black) after 266 nm laser pulsing and 630 nm (green) after 355 nm laser pulsing; the solid lines represent monoexponential fits to the decay curves.

The results for the LFP of the dyads **(S,S)-BP-DKP-Tyr** and **(S,R)-BP-DKP-Tyr** in ACN are listed in Table 3.2-3 and showed, in general, a remarkable difference in their triplet lifetimes. Especially astonishing is also the fact that there is a significant intramolecular reactivity of **(S,R)-BP-DKP-Tyr**, even though the benzophenone and the tyrosine moieties occupy opposite sides of the DKP ring (see discussion of DFT results).

In contrast to the largely solvent-independent behavior of **(S,S)-BP-DKP-Tyr**, the time evolution of the transient spectra of dyad **(S,R)-BP-DKP-Tyr** is strongly dependent on the nature of the solvent. In particular, the spectrum obtained after 200 ns in the ACN-H_2O (2:1 v/v) mixture differs dramatically from the one in pure ACN and is fully consistent with efficient formation of ketyl and tyrosyl radicals (Figure 3.2-15a, open symbols). In order to clarify the nature of this solvent effect, the transient spectra obtained for compound **(S,R)-BP-DKP-Tyr** in ACN and ACN-H_2O (1:1 v/v) were resolved into their spectral components from which concentration-time profiles were constructed.

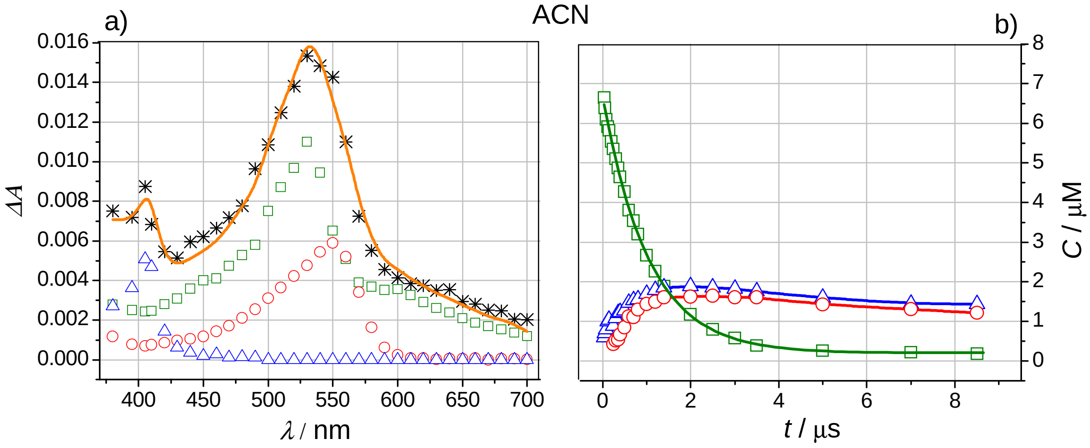

Figure 3.2-17 a) Resolutions of transient absorption spectra taken 1400 ns after 355 nm laser pulsing (5 mJ) of a solution of **(S,R)-BP-DKP-Tyr** in dry ACN; b) concentration profiles for the transients obtained from the resolution of the transient absorption spectra of **(S,R)-BP-DKP-Tyr** in ACN. The symbols represent: □ for the triplet state ^{3}BP, ○ for the ketyl radical BPH$^•$, △ for the tyrosyl radical Tyr(O$^•$), and * for the experimental data; solid curves in a) and b) are the resulting fits from the regression analyses.

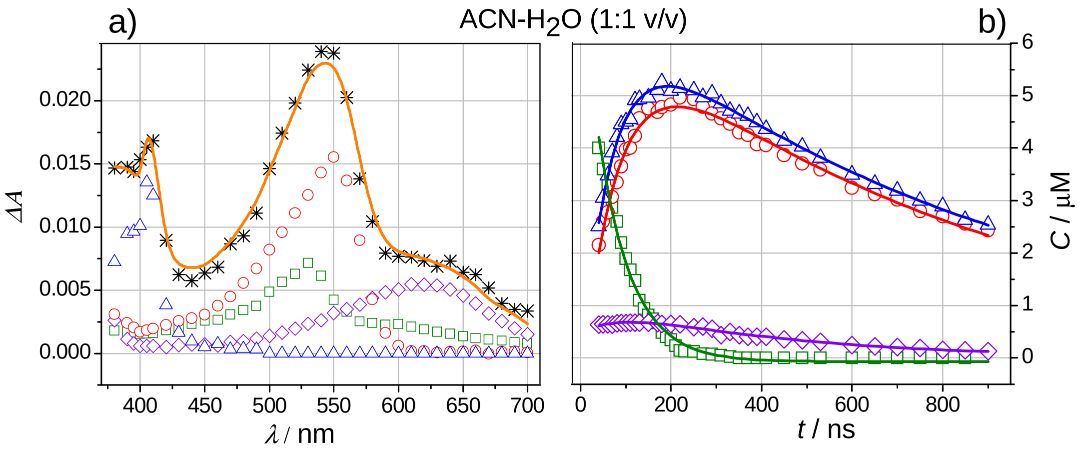

Figure 3.2-18 a) Resolutions of transient absorption spectra taken 200 ns after 355 nm laser pulsing (5 mJ) of a solution of **(S,R)-BP-DKP-Tyr** in ACN-H$_2$O (1:1 v/v); b) concentration profiles for the transients obtained from the resolution of the transient absorption spectra of **(S,R)-BP-DKP-Tyr** in ACN-H$_2$O (1:1 v/v). The symbols represent: □ for the triplet state ^{3}BP, ○ for the ketyl radical BPH$^•$, △ for the tyrosyl radical Tyr(O$^•$), ◊ for the BP radical anion BP$^{•-}$ and * for the experimental data; solid curves in a) and b) are the resulting fits from the regression analyses.

Typical resolutions are given in Figure 3.2-17a and Figure 3.2-18a, and the resulting concentration-time profiles are displayed in Figure 3.2-17b and Figure 3.2-18b. These profiles reveal the distinct difference in the triplet quenching of dyad **(S,R)-BP-DKP-Tyr** in the two solvents, which, as will be shown below, indicate two different dominating reaction mechanisms. To simulate quantitatively the experimental data obtained in ACN for dyad **(S,R)-BP-DKP-Tyr**, only three components were needed: the triplet state (^{3}BP), ketyl radicals (BPH$^•$), and tyrosyl radicals (Tyr(O$^•$)). The concentrations of $BPH^\bullet$ and $Tyr(O^\bullet)$ are found to be equal within the error estimation. The triplet lifetime obtained from the concentration profile is about 1 μs (green line in Figure 3.2-17b), which is in agreement with the triplet lifetime obtained from the kinetic traces at 630 nm (green line in Figure 3.2-16b). From the resolution of the transient absorption spectra and the resulting concentration profile, the quantum yield for the formation of both radicals was calculated to be equal to 25 % in ACN. The procedure for evaluating the quantum yield was the same as described in detail in one of the following paragraphs (after Eq 3.2-1). Based on the long lifetimes of the radicals which are decaying over tens of microseconds, it is concluded that they are formed mainly in self-quenching, i.e. intermolecular reactions.

A totally different situation was observed for dyad **(S,R)-BP-DKP-Tyr** in ACN-H_2O (1:1 v/v). First of all, the triplet lifetime was reduced by a factor of 10 (green lines in Figure 3.2-17b and Figure 3.2-18b). In addition, in order to reproduce the experimental data, four components have to be used, namely: ^3BP, ketyl radicals ($BPH^\bullet$), BP radical anions ($BP^{\bullet-}$), and tyrosyl radicals ($Tyr(O^\bullet)$). The formation of the radical anion ($BP^{\bullet-}$) indicates a likely ET mechanism; this aspect will, in fact, be discussed in Chapter 3.2.2.3.

The rates of formation of the radical species: ($BPH^\bullet$), ($BP^{\bullet-}$), and ($Tyr(O^\bullet)$) were, within experimental error, identical to the triplet-decay rate of the dyad **(S,R)-BP-DKP-Tyr**. The total amount of ($BPH^\bullet$) and ($BP^{\bullet-}$) together was equal to the ($Tyr(O^\bullet)$) concentration, within experimental error. Formation and decay of both the ketyl radical and the tyrosyl radical appear to follow the same decay law. This is in accord with an intramolecular-reaction mechanism. The initial triplet concentration, after extrapolation to the end of the pulse, was 7.1 μM. The maximum concentration of the tyrosyl radical was determined to be 6.9 μM. This value was obtained from a fitting the $Tyr(O^\bullet)$ concentration profile to a function which takes into account the growth and the decay of the species (Eq 3.2-1).

$$c_i(t) = c_{max}\left(exp(-k_2 t) - exp(-k_1 t)\right) \qquad \text{Eq 3.2-1}$$

where:

$c_i(t)$ – the concentration of the *i*th transient;

c_{max} – the maximum concentration of the *i*th transient if there was no decay, namely $k_2 = 0$;

k_1 – the rate constant of the formation of the *i*th transient;

k_2 – the rate constant of the decay of the *i*th transient.

From this value and the determined triplet concentration, the quantum yield of the tyrosyl radical is seen to be close to unity. The same procedure was applied to the BP radical anion, and its quantum yield of formation was estimated to be 0.18. The results prove that dyad **(S,R)-BP-DKP-Tyr**, which has the benzophenone and phenol moieties on opposite sides of the DKP ring, can, in fact, not only undergo intramolecular hydrogen atom transfer, but that this reaction can even occur with quantum yields close to unity. Analogous behavior was observed in another solvent mixture: ACN-H_2O (2:1 v/v) (Figure 3.2-19). As in the previous case, based on the concentration profiles of the tyrosyl radical and the ketyl radical, it can be seen that the radicals were formed in equal amounts. Moreover, the growth in the concentration of the biradical fit very well to the decay of the triplet state (k_1 values in Figure 3.2-19a,b,c). In addition, both the ketyl radical and the tyrosyl radical decayed on the same time scale of about 1 μs. Concentration profiles for $BPH^{\bullet}$ and $Tyr(O^{\bullet})$ were fit to Eq 3.2-1. That of the ketyl radical was in agreement with the kinetic traces at 340 nm. This was additional evidence that the concentration profiles were constructed properly (Figure 3.2-19d).

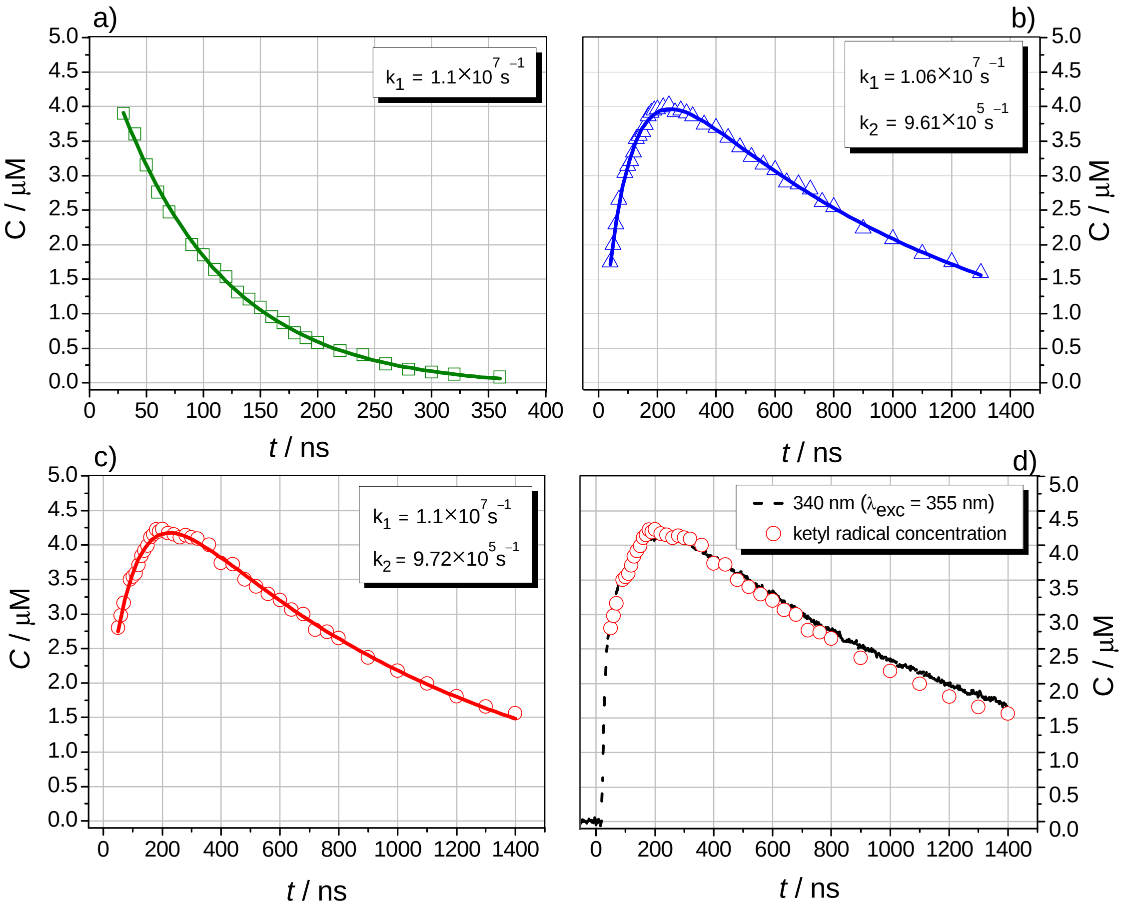

Figure 3.2-19 Concentration profiles for the transients ^{3}BP (green), BPH$^•$ (red), and Tyr(O$^•$) (blue), obtained from the resolution of the transient absorption spectra of **(S,R)-BP-DKP-Tyr** in ACN-H$_2$O (2:1 v/v). Solid lines represent fits to the decay curves; dashed black line in d) – scaled decay profiles monitored at 340 nm. Data in a) were obtained by a monoexponential fit to the triplet decay profile and data in b) and c) were obtained by fitting the concentrations profiles to Eq 3.2-1.

The steering effects of the solvents on the efficiency of the presumed intramolecular triplet quenching of the dyads **(S,S)-BP-DKP-Tyr** and **(S,R)-BP-DKP-Tyr** manifest themselves also in the triplet lifetimes, which exhibit a remarkably distinct influence of the solvents. Some typical kinetic profiles, recorded at 630 nm, that illustrate these dependencies are given in Figure 3.2-20. For dyad **(S,S)-BP-DKP-Tyr**, where the benzophenone and tyrosine moieties occupy the same side of the DKP ring, the kinetic profiles coincide with each other, irrespective of the solvent. This speaks in favor of only little impact of the solvent on the triplet lifetimes. A contrasting behavior was seen in dyad **(S,R)-BP-DKP-Tyr** where the triplet lifetimes were very sensitive to the solvents and vary between ca. 50 ns in HFIP and > 1000 ns in ACN or EtOAc. In general, the triplet lifetimes of **(S,R)-BP-DKP-Tyr** were reduced dramatically on going from non-protic to protic solvents. Thus, in contrast to the pair of open-chain epimeric dyads (Chapter 3.2.1.1), the triplet lifetimes of the two DKP-based structures exhibit distinct solvent dependencies.

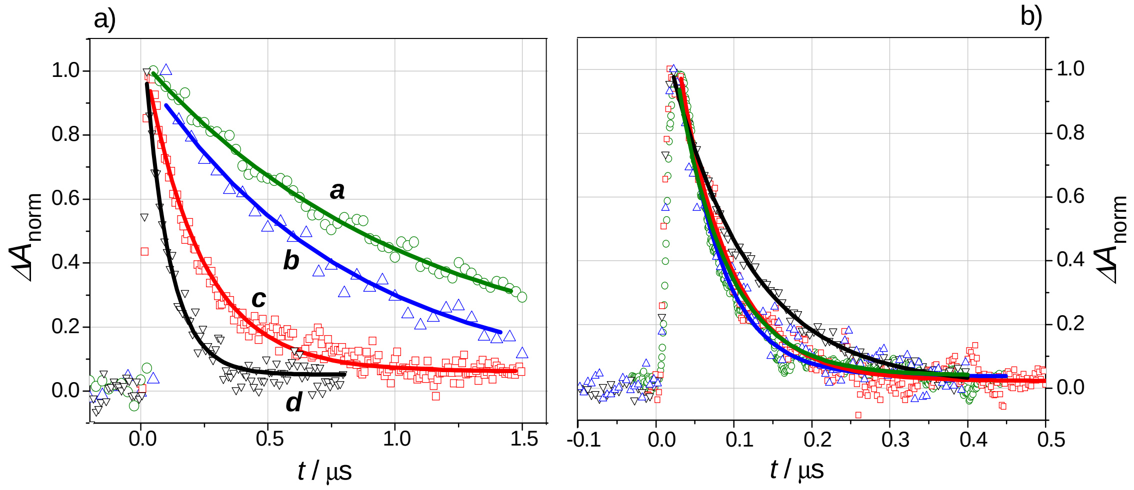

Figure 3.2-20 Normalized decay profiles observed at 630 nm and monoexponential fits to the decays for solutions of dyads a) **(S,R)-BP-DKP-Tyr** and b) **(S,S)-BP-DKP-Tyr**; solvent code: a – ethyl acetate (green), b – ACN (blue), c – ACN-H_2O (2:1 v/v) (red) and d – TFE (black).

In order to study the solvent effects on the intramolecular HAT pathway, the corresponding rate constants, k_H, were isolated from the observed gross triplet-decay rate constants, k_{obs}. The latter were extracted from the decay profiles at 630 nm (monoexponential fits), the decay profiles at 520 nm (biexponential fits), and, in some cases, from the triplet component of the concentration profiles. The evaluation procedures took into account (i) the solvent dependence of the intrinsic triplet lifetime of the BP chromophore by referencing it to the behavior of a benzophenone chromophore linked to the diketopiperazine ring in the respective solvent (data in Chapter 3.5.2.1) and (ii) the effects of self-quenching (see below). A schematic view of the various competing quenching processes and a detailed kinetics-data evaluation can be found in Chapter 2.5.5.

While the triplet decay of the dyad **(S,S)-BP-DKP-Tyr** exhibited no significant concentration dependence (Figure 3.2-13b), LFP results for the dyad **(S,R)-BP-DKP-Tyr** in non-protic solvents, such as ACN or DCM, showed that the values for k_{obs} were concentration dependent (see Figure 3.2-16b). This behavior was due to contributions from bimolecular quenching (self-quenching) which leads to the ketyl radical and the tyrosyl radical with the rate constant k_{SQ}. The latter species decayed by bimolecular processes within tens of microseconds and therefore gave a virtually constant offset in the transient spectra on the shorter timescale of the experiment. The self-quenching process was particularly efficient in non-protic solvents where the reactivity toward intramolecular H-atom transfer was small. From the two sets of data points that were collected (from 337 nm excitation and 266 nm excitation) in ACN a self-quenching rate constant was estimated for the dyad **(S,R)-BP-DKP-Tyr** of $k_{SQ} = (5.5 \pm 1.0) \times 10^{8}\ \mathrm{M}^{-1}\ \mathrm{s}^{-1}$. (The low solubility of **(S,R)-BP-DKP-Tyr** prevented a more accurate measurement of its self-quenching). This estimated value is in good agreement with the rate constant for the self-quenching of the triplet of an open-chain benzophenone/phenol dyad.[65] Notably, the k_{H} calculated from experiments performed in ACN at different concentrations: 2×10^{-5} M (λ_{exc} = 266 nm) or 9×10^{-4} M (λ_{exc} = 337 nm), were in good agreement (Table 3.2-3). It is noted that the poor solubility of the cyclic dyads interfered with accurate measurements of the self-quenching rate constant for all studied solvents. For those calculations of intramolecular k_{H}, where the rate constant for self-quenching were needed, k_{SQ} from a structurally related, but open-chained benzophenone/phenol dyad was used.

The rate constants for the intramolecular HAT, k_{H}, as calculated for dyad **(S,R)-BP-DKP-Tyr**, cover a range from $< 1 \times 10^{5}\ \mathrm{s}^{-1}$ in EtOAc to $2 \times 10^{7}\ \mathrm{s}^{-1}$ in HFIP (see Table 3.2-3). On the other hand, the rate constants for the intramolecular HAT for dyad **(S,S)-BP-DKP-Tyr** varied only from $2.2 \times 10^{7}\ \mathrm{s}^{-1}$ in ACN to $8.2 \times 10^{6}\ \mathrm{s}^{-1}$ in TFE. It is noted that the uncertainty in rate constant values, derived in this manner, increases significantly with the H-abstraction contributions from the solvent.

The results presented in Table 3.2-3 reveal a striking contrast between the two diastereomers with regard to their k_{H} dependences on the solvent. The results show that the change in the configuration of just one chiral center produced distinct changes in the intramolecular H-atom transfer rates with a change in the solvent. The reaction rates for dyad **(S,R)-BP-DKP-Tyr** were found to be strongly solvent dependent, while the solvent was only of minor importance for the reaction rates of dyad **(S,S)-BP-DKP-Tyr**.

This contrasting solvent behavior toward the intramolecular H-atom transfer, observed in **(S,S)-BP-DKP-Tyr** and **(S,R)-BP-DKP-Tyr**, is unusual for a pair of diastereomers. In this regard, they are indeed a unique pair of diastereomers with a unique solvent dependence of their stereoselectivity. Both epimers, **(S,S)-BP-DKP-Tyr** and **(S,R)-BP-DKP-Tyr**, show reactivity with respect to intramolecular H-transfer, but with a remarkable chiral discrimination in their rate constants, which strongly depends on the solvents. Stereoselection in H-atom transfer rates of diastereomeric ketone-phenol dyads has been reported to be in the range of 2–10 when expressed as the ratio of the rate constants of the intramolecular H-atom transfer between remote phenol and ketone moieties of these compounds.[51, 54, 75] The highest stereoselectivity of the open-chain analogues of the cyclic dyads was obtained in MeOH and was equal to 3.5. The stereoselectivity, $S = k_{\mathrm{H}}(\boldsymbol{S,S})/k_{\mathrm{H}}(\boldsymbol{S,R})$, (measured in the same solvent) found in this work for the DKP-based dyads, varied from 131 to 0.74 (Table 3.2-3). In particular, the epimers revealed marked stereoselectivity in some of the non-protic solvents like EtOAc and benzonitrile, much higher than has ever been reported. Quite unexpectedly, the stereoselectivity was significantly reduced in protic solvents. At extremes, compound **(S,R)-BP-DKP-Tyr** which has the reactive moieties on opposite sides of the diketopiperazine ring, in hexafluoro-2-propanol became even more reactive than **(S,S)-BP-DKP-Tyr**.

Table 3.2-3. Summary of solvent parameters and of the kinetic data of the dyads **(S,S)-BP-DKP-Tyr** and **(S,R)-BP-DKP-Tyr**.

	Solvent	**solvent parameters**			**rate constants (10^6 s^{-1})**		***S***[d]
		$\Sigma\alpha_2^{\mathrm{H}}$ [b]	$\Sigma\beta_2^{\mathrm{H}}$ [b]	η[a]	k_{H} (**S,R**)[c]	k_{H} (**S,S**)[c]	
1	chloroform	0.15	0.02	0.537	(2.2)	(11.5)	5.2
2	dichloromethane	0.1	0.05	0.437	1.9 (2.0)	(14.5)	7.2
3	1.2-dichloroethane	0.1	0.11	0.77	(1.7)	(13.6)	10.7
4	acetonitrile	0.07	0.32	0.37	*0.3 (0.3)*	20.7 (20.0)	73.7
5	benzonitrile	0	0.33	1.2	*0.3*	9.5	31.6
6	ethyl acetate	0.0	0.45	0.423	*0.1*	14.4	131
7	trifluoroethanol	0.57	0.25	1.8[e]	8.5	8.2	0.97
8	methanol	0.43	0.47	0.544	*2.3 (2.8)*	*9.2*	3.9
9	HFIP	0.77	0.10	1.02	21.1	15.7	0.74
10a	ACN-H_2O (9:1 v/v)	0.55[f]	≈0.34[g]	-	3.0	-	-
10b	ACN-H_2O (4:1 v/v)	0.61[f]	≈0.34[g]	-	5.5	-	-
10c	ACN-H_2O (2:1 v/v)	0.62[f]	≈0.34[g]	-	8.4	13.9	1.7

[a] at 25°C; CRC Handbook of Chemistry and Physics. CRC Press. Boca Raton. 76th Ed. **1995**; [b] taken from ref.[72]; [c] results from 355 nm and 337 nm LFP, in 10^6 s^{-1}; experimental error ± 5 %, 0.7 mM ≤ [(S,S)-BP-DKP-Tyr], [(S,R)-BP-DKP-Tyr] ≤ 2.6 mM; data in italics: experimental error ±20 %; data in parentheses from 266 nm LFP, 20 μM ≤ [(S,S)-BP-DKP-Tyr], [(S,R)-BP-DKP-Tyr] ≤ 40 μM; [d] $S = k_{\mathrm{H}}(\mathrm{S,S})/k_{\mathrm{H}}(\mathrm{S,R})$; [e] taken from: Sierra, P. S.; Tejuca, C. C.; Garcia-Blanca, F. *Helv. Chim. Acta* **2005**, *88*, 312–324; [f] interpolated from data in: Marcus. Y.; Migron. Y. *J. Phys. Chem.* **1991**. *95*. 400–406; [g] linear interpolation from data in pure solvents, weighted by molar fractions.

3.2.2.2 **Theoretical calculations**

The results presented above of detailed laser-flash photolysis studies are supplemented by the results of DFT calculations and molecular-dynamics simulations of the ground-state structures and conformations. These studies establish a quantitative picture of the conformer distributions of the dyads and define the molecular prerequisites of the individual quenching geometries.

3.2.2.2.1 **DFT calculations**

The molecular conformations of **(S,S)-BP-DKP-Tyr** and **(S,R)-BP-DKP-Tyr** were addressed by DFT calculations in the gas phase (for ground states and triplet states) and by using an implicit solvent model (IEFPCM model parameterized for ACN). The conformations of aromatic cyclopeptide molecules can be characterized by three different orientations of the side-chain substituents (R) in relation to the DKP ring. The acronyms $\mathbf{E_N}$, $\mathbf{E_O}$, and **F** denote side-chain rotamers wherein the aromatic substituent R is extended to the adjacent nitrogen atom, extended to the adjacent carbonyl oxygen atom, and folded back across the diketopiperazine ring, respectively. This rotamer notation is based on the orientation of the side-chain substituent R (Figure 3.2-21) rather than on the dihedral angles, in order to simplify the comparison between the epimeric compounds **(S,R)-BP-DKP-Tyr** and **(S,S)-BP-DKP-Tyr**. In the rotamer notation the first symbol always correspond to the tyrosine side.

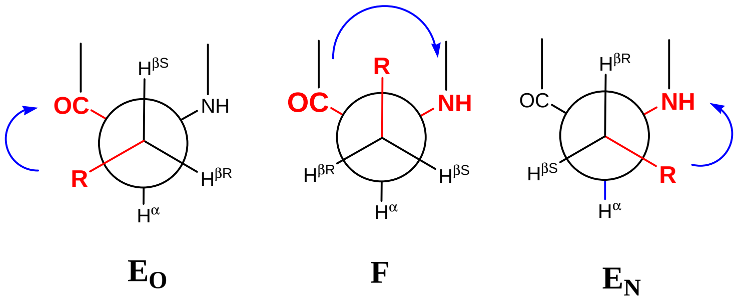

Figure 3.2-21 Notation of the side-chain rotamers (R denotes the respective aromatic moiety).

DFT calculations were performed for each of the nine combinations of the side-chain conformations of the Tyr and BP residues for each of the dyads.[148] The results for the gas-phase calculations of the ground state showed that conformations with favorable quenching geometries were available for both dyads. Surprisingly DFT calculations reveal that although dyad **(S,R)-BP-DKP-Tyr** has its benzophenone and phenol on opposite sides of the DKP ring, it was capable of forming a favorable geometry for hydrogen transfer (close contact of the reactive moieties). The energetic order of the rotamers in the gas phase showed a similar pattern for the dyads **(S,S)-BP-DKP-Tyr** and **(S,R)-BP-DKP-Tyr** in that structures containing a side-chain conformation $\mathbf{E_O}$ were strictly disfavored. This is in accord with NMR studies on aromatic diketopiperazines in organic solvents.[143, 149-151] In addition, these studies from the literature have shown that the conformational equilibria in solution are dominated by structures that allow folding of the aromatic side chain across the DKP ring.

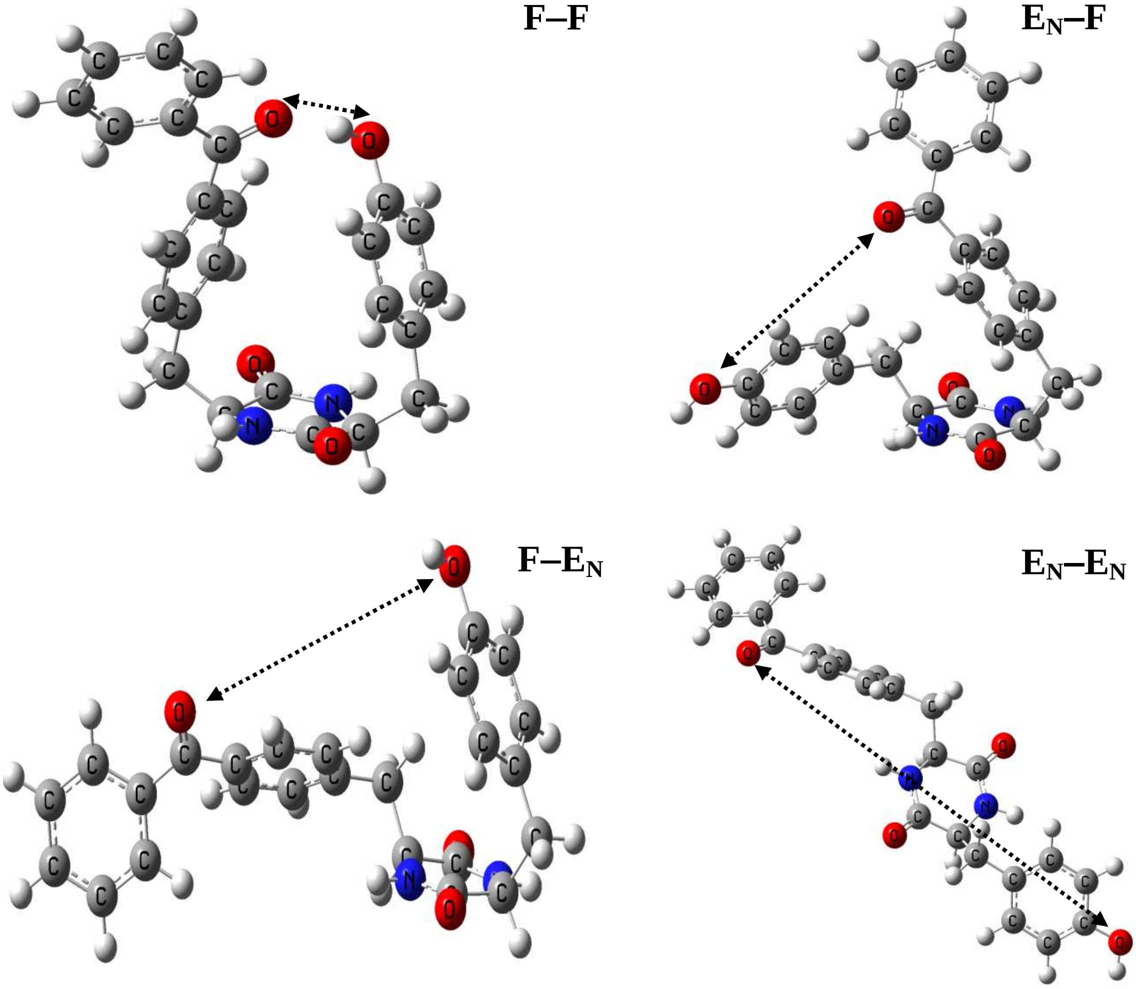

Figure 3.2-22 PBE1PBE/6-31G-optimized geometries of the ground state of the energetically lowest rotamers in the gas phase for the dyad **(S,S)-BP-DKP-Tyr**. The dotted arrow lines denote the O–O distances between the benzophenone carbonyl and the phenol oxygen. Notation of rotamer: first symbol corresponds to Tyr side and second to BP side.

Actually, the global minimum of **(S,S)-BP-DKP-Tyr** exhibited a structure **F–F** wherein both side chains were folded simultaneously across the ring. The favorable energy goes hand-in-hand with a short O–O distance, which makes the **F–F** rotamer a probable candidate for the quenching geometry of **(S,S)-BP-DKP-Tyr** (see Figure 3.2-22, Table 3.2-4). It is noted, based on the literature data, that there has been no definite answer from the experiment whether both side chains could share the space over the diketopiperazine ring in a face-to-face fashion, despite the fact that the conformational properties of the cyclic dipeptides containing aromatic amino acids have been studied using X-ray, CD, ^{1}H NMR and ^{13}C NMR, circular dichroism, and fluorescence anisotropy.[143, 150, 151] However, it was claimed that for cyclic dipeptides with L-Tyr and L-Phe as side chains, the face-to-face arrangement exists with a population of at least 24 % on average at 30 °C.[151]

Other optimized structures for the ground-state in the gas-phase were much higher in energy, for example (1) those with only one aromatic side chain folded over the DKP ring while the other is forced away from the space over the backbone ring (**F–E$_N$**, **E$_N$–F**), or (2) those with both aromatic side chains extended to the nitrogens (**E$_N$–E$_N$**). Such structures showed no favorable O–O distances (Figure 3.2-22, Table 3.2-4). The relative energies and the O–O distances between the BP carbonyl and the Tyr phenol for the rotamer minima of **(S,S)-BP-DKP-Tyr** are summarized in Table 3.2-4.

Table 3.2-4 Results of the four lowest-energy structures of the gas-phase (ground state S_o and triplet state T_1) and acetonitrile (ground state S_o) DFT calculations (PBE1PBE; 6-31G basis set) of the dyad **(S,S)-BP-DKP-Tyr**.

Rotamer	Distance *d*(O–O) / [Å]	Relative energy / [kcal/mol]		
		gas-phase S_o	gas-phase T_1	ACN S_o
F–F	2.8	0.0	0.0	0.0
E$_N$–F	6.6	7.2	3.5	1.5
F–E$_N$	7.9	7.5	3.3	0.9
E$_N$–E$_N$	15.6	8.1	3.7	2.1

In the dyad **(S,R)-BP-DKP-Tyr** the side chains were expected to occupy conformations on separate sides of the DKP ring, and consequently were expected to have long O–O distances. While this was actually found for eight of the side-chain conformations, unexpectedly, one structure with a short O–O distance was found to be the global minimum in the gas-phase calculations for the ground state (**F–eclipsed**, see Figure 3.2-23). Evidently this structure did not refer to one of the side-chain rotamers but forced the BP side chain into a conformation where H^{α} and C^{γ} were eclipsed.

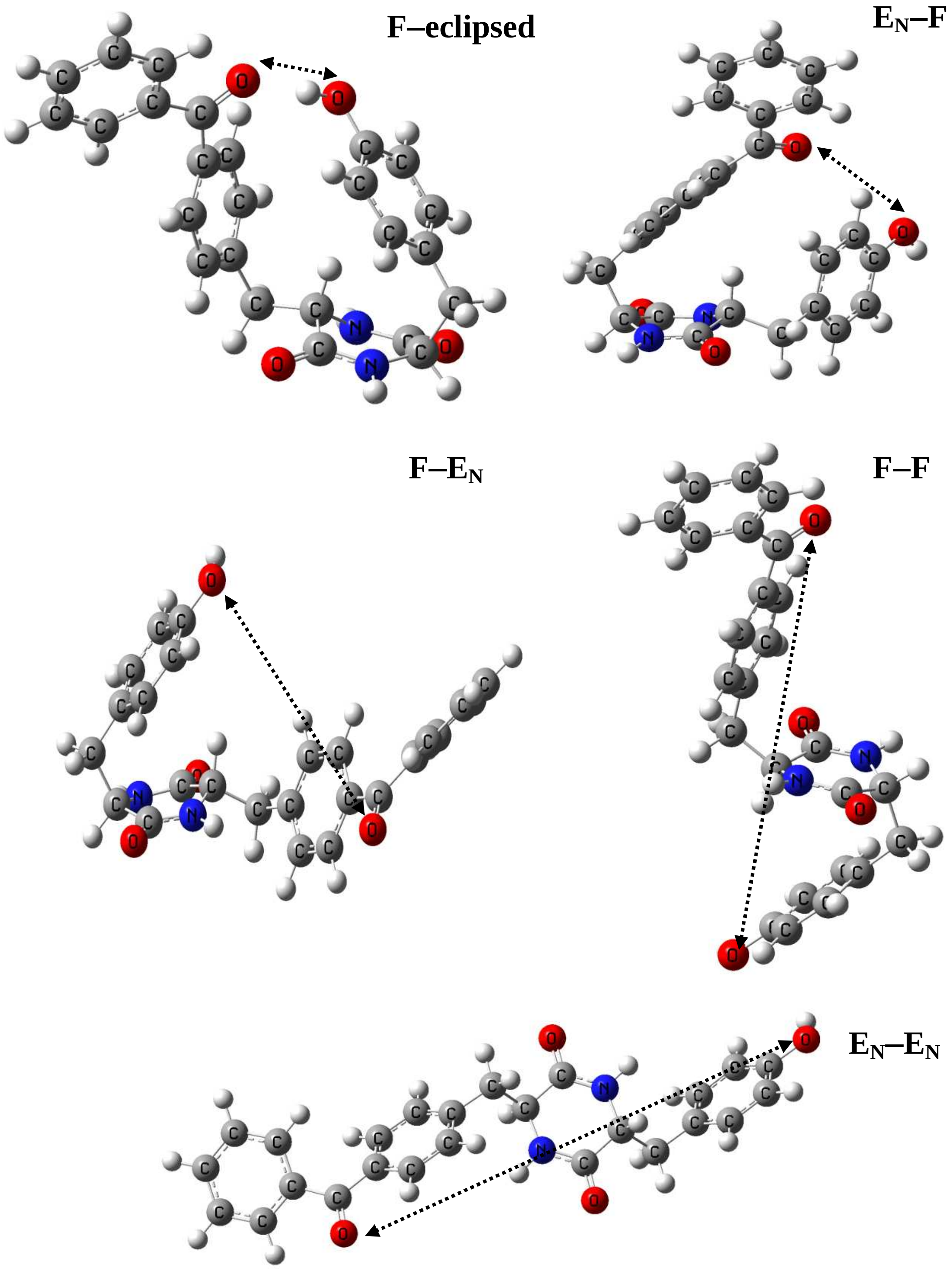

Figure 3.2-23 PBE1PBE/6-31G-optimized geometries of the ground state of the energetically lowest rotamers in the gas phase for the dyad **(S,R)-BP-DKP-Tyr**. The dotted arrow lines denote the O–O distances between the benzophenone carbonyl and the phenol oxygen. Notation of rotamer: first symbol corresponds to Tyr side and second to BP side.

Interestingly, the global minimum conformation of **(S,S)-BP-DKP-Tyr** found in the gas-phase calculations for the ground state was lower in energy by 5 kcal/mol than the respective minimum of **(S,R)-BP-DKP-Tyr**. Since the parameters describing the hydrogen-bonding geometry (distance and angle in the system O–H···O) were almost the same, it was assumed that the additional energy was due to stabilization of the conformation **F–F** for dyad **(S,S)-BP-DKP-Tyr**. This was also confirmed by single point calculations for both dyads after weakening the hydrogen-bonding by inverting the directionality of the system O–H···O to H–O···O.[152] The difference in energy for both dyads using this method was also 5 kcal/mol. Therefore the energy of the **F–eclipsed** structure was expected to be strongly susceptible to changes in the environment.

Accordingly, DFT calculations with a solvent (acetonitrile, IEFPCM model) provided evidence for substantial changes in the conformational equilibria of **(S,R)-BP-DKP-Tyr** (see Table 3.2-5).

Table 3.2-5 Results of the five lowest-energy structures of gas-phase (ground state S_o and triplet state T_1) and acetonitrile (ground state S_o) DFT calculations (PBE1PBE; 6-31G basis set) of the dyad **BP-DKP-Tyr-(R,S).**

Rotamer	Distance *d*(O–O)/ [Å]	Relative energy / [kcal/mol]		
		gas-phase S_o	gas-phase T_1	ACN S_o
F–eclipsed	2.8	0.0	1.4	2.8
F–F	12.5	5.2	1.2	0.0
E_N–F	5.5	3.5	0.0	1.7
F–E_N	8.7	4.4	0.1	1.5
E_N–E_N	15.5	4.6	0.4	4.5

In a polar solvent, i.e., in ACN, the **F–eclipsed** conformation of **(S,R)-BP-DKP-Tyr** was no longer a global minimum. The “double sandwich” **F–F** conformation of **(S,R)-BP-DKP-Tyr**, with an extremely long distance (12.5 Å) between its reactive moieties, lay 2.8 kcal/mol lower than the **F–eclipsed** conformation (see Figure 3.2-23, Table 3.2-5). Even structures with only one aromatic side chain folded over the DKP ring and the other one being forced away from the space over the backbone ring (**F–E_N**, **E_N–F**) were less energetic than the **F–eclipsed** conformation with the close contact of the reactive moieties. Thus, the **F–eclipsed** conformation for dyad **(S,R)-BP-DKP-Tyr** was much less populated in ACN solution than in the gas phase.

As stated above, the folded **F–F** conformation wherein both aromatic residues share the same half-space above of the DKP ring of the dyad **(S,S)-BP-DKP-Tyr** was strongly favored in the gas phase ground state. Next, there were two conformations that had energies higher by 7.2 and 7.5 kcal/mol than has the **F–F** conformation (Table 3.2-4). However, the energetic distance to those conformations in the ground state significantly decreased to 1.5 kcal/mol and 0.9 kcal/mol in ACN solution, respectively (Table 3.2-4).

It is well established that hydrogen-atom transfer reactions are initiated by the triplet-excited state of benzophenone so that, in addition to the calculations of the ground state, the DFT study was also performed on the triplet state. Optimized geometries of the triplet state did not differ from the corresponding conformations of the ground state. However, charge distribution and energy order of the rotamers demonstrated an important difference in comparison to the results for the ground state calculations (Table 3.2-4 and Table 3.2-5). In the excited n,π^* state of a C=O, the n-orbital is localized on the O atom of the group C=O and the π^* orbital is delocalized over the aromatic group.[153] So, as expected, there was a diminished electron density on the carbonyl oxygen in the calculated triplet state of the dyads. Thus, the BP triplet, being of an n,π^* character, was intrinsically less prone to H-bonding phenomena than was the ground state. This was reflected in the results for the energy of the triplet state. In the conformations with the closest distances of the reactive moieties in the ground state (**F–F** for **(S,S)-BP-DKP-Tyr** and **F–eclipsed** for **(S,R)-BP-DKP-Tyr**) where H-bonding was significant, the triplet state was influenced the most (Table 3.2-4 and Table 3.2-5). For example, the **F–eclipsed** triplet state conformation for the dyad **(S,R)-BP-DKP-Tyr** had the highest energy among the other structures whereas for the ground state of this configuration was the energetic minimum among ground-state configurations.

3.2.2.2.2 Molecular Dynamics

3.2.2.2.2.1 Conformational analysis

The molecular structure of the dyads could be clarified further through a molecular-dynamics simulations analysis. DFT calculations, as described above, revealed that the dyad **(S,R)-BP-DKP-Tyr** can have a significantly different energetic order for a rotamer in the gas-phase and in the acetonitrile. Therefore, it was of interest to verify, in an independent fashion, this information about the populations of the side-chain rotamers in the dyads' ground state. More generally, it was of interest to determine the probabilities of forming rotamers with the close contact necessary for intramolecular reaction between the Tyr and BP moieties. An important result from this analysis was that MD-derived populations of the side-chain rotamers were distinctly different between the pair of epimeric dyads. Additionally, the populations of the side-chain rotamers obtained from the MD simulations of dyads **(S,S)-BP-DKP-Tyr** and **(S,R)-BP-DKP-Tyr** revealed side-chain conformational preferences that differed significantly from those of the open-chain congeners (Chapter 3.2.1.3.2).

The conformational space of the diketopiperazines dyads was sampled by means of molecular dynamics for different solvents (implicit model), e.g. water, ACN, DCM, and dimethylsulfoxide, and also for different starting configurations. Based on the results it can be concluded that starting configurations did not affect the MD-computed populations of the side-chain rotamers. The MD simulations performed in various solvents gave qualitatively the same results although differences in the side-chain populations could be noted. In the following, the detailed analysis of MD simulations performed for ACN of the dyads **(S,S)-BP-DKP-Tyr** and **(S,R)-BP-DKP-Tyr** will be presented. The interconversion between different molecular conformations was studied by means of long-time molecular-dynamics simulations (implicit-solvent model for ACN). Figure 3.2-24 and Figure 3.2-25 summarize the time variation of three molecular parameters (side-chain dihedral angles; characteristic inter-side chain distance) within a 100-ns simulation time window for dyads **(S,S)-BP-DKP-Tyr** and **(S,R)-BP-DKP-Tyr**, respectively.

In agreement with the DFT results, mainly three rotamers (**E_N**, **E_O**, and **F**) of each side chain were populated during the simulations of both compounds. Of particular interest was the probability of the **F-F** conformation of **(S,S)-BP-DKP-Tyr**, which allows for close contacts < 4.0 Å (red dashed line in Figure 3.2-24a) between the reacting moieties and closely resembles the quenching geometry of this dyad. The calculated probability for the population of the **F–F** conformation was only 2.7 %. This low population of **F–F** is of importance for the interpretation of the excited-state dynamics of **(S,S)-BP-DKP-Tyr** because photoinduced hydrogen–atom transfer within **(S,S)-BP-DKP-Tyr** is limited to the **F–F** conformation of the side chains wherein both aromatic moieties are back-folded across the DKP ring at the same time. It appears that repulsive interactions between the bulky aromatic groups favored the population of sterically less crowded conformations for the dyad **(S,S)-BP-DKP-Tyr**. In particular, the simultaneous population of the **F** rotamer by both side chains appeared but with low probability. In conclusion, although the **F–F** conformation was shown to be a rare conformation during the simulations on **(S,S)-BP-DKP-Tyr**, irrespective of the chosen starting geometry, its population pattern is sufficient to explain the reactivity toward intramolecular HAT in the range of 10^7 s^{-1} (see Chapter 3.2.2.2.2.2).

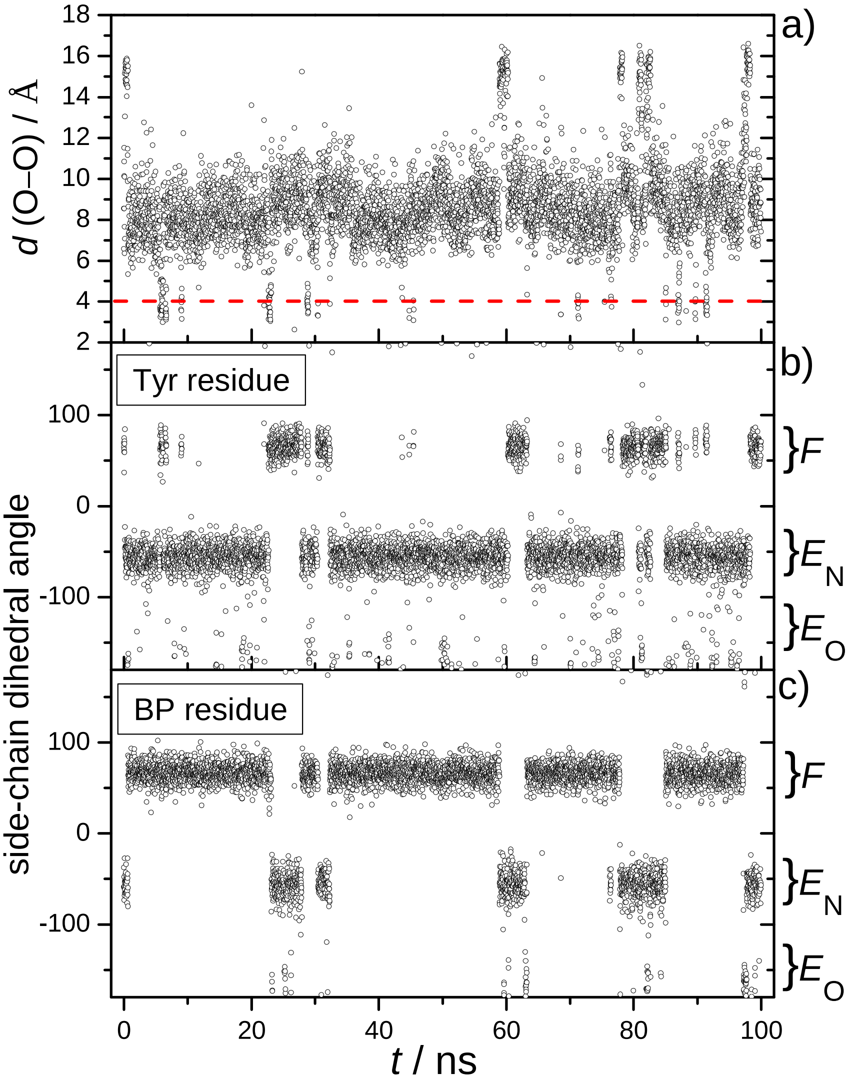

Figure 3.2-24 Long-time molecular-dynamics simulations for **(S,S)-BP-DKP-Tyr** (implicit-solvent model for ACN); a) time variation of the inter-side-chain distance d(O–O) between the Tyr hydroxylic oxygen atom and the BP carbonyl oxygen atom; b) time variation of the Tyr side-chain dihedral angle; c) time variation of the BP side-chain dihedral angle.

The probabilities for the population of the most likely conformations of the cyclic-linked dyads were larger than the probabilities for the most likely conformations of the open chain analogues. This can be seen by analysing the joint probabilities (the probability of both events occurring together at the same time) for the Tyr and BP side chains. From Figure 3.2-24b,c it can be seen that the most preferable configuration is when the tyrosine side was extended to nitrogen and the BP side is folded back across the diketopiperazine ring (**E_N–F**). The second most favorable configuration is when the BP is extended to nitrogen and the tyrosine side is folded back across the DKP ring (**F–E_N**). The probability of the dyad **(S,S)-BP-DKP-Tyr** to be in one of these two conformations is nearly 90 % (Table 3.2-6). The calculated probability of the configuration with both side-chains extended to nitrogen, with an extremely long distance between the reactive moieties (**E_N–E_N**), is just 3.5 %. The total probability for the dyad **(S,S)-BP-DKP-Tyr** to be in one of the four structures: **F–F**, **E_N–F**, **F–E_N**, **E_N–E_N** is in agreement with the DFT calculations. However, based on a comparison of the DFT calculated energy order of the rotamers (Table 3.2-4) with the MD-calculated probabilities of the side-chain rotamer population (Table 3.2-6), it can be concluded that the DFT calculations overestimated the presence of the **F–F** conformation.

Table 3.2-6 Summary of the side-chain rotamer joint probabilities for **(S,S)-BP-DKP-Tyr** and **(S,R)-BP-DKP-Tyr** computed from the molecular dynamics simulation (implicit ACN model).

Conformation	Joint probability	
	(S,S)-BP-DKP-Tyr	**(S,R)-BP-DKP-Tyr**
F–F	0.027	0.19
E_N–F	0.72	0.34
F–E_N	0.16	0.26
E_N–E_N	0.035	0.16

As shown by DFT studies, close contacts < 4 Å within the dyad **(S,R)-BP-DKP-Tyr** require the population of **F–eclipsed** conformations. In contrast to DFT calculations, the formation of such structures does not appear at all during the 100 ns simulation (red dashed line in Figure 3.2-25a). For **(S,R)-BP-DKP-Tyr**, wherein aromatic residues share the opposite half-spaces above of the DKP ring, the side-chain preferences were less expressed relative to **(S,S)-BP-DKP-Tyr**. Based on the analysis of the MD simulations results, there was no one single conformation which clearly prevailed in solution for **(S,R)-BP-DKP-Tyr**. MD simulation in the ACN implicit model showed that four structures: **F–F**, **E_N–F**, **F–E_N**, **E_N–E_N** occurred with similar probability (Table 3.2-6). Compared with **(S,S)-BP-DKP-Tyr**, in **(S,R)-BP-DKP-Tyr** significantly higher populations were obtained for the rotamer where both aromatic residues populate the back-folded **F–F** conformation (Table 3.2-6). Thus, in full agreement with the outcomes of the DFT studies in an ACN continuum, a "double-sandwich" like structure of **(S,R)-BP-DKP-Tyr** was also one of the four most probable conformations arising from the MD simulations (Table 3.2-6). This double-sandwich structure implies long inter-side-chain distances. In addition, the configuration with both residues extended to nitrogen, with an extremely long distance between the reactive moieties (≈ 15.5 Å), was also much more probable than in the **(S,S)-BP-DKP-Tyr** dyad.

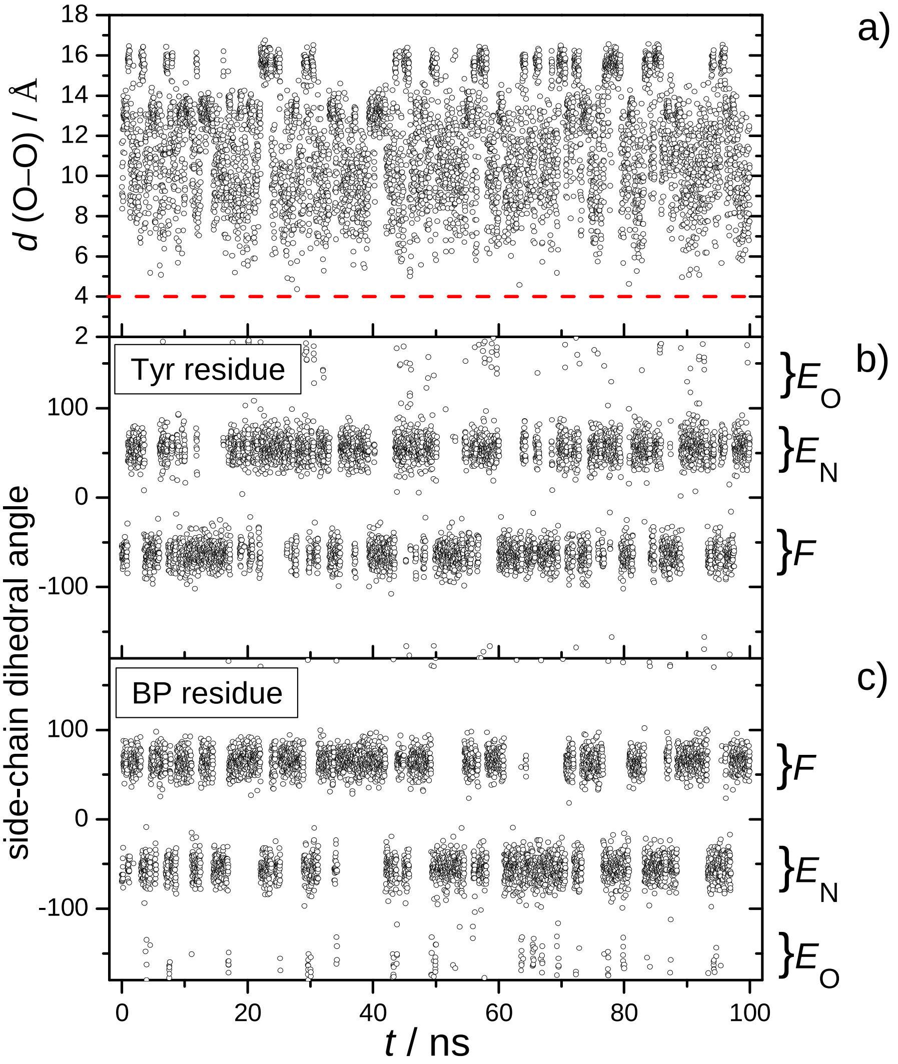

Figure 3.2-25 Long-time molecular-dynamics simulations for **(S,R)-BP-DKP-Tyr** (implicit-solvent model for ACN); a) time variation of the inter-side-chain distance *d*(O–O) between the Tyr hydroxylic oxygen atom and the BP carbonyl oxygen atom; b) time variation of the Tyr side-chain dihedral angle; c) time variation of the BP side-chain dihedral angle.

Pair-distribution functions of the carbonyl/hydroxylic group distance *d*(O–O) in Figure 3.2-26 were calculated based on the data from the MD simulations. They revealed very important differences between the pair of diastereoisomers. Importantly, only **(S,S)-BP-DKP-Tyr** was capable of the formation of rotamers with close-contacts between the hydroxylic group and the carbonyl oxygen. The sampling of **(S,S)-BP-DKP-Tyr** in a implicit model of acetonitrile solution gave a quite narrow pair distribution function with a maximum at a distance *d*(O–O) = 8.5 Å. This distance can be attributed to the conformations in which one of the side-chain is folded-back across the DKP ring and the second one is extended to nitrogen (**E_N–F** and **F–E_N**). These conformations were found to be the most favorable ones for **(S,S)-BP-DKP-Tyr**. Additionally the pair-distribution function shows two smaller peaks with maxima at distances *d*(O–O) = 4 Å and *d*(O–O) = 16 Å. These maxima can be attributed to the conformations **F–F** and **E_N–E_N**, respectively.

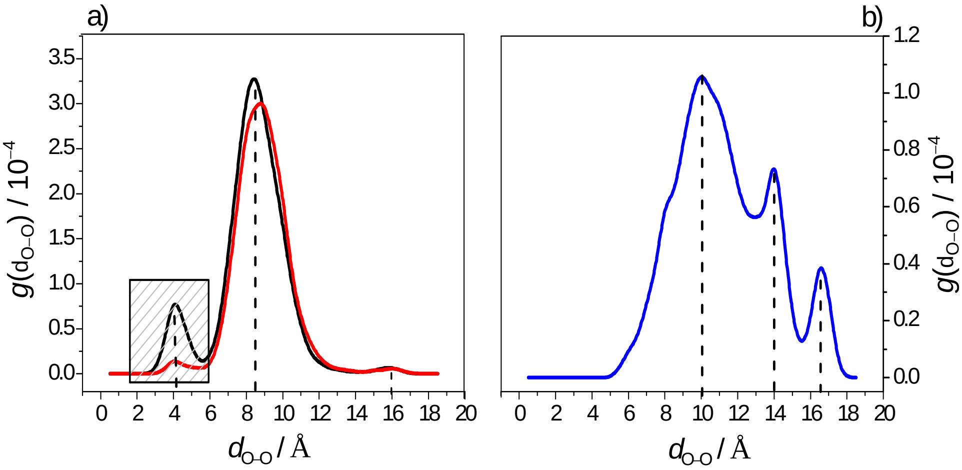

Figure 3.2-26 Pair-distribution functions of the carbonyl/hydroxylic group distance *d*(O–O), obtained with molecular dynamics simulation in ACN for a) **(S,S)-BP-DKP-Tyr** black: ground state charges, red: triplet state charges; b) **(S,R)-BP-DKP-Tyr**.

The situation is different for the **(S,R)-BP-DKP-Tyr** for which the pair-distribution function of the carbonyl/hydroxylic group distance *d*(O–O) is much wider compared to the one for **(S,S)-BP-DKP-Tyr**. This wide distribution reflects the lack of a most favorable conformation. Additional spread in the distribution is provided by significant populations of conformations with long distances *d*(O–O), namely **F–F** ("double sandwich") and **E_N–E_N**.

3.2.2.2.2.2 **Calculation of the rate constants of close-contact formation**

In order to gain further insight into the nature of the intramolecular H-atom transfer process, a rate constant k_{OO} for **(S,S)-BP-DKP-Tyr** was computed from MD simulations in an attempt to match the experimentally measured k_{H}. The rate constant, k_{OO}, for forming close contacts between the reacting moieties, was evaluated from the MD simulations by means of number correlation functions. These functions were computed following routines that have been described in detail by Pogocki.[154] The conceptual basis for these routines is as follows. The reactive and non-reactive conformations are considered as being in equilibrium, but the overall H-abstraction reaction is considered to be very fast compared to the relaxation of the equilibrium between the conformations. If these circumstances prevail, then the observed rate constant k_{H} should be comparable to a theoretical rate constant, k_{OO}, computed from the simulation *via* Eq 3.2-2 to Eq 3.2-4.[154] The numerator, $\langle N_{\mathrm{OO}}\rangle$, in Eq 3.2-2 is the fraction of the time that the distance between the carbonyl and hydroxyl oxygens was less than 4 Å during a 100 ns time MD trajectory. The denominator, τ_{rxn} in Eq 3.2-2, is the relaxation time for the equilibrium between the reactive and non-reactive conformations. It is related to a correlation function, $C_{\mathrm{N}}(t)$, by the fluctuation-dissipation theorem.[155] The normalized number correlation function $C_{\mathrm{N}}(t)$ is defined in Eq 3.2-4 and was used to calculate τ_{rxn}, see Eq 3.2-3.

$$k_{OO} = \frac{\langle N_{OO}\rangle}{\tau_{rxn}} \qquad \text{Eq 3.2-2}$$

$$\tau_{rxn} = \int_0^{+\infty} C_N(t)dt \qquad \text{Eq 3.2-3}$$

which has the form

$$C_N(t) = \frac{\langle \delta N_{OO}(t)\delta N_{OO}(0)\rangle}{\langle \delta N_{OO}^2\rangle} \qquad \text{Eq 3.2-4}$$

Here $\delta N_{\mathrm{OO}}(t) = N_{\mathrm{OO}}(t) - \langle N_{\mathrm{OO}}\rangle$ and $N_{\mathrm{OO}}(t) = 1$ for $d(\mathrm{O{-}O}) \leq 4.0$ Å and $N_{\mathrm{OO}}(t) = 0$ for $d(\mathrm{O{-}O}) > 4.0$ Å. Note that $\langle \delta N_{\mathrm{OO}}^2\rangle = \langle N_{\mathrm{OO}}\rangle - \langle N_{\mathrm{OO}}\rangle^2$. The statistical error of the evaluation was taken into account following the approach of Zwanzig and Ailawadi.[155, 156] In the calculation of the relaxation time τ_{rxn} the negative values of $C_N(t)$, that occur for $t > 1.4$ ns, were neglected since they were becoming artificially large with increasing delay times. Neglecting these negative values of $C_N(t)$ means that the computed value of 0.3 ns for the relaxation time, is an upper limit. The average fraction of conformations $\langle N_{OO} \rangle$ with the O–O distance less than 4 Å was determined to be equal to 0.027 (Table 3.2-6). Using this value and the τ_{rxn} from Eq 3.2-3, the estimated value of k_{OO} was calculated to be $(8.5 \pm 0.5) \times 10^7$ s^{-1} (from Eq 3.2-2). The formation rate constant k_{OO} calculated for all simulations performed for **(S,S)-BP-DKP-Tyr** (different starting configurations and solvents) varied from 8.5×10^7 s^{-1} to 1.3×10^8 s^{-1}. The calculated rate constants k_{OO} are found to be about 5 times larger than the experimental value of the intramolecular HAT, k_H (see Table 3.2-3). One possible explanation for this discrepancy might be that HAT occurs from the triplet state whereas the parameters used in MD are defined for the ground state. To get a better approximation of what might be happening in a triplet state reaction, Mulliken charges for the lowest-energy triplet state of **(S,S)-BP-DKP-Tyr** were calculated using the Gaussian03 package. Subsequently, these charges were used as the initial parameters in further MD simulations. The comparison of the pair distribution function of the carbonyl/hydroxylic group distance d(O–O) for simulations performed with charges for ground state and triplet state revealed that close contact of the reactive moieties is less favorable when charges were applied for the triplet state (Figure 3.2-26a). This is likely the result of the diminished n-electron density on the carbonyl oxygen which decreased the attractive interaction with the OH group from the tyrosine. The rate constant of the close-contact formation between the reacting moieties, k_{OO}, evaluated from the MD simulations using charges for the triplet state was equal to $(3 \pm 0.1) \times 10^7$ s^{-1}, which is in good agreement with the experimental data. This also clearly identifies the triplet to be the dominant reactive state.

3.2.2.2.2.3 **Evaluation of the spin-spin coupling constants**

The molecular-dynamics simulations were finally combined with the DFT calculations in order to calculate the $^3J(H^{\alpha}–H^{\beta(S/R)})$ spin-spin coupling constants values for the cyclic dyads: **(S,S)-BP-DKP-Tyr** and **(S,R)-BP-DKP-Tyr** (see notation of hydrogen atoms in Figure 3.2-27). The theoretical values were compared with the experimental data obtained from the NMR and NOE (2D Nuclear Overhauser Enhancement) spectra. The possibility of comparing theoretically calculated values with those obtained from the NMR and NOE experiments provides a way of verifying the reliability of the MD simulations. In addition, the procedure of combining the MD simulations with the DFT calculations in order to match the experimental values of the spin-spin coupling constants is a new technique, and it was of interest to validate this approach.

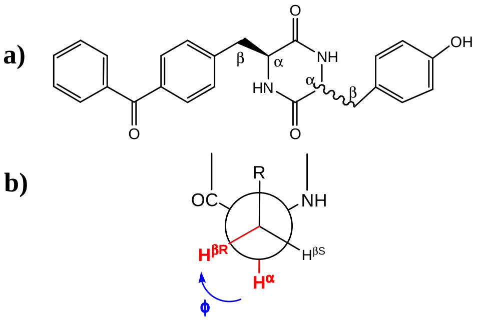

Figure 3.2-27 a) Assignment of hydrogen atoms in the Tyr and BP moieties of BP-DKP-Tyr dyads and b) Newman projection defining the H^{α}–C–C–H^{β} dihedral angle ϕ.

^{1}H NMR spectra were recorded at 200/400 MHz in per-deuterated dimethylsulfoxide ([D6]-DMSO). Assignments of ^{1}H resonances were based on two-dimensional homo and heteronuclear NMR techniques. An unambiguous assignment of the strongly overlapping β-proton resonances of the BP and the Tyr residues was accomplished by careful inspection of NOE spectra. The NMR analyses have been carried out by Hörner from the "Institut für Chemie, Technische Universität Berlin".

In order to theoretically match the experimental vicinal coupling constants between the nuclear spins of the diastereotopic β-protons and the α-proton $^3J(H^{\alpha}–H^{\beta R})$ and $^3J(H^{\alpha}–H^{\beta S})$, it was necessary to account for the strong dependence of $^3J(H^{\alpha}–H^{\beta(S/R)})$ on the dihedral angle H^{α}–C–C–$H^{\beta R/S}$.[157] In order to do this, the methodology of calculating the spin-coupling constants incorporated an analysis for determining the probability distribution of the dihedral angle H^{α}–C–C–$H^{\beta R/S}$ as followed by long time MD simulations. Figure 3.2-28b,d, Figure 3.2-30b,d, Figure 3.2-32b,d and Figure 3.2-34b,d summarize the time variation of the dihedral angles H^{α}–C–C–$H^{\beta R/S}$ within 100-ns simulation time windows for the Tyr and BP side chains of the dyads **(S,S)-BP-DKP-Tyr** and **(S,R)-BP-DKP-Tyr**. From these figures it can be seen that the dihedral angles for the BP and Tyr side chains of both dyads do not cover the whole range of 360 degrees. These dihedral angles adopt limited values during the simulations, e.g. the tyrosine side chain of **(S,S)-BP-DKP-Tyr** populates principally only the dihedral angle H^{α}–C–C–$H^{\beta R}$ from the ranges: -155 – (-180), 155 – 180, -35 – (-85) (Figure 3.2-28b) and the dihedral angle H^{α}–C–C–$H^{\beta S}$ from the ranges: 35 – 85, -35 – (-85) (Figure 3.2-28d).

DFT methods were afterwards used to compute spin-spin coupling constants for appropriately extracted structures (sets of Cartesian coordinates) from the MD simulations. The procedure of choosing the coordinates, from which the spin-spin coupling constants were obtained, was as follow. Dihedral angles were divided into 8 ranges of 10 or 15 degrees. Then, for each angular range, at least one configuration with a dihedral angle lying in the middle of that range was chosen. In this manner, the chosen configurations covered the whole range of the dihedral angle H^{α}–C–C–$H^{\beta R/S}$ adopted during the MD simulation.

NMR data reflect the averaged conformational preferences of the compound in solution. Thus, in order to theoretically calculate the spin-spin coupling constants that can be compared with experimental values, it is necessary to take into account the probability of the dyads to adopt certain dihedral angles. The MD-computed weights for all dihedral angles H^{α}–C–C–$H^{\beta R/S}$ in the chosen ranges are displayed in Figure 3.2-28a,c, Figure 3.2-30a,c, Figure 3.2-32a,c and Figure 3.2-34a,c. Spin-spin coupling constants with large weights contribute more to the weighted mean, e.g. from the range 50 – 60 degrees from the Figure 3.2-28c, than do elements with a small weight, e.g. from the range 35 – 50 from the same Figure.

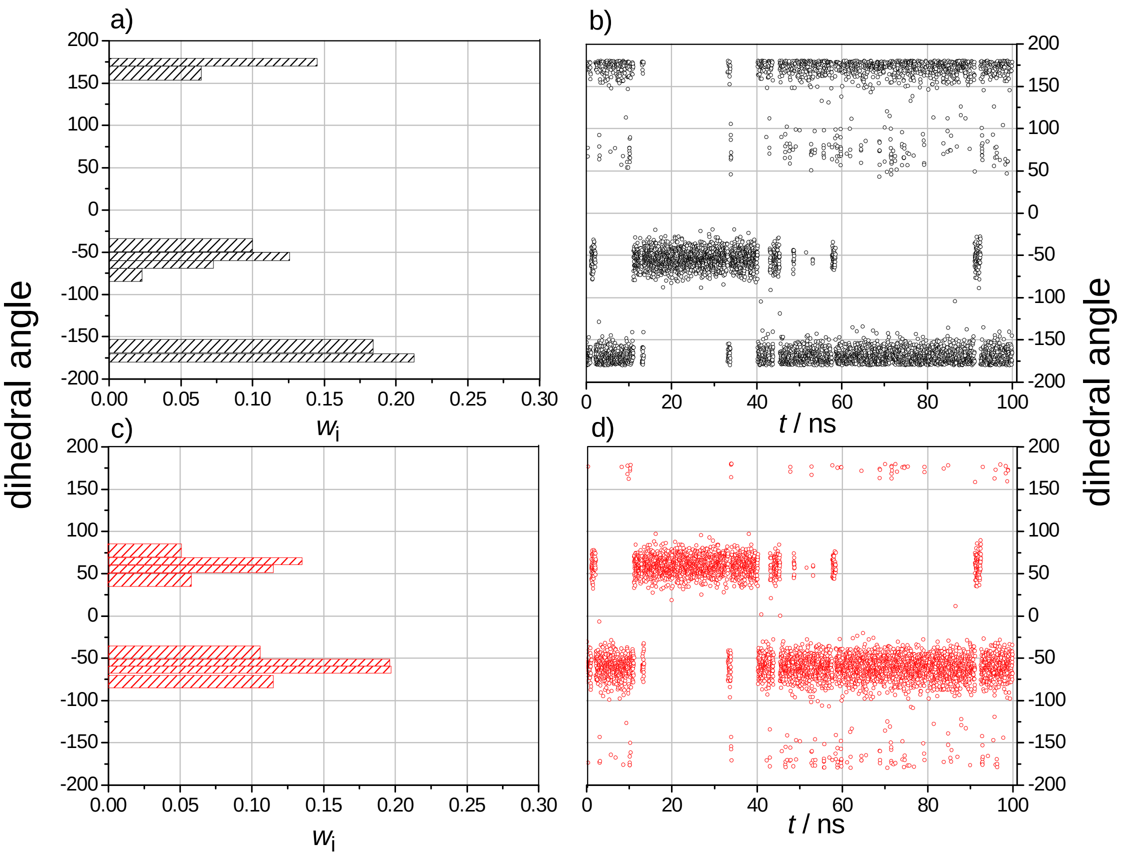

Figure 3.2-28 Long-time molecular-dynamics simulations for dyad **(S,S)-BP-DKP-Tyr**: time variation of dihedral angles of the Tyr side chain: b) the H^{α}–C–C–$H^{\beta R}$; d) H^{α}–C–C–$H^{\beta S}$; representation of the MD-computed weighting for the a) H^{α}–C–C–$H^{\beta R}$ dihedral angle c) H^{α}–C–C–$H^{\beta S}$ dihedral angle for the selected ranges.

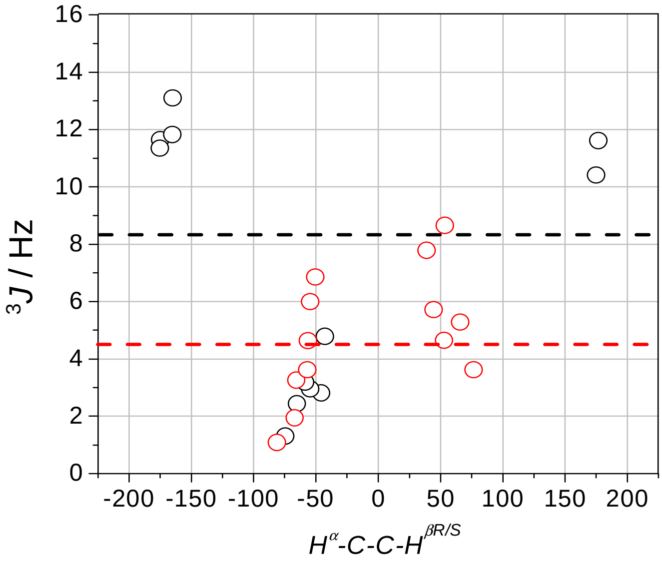

Figure 3.2-29 Computed $^{3}J(H^{\alpha}–H^{\beta(S/R)})$ spin-spin coupling constants of the Tyr side chain of **(S,S)-BP-DKP-Tyr** as a function of dihedral angle: H^{α}–C–C–$H^{\beta S}$ (red symbols), H^{α}–C–C–$H^{\beta R}$ (black symbols). Dashed lines indicate the theoretically obtained spin-coupling constants from the weighted average Eq 3.2-5: $^{3}J(H^{\alpha}–H^{\beta S})$ – red line, $^{3}J(H^{\alpha}–H^{\beta R})$ – black line.

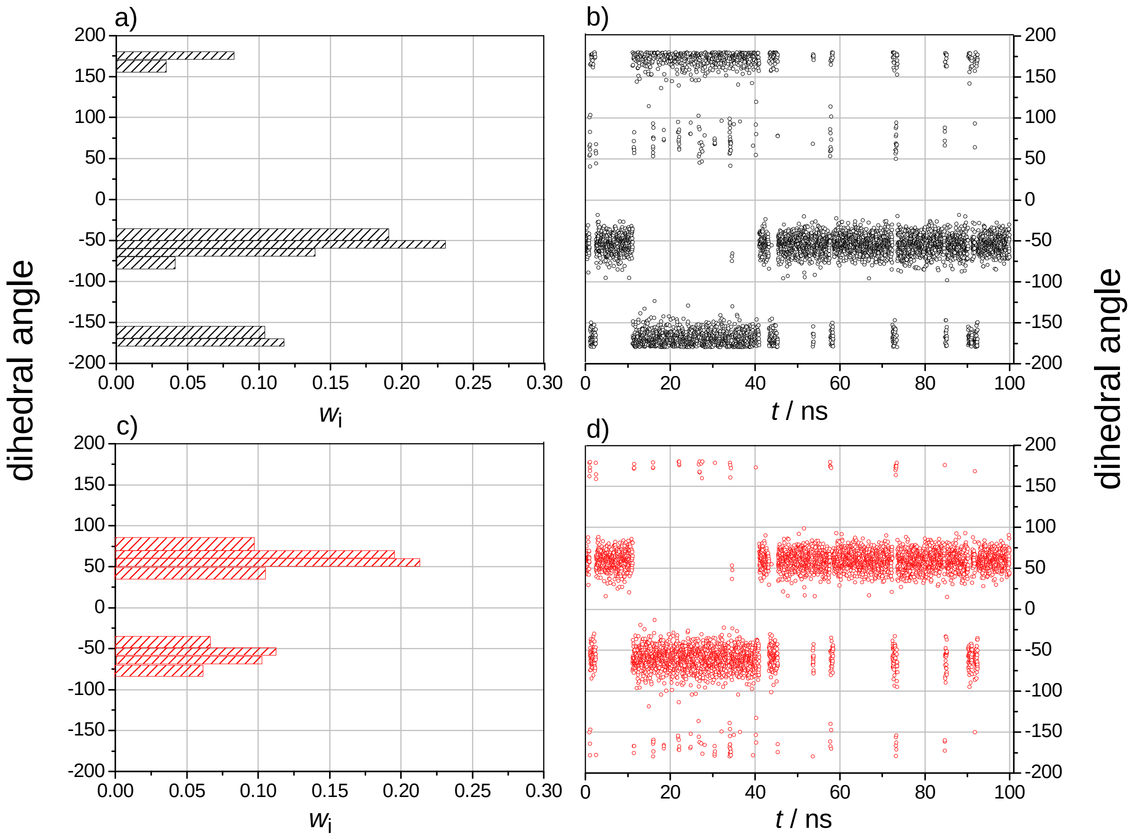

Figure 3.2-30 Long-time molecular-dynamics simulations for dyad **(S,S)-BP-DKP-Tyr**: time variation of dihedral angles of the BP side chain: b) the H^{α}–C–C–$H^{\beta R}$; d) H^{α}–C–C–$H^{\beta S}$; representation of the MD-computed weighting for the a) H^{α}–C–C–$H^{\beta R}$ dihedral angle c) H^{α}–C–C–$H^{\beta S}$ dihedral angle for the selected ranges.

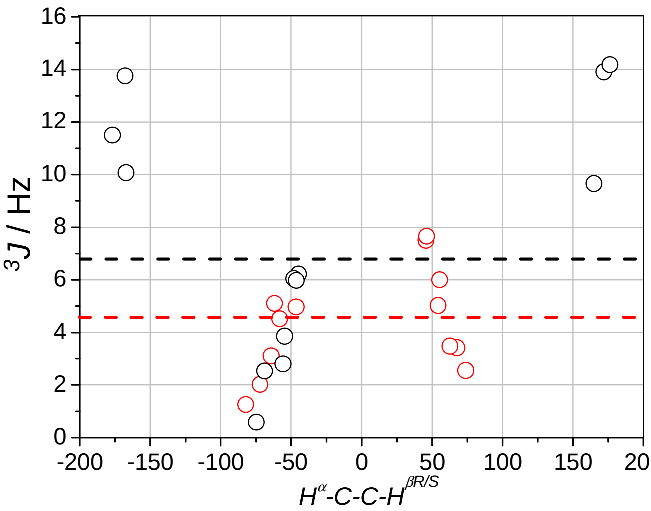

Figure 3.2-31 Computed $^3J(H^{\alpha}–H^{\beta(S/R)})$ spin-spin coupling constants of the BP side chain of **(S,S)-BP-DKP-Tyr** as a function of dihedral angle: H^{α}–C–C–$H^{\beta S}$ (red symbols), H^{α}–C–C–$H^{\beta R}$ (black symbols). Dashed lines indicate the theoretically obtained spin-coupling constants from the weighted average Eq 3.2-5: $^3J(H^{\alpha}–H^{\beta S})$ – red line, $^3J(H^{\alpha}–H^{\beta R})$ – black line.

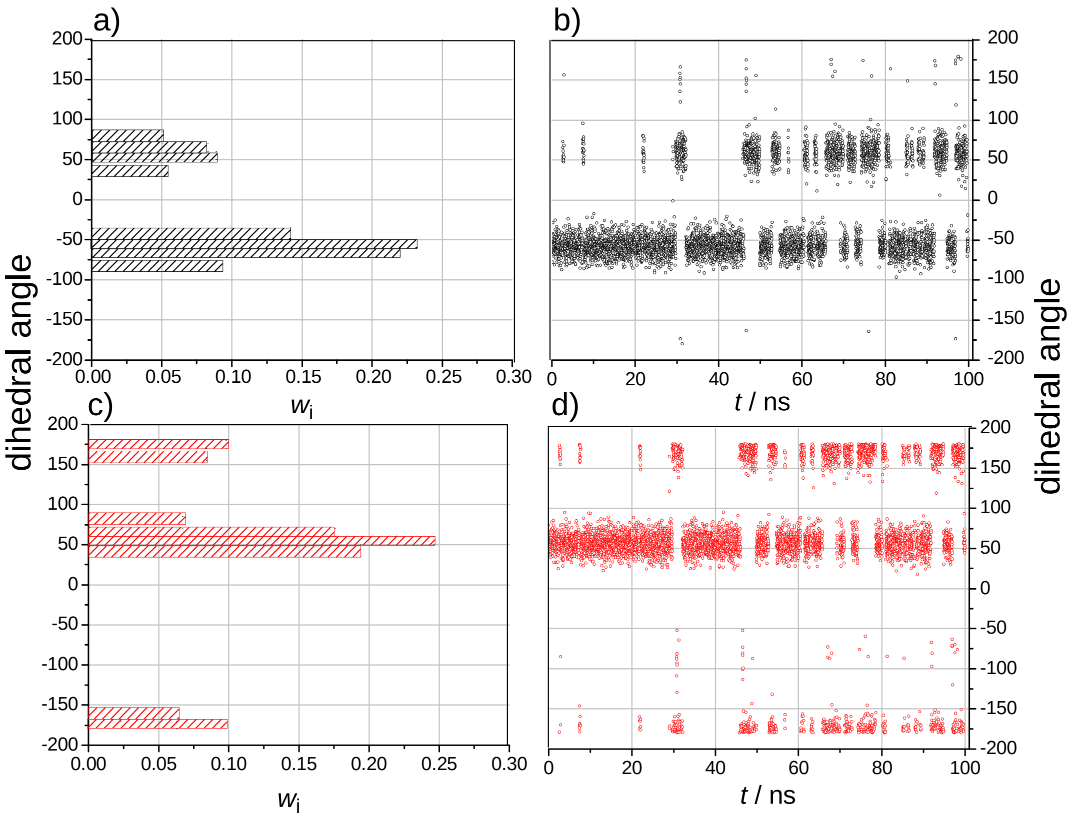

Figure 3.2-32 Long-time molecular-dynamics simulations for dyad **(S,R)-BP-DKP-Tyr**: time variation of dihedral angles of the Tyr side chain: b) the H$^{\alpha}$–C–C–H$^{\beta R}$; d) H$^{\alpha}$–C–C–H$^{\beta S}$; representation of the MD-computed weighting for the a) H$^{\alpha}$–C–C–H$^{\beta R}$ dihedral angle c) H$^{\alpha}$–C–C–H$^{\beta S}$ dihedral angle for the selected ranges.

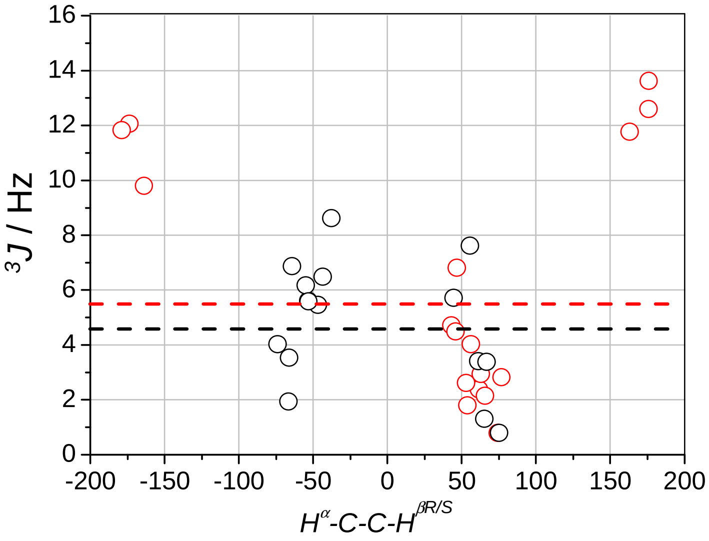

Figure 3.2-33 Computed ^3J(H$^{\alpha}$–H$^{\beta(S/R)}$) spin-spin coupling constants of the Tyr side chain of **(S,R)-BP-DKP-Tyr** as a function of dihedral angle: H$^{\alpha}$–C–C–H$^{\beta S}$ (red symbols), H$^{\alpha}$–C–C–H$^{\beta R}$ (black symbols). Dashed lines indicate the theoretically obtained spin-coupling constants from the weighted average Eq 3.2-5: ^3J(H$^{\alpha}$–H$^{\beta S}$) – red line, ^3J(H$^{\alpha}$–H$^{\beta R}$) – black line.

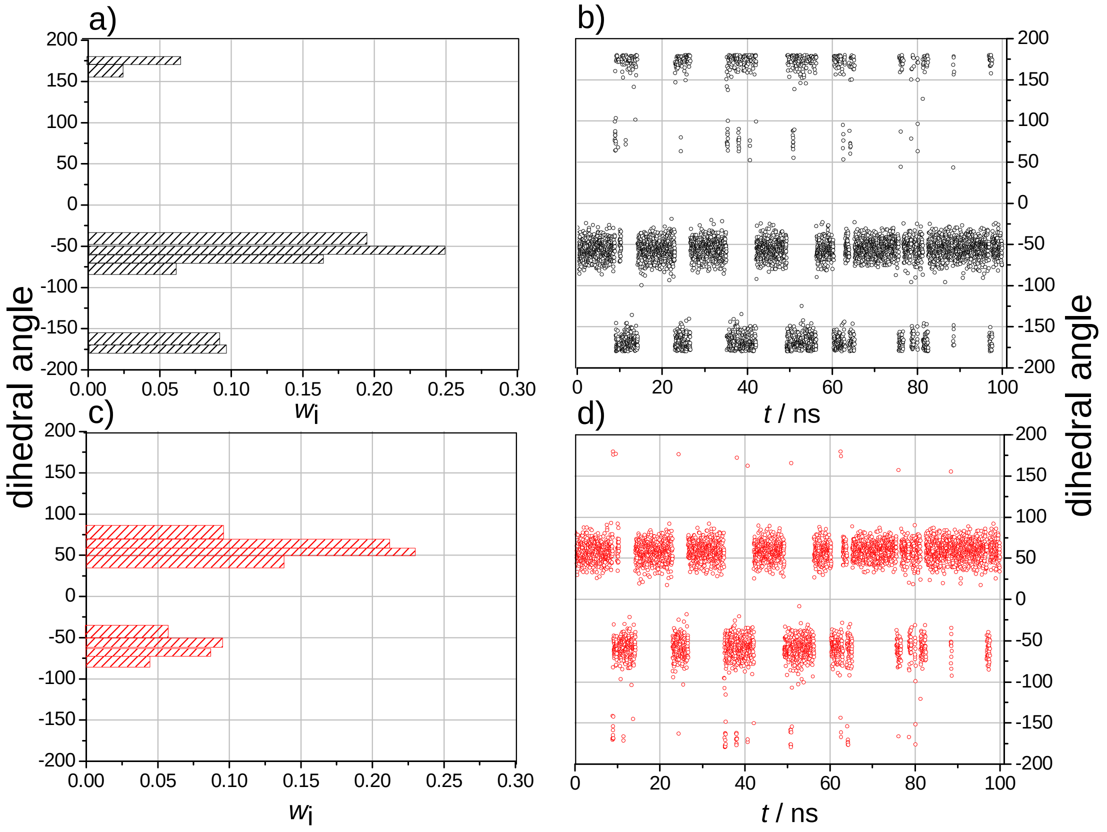

Figure 3.2-34 Long-time molecular-dynamics simulations for dyad **(S,R)-BP-DKP-Tyr:** time variation of dihedral angles of the BP side chain: b) the H^{α}–C–C–$H^{\beta R}$; d) H^{α}–C–C–$H^{\beta S}$; representation of the MD-computed weighting for the a) H^{α}–C–C–$H^{\beta R}$ dihedral angle c) H^{α}–C–C–$H^{\beta S}$ dihedral angle for the selected ranges.

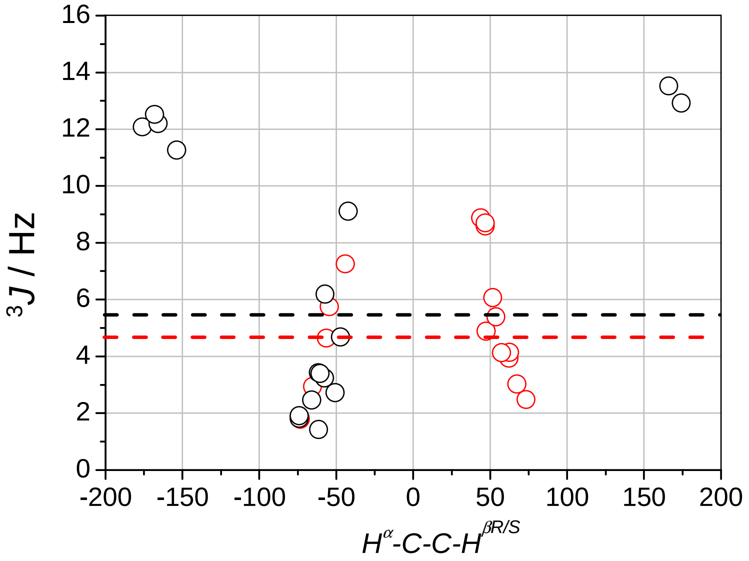

Figure 3.2-35 Computed $^3J(H^{\alpha}–H^{\beta(S/R)})$ spin-spin coupling constants of the BP side chain of **(S,R)-BP-DKP-Tyr** as a function of dihedral angle: H^{α}–C–C–$H^{\beta S}$ (red symbols), H^{α}–C–C–$H^{\beta R}$ (black symbols). Dashed lines indicate the theoretically obtained spin-coupling constants from the weighted average Eq 3.2-5: $^3J(H^{\alpha}–H^{\beta S})$ – red line, $^3J(H^{\alpha}–H^{\beta R})$ – black line.

At the selected geometries, indirect spin-spin coupling constants $^3J(\mathrm{H}^{\alpha}\text{–}\mathrm{H}^{\beta(S/R)})$ were computed using DFT by analytic methods[158, 159] contained in the Gaussian 03 suite of programs. The B3LYP functional was chosen since it has been shown to produce reliable three-bond couplings.[160] While such interactions are usually dominated by the Fermi contact term, all components of the couplings were calculated but only the total value reported (Table 3.2-7). The contracted basis set employed, denoted [5s2p1d,3s1p],[161] achieves a balance between economical computational cost and numerical reliability in systems of the size tackled here. The calculations were performed by Ian Carmichael from the Radiation Laboratory, University of Notre Dame. The computed values of $^3J(\mathrm{H}^{\alpha}\text{–}\mathrm{H}^{\beta(S/R)})$ spin-spin coupling constants for the Tyr and BP side chains of **(S,S)-BP-DKP-Tyr** are plotted in Figure 3.2-29 and Figure 3.2-31, respectively. The points overlap in Figure 3.2-29 and Figure 3.2-31 in the range of -35 – (-85) degrees, since based on the MD simulations, both dihedral angles H^{α}-C–C–$\mathrm{H}^{\beta S}$ and H^{α}-C–C–$\mathrm{H}^{\beta R}$ for the Tyr- and as well as for BP-side chain are populated in that range of dihedral angles. Figure 3.2-33 and Figure 3.2-35 present the analogously computed values of $^3J(\mathrm{H}^{\alpha}\text{–}\mathrm{H}^{\beta(S/R)})$ spin-spin coupling constants for the Tyr and BP side chains of **(S,R)-BP-DKP-Tyr**, respectively. The plots of the spin-spin coupling constants as a function of dihedral angle H^{α}–C–C–$\mathrm{H}^{\beta R/S}$ have the same features for both of the BP side-chains of **(S,S)-BP-DKP-Tyr** and **(S,R)-BP-DKP-Tyr** (Figure 3.2-31, Figure 3.2-35), respectively. On the other hand, the Tyr side-chain dihedral angles H^{α}–C–C–$\mathrm{H}^{\beta R/S}$ were adopting different values for **(S,S)-BP-DKP-Tyr** and **(S,R)-BP-DKP-Tyr**. This can be attributed to the change in the chiral center configurations on the Tyr side (Figure 3.2-28b,d, Figure 3.2-32b,d).

In order to calculate the spin-spin coupling constants, which could be compared with the values obtained *via* NMR, weighted averages had to be computed:

$$^3J\left(H^{\alpha}-H^{\beta R/S}\right) = \frac{\sum_{i=1}^{8} w_i \cdot {}^3J\left(H^{\alpha}-H^{\beta R/S}\right)_i}{\sum_{i=1}^{8} w_i} \qquad \text{Eq 3.2-5}$$

where:

w_i – MD-computed weighting for the dihedral angle in the *i*-th range;

$^3J\left(H^{\alpha}-H^{\beta R/S}\right)_i$ – arithmetic average of all the DFT calculated *J*'s for structures having dihedral angles H^{α}–C–C–$\mathrm{H}^{\beta R/S}$ in the *i*-th range.

The comparison of the theoretically obtained spin-spin coupling constants from the weighted average (Eq 3.2-5) with the experimental values is presented in Table 3.2-7. In addition, calculated spin-spin coupling constants based on MD-simulations and the DFT method are plotted as dashed lines in Figure 3.2-29, Figure 3.2-31, Figure 3.2-33, Figure 3.2-35. Based on the analysis of the calculated and experimentally obtained spin-spin coupling constants, it can be stated that the agreement is satisfactory. Significant discrepancy between the spin-spin coupling constants was observed only for the $^{3}J(\mathrm{H}^{\alpha}–\mathrm{H}^{\beta R})$ of the Tyr side-chain of **(S,S)-BP-DKP-Tyr**. This might be the result on an over-estimation of the population of the conformer $\mathbf{E_N}$ in the Tyr side chain from the MD simulation. However, in general the trends in the calculated spin-spin coupling constants were preserved, namely higher experimental values corresponds to higher calculated values. In conclusion, it can be stated that MD-simulations reflect quite well the conformational preferences of the cyclic DKP-based dyads.

Table 3.2-7 Comparison of the theoretically obtained spin-spin coupling constants $^{3}J(\mathrm{H}^{\alpha}–\mathrm{H}^{\beta(S/R)})$ with the data obtained from NMR and NOE experiments for dyad **(S,R)-BP-DKP-Tyr** and **(S,S)-BP-DKP-Tyr.**

	(S,S)-BP-DKP-Tyr				**(S,R)-BP-DKP-Tyr**			
	Tyr side-chain		**BP side-chain**		**Tyr side-chain**		**BP side-chain**	
	$^{3}J(\mathrm{H}^{\alpha}\mathrm{H}^{\beta R})$ /Hz	$^{3}J(\mathrm{H}^{\alpha}\mathrm{H}^{\beta S})$ /Hz	$^{3}J(\mathrm{H}^{\alpha}\mathrm{H}^{\beta R})$ /Hz	$^{3}J(\mathrm{H}^{\alpha}\mathrm{H}^{\beta S})$ /Hz	$^{3}J(\mathrm{H}^{\alpha}\mathrm{H}^{\beta R})$ /Hz	$^{3}J(\mathrm{H}^{\alpha}\mathrm{H}^{\beta S})$ /Hz	$^{3}J(\mathrm{H}^{\alpha}\mathrm{H}^{\beta R})$ /Hz	$^{3}J(\mathrm{H}^{\alpha}\mathrm{H}^{\beta S})$ /Hz
$^{3}\mathbf{J}_{\mathbf{calc.}}$	8.4[a]	4.5[b]	6.8[a]	4.5[b]	4.5[b]	5.5[c]	5.5[c]	4.7[b]
$^{3}\mathbf{J}_{\mathbf{exp.}}$[d]	5.5	4.8	7.2	4.8	3.4	4.6	5	3.8

[a] estimated error ± 0.9 Hz; [b] estimated error ± 0.1 Hz; [c] estimated error ± 0.6 Hz; [d] error ± 0.2 Hz.

3.2.2.3 Discussion

In this study the excited-state dynamics of **(S,R)-BP-DKP-Tyr** and **(S,S)-BP-DKP-Tyr** were taken as probes of structural effects on the efficiencies and rates of intramolecular hydrogen-atom transfer reactions.[147] The different steric constraints of the dyads were found to be reflected in the distinct dynamics of the dyads' triplet states. The dyads differ particularly in their dependencies on the medium, as is discussed in the following.

Intramolecular H-atom transfer in the triplet state of dyad **(S,R)-BP-DKP-Tyr** was found to be strongly solvent dependent with rate constants k_{H} ranging from $< 1 \times 10^{5}$ s^{-1} to 2×10^{7} s^{-1}. A similar range of triplet-state rate constants has recently been observed for the intramolecular HAT in the open-chain BP-Tyr dyad,[76] but these triplet HAT reactions in the open-chain congeners of **(S,R)-BP-DKP-Tyr** and **(S,S)-BP-DKP-Tyr** are generally faster by one to two orders of magnitude in any given solvent (Table 3.2-1).[75] Such solvent-driven changes in the bimolecular HAT reactions rates of phenols have generally been explained in terms of specific solvation effects on the phenol. These effects were named as Kinetic Solvent Effect (KSE). In particular, the previous work on the bimolecular HAT of phenols has shown that the rate constants can be correlated with the solvents' hydrogen-bond acceptor ability (see Chapter 1.3.1.1.1.2).[13-17, 69-71] That is, the logarithmic rate constants depended linearly on a single solvent parameter, namely on Abraham's H-bond acceptor ability,[70, 73] irrespective of the molecularity of the reaction.[75] However, the solvent dependence observed for **(S,R)-BP-DKP-Tyr** cannot be fully explained on the basis of solute-solvent interactions of the tyrosine moiety. Although, this single-parameter dependence of the intramolecular H-transfer reaction is adequate to explain the reactivity of the open-chain congeners of the cyclic **(S,R)-BP-DKP-Tyr** and **(S,S)-BP-DKP-Tyr**[75] (see Chapter 3.2.1.4), it is not sufficient to explain the difference in the reaction rate constants of the cyclic dyad **(S,R)-BP-DKP-Tyr**. These results on **(S,R)-BP-DKP-Tyr** show that, in contrast to the phenomenology of the KSE, which necessarily connects specific solvation with retarding effects, specific solvation can also accelerate the HAT reaction rates of phenols.

In the following the focus will first be on the data of dyad **(S,R)-BP-DKP-Tyr** displayed in Figure 3.2-36a,b with the red symbols.

Accordingly, a plot of the kinetic data for dyad **(S,R)-BP-DKP-Tyr** from Table 3.2-3 against the effective H-bond acceptor ability of the solvents (Figure 3.2-36a) exhibits two different regions that reflect the character of the solvents. HAT rates in non-protic solvents with weak effective H-bond donor abilities $\Sigma\alpha_2^H$ (red filled symbols in Figure 3.2-36a) are actually found to follow a linear dependence on $\Sigma\beta_2^H$ with a slope b = – 3.1 ($r^2 = 0.995$) and an intercept of 6.5. Thus, this dyad is another example where the slopes of the logarithmic intramolecular HAT rate constants *vs*. $\Sigma\beta_2^H$ plots are individual characteristics for each dyad, but not the characteristic of each H-atom donor as expected from the theory of the Kinetic Solvent Effect (see Chapter 1.3.1.1.1.2).[75, 76] The second region in Figure 3.2-36a is that formed by the protic solvents with significant H-bond donor abilities (red open symbols). The protic solvents seem to allow much higher rate constants when compared to their non-protic counterparts having similar H-bond acceptor abilities (nearly matching $\Sigma\beta_2^H$). For example, ethyl acetate and MeOH have almost the same H-bond acceptor ability, but the k_H values for **(S,R)-BP-DKP-Tyr** differ by a factor of 10. A similar example is the contrasting behavior of pure ACN and the ACN-H_2O (2:1v/v) mixture in which k_H values for **(S,R)-BP-DKP-Tyr** differ by a factor of 25. The possible reason for the large increase in the intramolecular hydrogen-atom rate constant in protic solvents might be due to a switch in the mechanism.

The decrease of the HAT rates with the H-bond acceptor ability of the non-protic solvents suggests that negligible intramolecular reactivity is expected for dyad **(S,R)-BP-DKP-Tyr** in solvents with $\Sigma\beta_2^H > 0.3$. However the data in Table 3.2-3 show that protic solvents with high values of $\Sigma\beta_2^H$ show significant reactivity in **(S,R)-BP-DKP-Tyr**.

In Figure 3.2-36b, data (from Table 3.2-3) are plotted *vs*. the H-atom donor ability $\Sigma\alpha_2^H$ which, with the exception of the chlorohydrocarbon solvents, show a linear correlation for dyad **(S,R)-BP-DKP-Tyr** with a positive slope of b = 2.3 ($r^2 = 0.977$) and an intercept of 5.2. That is, the reactivity increases with the strength of the solvent-solute interaction.

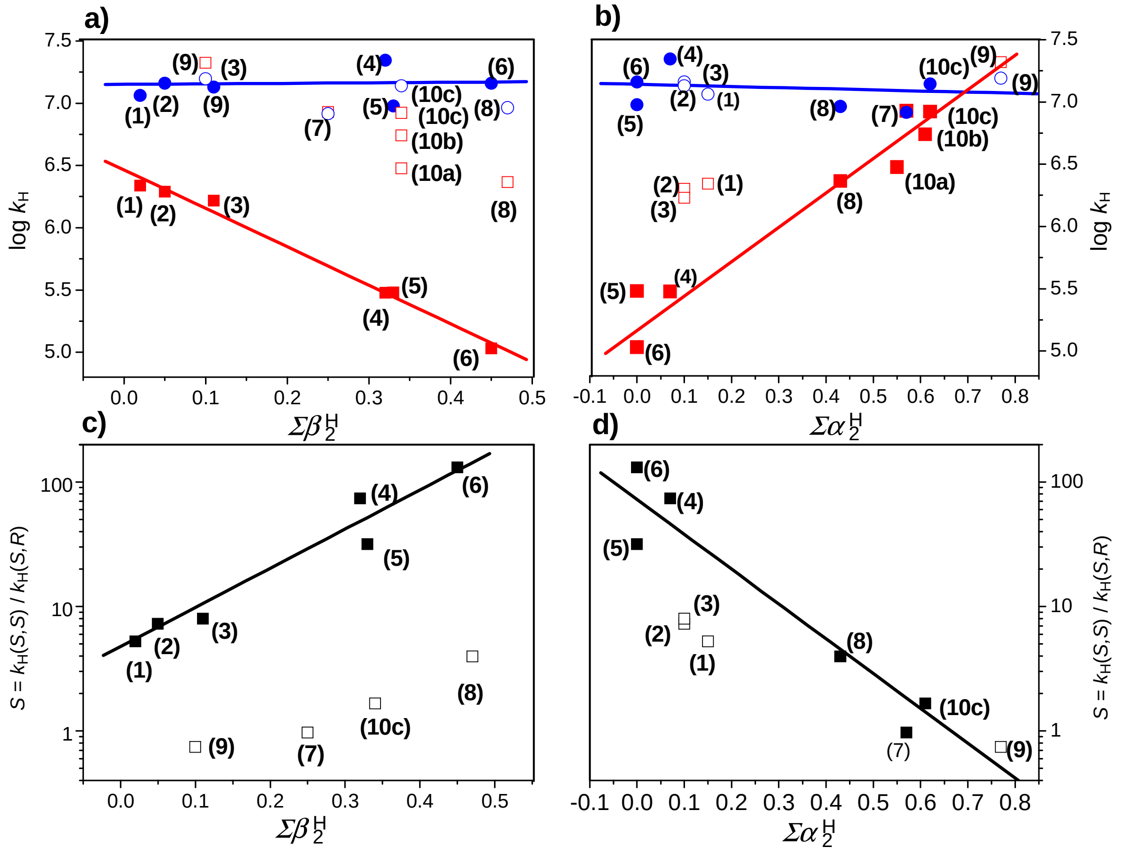

Figure 3.2-36 a) Plot of the H-atom transfer rate constants, log k_H against Abraham's *et al.* effective H-bond acceptor ability, $\Sigma\beta_2^H$, open symbols: protic solvents; filled symbols: non-protic solvents; b) plot of the H-atom transfer rate constants, log k_H, against Abraham's *et al.* effective H-bond donor ability, $\Sigma\alpha_2^H$; filled symbols: solvents with $\Sigma\beta_2^H \geq 0.25$; open symbols: solvents with $\Sigma\beta_2^H \leq 0.11$, red symbols: data for **(S,R)-BP-DKP-Tyr**, blue symbols: data for **(S,S)-BP-DKP-Tyr**, c) semilogarithmic plot of stereoselectivity of the H-atom transfer in the dyads as a function of the solvents H-bond acceptor ability; open symbols: protic solvents, d) semilogarithmic plot of stereoselectivity of the H-atom transfer in the dyads as a function of the solvents H-bond donor ability; open symbols: solvents with $\Sigma\beta_2^H \leq 0.11$, solvent code as in Table 3.2-3.

In summary, opposite effects were exerted by non-protic and protic solvents on the intramolecular H-transfer in the triplet state of dyad **(S,R)-BP-DKP-Tyr**. The relevant solvent parameters favoring efficient intramolecular hydrogen transfer for dyad **(S,R)-BP-DKP-Tyr** are the solvents' small values of their hydrogen-atom acceptor ability $\Sigma\beta_2^H$ and their high values of hydrogen-atom donor ability $\Sigma\alpha_2^H$. This was realized by HFIP, for example. The opposite behavior was seen in the poor reactivity of EtOAc which can be explained on the basis of its high $\Sigma\beta_2^H$ (0.45) and low $\Sigma\alpha_2^H$ (0.00). In conclusion, the solvent dependence of the cyclic dyad **(S,R)-BP-DKP-Tyr** sharply diverges from the behavior of its open-chain congener[75] (Chapter 3.2.1.4), but its solvent dependence largely coincides with the phenomenology observed recently for a more rigid open-chain dyad.[76] Obviously, the observed phenomenology of the kinetic solvent effect reflects structural parameters of the dyads. This becomes most evident from the behavior of the cyclic dyad **(S,S)-BP-DKP-Tyr** that lacks any significant dependence on the H-bonding properties of the solvent; this case is described next.

The plots of the logarithmic rate constants *vs*. $\Sigma\beta_2^{H}$ and $\Sigma\alpha_2^{H}$ for dyad **(S,S)-BP-DKP-Tyr** exhibit no significant variance, neither with the solvents' H-bond accepting nor with H-bond donating properties (blue symbols in Figure 3.2-36a,b). Actually, the slopes are close to zero in both cases, which means that the rate constants for H-atom transfer for the dyad **(S,S)-BP-DKP-Tyr** are independent of these parameters. Accordingly, the stereoselectivity of the triplet HAT in **(S,R)-BP-DKP-Tyr** and **(S,S)-BP-DKP-Tyr**, as expressed as the ratio of the rate constants and shown in Figure 3.2-36c,d, directly reflects the solvent dependence of the HAT of **(S,R)-BP-DKP-Tyr**. The sharp decrease of the H-atom transfer reaction rates for dyad **(S,R)-BP-DKP-Tyr** in non-protic solvents with hydrogen-bond acceptor tendencies, and the sharp increase of the reaction rates in protic solvents with their hydrogen-bond donor ability are the dominant sources of the solvent dependence on the stereoselectivity (Figure 3.2-36c,d). These findings are in contrast to results of the open-chain congener of the cyclic dyads where the stereoselectivity of the triplet HAT process was solely dependent on $\Sigma\beta_2^{H}$, irrespective of the protic or non-protic character of the solvents (Chapter 3.2.1.4).[75]

In conclusion, the behavior of the two cyclic-bridged dyads was studied in 12 different solvents and mixtures. It was shown that the ability of the solvent to act as a hydrogen-bond donor and/or an acceptor plays an important role in determining the hydrogen-atom transfer rate constants only in one of the two epimers in this study.

The contrasting solvent dependencies of the H-atom transfer rate constants for dyad **(S,R)-BP-DKP-Tyr** in protic and non-protic solvents can be interpreted as being due to fundamentally different H-atom transfer mechanisms in the respective solvents. In favor of this interpretation are the significant enhancement of the reaction rates in protic solvents and the presence of the $BP^{\bullet-}$ radical anion in an ACN-H_2O (1:1 v/v) mixture. In addition, it is important to note that the intercepts of the single-solvent parameter regressions in Figure 3.2-36a,b (red lines) differ by more than one order of magnitude. These values represent the isolated and solvent-independent HAT rate constants, and, thus, they should not vary if there were only a single common mechanism of H-atom transfer in protic and non protic solvents.[76]

Moreover, molecular-dynamics simulations and DFT results[148] showed that conformations with long distances (> 8 Å) between their reactive moieties are the most favorable ones in solutions (Table 3.2-5 and Table 3.2-6). The H-transfer rates in non-protic solvents are limited by the accessibility of free, that is, not H-bonded, tyrosine. In contrast, the kinetic data obtained in protic media follow a correlation with the H-bond donor ability of the solvent. Thus, it seems that for intramolecular HAT reactions, the solvation of the abstracting species cannot be neglected.

Several pieces of evidence favor electron-transfer involving pathways that are driven by specific H-bonding interactions of the electron-acceptor with the protic solvent. An electron-transfer pathway in protic solvents has been observed recently for a sterically restricted BP-Tyr dyad.[162] In this structure, the directionality of the benzamide linker of the dyad effectively excludes close intramolecular contacts. Studies of the solvent effects on the nanosecond-transient dynamics and on the chemically induced dynamic nuclear polarization (CIDNP), following LFP, has shown that in protic solvents the H-abstraction reaction was initiated by ET.[162] Similar conclusions have been drawn from studies of the bimolecular ET between anisole and ^{3}BP where dramatic activating effects of strongly H-bonding solvents on the one-electron oxidation of anisole by ^{3}BP show that the reactivity of an electronically excited molecule can be greatly enhanced by changes in the nature of the solvent (Chapter 3.6).[18]

In contrast to the above discussion, neither of the rate-determining effects of solvation seems to be of importance for the HAT in the dyad **(S,S)-BP-DKP-Tyr** which exhibits little solvent variation in its k_H rate constants. The ratio of the highest rate constants k_H, obtained in ACN, and the smallest, determined in TFE, was just 2.4 for the triplet dyad **(S,S)-BP-DKP-Tyr**. The absence of a marked solvent dependence, which was observed for all other dyads,[65, 75, 76] is a noteworthy finding.

The observation that the triplet state of dyad **(S,S)-BP-DKP-Tyr** was quenched slightly slower in solvents with higher viscosity, which leads to smaller values of the k_H (TFE and benzonitrile, see Table 3.2-3), points to the importance of the intramolecular dynamics. The observation of a greatly diminished triplet reactivity of **(S,S)-BP-DKP-Tyr** in highly viscous *tert*-butanol further corroborates viscosity as another source of kinetic diversity. That is, the dynamics of the molecular motions bringing dyad **(S,S)-BP-DKP-Tyr** to its reactive state appear to be rate determining in all solvents, which implies that the intrinsic HAT reaction rate of the dyad, irrespective of its state of solvation, markedly exceeds the rates of the intramolecular motions.

In order to check whether molecular dynamics are the rate-determining steps of the intramolecular HAT of dyad **(S,S)-BP-DKP-Tyr**, the rate constant for the formation of close-contact conformations, k_{OO}, was calculated on the basis of the MD-trajectories (see Chapter 3.2.2.2.2.2). The resulting good agreement between the thus rate constant and the experimental value of the intramolecular H-atom rate constant in ACN (see Table 3.2-3) indicates that intramolecular dynamics are the rate-determining step of the intramolecular HAT in this case.

As discussed above (Chapter 3.2.2.2.1), DFT calculations in a continuum solvent model suggested the presence of a number of different conformers of **(S,S)-BP-DKP-Tyr** with similar energies. In particular, calculations in the presence of an ACN continuum highlighted the competition between a conformer with a short O–O distance as a probable candidate for the quenching geometry with other, more extended conformers of similar energy. This situation was put to the test by molecular-dynamics simulations. Based on the good agreement between the spin-spin coupling constants measured by NMR and calculated from MD simulations/DFT calculations, it can be concluded that conformational preferences found in MD simulations are reliable (Chapter 3.2.2.2.2.3). The simulations show that conformers which allow for close contacts between the reacting centers have significant steric constraints. While the energetic differences between all of the side-chain rotamers in ACN appear to be rather small in DTF calculations (< 2.1 kcal/mol, Table 3.2-4), other, intrinsically non-reactive, structures of dyad **(S,S)-BP-DKP-Tyr** with only one aromatic side chain folded over the DKP ring are certainly favored as became evident from MD data (Figure 3.2-24). Thus, significant intramolecular rearrangements have to precede the reaction and can be even rate determining, as soon as the intrinsic HAT rate exceeds the rate of formation of the quenching geometry. This condition actually seems to hold for dyad **(S,S)-BP-DKP-Tyr**. As stressed before, the long-term dynamics simulations concerning this dyad indicated the formation of close-contact structures. In particular, the rate of its formation in an ACN continuum with $k_{OO} = (3 \pm 0.1) \times 10^{7}\ s^{-1}$ (computed from Eq 3.2-2 to Eq 3.2-4) shows good agreement with the observed rate constant of the HAT in this solvent (see Table 3.2-3).

In summary, effects of specific solvation as well as effects of the bulk viscosity were identified as important controls of the intramolecular reactivity. In contrast to the open-chain analogues, the limited intramolecular mobility imposed by the rigid peptide environment of the diketopiperazine spacer translates into strongly contrasting solvent effects observed with the individual epimers. Most interestingly the presented experimental and theoretical results imply that the kinetic effects that are imposed by the solvent and those that are due to the dyad structure are correlated with each other and that they must not be treated separately.

3.3 Benzophenone–methionine bichromophore systems

In the following sections, the mechanisms of the photosensitized oxidation of the synthesized model bichromophoric compounds containing covalently linked benzophenone and methionine will be presented and discussed. The investigation addresses quantitatively the parameters that influence the quenching of the triplet state in these dyads and the quantum yields of substrate disappearance. The presence of the covalently bound, electron donating residue affects the lifetime of the triplet state of benzophenone in a way strongly controlled by the connectivity. So, the diastereomeric pairs with variations in conformational freedom were studied by laser flash and steady-state photolysis. The experimental results have been correlated with theoretical calculations and molecular-dynamics simulations. In addition, special attention was also paid to issues such as: the effect of chiral-center configurations on the diastereo-selectivity of the quenching process and the influence of the solvent on the reactivity of the compounds. The structures of the investigated compounds were analogues of the benzophenone-tyrosine dyads in which tyrosine were substituted by methionine. In the first part of the study, the two chromophores were connected *via* an open-chain peptide linker. This flexible diastereomer produced, however, only small stereo effects. Therefore, in the second part of this work, again a more rigid linker, namely, DKP was introduced into the benzophenone-methionine pair. As before in the case of BP-Tyr dyadsthese DKP-linked BP-Met dyads will in the following, for abbreviation, be denoted as “cyclic” dyads.

3.3.1 Open chain diastereoisomers

3.3.1.1 Nanosecond flash photolysis: spectral and kinetic analysis

The excited-state dynamics of **(S,S)-BP-Met** and **(R,S)-BP-Met** were studied by means of nanosecond-laser photolysis in two different solvents: ACN and TFE, and one solvent mixture: ACN-H_2O (1:1 v/v). The work addressed, in particular, the diastereo-selectivity and the medium effects on methionine’s role in the triplet quenching. This stereodifferentiation was investigated through a comparison of the reactivities of the two dyads in the respective solvents. In order to avoid bimolecular-quenching processes, that could be observed for these compounds, excitation at 266 nm was used in addition to excitation at 337 nm. The more intense absorption of the compounds at

266 nm allowed to operate with lower dyad concentrations, which, in turn, permitted an exclusive study of the intramolecular processes.

For the bichromophores **(S,S)-BP-Met** and **(R,S)-BP-Met**, in any solvent, the transient decays of the initial signals were very rapid. Triplet lifetimes were obtained from mono- or biexponential fits to the transient decays at 630 and 520 nm, respectively and found to vary from 30 ns to 56 ns for **(S,S)-BP-Met**, and from 13 ns to up to 22 ns for **(R,S)-BP-Met** depending on the nature of the solvent. In both systems the triplet lifetimes of the compounds decreased by a factor less than two on going from non-protic to protic solvents. In all cases, the triplet state was identified as the dominate intermediate in the early transient spectra through its characteristic absorption bands with maxima at 325 nm and 525 nm, in addition to a long-wavelength absorption above 600 nm (Figure 3.3-1a).

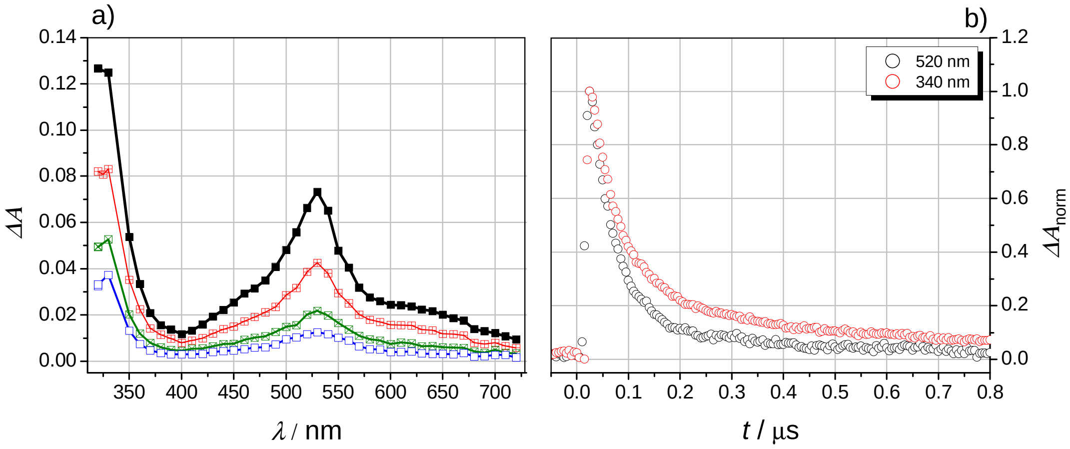

Figure 3.3-1 Summary of the results obtained during laser flash photolysis at 337 nm of a deoxygenated solution of **(S,S)-BP-Met** in dry ACN; a) transient absorption spectra: time delays after flash (from top to bottom): 30, 60, 100, 150 ns; b) normalized decay profiles of the transient absorption monitored at 520 nm (black) and 340 nm (red).

Although the triplet decay was very rapid and, in fact, shorter than the triplet decay of the monochromophoric reference compound by a factor of greater than 100, the triplet decays of both dyads in ACN were not accompanied by any measurable spectral evolution (Figure 3.3-1a). In addition, only small differences in the decay profiles monitored at distinct wavelengths were observed (Figure 3.3-1b).

In the case of **(R,S)-BP-Met** the transient absorption spectrum above 560 nm was strongly disturbed by a strong emission signal with the maximum at 590 nm (Figure 3.3-2). That emission could be attributed to the fluorescence of excited ketyl radicals, which was reported to have a maximum at 582.1 nm.[163] Fluorescence of the excited ketyl radical can, however, only be observed in the LFP experiments when the ketyl-radical formation occurs efficiently in the triplet-quenching process. Moreover, the triplet state must be quenched fast enough to form significant amounts of ketyl radicals before the end of the laser pulse, so that enough ketyl radicals can become photoexcited by the laser pulse. (Triplet to doublet energy transfer is possible, but unlikely considering the concentrations being used). For **(R,S)-BP-Met** in ACN it seems to be possible because the triplet lifetime was measured to be only 22 ns.

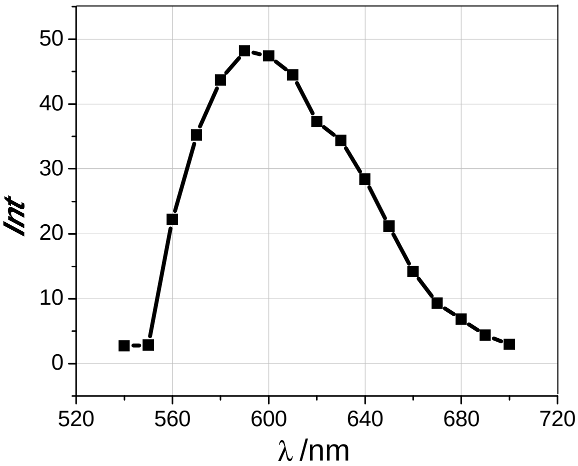

Figure 3.3-2 Emission spectra recorded during laser flash photolysis at 337 nm of a deoxygenated solution of **(R,S)-BP-Met** in dry ACN.

Surprisingly, fast triplet decay of the dyads in dry ACN is not accompanied by formation of free radical ions, as could have been expected based on the reports of the bimolecular quenching of the 4-carboxybenzophenone triplet state by methionine, where the initial step in the quenching process was assigned to an electron transfer from the methionine to the triplet state.[2, 103] However, the short triplet lifetimes of the dyads **(S,S)-BP-Met** and **(R,S)-BP-Met** do not necessarily mean that radical ions were not formed. It still leaves open the possibility that the radical ions may escape detection because of fast deactivation. The two possible paths for deactivating the radical ions are back electron transfer and secondary reactions that lead to stable products. The efficiency of the formation of the stable products was studied by steady-state irradiation (Chapter 3.3.1.2).

A totally different situation was observed in the LFP experiments of the dyads in ACN-H_2O (1:1 v/v) and TFE. While the transient absorption spectra of the dyads **(S,S)-**

BP-Met and **(R,S)-BP-Met** exhibited no spectral evolution in ACN, the corresponding LFP results in protic solvents, on the other hand, revealed an obvious spectral change with time delay (Figure 3.3-3a).

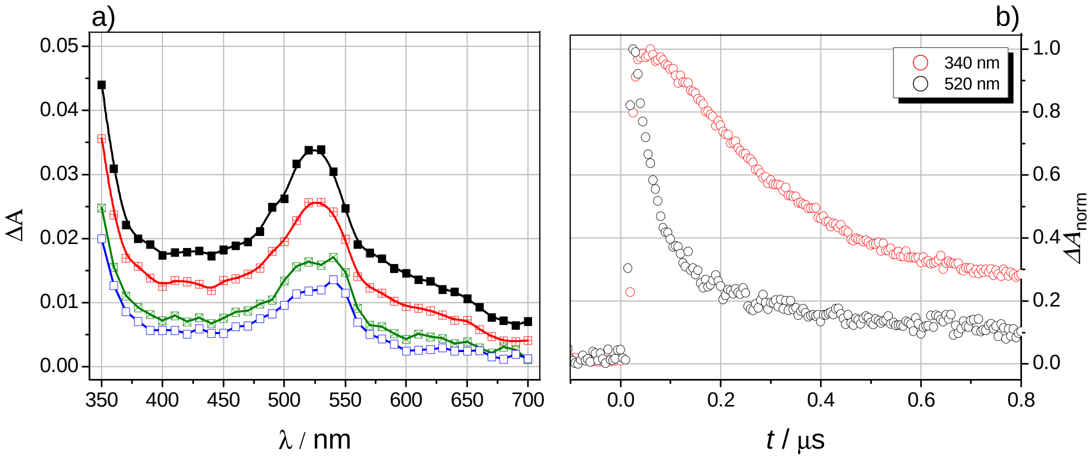

Figure 3.3-3 Summary of the results obtained during laser flash photolysis at 337 nm of a deoxygenated solution of **(S,S)-BP-Met** in TFE; a) transient absorption spectra: time delays after flash (from top to bottom): 40, 60, 100, 150 ns; b) normalized decay profiles of the transient absorption monitored at 520 nm (black) and 340 nm (red).

The triplet decays of the dyads were followed by spectral shifts from 325 to 340 nm (not shown), and from 525 to 540 nm. In contrast to the results obtained in ACN, comparisons of the decay profiles at different wavelengths in TFE revealed significant differences (Figure 3.3-3b). After complete decay of the absorption from the triplet state (black symbols in Figure 3.3-3b) there is an intermediate which decays on a much longer timescale than does its parent triplet (red symbols in Figure 3.3-3b). The spectral evolution, together with the wavelength-dependent decay profiles, points at a fast triplet quenching leading to ketyl-radical BPH$^{\bullet}$ formation.

A plausible mechanism for the formation of BPH$^{\bullet}$ is based on the analogy to the intermolecular reactions of CB and methionine-containing compounds. Accordingly, a proton transfer is assumed to occur within an initially formed charge-transfer complex, leading to the ketyl radical and an α-thio-alkyl radical.

3.3.1.2 Steady-state irradiation

Information concerning the mechanism of the quenching of the triplet state of the BP-Met dyads could also be obtained from steady-state irradiations. Steady-state consumption during irradiation of 2 mM solutions of **(S,S)-BP-Met** and **(R,S)-BP-Met** at 351 nm in ACN with an argon ion laser, was quantified by HPLC with UV-detection (Figure 3.3-4 and Figure 3.3-5).

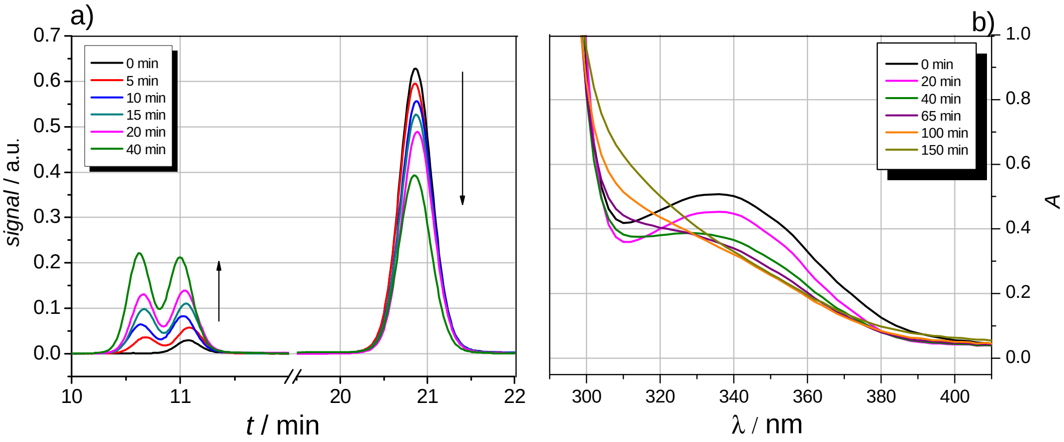

Figure 3.3-4 a) HPLC chromatograms recorded after irradiation of **(R,S)-BP-Met** (2 mM) in ACN (λ_{irr}= 351 nm), monitored at λ_{monit} = 205 nm b) absorption spectra recorded after irradiation of **(R,S)-BP-Met** (2 mM) in ACN.

Quantum yields of substrate disappearance (Φ_{irr}), based on the Reinecke’s actinometer, for **(S,S)-BP-Met** and **(R,S)-BP-Met** were found to be equal to 0.082 and 0.052, respectively.

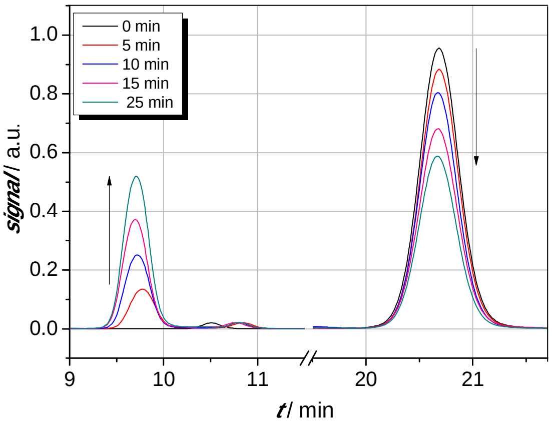

Figure 3.3-5 HPLC chromatograms recorded after irradiation of **(S,S)-BP-Met** (2 mM) in ACN (λ_{irr} = 351 nm), monitored at λ_{monit} = 205 nm.

Typical HPLC chromatograms showed that for **(R,S)-BP-Met** two stable products were formed (Figure 3.3-4) and for **(S,S)-BP-Met** only one stable product was detected (Figure 3.3-5). LFP at 337 nm excitation of the dyads in ACN at millimolar concentrations showed that the intramolecular quenching was efficient for both compounds (very short triplet lifetimes). Self-quenching may not be totally neglible, but it would only be of minor importance. Since the interest of this work is focused on the intramolecular reactivity of these compounds, steady-state irradiations were additionally performed on **(S,S)-BP-Met** and **(R,S)-BP-Met** solutions in ACN at lower concentration (10^{-5} M) and with 254-nm irradiation. As before, the steady-state consumption of the dyads was quantified *via* HPLC with UV-detection and by monitoring the UV spectra at regular time intervals (Figure 3.3-6). Interestingly, the resulting spectra show the disappearance of the characteristic $\pi \rightarrow \pi^*$ absorption of the BP chromophore at 250 nm

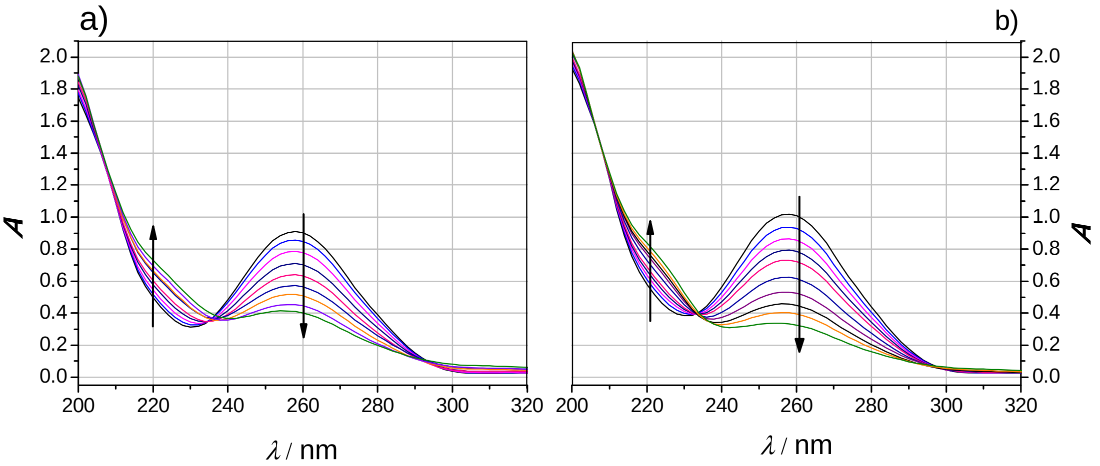

Figure 3.3-6 Absorption spectra recorded after irradiation at 254 nm in ACN of a) **(R,S)-BP-Met** (4.8 × 10^{-5} M) and b) **(S,S)-BP-Met** (5.3 × 10^{-5} M); time of irradiation from 0 to 300 s (follow direction of arrows).

The quantum yields obtained upon irradiation of **(S,S)-BP-Met** and **(R,S)-BP-Met** at 254 nm were found to be 0.06 and 0.05, respectively. It can be noted that only for **(S,S)-BP-Met** the quantum yields were slightly dependent on concentration indicating that the triplet quenching involved intermolecular processes in addition to the main intramolecular quenching pathway. This became apparent when a 2 mM concentration of the dyad was used. In the case of **(R,S)-BP-Met**, the quantum yields were not affected by lowering the concentration from 10^{-3} to 10^{-5} M. So, it is concluded that intermolecular processes are not taking place in the triplet quenching of **(R,S)-BP-Met** even at millimolar concentrations. For **(R,S)-BP-Met** the triplet lifetime was two times shorter (in ACN) compared to that of **(S,S)-BP-Met**. So, the rapid intramolecular reactions limited completely the possibility for observing any bimolecular pathways in the triplet quenching of **(R,S)-BP-Met**.

Overall, the formation of stable products was not very efficient (ca. 0.05-0.06) indicating that deactivation of the triplet state of the flexible open-chain BP-Met dyads in ACN led to regeneration of the substrate (ca 95 %). No attempts were made to identify the stable products at this stage.

3.3.1.3 **Theoretical calculations**

In order to aid in the interpretation of the large intramolecular reactivity of **(R,S)-BP-Met** and **(S,S)-BP-Met** in the laser-flash photolysis studies presented above, theoretical techniques analogous to those used for BP-Tyr dyads were employed. The results of DFT calculations and molecular-dynamics simulations of the ground-state structures and conformations established a quantitative picture of the conformer distributions of the dyads and defined the distance distributions from the sulfur to the carbonyl oxygen.

3.3.1.3.1 **DFT calculations**

The molecular conformations of **(R,S)-BP-Met** and **(S,S)-BP-Met** in the ground state were addressed by DFT calculations in the gas-phase. The notation of conformations used for open-chain BP-Met dyads is analogous to that used previously where the results for the theoretical calculations on **(R,S)-BP-Tyr** and **(S,S)-BP-Tyr** were presented (Chapter 3.2.1.3.1). DFT calculations (PBE1PBE; 6-31+G(d)) were undertaken for each of the nine combinations of the side-chain conformations of the Met and BP residues of both **(S,S)-BP-Met** and **(R,S)-BP-Met** in order to access the relative energies of the molecular conformations. In the rotamer notation, the first symbol always corresponds to the methionine side chain.

Table 3.3-1 summarizes the relative energies and the S–O distances between the BP carbonyl and the sulfur from the methionine for the nine optimized conformations in the gas phase for both stereoisomers. Importantly, the low-energy structures were accessible for various side-chain conformers, and there is no rotational isomer that is strongly disfavored. The results clearly show no structural preferences.

Table 3.3-1 Results of the lowest-energy structures of the gas-phase (ground state S_o) DFT calculations (PBE1PBE; 6-31+G(d) basis set) of the dyads **(S,S)-BP-Met** and **(R,S)-BP-Met**.

Rotamer	**(S,S)-BP-Met**		**(R,S)-BP-Met**	
	Distance *d*(S–O) / [Å]	Relative energy / [kcal/mol]	Distance *d*(S–O) / [Å]	Relative energy / [kcal/mol]
g–g–	12.5	2.4	10.8	0.17
g–g+	5.7	0.65	6.4	1.2
g+g–	12.2	1.9	11.7	0.0
g+g+	6.4	0.0	13.5	2.1
g–t	4.5	3.9	8.5	1.8
g+t	4.8	3.4	10.7	2.0
tg–	13.8	3.3	12.2	0.8
tg+	6.8	1.7	13.4	2.4
tt	12.7	4.7	7.7	0.5

The energies of all nine structures for **(R,S)-BP-Met** and five structures for **(S,S)-BP-Met** were found to be in close proximity (ΔE < 2.4 kcal/mol) (Table 3.3-1), where ΔE is the difference between the lowest-energy conformation of a particular stereoisomer and the energy of other conformers of that same stereoisomer. This means that there is no one favorable conformation that could prevail in solution for either dyad. The small energy differences between the rotamers are considered to reflect a high flexibility of the linkage between the BP and the Met moieties which cause no constraints that could limit the motions on the side chains in both dyads. In addition, in contrast to the BP-Tyr dyads, there is no possibility to stabilize any of the rotamers *via* aromatic-aromatic or hydrogen-bonding interactions. It is worth noting that conformations with similar relative energy correspond to conformations with a wide spread of *d*(S–O) distances from 4.5 Å to 13.8 Å for **(S,S)-BP-Met** and from 6.4 Å to 13.5 Å for **(R,S)-BP-Met**.

The DFT calculations thus revealed that a variety of structures, differing in their relative side-chain orientations and S–O, distances should be energetically accessible in solution.

3.3.1.3.2 Molecular Dynamics

Insight into the dynamics of the two open-chain BP-Met dyads came through molecular dynamics calculations, which helped in establishing the distribution of the sulfur to carbonyl oxygen distances and in obtaining quantitative information about the populations of the side-chain rotamers of the dyads' ground states. Here, the results of the molecular-dynamics simulations for an implicit ACN solvent model will be presented. The interconversion between different molecular conformations has been studied by means of long-time molecular-dynamics simulations (implicit-solvent model for ACN). The conformations of the BP-Met molecules can be characterized by side-chain conformations of the Met and BP residues. Definition of the side-chain dihedral angle can be found in Chapter 3.2.1.3.1. Since quenching of the triplet state of the BP residue by methionine may depend on *d*(S–O) between the sulfur atom and the BP carbonyl oxygen atom, quantitative analysis of this parameter was also performed. Figure 3.3-7 and Figure 3.3-8 summarize the time variation of three molecular parameters (side-chain dihedral angles on the Met and BP sides; characteristic inter-side chain *d*(S–O) distance) within a 100-ns simulation for dyads **(S,S)-BP-Met** and **(R,S)-BP-Met**, respectively.

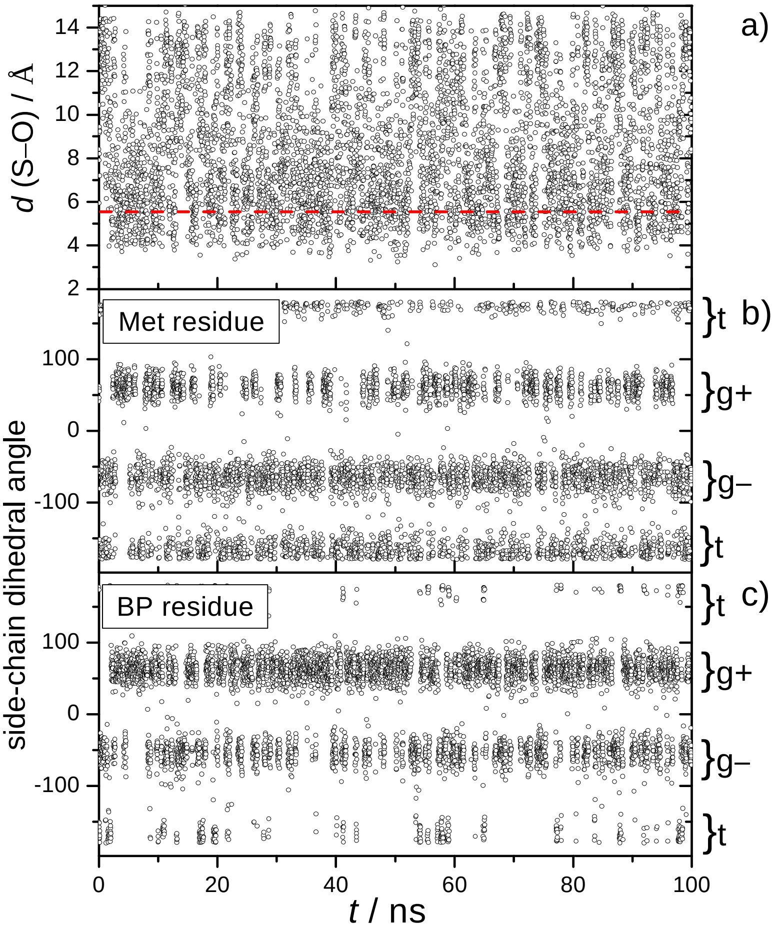

Figure 3.3-7 Long-time molecular-dynamics simulations for **(S,S)-BP-Met** (implicit-solvent model for ACN); a) time variation of the inter-side-chain distance *d*(S–O) between the sulfur atom from Met and the BP carbonyl oxygen atom; b) time variation of the Met side-chain dihedral angle; c) time variation of the BP side-chain dihedral angle.

As expected from the DFT results all three rotamers (**g+**, **g–**, **t**) of each side chain were populated during the simulation of both compounds, although with different probabilities. The Met side chains in both dyads adopt all three rotamers **g+**, **g–**, **t** with almost equal probability (Figure 3.3-7b and Figure 3.3-8b).

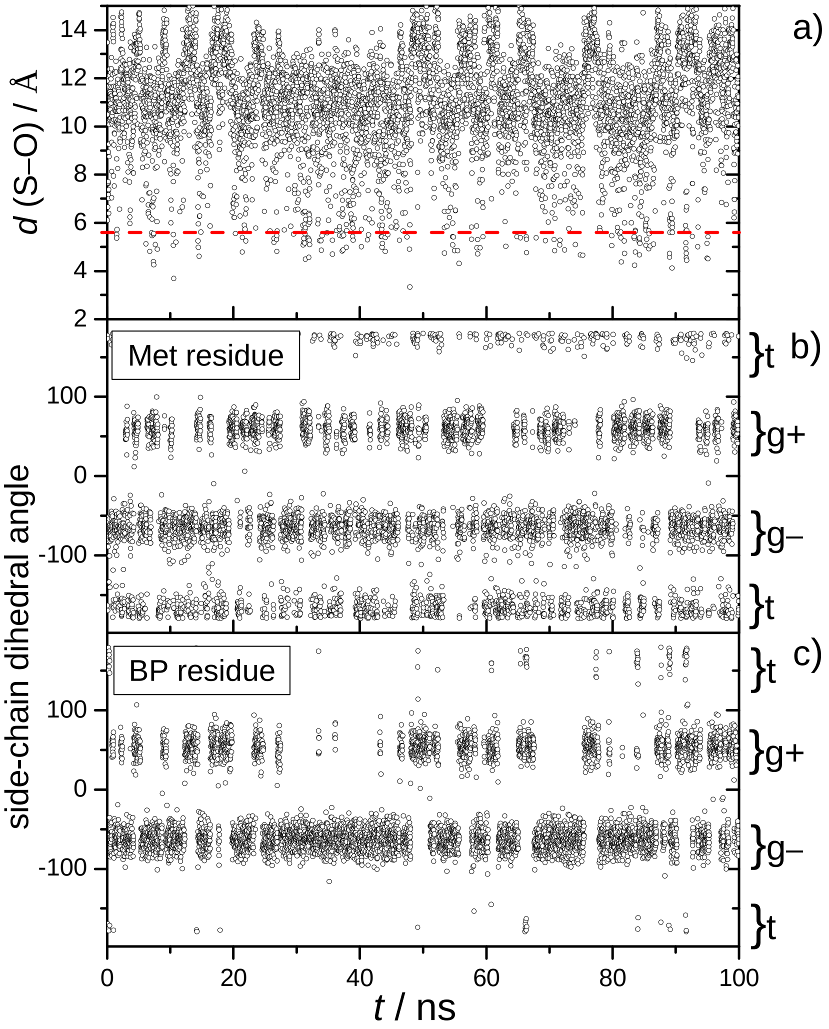

Figure 3.3-8 Long-time molecular-dynamics simulations for **(R,S)-BP-Met** (implicit-solvent model for ACN); a) time variation of the inter-side-chain distance *d*(S–O) between the sulfur atom from Met and the BP carbonyl oxygen atom; b) time variation of the Met side-chain dihedral angle; c) time variation of the BP side-chain dihedral angle.

The probabilities for the Met side chain in **(S,S)-BP-Met** to be in the rotamer **g+**, **g–**, **t** states, as calculated from these simulations, were 0.28, 0.36, 0.31, respectively. Analogous values calculated for the Met side chain of **(R,S)-BP-Met** were 0.31, 0.41, 0.25. It can be concluded from all these numbers that the Met side chain has no clear conformational preferences.

For the BP side-chain, in contrast, the MD simulations clearly revealed favorable conformations. For the BP side-chain of **(S,S)-BP-Met** the highest populated conformation was the **g+** rotamer, while the **t** rotamer, on the other hand, was clearly disfavored (Figure 3.3-7c). The respective calculated probabilities were 0.57 and 0.07. For **(R,S)-BP-Met**, the BP side-chain preferably populated the rotamer **g–**, whereas the rotamer **t** was also strongly disfavored as it was in **(S,S)-BP-Met**. The respective calculated probabilities were 0.64 and 0.02. An important further result from this analysis was that the MD-derived populations of the BP side-chain rotamers showed almost no difference between the open chain BP-Tyr and the BP-Met dyads (Chapter 3.2.1.3.2). This indicates that replacement of the tyrosine group by a methionine residue did not affect the dynamics of the benzophenone moieties or the probability of their forming particular conformations.

As it appears from Figure 3.3-7a and Figure 3.3-8a, the dyad **(R,S)-BP-Met** adopts less frequently, than does the dyad **(S,S)-BP-Met**, conformations with a *d*(S–O) distance < 10.0 Å. This is in agreement with the DFT calculations (Table 3.3-1) which showed that for the nine conformations optimized for **(R,S)-BP-Met**, six of them were characterized by *d*(S–O) distances > 10.0 Å, whereas for **(S,S)-BP-Met** only four conformations had distances *d*(S–O) larger than 10.0 Å.

In addition to the time variation of the inter-side-chain distance *d*(S–O) presented above, pair-distribution functions of the carbonyl/sulfur group distance *d*(S–O) were calculated based on the data from the MD simulations (Figure 3.3-9).

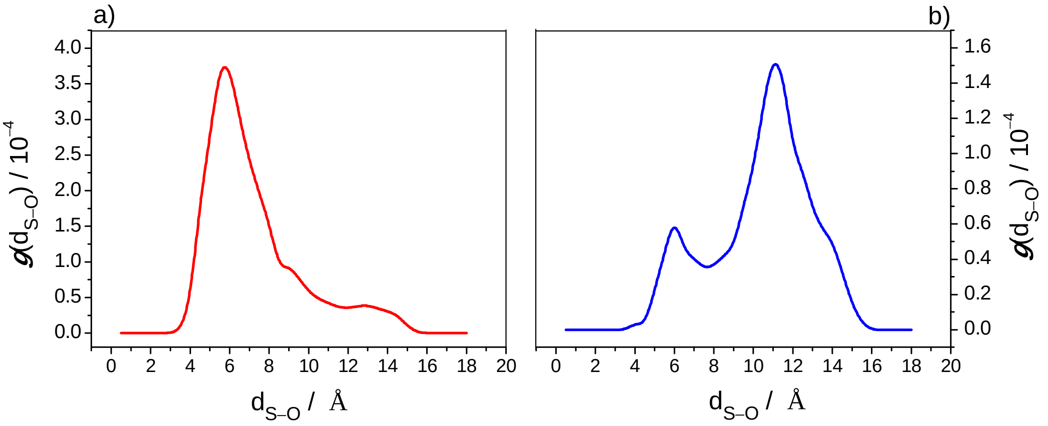

Figure 3.3-9 Pair-distribution functions of the carbonyl/sulfur group distance *d*(S–O), obtained with molecular-dynamics simulation in ACN for a) **(S,S)-BP-Met**; b) **(R,S)-BP-Met**.

Importantly, the pair-distribution functions showed that both BP-Met dyads were capable of the formation of rotamers with close-contacts between the sulfur atom and the carbonyl oxygen. Specifically, **(S,S)-BP-Met** mostly adopts conformations with *d*(S−O) between 4 Å to 8 Å in a quite narrow pair distribution function, whereas **(R,S)-BP-Met** greatly enhances conformations with *d*(S−O) > 10 Å and displays, in fact, two distinct maxima near 6 Å and 11 Å, with the latter dominating.

3.3.1.4 **Discussion**

Very fast intermolecular BP and CB triplet quenching has been reported to occur by thioether quenchers, as well as by the amino acid methionine containing this sulfide functional group.[2, 100, 102, 103] The primary photochemical step in these reactions involves an electron transfer from the sulfur atom to the triplet state of the carbonyl. This was suggested by the large values of the quenching rate constants and confirmed by direct observation of various electron-transfer intermediates.[2, 100, 102, 103] In this current thesis the analysis of intramolecular triplet quenching in *de-novo* synthesized benzophenone-methionine pairs was addressed. It is thought to be a step towards the study of photo-initiated electron transport in complex peptides. The open-chain BP-Met pair with variations in stereochemistry was studied by laser flash and steady-state photolysis, correlated with molecular-dynamics simulations and DFT calculations.

First of all, both of the investigated compounds showed high efficiency of the triplet excited state quenching. For the bichromophores **(S,S)-BP-Met** and **(R,S)-BP-Met** the BP-triplet decays were shorter by a factor of greater than 100 relative to the triplet decays of the monochromophoric reference compound not containing the methionine moiety. Interestingly, quenching in ACN proceeded for both compounds without net-formation of any ionic species. In fact, lack of any observable intermediates at all makes the interpretation of the mechanism difficult. However, based on the short triplet lifetimes and by analogy to the data on intermolecular triplet-state quenching by compounds containing a methionine group, it seems reasonable to assume, though, that intramolecular electron transfer from the sulfur atom to the triplet state of the BP is, nevertheless, the primary photochemical step. The steady-state irradiations showed that secondary reactions which could lead to stable products occurred only with relatively low efficiency of 5 – 6 %. So, it appears that secondary reactions are not competitive with fast back electron transfer.

The high flexibility of the linkage between BP and Met is expressed in the finite formation probabilities of conformations with close contact between the reactive moieties. These probabilities were computed from MD simulations. Thus, the observed significant intramolecular reactivity within **(S,S)-BP-Met** and **(R,S)-BP-Met** is in accord with a quenching mechanism which is dependent on close contact of the BP and Met residues. Along this line, Hörner recently concluded that efficient intramolecular BP triplet quenching by thioethers in the absence of water appears to be entirely controlled by the probability of close contacts between the reacting sub-units, i.e., by the flexibility of the molecule.[164] In support of this conclusion, he convincingly argued that any long-distance electron transfer through space, e.g., in a BP-Met dyad connected *via* a rigid amide bond, is not effective.[164]

Solvent effects on the reactivity of the **(S,S)-BP-Met** and **(R,S)-BP-Met** were suppressed by yet another factor influencing the reactivity, namely, the geometry of the compounds which, due to high conformational freedom, was favorable for fast intramolecular reaction. It can be noted that the triplet lifetimes of both compounds were decreased by a factor less than two on going from non-protic to protic solvents. This suggests that, in the case of open-chain BP-Met dyads, it is a structural factor that contributes the most to the rate constants of the quenching process. On the other hand, protic solvents, e.g TFE, influenced the evolution of the transient absorption spectra. In contrast to experiments performed in ACN, the triplet decay in TFE was accompanied by ketyl radical $BPH^{\bullet}$ formation. The mechanism of the formation of this species may be proposed based on the analogy to the intermolecular reactions of CB and methionine-containing compounds. After the electron transfer step that leads to an initial radical-ion pair complex, a proton transfer is assumed to occur within this complex leading to ketyl radical and an α-thio-alkyl radical. It seems that in protic solvents this secondary reaction competes with back electron transfer more efficiently than in ACN.

The high flexibility of the peptide linker in **(S,S)-BP-Met** and **(R,S)-BP-Met** blurs also the chiral discrimination in the triplet quenching. The stereoselectivity of the open-chain BP-Met expressed as the ratio of the triplet lifetimes was found to vary only from 2.3 in TFE to 2.5 in ACN.

So, in order to get deeper insight into the relationship between the kinetic phenomenology and molecular structure, the conformational freedom of the BP-Met dyads was diminished by introducing a rigid linker: DKP. The results for the rigid pair of the BP-Met dyads will be presented in the following subchapter.

3.3.2 **Rigidly linked “cyclic” diastereoisomers**

3.3.2.1 **Nanosecond flash photolysis: spectral and kinetic analysis**

Nanosecond-laser photolysis was carried out to charactereize the excited-state dynamics of the **(S,S)-BP-DKP-Met** and **(S,R)-BP-DKP-Met** dyads and to establish the structural conditions that maximize the efficiency of the intramolecular reactivity of the triplet states. This work addressed, in particular, the effect of chiral-center configurations on the diastereo-selectivity of the triplet-state quenching by the methionine residue. It was accomplished through a comparison of the reactivities of the above pair of the cyclic diastereoisomers.

LFP of the **(S,S)-BP-DKP-Met** dyad was performed only in ACN at a concentration of 2×10^{-5} M and with excitation only at 266 nm. The low solubility of the compound limited the possibility of measuring the transient absorption spectra of **(S,S)-BP-DKP-Met** at higher concentrations and/or with 337 nm or 355 nm excitation. LFP of **(S,R)-BP-DKP-Met**, on the other hand, could be carried out at two different concentrations: 2×10^{-5} M and 1×10^{-3} M with excitation at 266 nm and 337 nm, respectively. In contrast to the data obtained for the open-chain BP-Met dyads which showed only small stereo effects, the quenching of the triplet state of the cyclic BP-Met dyads revealed significant chiral discrimination. The effect of a change in the chirality of one stereocenter on the reactivity is illustrated by the comparison of the transient absorption spectra and decay profiles observed for solutions of **(S,S)-BP-DKP-Met** and **(S,R)-BP-DKP-Met** in ACN (Figure 3.3-10 and Figure 3.3-12). First of all, in contrast to the results obtained for open-chain BP-Met dyads, the spectra obtained for **(S,S)-BP-DKP-Met** could not be assigned to the triplet state unambiguously. Even at short times after the laser pulse, e.g. after 22 ns, the transient absorption spectra contained already a significant contribution from ketyl radicals (Figure 3.3-10a).

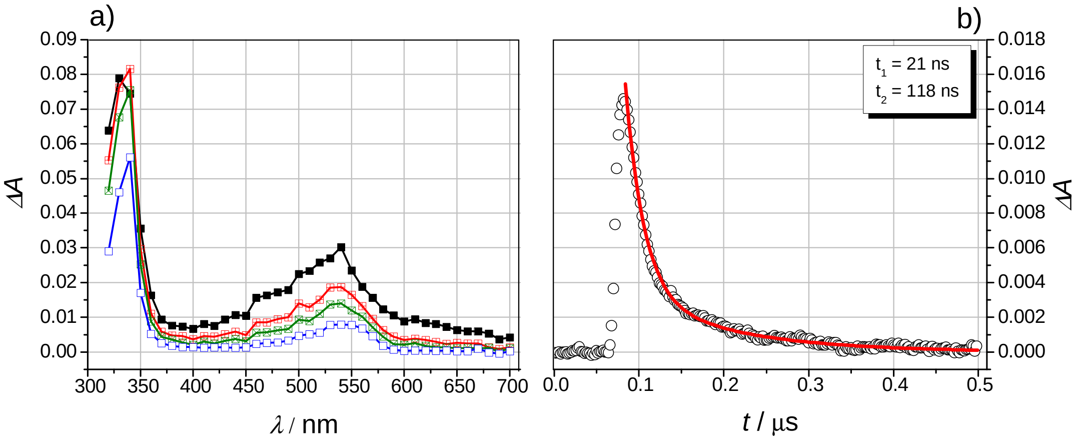

Figure 3.3-10 Summary of the results obtained during laser flash photolysis at 266 nm of a deoxygenated solution of **(S,S)-BP-DKP-Met** in dry ACN; a) transient absorption spectra: time delays after flash (from top to bottom): 22, 40, 50, 80 ns; b) decay profiles of the transient absorption monitored at 520 nm (black); the solid red line represents a biexponential fit to the decay curve; numbers represent the value obtained from the fit.

The presence of the ketyl radical was identified through its characteristic spectrum with maxima at 340 nm and 540 nm.

Spectral resolution techniques were used in order to unravel the nature of the intermediates in the excited-state processes of **(S,S)-BP-DKP-Met**. Although the presence of the triplet state was not obvious from the transient absorption spectra, resolution into spectral components revealed the presence of the triplet state at the short delay times. To simulate the experimental data quantitatively, three components were needed: the triplet state ^{3}BP, the ketyl radical BPH$^\bullet$ and the benzophenone radical anion BP$^{\bullet-}$ (Figure 3.3-11a). It is worth noting that the concentration of BP$^{\bullet-}$ was found to be very small ≤ 0.4 μM, so any unambiguous conclusion concerning the presence and the mechanism of the formation of BP$^{\bullet-}$ cannot be made. The triplet concentration, actinometrically determined, was 7.9 μM. The maximum concentration of the ketyl radical was determined to be 4.7 μM. This value was obtained from fitting the BPH$^\bullet$ concentration profile to a function which takes into account the growth and the decay of the species (Eq 3.2-1). The quantum yield of ketyl radical formation was calculated to be 0.6. The uncertainty of this figure, obtained from the concentration profile, is quite large due its rapid decay and is estimated to be ± 0.1.

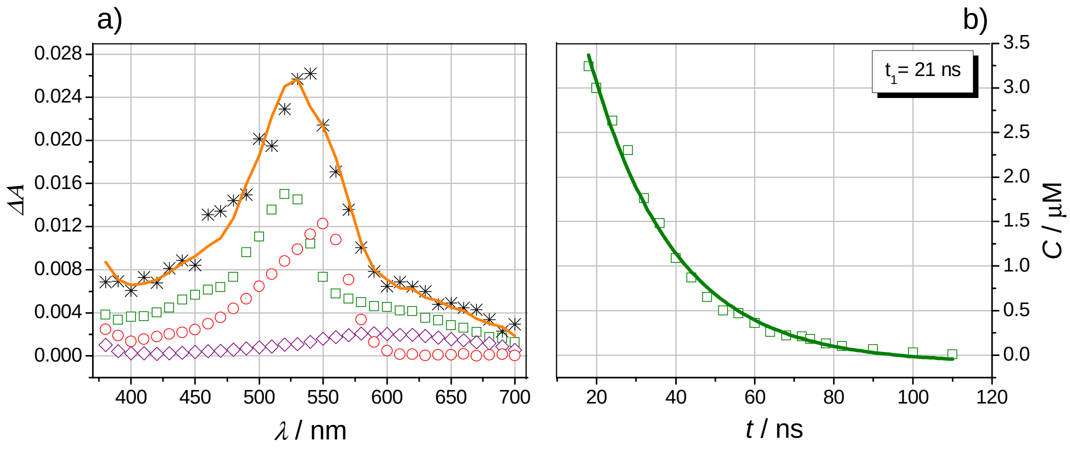

Figure 3.3-11 a) Resolutions of transient absorption spectra taken 28 ns after 266 nm laser pulsing (5 mJ) of a solution of **(S,S)-BP-DKP-Met** in ACN; b) concentration profiles for the triplet state obtained from the resolution of the transient absorption spectra of **(S,S)-BP-DKP-Met** in ACN. The symbols represent: □ for the triplet state ^{3}BP, ○ for the ketyl radical BPH$^\bullet$, ◊ for the BP radical anion BP$^{\bullet-}$ and * for the experimental data; solid curves in a) and b) are the resulting fits from the regression analyses, the number represents the value obtained from the fit.

While the transient spectrum obtained from **(S,S)-BP-DKP-Met** in pure ACN carries significant contributions from a ketyl radical already after 22 ns, the spectrum obtained from **(S,R)-BP-DKP-Met** after 500 ns still largely resembles the original triplet spectrum (Figure 3.3-12a). Actually, in the case of the latter, hardly any evolution of further transient absorption spectra was noticeable beside the triplet absorption decay (Figure 3.3-12a). However, the normalized spectra from **(S,R)-BP-DKP-Met** obtained 70 ns and 500 ns after the flash did not overlap (Figure 3.3-13), which would be expected if no additional intermediates were formed.

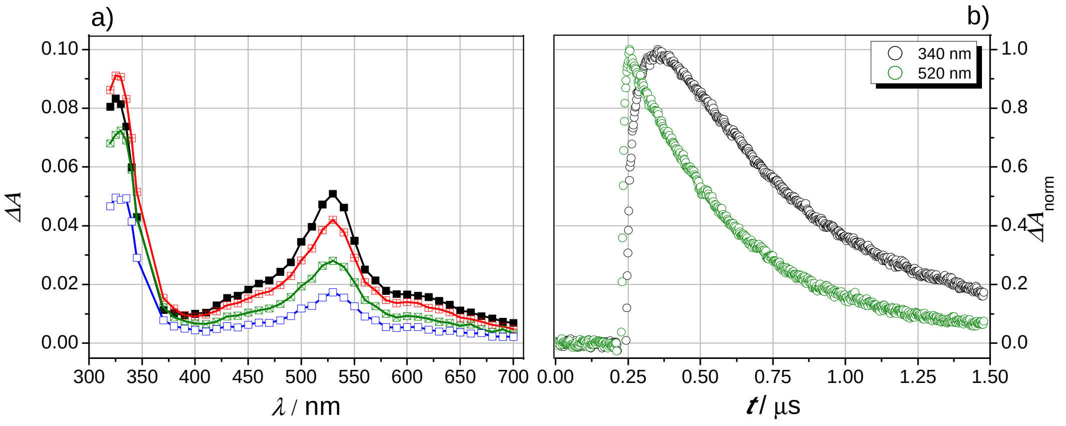

Figure 3.3-12 Summary of the results obtained during laser flash photolysis at 266 nm of a deoxygenated solution of **(S,R)-BP-DKP-Met** in dry ACN; a) transient absorption spectra: time delays after flash (from top to bottom): 70, 150, 500, 800 ns; b) normalized decay profiles of the transient absorption monitored at 520 nm (green) and 340 nm (black).

Further evidence for the formation of intermediates in the quenching process of **(S,R)-BP-DKP-Met** in ACN came from a kinetic treatment of the transient decays. The kinetic traces at 340 nm and 520 nm did not coincide with each other (Figure 3.3-12b). The kinetic trace at 520 nm (green symbols in Figure 3.3-12b) decays faster, than that at 340 nm (black symbols in Figure 3.3-12b), but the respective decay components of these traces are not significantly different. That explains why, at first sight, it was difficult to see spectral evolution in the transient absorption spectra. Comparison of both kinetic traces (340 nm and 520 nm) and the normalized transient absorption spectra speaks, however, clearly in favor of the formation of an intermediate after the triplet decay, which due to its maximum absorption at 340 nm can be assigned to the ketyl radical.

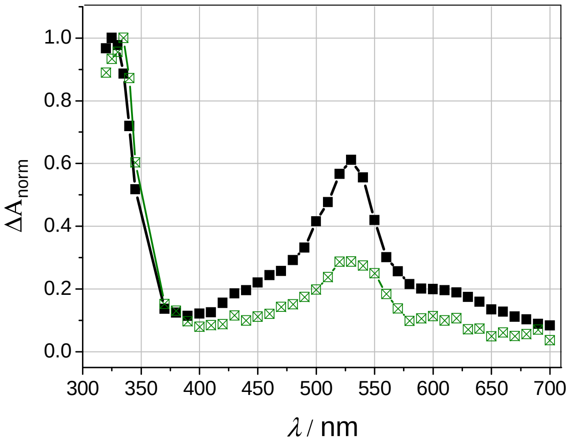

Figure 3.3-13 Normalized transient absorption spectra obtained during laser flash photolysis at 266 nm of a deoxygenated solution of **(S,R)-BP-DKP-Met** in dry ACN; time delays after flash: 70 ns – (black), 500 ns – (green).

The chiral effects on the intramolecular triplet quenching of the pair of diastereoisomers are reflected also in the triplet lifetimes, which exhibited remarkable differences. The triplet lifetime of the **(S,S)-BP-DKP-Met** dyad in ACN, obtained from a biexponential fit to the transient decay at 520 nm under assumption that the decay of the fast component can be attributed to the triplet state (Figure 3.3-10b), was found to be only 21 ns. This value was cross-checked by comparison with the rate constant obtained from a mono-exponential fit to the triplet concentration-time profile resulting from the spectral resolutions (Figure 3.3-11b). It was, within experimental error, identical with the triplet-decay rate obtained from the kinetic decays at 520 nm. The very short triplet lifetime is taken as evidence for the intramolecular nature of the quenching process.

On the other hand, triplet lifetimes obtained from mono- or biexponential fits to the transient decays at 630 and 520 nm, respectively, for dyad **(S,R)-BP-DKP-Met** in ACN show a concentration dependent triplet decay. The triplet lifetimes were found to be 230 ns and 330 ns for the concentrations of 1×10^{-3} M and 2×10^{-5} M, respectively. This behavior is due to a bimolecular self quenching process involving unexcited dyads. From the two sets of data points that were collected (from 337 nm excitation and 266 nm excitation) in ACN, the self-quenching rate constant for the dyad **(S,R)-BP-DKP-Met** was estimated to be $k_{SQ} = (1.3 \pm 1.0) \times 10^9$ M^{-1} s^{-1}. This value is in good agreement with the rate constant for the bimolecular quenching of the triplet state of CB by methionine.[103] Such a large self-quenching rate constant in connection with the relatively low intramolecular reactivity of **(S,R)-BP-DKP-Met**, implies that even at a concentration of 2×10^{-5} M, self-quenching processes cannot be neglected.

It is worth noting that the triplet lifetimes of the two diastereoisomers **(S,R)-BP-DKP-Met** and **(S,S)-BP-DKP-Met**, measured for the same concentration (2×10^{-5} M), differed by a factor of 15 in ACN. As in the case of the cyclic BP-Tyr dyads, the change in the configuration at a single chiral center in the cyclic BP-Met dyads produced a marked stereoselectivity, indicating that there are also special structural constraints on the triplet-state quenching by the methionine residue.

Based on the efficient formation of the ketyl radical in the LFP of **(S,S)-BP-DKP-Met**, it can be concluded that the triplet decay of the compound in which both reactive moieties, BP and Met, occupy the same side of the DKP ring can actually be attributed to an efficient H-atom transfer reaction. The mechanism of the reaction, as in the case of the open-chain BP-Met dyads, may be proposed based on the analogy to the intermolecular reactions of triplet CB with methionine-containing compounds. After an electron-transfer step, leading to an initial radical-ion pair complex, a proton transfer is assumed to occur within this complex, leading to a ketyl radical and an α-thio-alkyl radical. It seems that this secondary reaction is much more efficient for **(S,S)-BP-DKP-Met** than in the case of the open-chain BP-Met dyads, where the ketyl radical was not observed in the transient absorption spectra in ACN. Further evidence for the proposed mechanism will be presented based on the results of the efficiency of the formation of the stable products and an analysis of their structure studied after steady-state irradiation

(Chapter 3.3.2.2). Due to favorable geometry for intramolecular reactivity, the triplet lifetime of the dyad **(S,S)-BP-DKP-Met** was very short; too short, in fact, to allow any study of the solvent effect on the reactivity for this diastereomer.

In the case of **(S,R)-BP-DKP-Met**, on the other hand, a solvent-effect study on the triplet quenching was possible because of the relatively much longer triplet lifetime in ACN. The LFP results on **(S,R)-BP-DKP-Met** in TFE as solvent were, however, totally different than those observed in ACN. First of all, the triplet lifetime was reduced by a factor of 10 (green symbols in Figure 3.3-14b *vs*. Figure 3.3-12b). Analogous changes on going from ACN to TFE were observed for the triplet lifetimes of **(S,R)-BP-DKP-Tyr**. In addition, the triplet decays of **(S,R)-BP-DKP-Met** in TFE were connected with the formation of ketyl radicals (Figure 3.3-14a).

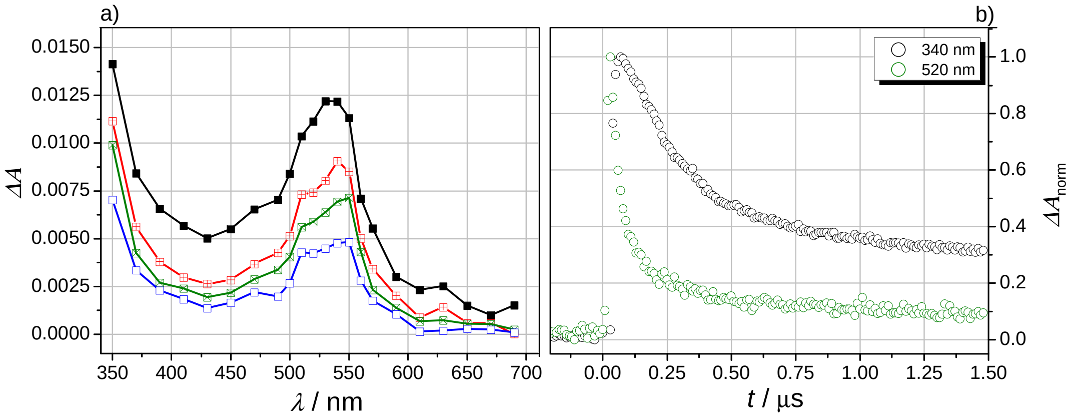

Figure 3.3-14 Summary of the results obtained during laser flash photolysis at 266 nm of a deoxygenated solution of **(S,R)-BP-DKP-Met** in dry TFE; a) transient absorption spectra: time delays after flash (from top to bottom): 60, 120, 200, 500 ns; b) normalized decay profiles of the transient absorption monitored at 520 nm (green) and 340 nm (black).

The results showed that the dyad **(S,R)-BP-DKP-Met**, which has the benzophenone and methionine moieties on opposite sides of the DKP ring, can also undergo intramolecular hydrogen-atom transfer. This dyad is another example showing that the reactivity of an electronically excited molecule can be greatly enhanced by changes in the nature of the solvent.

3.3.2.2 **Steady-state irradiation**

Mechanistic information concerning quenching of the triplet states of **(S,S)-BP-DKP-Met** and **(S,R)-BP-DKP-Met** could also be obtained from steady-state irradiations and product analyses. Steady-state irradiations were conducted for 4.75 × 10^{-5} M deoxygenated acetonitrile solutions of **(S,S)-BP-DKP-Met** and **(S,R)-BP-DKP-Met** with a low-pressure mercury lamp (254 nm). Concentrations in the range of 10^{-5} M were chosen due to low solubility of **(S,S)-BP-DKP-Met**, and also in order to limit the intermolecular quenching pathway with **(S,R)-BP-DKP-Met** which was shown to occur in the LFP experiments in ACN. The course of the reactions was followed by HPLC analyses (Figure 3.3-15). In both cases, as the reaction proceeded, a new peak progressively emerged in the HPLC profile at the expense of the substrate. Based on Figure 3.3-15, it can be noted that **(S,S)-BP-DKP-Met** disappeared faster than its diastereoisomer **(S,R)-BP-DKP-Met**. Quantum yields of substrate disappearance (Φ_{irr}), for **(S,S)-BP-DKP-Met** and **(S,R)-BP-DKP-Met** were found to be 0.35 and 0.18, respectively.

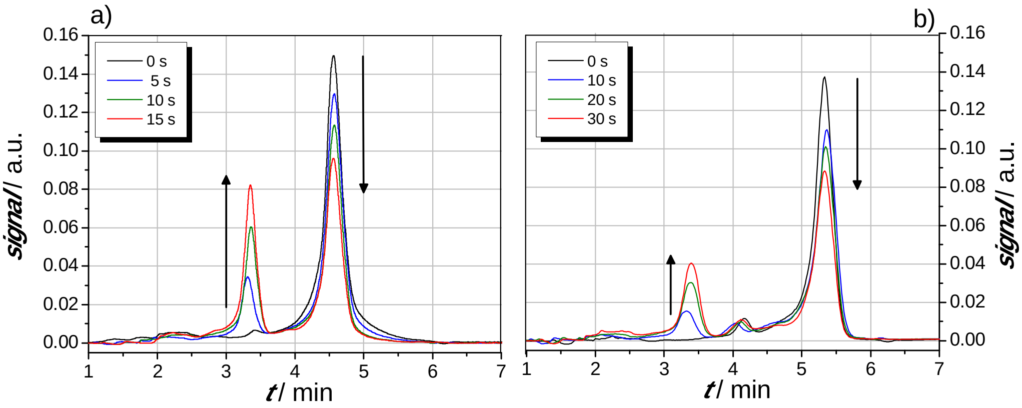

Figure 3.3-15 HPLC chromatograms recorded after irradiation of a) **(S,S)-BP-DKP-Met** (4.75 × 10^{-5} M); b) **(S,R)-BP-DKP-Met** (4.75 × 10^{-5} M) in ACN (λ_{irr} = 254 nm), monitored at λ_{monit} = 210 nm.

The quantum yields of substrate disappearance for the DKP-based BP-Met dyads were found to be much larger than the respective values measured for their open-chain analogues. Although the triplet lifetimes of **(S,S)-BP-DKP-Met** and **(R,S)-BP-Met** in ACN obtained from LFP were very short and similar (ca. 20 ns), the steady-state experiments showed a distinctly different picture. Thus the triplet quenching of the open-chain dyad, despite being a quantitative process, resulted in an only 5 % depletion of the dyad and, therefore, seems to be mostly, i.e. to about 95 %, a reversible process. The triplet-state quenching process for **(S,S)-BP-DKP-Met**, on the other hand, led to a dyad depletion of about 35 % and thus showed a much higher degree of irreversibility.

The steady-state consumption of the two DKP-based dyads in ACN was also monitored by measuring the entire UV spectra at regular time intervals (Figure 3.3-16). The resulting UV spectra showed disappearance of the absorption band at 258 nm which is characteristic for the $\pi\rightarrow\pi^*$ transition of the benzophenone chromophore. This indicates the absence of this moiety in the products of the irradiations of **(S,S)-BP-DKP-Met** and **(S,R)-BP-DKP-Met**.

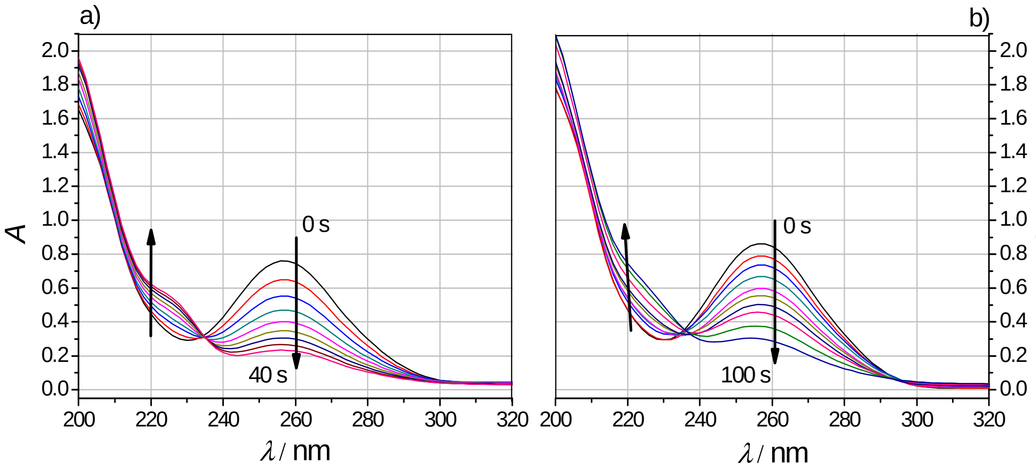

Figure 3.3-16 Absorption spectra recorded after irradiation at 254 nm in ACN a) **(S,S)-BP-DKP-Met** (4.75×10^{-5} M), b) **(S,R)-BP-DKP-Met** (4.75×10^{-5} M); time of irradiation from a) 0 to 40 s b) 0 to 100 s (follow direction of arrows).

To aid in the understanding of the mechanism of intramolecular triplet-state quenching by the methionine residue in the cyclic DKP-based BP-Met dyads, it was of interest to identify the structure of the photoproducts. In order to isolate products of the photoreaction of **(S,S)-BP-DKP-Met**, as example, irradiations were carried out in a photoreactor on a preparative scale with 4.75×10^{-5} M solutions. The apparatus allowed for irradiating 50 ml of **(S,S)-BP-DKP-Met** solution at one time, and the procedure was repeated 30 times. The time of the irradiation was chosen so as not to decompose the entire substrate. After the irradiations, the solutions were concentrated by evaporating the solvent, and, subsequently, the products were isolated by thin-layer chromatograpy (TLC). Actually, the reaction led to one major photoproduct, and a second product formed with significantly lower quantum yields. Further analyses were performed only on the main photoproduct.

This photoproduct was separately analyzed by UV/Vis, mass spectrometry, and NMR techniques. Based on the collected data, a cyclic tertiary alcohol can be proposed as the structure of this product from **(S,S)-BP-DKP-Met** (Figure 3.3-17). The stereochemistry of this photoproduct was not determined at this stage.

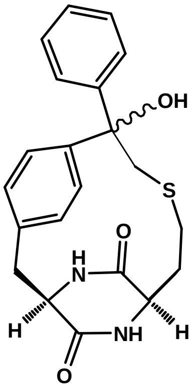

Figure 3.3-17 Proposed chemical structure of the product of the photoreaction of the **(S,S)-BP-DKP-Met**.

The UV spectrum of the product is consistent with the reduction of the benzophenone chromophore, since the typical absorption band at 258 nm has disappeared (Figure 3.3-18).

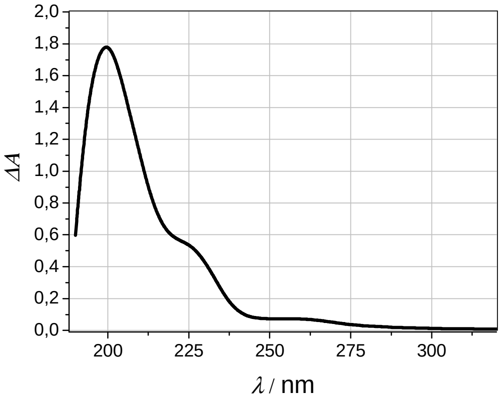

Figure 3.3-18 Absorption spectra of the photoproduct of the irradiation of **(S,S)-BP-DKP-Met** in ACN (6 × 10^{-5} M).

Next, the mass spectrum of the product was recorded on an Intectra AMD 402 Mass Spectrometer (Figure 3.3-19). A high resolution EI-MS analysis of the product showed a molecular ion at m/z = 382.13581, which corresponds to an atomic composition of $C_{21}H_{22}N_2O_3S$ (calculated 382.13510). Mass spectrometry data confirmed that the product and the starting compound are isomers. The major peaks at 196.2, 187.1, 224.1 and 308.2 are assigned to the fragments of the molecules presented in red at the top of the MS spectrum (Figure 3.3-19). High resolution EI-MS analysis of the base peak (m/z = 196.2) confirmed its proposed atomic composition of $C_{14}H_{12}O$ (mass obtained: 196.08837, mass calculated: 196.08882). In addition, very similar peaks were recognized in the MS spectra of the substrate and the product which can be understood if the fragmentation pathway is connected with the cleavage of the bond which is formed during the irradiation of **(S,S)-BP-DKP-Met**, namely, that between the carbonyl carbon and the carbon, α-CH_3, adjacent to the sulfur.

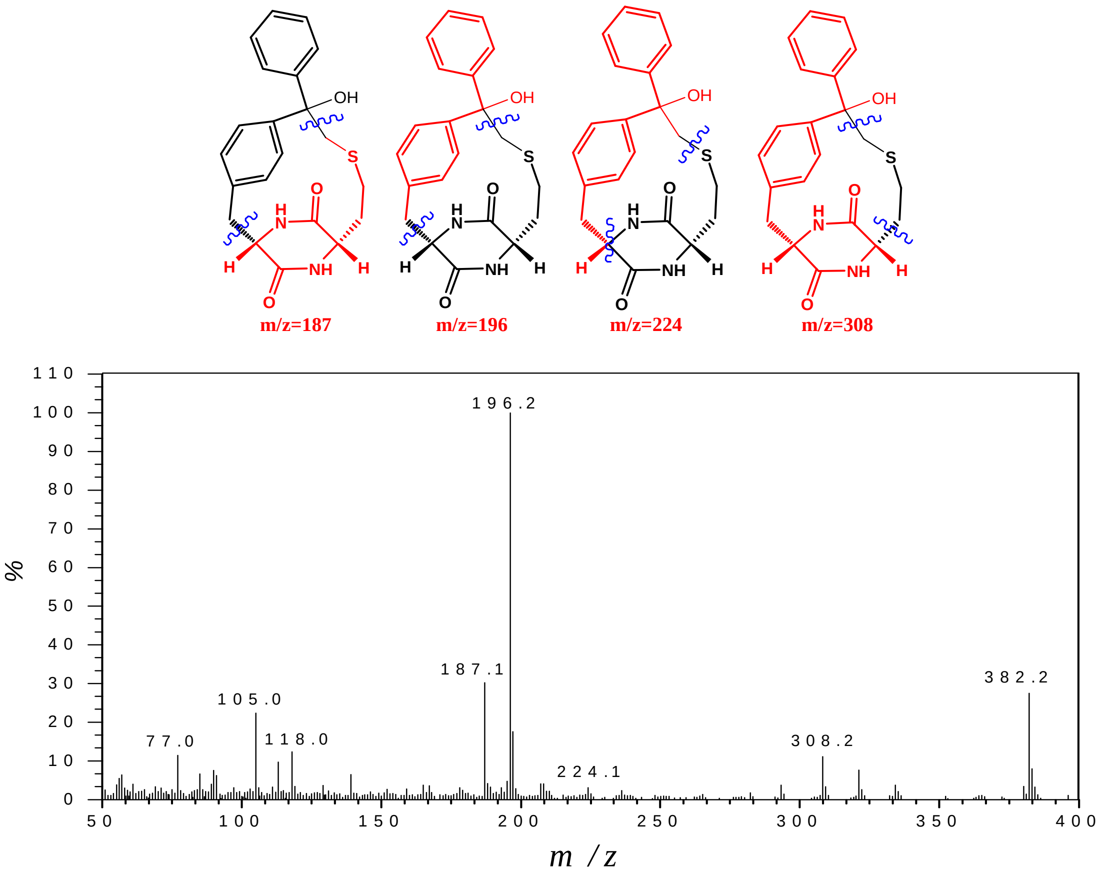

Figure 3.3-19 MS spectrum of the photoproduct of the irradiation of **(S,S)-BP-DKP-Met** in ACN (6 × 10^{-5} M); in the top of the figure proposition of the assignment of the peaks in the MS spectrum to the fragments of molecules (red).

The 300 MHz NMR spectra of the substrate and the product were recorded in DMSO. It is evident that the characteristic signal at δ = 2.1 ppm for the methionine residue α-CH_3 (carbon adjacent to sulfur) in the spectrum of **(S,S)-BP-DKP-Met** is missing in the NMR spectra of the product.

3.3.2.3 **Theoretical calculations**

In the light of the results from the time-resolved and steady-state studies on the cyclic BP-Met dyads, it is clear that the origin of the observed differences in the triplet lifetimes between the diastereoisomers should be sought from the conformational preferences and differences in the distance distributions from the sulfur to the carbonyl oxygen. In order to gain an understanding of the geometrical requirements underpinning the observed differences in the reactivity of the pair of diastereoisomers, extensive DFT calculations and MD simulations on **(S,S)-BP-DKP-Met** and **(S,R)-BP-DKP-Met** were performed, and the relevant results are presented in the following.

3.3.2.3.1 **DFT calculations**

To give an explanation for the observed stereodifferentiation in the triplet quenching of **(S,S)-BP-DKP-Met** and **(S,R)-BP-DKP-Met**, the molecular conformations of the ground state were studied by DFT calculations. The notation of conformations used for cyclic BP-Met dyads is analogous to that used previously where the results for the theoretical calculations on DKP-based BP-Tyr dyads were presented (Chapter 3.2.2.2). To examine the preferred conformations of the dyads, nine minimum energy structures with different combinations of the side-chain conformations of the Met and BP residues for both **(S,S)-BP-DKP-Met** and **(S,R)-BP-DKP-Met** were calculated at the level of PBE1PBE; 6-31+G(d). In the rotamer notation, the first symbol always corresponds to the methionine side chain. The relative energies and the S–O distances between the BP carbonyl oxygen and the methionine sulfur for rotamers, having local-energy minima, are summarized in Table 3.3-2 for (**S,S)-BP-DKP-Met** and **(S,R)-BP-DKP-Met** in the gas phase.

The calculations revealed that the low-energy structures were accessible for different side-chain conformations (Table 3.3-2). In contrast to the cyclic BP-Tyr dyads, energetic differences between rotamers in the cyclic BP-Met dyads were found to be less pronounced. For example, in the **(S,S)-BP-DKP-Tyr** dyads, the structure with the second to lowest energy had an energy already higher by 7.2 kcal/mol (Table 3.2-4) than the low-energy configuraton while, in the case of **(S,S)-BP-DKP-Met**, there are five structures within less than ΔE < 2.2 kcal/mol (Table 3.3-2) of the lowest energy structure (Δ*E* is defined as the difference in energy between that of a given structure and the energy of the lowest-energy structure for a given diastereomer).

Table 3.3-2 Results of the lowest-energy structures in the gas-phase (ground state S_o) DFT calculations (PBE1PBE; 6-31+G(d) basis set) of **(S,S)-BP-DKP-Met** and **(S,R)-BP-DKP-Met**.

Rotamer	**(S,S)-BP-DKP-Met**		**(S,R)-BP-DKP-Met**	
	Distance *d*(S–O) / [Å]	Relative energy / [kcal/mol]	Distance *d*(S–O) / [Å]	Relative energy / [kcal/mol]
F–F	4.8	4.2	10.1	3.1
F–E$_{N}$	8.5	1.2	8.7	0.0
E$_{N}$–F	5.6	0.0	5.5	1.8
E$_{N}$–E$_{N}$	12.5	0.9	12.5	0.9
F–E$_{O}$	10.2	5.3	9.8	5.2
E$_{N}$–E$_{O}$	11.8	3.7	11.7	4.4
E$_{O}$–F	6.6	1.9	7.1	2.2
E$_{O}$–E$_{N}$	11.5	2.2	8.0	3.7
E$_{O}$–E$_{O}$	11.1	4.8	10.6	4.9

The strongly favorable **F–F** structure of **(S,S)-BP-DKP-Tyr**, wherein the side chains are folded simultaneously across the ring, can be stabilized additionally *via* aromatic-aromatic and hydrogen bonding interactions. This type of stabilization cannot occur in the cyclic BP-Met dyads which may explain why there are several different side-chain rotamers that were found to have similar energy. Structures with slightly higher energy (Δ*E* > 3.5 kcal/mol) for both cyclic BP-Met dyads were those with the BP side chain extended to oxygen (**F–E$_{O}$**, **E$_{N}$–E$_{O}$**, **E$_{O}$–E$_{O}$**) and also rotamers **F–F**, **E$_{O}$–E$_{O}$**, meaning that these structures are less populated. The conformations with similar relative energy (Δ*E* < 2.0 kcal/mol) correspond to structures with a wide spread of *d*(S–O) distances from 5.6 Å to 12.5 Å for **(S,S)-BP-DKP-Met** and from 5.5 Å to 12.5 Å for **(S,R)-BP-DKP-Met**. Although the spread of *d*(S–O) distances seems to be similar for both cyclic BP-Met dyads, the MD simulations, as shown below, revealed significant differences between the **(S,S)-BP-DKP-Met** and **(S,R)-BP-DKP-Met** (Chapter 3.3.2.3.2) concerning the probabilities of adopting structures with smaller *d*(S–O) distance.

.

3.3.2.3.2 Molecular Dynamics

The goals of the MD simulations of the DKP-based BP-Met dyads were to establish the distribution of the sulfur to carbonyl oxygen distances and to see how the change of a single chiral center changes the populations of the side-chains rotamers. The definition of the side-chain dihedral angle can be found in Chapter 3.2.1.3.1. The conformational space of **(S,S)-BP-DKP-Met** and **(S,R)-BP-DKP-Met** was sampled by means of long-time MD simulations in an ACN implicit solvent model. Since quenching of the triplet state of the BP residue by methionine may depend on the distance between the sulfur atom and the BP carbonyl oxygen atom, *d*(S‒O), a quantitative analysis of this parameter was performed. Figure 3.3-20 and Figure 3.3-21 summarize the time variation of three molecular parameters (side-chain dihedral angles on the Met and BP sides; characteristic inter-side chain *d*(S‒O) distance) within two 100-ns simulations, one simulation for each of the dyads **(S,S)-BP-DKP-Met** and **(S,R)-BP-DKP-Met**, respectively. The red horizontal dashed lines indicate the “close-contact” *d*(S‒O) distance.

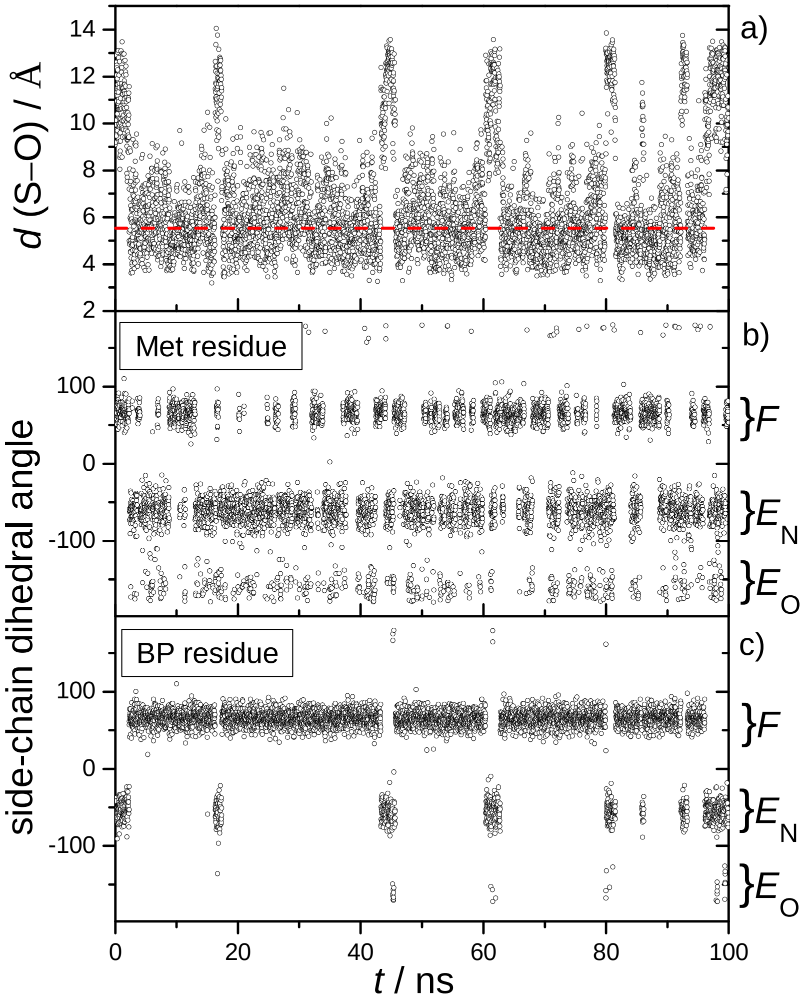

Figure 3.3-20 Long-time molecular-dynamics simulations for **(S,S)-BP-DKP-Met** (implicit-solvent model for ACN); a) time variation of the inter-side-chain distance *d*(S–O) between the sulfur atom from Met and the BP carbonyl oxygen atom; b) time variation of the Met side-chain dihedral angle; c) time variation of the BP side-chain dihedral angle.

In agreement with the DFT results, mainly three rotamers ($\mathbf{E_O}$, $\mathbf{E_N}$, **F**) of the methionine and only two rotamers ($\mathbf{E_N}$, **F**) of the benzophenone side chain are populated. The probabilities for the population of the most likely conformations of the DKP-based BP-Met dyads are larger than those for the open-chain analogues. Especially the conformational preferences of the BP side chain of both dyads are well defined, meaning that the probabilities for the most likely conformations are large.

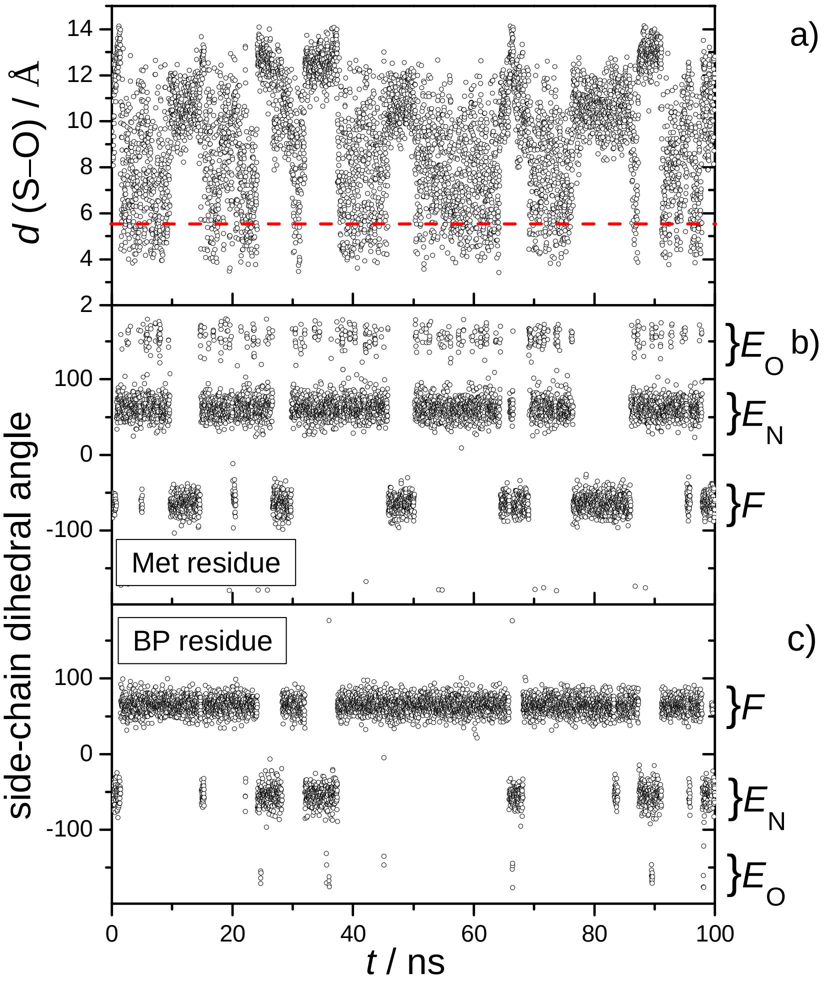

Figure 3.3-21 Long-time molecular-dynamics simulations for **(S,R)-BP-DKP-Met** (implicit-solvent model for ACN); a) time variation of the inter-side-chain distance *d*(S–O) between the sulfur atom from Met and the BP carbonyl oxygen atom; b) time variation of the Met side-chain dihedral angle; c) time variation of the BP side-chain dihedral angle.

The total probabilities for the BP side chain of **(S,S)-BP-DKP-Met** and **(S,R)-BP-DKP-Met** to be in the **F** structure were found to be 0.85 and 0.79, respectively. From the analysis of the data presented in Figure 3.3-20b,c and Figure 3.3-21b,c, it can be seen that there are two most preferable configurations for both dyads, namely **E_N–F** and **F–F**. The probabilities of the dyads **(S,S)-BP-DKP-Met** and **(S,R)-BP-DKP-Met** to be in one of these two conformations was 78 % and 72 %, respectively (Table 3.2-6). A comparison of the DFT calculated order of the rotamers (Table 3.3-2) with the MD-calculated probabilities of the side-chain rotamer population (Table 3.3-3) reveals that the MD simulations predict a higher population of **F–F** than would be expected from the DFT results.

Table 3.3-3 Summary of the side-chain rotamer joint probabilities of **(S,S)-BP-DKP-Met** and **(S,R)-BP-DKP-Met** computed from the molecular-dynamics simulations (implicit ACN model).

Conformation	Joint probability	
	(S,S)-BP-DKP-Met	**(S,R)-BP-DKP-Met**
F–F	0.31	0.23
E_N–F	0.47	0.49
F–E_N	0.07	0.07
E_N–E_N	0.02	0.12
E_O–F	0.07	0.07

It is important to note that the **F–F** structure of **(S,S)-BP-DKP-Met** corresponds to a conformation of the side chains wherein both moieties (BP, Met) are back folded across the DKP ring at the same time (Figure 3.3-22a).

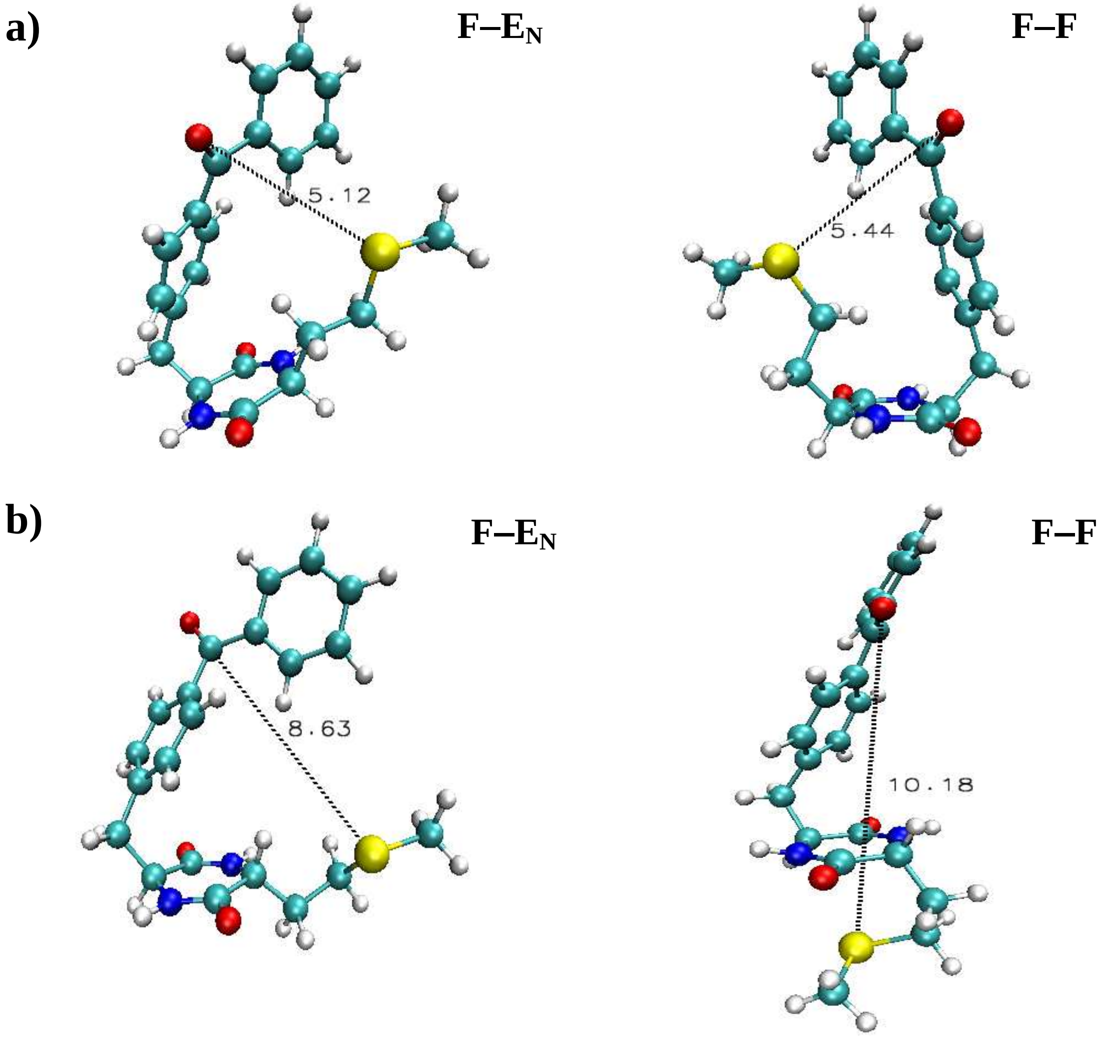

Figure 3.3-22 Two types of the most populated conformations found in long time MD simulations (implicit-solvent model for ACN) for a) **(S,S)-BP-DKP-Met** and b) **(S,R)-BP-DKP-Met**; numbers denote the S–O distance in Ǻ; Yellow: sulfur; red: oxygen; dark blue: nitrogen.

As can be seen, the **F–F** structure of **(S,S)-BP-DKP-Met** allows for close contact of the sulfur and carbonyl oxygen. On the other hand, that same type of conformation, **F–F**, for **(S,R)-BP-DKP-Met** corresponds to a structure, with a long inter-side-chain S–O distance (Figure 3.3-22b). It is worth noting that another type of conformation, namely **E_N–F**, also gives different S–O distances for both dyads **(S,S)-BP-DKP-Met** and **(S,R)-BP-DKP-Met** (Figure 3.3-22a,b).

Based on the MD simulations, pair-distribution functions were calculated for the carbonyl/sulfur distance *d*(S–O) (Figure 3.3-23). While the populations of the particular conformations were found to be quite similar, the pair-distribution functions revealed very important differences between this pair of diastereoisomers. The sampling of **(S,S)-BP-DKP-Met** in an implicit model of acetonitrile solution gave a quite narrow pair-distribution function with a maximum at a distance *d*(S–O) = 5 Å. The situation is different for the **(S,R)-BP-DKP-Met** for which the pair-distribution function of the carbonyl/sulfur distance *d*(S–O) not only is much wider compared to the one for **(S,S)-BP-DKP-Met** but exhibits even another noticeable maximum at about 10.6 Å.

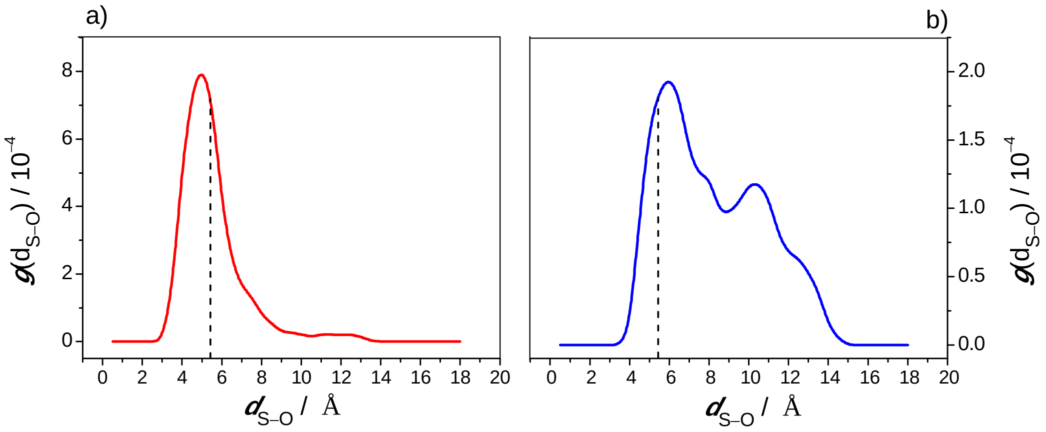

Figure 3.3-23 Pair-distribution functions of the carbonyl/sulfur group distance *d*(S–O), obtained with molecular-dynamics simulation in ACN for a) **(S,S)-BP-DKP-Met**; b) **(S,R)-BP-DKP-Met**.

The most important observation based on the pair-distribution functions is that, although both dyads were capable of forming rotamers with relatively close-contact between the sulfur and carbonyl oxygen, the probability of *d*(S–O) to be less than 5.5 Å (vertical dashed lines in Figure 3.3-23) was calculated to be only 0.09 for **(S,R)-BP-DKP-Met**, while the analogous value for **(S,S)-BP-DKP-Met** was 0.42. That may give an explanation for the observed stereodifferentiation in the triplet quenching of **(S,R)-BP-DKP-Met** and **(S,S)-BP-DKP-Met**.

3.3.2.4 **Discussion**

Intramolecular excited triplet-state quenching in diastereomeric compounds composed of a benzophenone chromophore and a methionine moiety were investigated by laser flash photolysis and steady-state irradiations in order to gather information about chiral discrimination in the primary step, as well as in the overall photoprocess. Moreover, Moretto *et al.* have recently reported data on an efficient intramolecular side-chain to side-chain macrocyclization reaction between BP and Met residues in a helical heptapeptide.[165] This type of photocyclization reaction is being intensively investigated because it is a useful method for achieving stabilization of specific conformations of the peptide and improving resistance toward proteolytic degradation.[165-168] Thus it was of interest to check if this type of intramolecular side-chain to side-chain ring formation can occur in the already quite rigid structure of a DKP-based BP-Met.

As expected, introduction of a rigid linker between the reactive moieties became manifested in a significant chiral discrimination of the triplet-state quenching between the **(S,R)-BP-DKP-Met** and **(S,S)-BP-DKP-Met** pair of diastereoisomers. It is noted, that stereoselectivity, expressed as the ratio of the triplet lifetimes for the diastereoisomers measured in ACN, was found to be 15, whereas triplet lifetimes of the flexible open-chain BP-Met dyads differed only by a factor 2.5. As the benzophenone moiety is covalently linked to the methionine, the stereodifferentiation must be the result of the steric hindrance introduced by the rigid spacer with respect to a close approach between the two active moieties. The reactivity trend was rationalized by MD simulations that showed a marked difference between these two stereoisomers in regard to their probabilities of forming rotamers with relatively close contact between the sulfur and carbonyl oxygen. The much higher probability of forming a close contact distance d(S–O), found for **(S,S)-BP-DKP-Met**, coincides, indeed, with a faster triplet state quenching.

Based on the analogy to the data on intermolecular triplet-state quenching of benzophenones by compounds containing a methionine group, it was assumed that intramolecular electron transfer from the sulfur atom to the triplet state of the BP is the primary photochemical step in the triplet-state quenching of both diastereoisomers.

Decay of the initial charge-transfer complex may involve (1) back electron transfer and (2) proton transfer within the complex. Reaction of the BP ketyl radical and an α-thio-alkyl radical may subsequently lead to stable products, or the system may revert to the starting materials. The contributions of different decay pathways were studied by LFP and steady-state irradiations. Importantly, the spectrum obtained for **(S,S)-BP-DKP-Met** in pure ACN carries significant contributions from a ketyl radical. Based on the spectral resolution technique, it was shown that the quantum yield of ketyl-radical formation is $\Phi \approx 0.6$ (Scheme 3.3-1). Quenching of the triplet state of **(S,S)-BP-DKP-Met** can thus be attributed to a fairly efficient intramolecular H-atom transfer reaction.

On the other hand, the transient absorption spectra of **(S,R)-BP-DKP-Met** showed basically just the benzophenone triplet-state absorption and only a weak absorption that could be assigned to ketyl radicals. This points to an efficient back electron transfer and/or to a short lifetime of the ketyl radical, either or both of which do not allow the ketyl radical to accumulate.

Further mechanistic information concerning the triplet-state quenching for **(S,S)-BP-DKP-Met** and **(S,R)-BP-DKP-Met** was obtained from steady-state irradiations and product analyses. In addition, as outlined above from the LFP studies, the diastereodifferentiation in the quenching of the excited triplet benzophenone chromophore by methionine was inferred to be significant for **(S,R)-BP-DKP-Met** and **(S,S)-BP-DKP-Met**. So, it was also important to check whether a similar diastereodifferentiation is observed in the overall photoreaction quantum yields. **(S,S)-BP-DKP-Met** and **BP-DKP-Met-(R,S)** were the only compounds, among the ones investigated in this thesis, for which the triplet-state quenching process showed a high degree of irreversibility. A higher quantum yield of substrate disappearance ($\Phi = 0.35$) was measured for **(S,S)-BP-DKP-Met**, for which also a faster triplet quenching was observed by LFP. For the second diastereoisomer, **(S,R)-BP-DKP-Met**, the quantum yield of substrate disappearance was found to be $\Phi = 0.18$. Interestingly, although the triplet-state quenching of the compounds **(S,S)-BP-DKP-Met** and **(S,R)-BP-DKP-Met** showed high chiral discrimination, the quantum yield of the substrate disappearance differed only by a factor of 2. In addition, the triplet states of **(S,S)-BP-DKP-Met** and **(R,S)-BP-Met** were found to be quenched with the same rate constants in ACN, but the respective quantum yields of substrate disappearance for these compounds differed by a factor of 7. This distinct behavior in regard to the efficiency of the substrate consumption between these two dyads indicates that there are not only special structural constraints influencing on the triplet-state quenching rate constants but also additional geometric factors that control the efficiency of the secondary reactions that may lead to stable products.

To gain further insight into the mechanism of the triplet-state quenching of BP by methionine, the photoproduct from the irradiation of **(S,S)-BP-DKP-Met** was analysed. Combining the results of the analysis of the LFP experiments and molecular structure of the stable product of the irradiation of **(S,S)-BP-DKP-Met** helped in establishing the complete mechanism of the reaction (Scheme 3.3-1). The suggested mechanism for the formation of this product is as follows. First, there is an electron-transfer step, resulting in a radical-ion pair complex. Second, within this complex, an intramolecular proton transfer occurs, involving exclusively the α-CH_3 group, adjacent to the sulfur. The result of this two-step process is a biradical: a ketyl radical and an α-thio-alkyl radical. Subsequently, these biradicals undergo intramolecular recombination to the macrocyclic ring system (Φ = 0.35). The generated carbon-centered biradicals can also revert to the starting materials *via* back hydrogen transfer ($\Phi \approx 0.25$), as shown in Scheme 3.3-1.

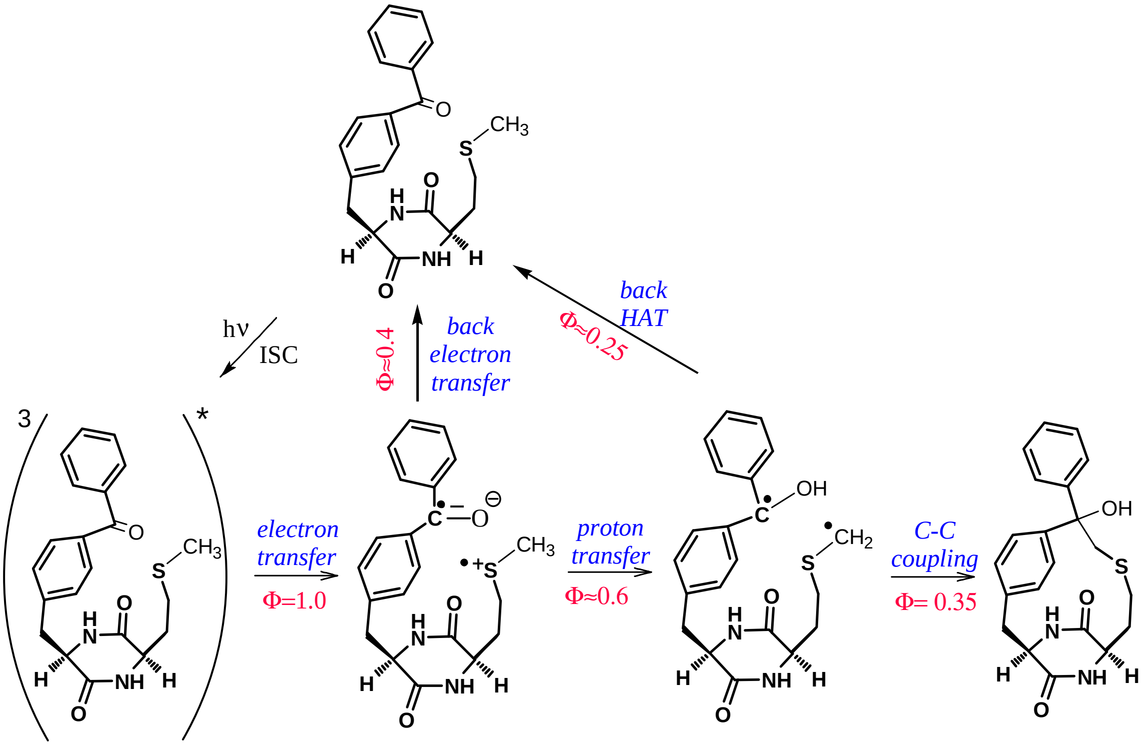

Scheme 3.3-1 Overview of mechanistic pathways upon excitation of **(S,S)-BP-DKP-Met**.

Interestingly, the investigated intramolecular photoreaction of **(S,S)-BP-DKP-Met** was found to be strictly regioselective, involving only the original Met side-chain α-CH_3 carbon (α to the sulfur). This exclusiveness is likely to be a consequence of the higher strain that is expected if the neighboring Met side-chain α-CH_2 group (α to the sulfur) were involved. The regioselectivity trend was quantitatively rationalized by DFT (PBE1PBE, 6-31+G(d)) by optimizing the structures of the two possible macrocyclic products. These calculations confirmed that a proton transfer involving the Met side-chain α-CH_2 carbon would, indeed, give rise to a highly strained product, with an energy higher by 20 kcal/mol than the energy of the identified product. It is worth noting though that the observation of exclusive deprotonation from the Met side-chain α-CH_3 carbon does not necessarily exclude the possibility of a deprotonation from the Met side-chain α-CH_2 carbon in other peptide or protein substrates with different geometrical characteristics.

In conclusion, the experimental results showed that quenching of the triplet state of the **(S,S)-BP-DKP-Met** led to a biradical which recombined to a macrocyclic photoproduct with one additional asymmetric carbon center. Such intramolecular carbon-carbon bond formation reaction might thus be a useful tool in synthetic organic photochemistry for the preparation of small rings and large macrocycles.

3.4 Trichromophores: benzophenone–methionine–tyrosine and benzophenone–leucine–tyrosine

It is well documented that both tyrosine and methionine, as single amino acids exhibit high reactivity towards triplet states of carbonyl compounds, i.e. benzophenone and 4-carboxybenzophenone. The efficient intramolecular quenching of benzophenone triplets by methionine and tyrosine in the dyads benzophenone-tyrosine and benzophenone-methionine, described earlier in this thesis, raised the natural question whether the presence of both triplet quenchers, tyrosine and methionine, in the same chemical structure would have a synergistic effect on the intramolecular triplet-quenching process. Two triads were investigated: carboxybenzophenone-methionine-tyrosine and carboxybenzophenone-leucine-tyrosine, to probe this question. The latter compound was used as a comparative reference, in which methionine was substituted by leucine which itself should be nonreactive; hence, no synergistic effect would be expected for this compound.

As in the case of the dyads, the photochemical experiments were complemented by theoretical calculations, especially on the three-dimensional structures of the triads in their reactive states which may allow for intramolecular H-atom- and electron-transfer processes.

3.4.1 Flash photolysis: spectral and kinetic analysis

The excited-state dynamics of **CB-Met-Tyr** and **CB-Leu-Tyr** were studied by means of nanosecond-laser photolysis in 3 different solvents: ACN, ACN-H_2O (1:1 v/v), and TFE. The work addressed, in particular, the medium effect on methionine’s role in the triplet quenching. This was investigated through a comparison of the reactivities of the two triads. In order to avoid bimolecular-quenching processes, that were observed for these compounds at higher concentrations, excitation at 266 nm was used in addition to excitation at 355 nm. The more intense absorption of the compounds at 266 nm allowed the use of lower triad concentrations, which, in turn, permitted an exclusive study of the intramolecular processes.

In ACN solutions, the triplet state was identified as the dominate intermediate in the early transient absorption spectra by its characteristic absorption maxima at 350 nm (not shown) and at 550 nm, in addition to a long-wavelength absorption above 600 nm.

It is noted that for the triads i.e., para-substituted benzophenones connected *via* amidoethyl linkers, both absorption maxima are red shifted by 20 nm compared to pure benzophenone.[65] For both compounds a significant spectral evolution was observed with a spectral shift from 550 to 570 nm, accompanied by a growth at 405 nm. This indicated the formation of ketyl and tyrosyl radicals, respectively (Figure 3.4-1). The short intrinsic triplet lifetimes of the triads gave evidence for high intramolecular reactivity. There was no visible difference in the transient absorption spectra between **CB-Met-Tyr** and **CB-Leu-Tyr** which might have pointed to some contribution from methionine in the triplet quenching. The absence of any differences in the transient absorption spectra between these two trichromophores did, however, not necessarily mean that methionine did not directly participate in the triplet quenching. In particular, methionine quenched the triplet states efficiently in **(S,S)-BP-Met** and **(R,S)-BP-Met** (very short triplet lifetime) in ACN although the transient decays were not connected with any significant spectral evolutions, except for enhanced triplet decays (Chapter 3.3.1.1).

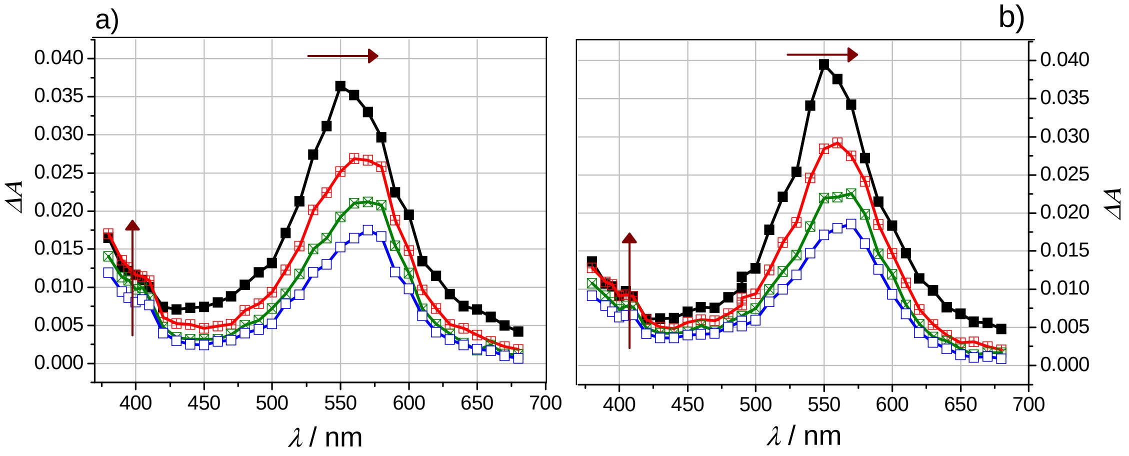

Figure 3.4-1 Transient absorption spectra obtained during laser flash photolysis at 266 nm of deoxygenated solutions (3 × 10^{-5} M) in ACN of compounds a) **CB-Met-Tyr**; b) **CB-Leu-Tyr**; time delays after flash (from top to bottom): 30, 70, 110, 150 ns.

Furthermore, no distinction in the triplet quenching of the two triads in ACN could be seen, neither from a comparison of the decay profiles monitored at a wavelength characteristic for the ketyl radical, 570 nm (Figure 3.4-2a) nor at 650 nm, which can be assigned to the triplet state when no radical anion is present (Figure 3.4-2b). Comparison of the kinetics profiles at 650 nm in ACN showed that the decay of the triplet for **CB-Met-Tyr** was only slightly faster than the triplet decay of **CB-Leu-**

Tyr. Triplet lifetimes were obtained from the short-lived components of biexponential fits to the transient decays at 650 nm. They were equal to 57 ns and 54 ns for **CB-Leu-Tyr** and **CB-Met-Tyr**, respectively.

Based on the good overlap of the normalized transient absorption spectra of the two triads at various time delays and on the small difference in their triplet lifetimes it was concluded that methionine was inert in the quenching of the triplet state of **CB-Met-Tyr** in ACN. This is in accord with the results obtained by Hörner for the benzophenone-methionine dyad where the orientation (para position) and linkage (amide bond) of the benzophenone and methionine chromophores were exactly the same as in the trichromophore **CB-Met-Tyr**.[164] As with **CB-Met-Tyr**, this benzophenone-methionine dyad was found to be inert toward intramolecular triplet quenching.[164]

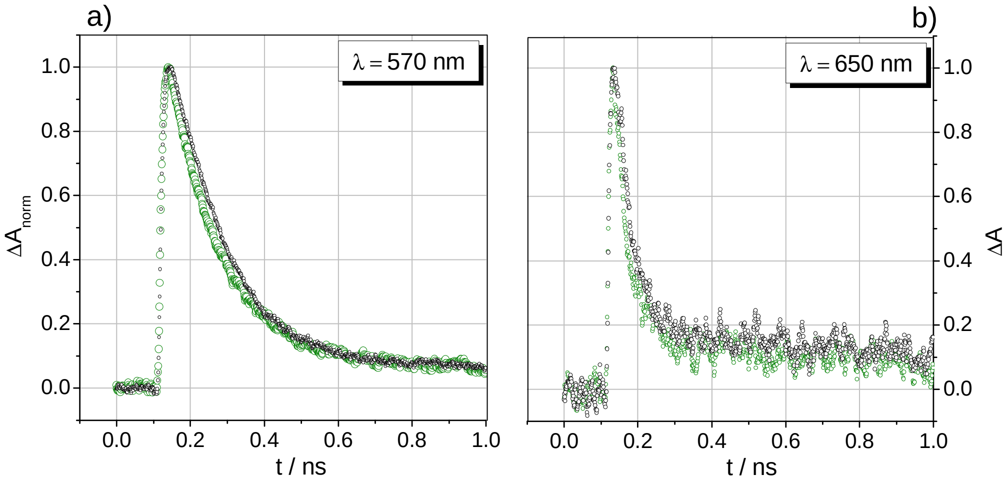

Figure 3.4-2 Normalized decay profiles of the transient absorption monitored at a) 570 nm b) 650 nm for triads after 266 nm laser pulsing in ACN: **CB-Met-Tyr** (green), **CB-Leu-Tyr** (black).

Intramolecular H-atom transfer rate constants for both trichromophores were calculated from two independent experiments performed at 355 nm excitation, with the concentration of the compounds at 2.4×10^{-3} M, and at 266 nm excitation, with the concentration of the compounds at 3×10^{-5} M. In the latter excitations, contributions from the self-quenching processes were negligible. It is noted that the k_H values calculated for **CB-Met-Tyr** and **CB-Leu-Tyr** were found to be equal, within experimental error. This behavior can be understood on the basis of the MD simulation results. These simulations showed that substitution of leucine by methionine did not affect the dynamics of the tyrosine side-chain. Furthermore, the pair-distribution functions for the carbonyl to hydroxylic group distances d(O–O) in the two triads were found to overlap (see Chapter 3.4.3.2).

Table 3.4-1 Intramolecular H-atom transfer rate constants obtained for the **CB-Met-Tyr** and **CB-Leu-Tyr** in ACN.

Triads	**k_H (10^7 s^{-1})**	
	355 nm excitation[a]	266 nm excitation[b]
CB-Met-Tyr	1.83	1.6
CB-Leu-Tyr	1.74	1.7

[a] estimated error ± 10 %; [b] estimated error ± 5 %

In summary, the LFP experiments showed that the triplet decay of both **CB-Leu-Tyr** and **CB-Met-Tyr** can actually be attributed to an efficient intramolecular H-atom transfer reaction.

In order to examine the solvent dependence of the triplet quenching in the two triads, LFP was also performed in two protic solvents: an ACN-H_2O (1:1 v/v) mixture and TFE. In contrast to the results obtained in ACN, the spectra of both triads in TFE could not be assigned to the triplet state unambiguously, even at short times after the laser pulse. Even at these short delay times, the transient absorption spectra carried already significant contributions from tyrosyl radicals and ketyl radicals (Figure 3.4-3). It was concluded, that the triplet lifetimes of the triads were dramatically reduced on going from the non-protic to the protic solvents.

The triplet decays of **CB-Met-Tyr** in TFE were connected with the formation of ketyl radicals $CBH^{\bullet}$ and tyrosyl radicals Tyr($O^{\bullet}$) (Figure 3.4-3). However, in contrast to the transient absorption spectra of **CB-Leu-Tyr**, the transient absorption spectra obtained for **CB-Met-Tyr** clearly indicated also the presence of the CB radical anion, $CB^{\bullet-}$, with an absorption above 600 nm (Figure 3.4-3). Formation of the $CB^{\bullet-}$ in the triplet quenching of **CB-Met-Tyr** was attributed to an intramolecular electron transfer from the methionine residue (Figure 3.4-3). A bimolecular path for the formation of $CB^{\bullet-}$ could be neglected because of the low concentrations used in the experiments and, in addition, due to the observed very fast intramolecular quenching.

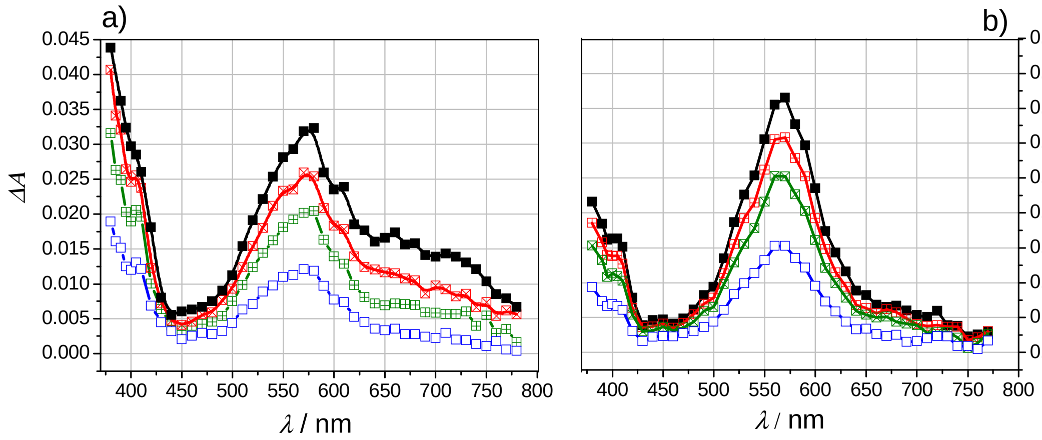

Figure 3.4-3 Transient absorption spectra obtained during laser flash photolysis at 266 nm of deoxygenated solutions (2.8×10^{-5} M) in TFE of compounds a) **CB-Met-Tyr**; b) **CB-Leu-Tyr**; time delays after flash (from top to bottom): 30, 60, 100, 200 ns.

Further evidence for the different nature of the quenching processes of **CB-Leu-Tyr** and **CB-Met-Tyr** in TFE came from a kinetic treatment of the transient decays. For **CB-Leu-Tyr**, the kinetic profiles coincide with each other, irrespective of the wavelengths (Figure 3.4-4b). This speaks in favor of the presence of only one intermediate in the system, namely the biradical (CBH$^{\bullet}$–Tyr(O$^{\bullet}$)), formed *via* intramolecular H-atom transfer. However, for **CB-Met-Tyr**, the kinetic profile at 650 nm (blue symbols in Figure 3.4-4a) decays faster than the kinetic profiles for wavelengths below 600 nm. This difference confirmed that the origin of the absorption above 600 nm for **CB-Met-Tyr** in TFE is different from that of the species absorbing below 600 nm.

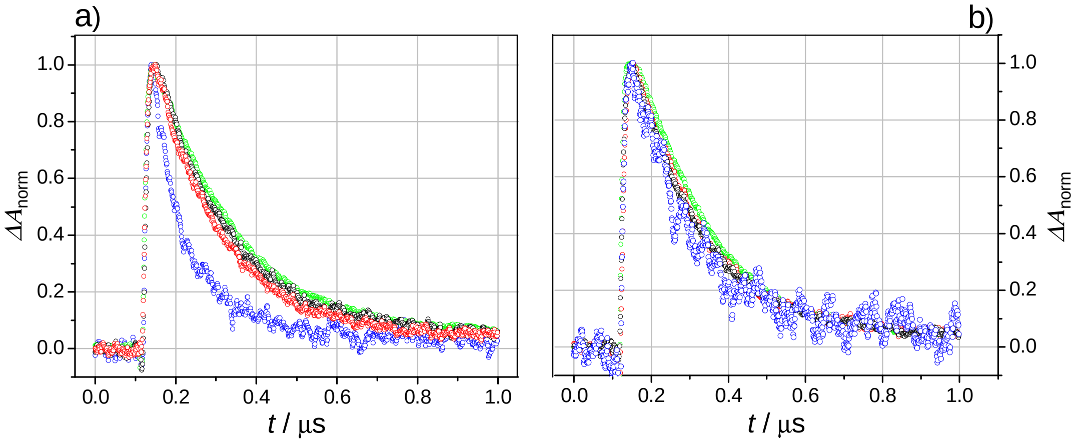

Figure 3.4-4 Normalized decay profiles of the transient absorption monitored at different wavelengths for a) **CB-Met-Tyr** b) **CB-Leu-Tyr** after 266 nm laser pulsing in TFE; wavelengths code: 650 nm (blue), 340 nm (green), 550 nm (red), 570 nm (black).

Spectral-resolution techniques were applied, in order to unravel the nature of the intermediates of the excited-state processes for **CB-Met-Tyr** in TFE. Over the complete time scale of the transient decay, only the spectral components for CBH$^{\bullet}$, Tyr(O$^{\bullet}$) and CB$^{\bullet-}$ were needed to simulate the experimental data quantitatively (Figure 3.4-5). Reference spectra for the ketyl radical CBH$^{\bullet}$, tyrosyl radical Tyr(O$^{\bullet}$) and radical anion CB$^{\bullet-}$ obtained following flash photolysis in aqueous solutions were used in the spectral resolution under the assumption that the shapes of the spectra and the molar absorption coefficients remained unchanged in TFE. From the resolution of the transient absorption spectra and the resulting concentration profiles, the maximum concentrations of CBH$^{\bullet}$ and CB$^{\bullet-}$ were determined to be 8.6 μM and 4.6 μM, respectively. From these values and the actinometrically determined triplet concentration (14 μM), the quantum yields of CBH$^{\bullet}$ and CB$^{\bullet-}$ were found to be 0.61 and 0.33, respectively.

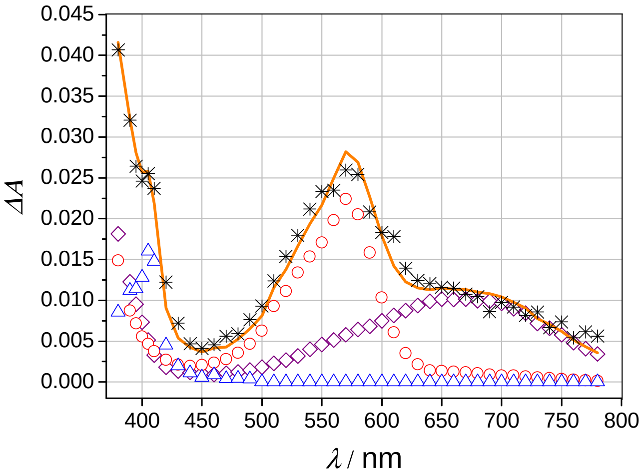

Figure 3.4-5 Resolutions of transient absorption spectra taken 60 ns after 266 nm laser pulsing (8 mJ) of a solution of **CB-Met-Tyr** in TFE; the symbols represent: ○ for the ketyl radical CBH$^{\bullet}$, Δ for the tyrosyl radical Tyr(O$^{\bullet}$), ◊ for the CB radical anion CB$^{\bullet-}$ and * for the experimental data. The solid curve is the resulting fit from the regression analysis.

In conclusion, the nanosecond flash photolysis performed in TFE revealed significant differences between the two investigated triads and gave evidence that in a protic solvent (TFE), in contrast to a non-protic solvent (ACN), intramolecular electron transfer from the methionine residue was involved in one of the triplet-state quenching pathways.

Femtosecond flash photolysis

The fact that the triplet states of interest could not be detected in protic solvents even at the early times after a nanosecond laser pulse, suggested that these triplet states decayed too rapidly for observing them on a ns time scale. Therefore, the measurements were extended into the femtosecond time domain, using the equipment provided by the Radiation Laboratory at the University of Notre Dame.

For both trichromphores, the initial signal, following the femtosecond laser pulse, showed a maximum at 600 nm which is assigned to the excited singlet state absorptions. Decay of these absoptions was in agreement with the formation of the absorption bands in both triads at 550 nm (Figure 3.4-6 and Figure 3.4-7). In the case of 258 nm photolysis, excitation of the tyrosine chromophore cannot be avoided, but comparison of the molar absorption coefficients shows that excitation of the tyrosine moiety amounts to less than 10 %. In addition, although the $S_1 \rightarrow S_n$ transient absorption spectra of phenol reported by Herman *et al.* exhibits a maximum absorption at 600 nm, it is much broader than that observed in the femtosecond flash photolysis experiment of the triads.[169]

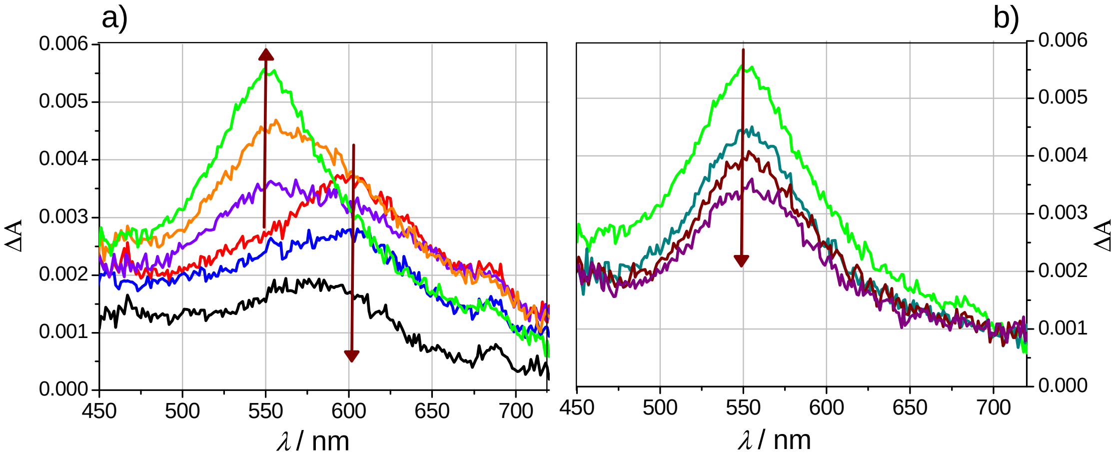

Figure 3.4-6 Transient absorption spectra obtained during femtosecond laser flash photolysis at 258 nm of a deoxygenated solution (2.8×10^{-5} M) in TFE of **CB-Met-Tyr**; time delays after flash a) 0.4 (red trace), 0.6, 0.8, 3, 6, 20 (green trace) ps; b) 20, 400, 600, 1100 ps.

The lifetime of the initially formed intermediate obtained by a monoexponential fit to the experimental decay profiles at 600 nm to the first 100 ps was equal to 15 ps. Peters *et al.* reported a singlet lifetime of benzophenone in ethanol to be 16.5 ps.[170] In addition, the maximum absorption of the excited singlet state of benzophenone was observed at 575 nm.[171] Taking into account that the transient absorption spectra of the triplet state of CB and the ketyl radical CBH$^\bullet$ were red shifted by 20 nm relative to benzophenone, it is probable that the initially observed intermediates with the maximum absorption at 600 nm are the excited singlet states of **CB-Leu-Tyr** and **CB-Met-Tyr**.

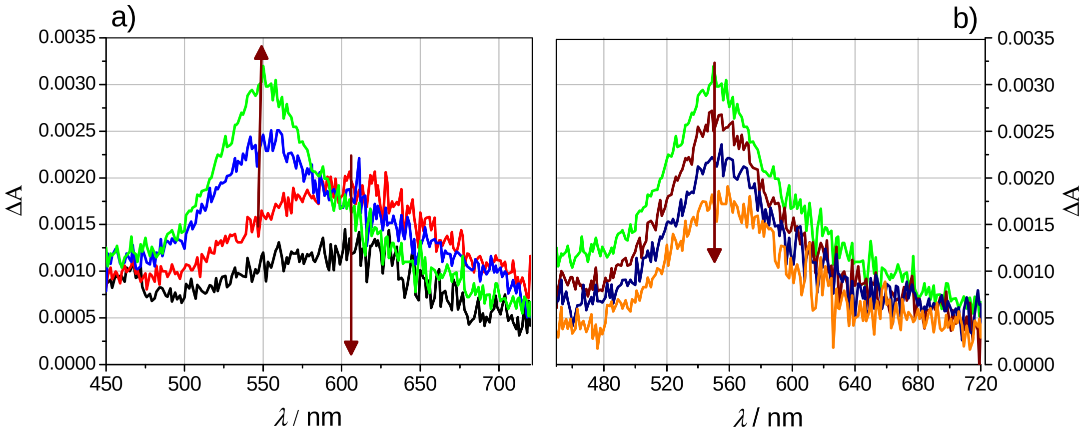

Figure 3.4-7 Transient absorption spectra obtained during femtosecond laser flash photolysis at 258 nm of a deoxygenated solution (2.8 × 10^{-5} M) in TFE of **CB-Leu-Tyr**; time delays after flash: a) 0.4 (red trace), 0.8, 5, 20 (green trace) ps; b) 20, 200, 500, 1000 ps.

The absorption with a maximum at 550 nm, observed after complete decay of the absorption with the maximum at 600 nm, matches to the transient absorption spectra of the triplet state of the triads observed in the nanosecond flash photolysis experiment in ACN (Figure 3.4-1). The kinetic profiles at the maximum absorptions at 550 nm showed a decay, although this was not complete within 1.2 ns (Figure 3.4-8), which is the upper limit of the timescale available with the fs apparatus.

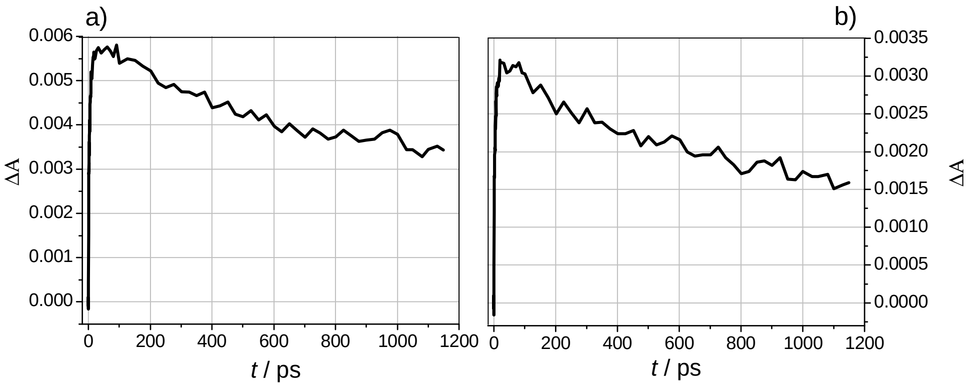

Figure 3.4-8 Decay profiles of the transient absorption monitored at 550 nm for triads after 258-nm femtosecond laser pulsing in TFE: a) **CB-Met-Tyr**; b) **CB-Leu-Tyr**.

Based on the shape of the spectra and the position of the maximum, it seems reasonable to attribute the band with 550 nm to the triplet state. However, then the lack of any spectral shift from 550 nm to 570 nm due to ketyl radical formation remains unexplained. Any speculation on this will not be made here.

3.4.2 Steady-state irradiation

Information about differences in reactivity between the two trichromophores could also be obtained from steady-state irradiations. Steady-state consumption during irradiation of 2 mM solutions of **CB-Met-Tyr** and **CB-Leu-Tyr** at 313 nm in ACN and TFE, was quantified by HPLC with UV-detection. Quantum yields of substrate disappearance for **CB-Met-Tyr** and **CB-Leu-Tyr** in ACN were found to be 0.049 and 0.035, and in TFE 0.013 and < 0.005, respectively. Differences in the quantum yields of the substrate disappearance between the dyads were not significant, but, for both compounds, higher quantum yields were obtained in ACN as solvent.

LFP of the triads showed that, for both compounds, triplet lifetimes were significantly reduced by much faster intramolecular reactions in TFE compared to ACN. The rapid intramolecular reactions limited the possibility of measuring the bimolecular-quenching pathways. Although the time-resolved technique revealed a significant enhancement of electron transfer from methionine to the carbonyl triplet state of **CB-Met-Tyr** in TFE, the quantum yields of substrate disappearance obtained from the steady-state irradiation were almost the same as for **CB-Leu-Tyr** and also very small. Based on the small quantum yields of disappearance of **CB-Leu-Tyr** in TFE, it can be stated that intramolecular HAT is practically a reversible reaction. The same conclusion holds also for the electron-transfer process from methionine since, even though electron transfer was found to be a fairly efficient quenching pathway for the triplet state, it did not lead to significant substrate disappearance during irradiation.

LFP of the triads in ACN at 355 nm excitation at millimolar triad concentrations showed that for both compounds the intramolecular H-atom transfer reactions were efficient. However with the triplet lifetimes of 54 ns and 57 ns for **CB-Met-Tyr** and **CB-Leu-Tyr**, respectively, the self-quenching processes could not be neglected although they would be of minor importance. Thus, the higher quantum yields found in ACN, in comparison to TFE, were attributed to self-quenching processes from the tyrosine side-chain of **CB-Leu-Tyr** and from tyrosine and methionine side-chains of **CB-Met-Tyr**. No attempts were made to identify the stable products at this stage.

3.4.3 **Theoretical calculations**

In order to aid in the interpretation of the LFP results presented above on **CB-Met-Tyr** and **CB-Leu-Tyr**, theoretical calculations were performed, and the relevant results will be presented in the following. These studies establish a quantitative picture of the distributions of the sulfur to carbonyl oxygen and hydroxylic oxygen to carbonyl oxygen distances of the triads. The calculations also define the molecular prerequisites on the quenching geometries.

3.4.3.1 **DFT calculations**

The molecular conformations of **CB-Met-Tyr** and **CB-Leu-Tyr** were addressed by ground-state DFT calculations in the gas phase. Structural searches by energy minimizations were performed for three side-chain conformers of tyrosine and methionine or tyrosine and leucine for **CB-Met-Tyr** and **CB-Leu-Tyr**, respectively. In addition, two different relative orientations of the carbonyl groups attached to the benzophenone moiety, *syn* and *anti*, were considered. The results for the gas-phase calculations of the ground state showed that conformations with favorable quenching geometries for H-atom transfer (close contact of the carbonyl oxygen and hydroxylic oxygen) were available for both triads. Those conformations that were found to have the lowest energy are shown in Figure 3.4-9.

Surprisingly, the limited flexibility of the CB side-chain, due to the rigid amide bond associated with the methionine or leucine linkers, did not influence the possibility of forming a conformation with a short O–O distance. The theoretical studies showed that both triads can form stable conformations that involve a close approach of the HAT reactive moieties, which seems to be reflected in the high intramolecular reactivity of both compounds.

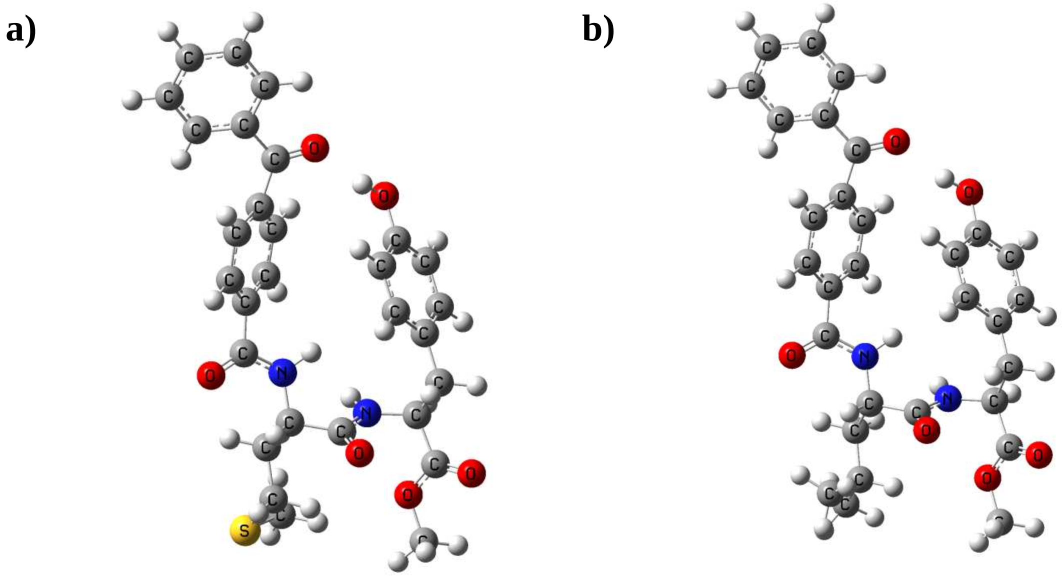

Figure 3.4-9 PBE1PBE/6-31G-optimized geometries in the gas phase of the lowest energy structure for ground state of a) **CB-Met-Tyr** b) **CB-Leu-Tyr**.

3.4.3.2 Molecular Dynamics

Insight into the dynamics of the two trichromophores came through molecular-dynamics calculations, which helped in establishing the distribution of the sulfur to carbonyl oxygen and the hydroxylic oxygen to carbonyl oxygen distances. From these distributions it was possible to see how the intramolecular reactivity of **CB-Met-Tyr** and **CB-Leu-Tyr** developed in time.

Here, the results of the molecular-dynamics simulations for an implicit ACN solvent model will be presented. The interconversion between different molecular conformations was studied by means of long-time molecular-dynamics simulations (implicit-solvent model for ACN). The conformations of the triad molecules can be characterized by side-chain conformations of the Tyr and Met or Leu residues. Benzophenone is connected with the residues (Met or Leu) *via* an amide bond which limited rotational freedom of that moiety so that only two different relative orientations of the carbonyl groups attached to the benzophenone moiety, namely *syn* and *anti* could be considered. It is well known, that hydrogen-atom transfer reactions demand close contact between the H-atom donor and the accepting carbonyl moiety. So, it was of principal interest to determine the probabilities of forming rotamers with the close contact necessary for intramolecular reaction of the Tyr and BP moieties. Figure 3.4-10 and Figure 3.4-11 summarize the time variation of two molecular parameters (side-chain dihedral angle from the Tyr side; characteristic inter-side chain *d*(O–O) distance) within a 100-ns simulation for triads **CB-Met-Tyr** and **CB-Leu-Tyr**, respectively. Definition of the side-chain dihedral angle can be found in Chapter 3.2.1.3.1.

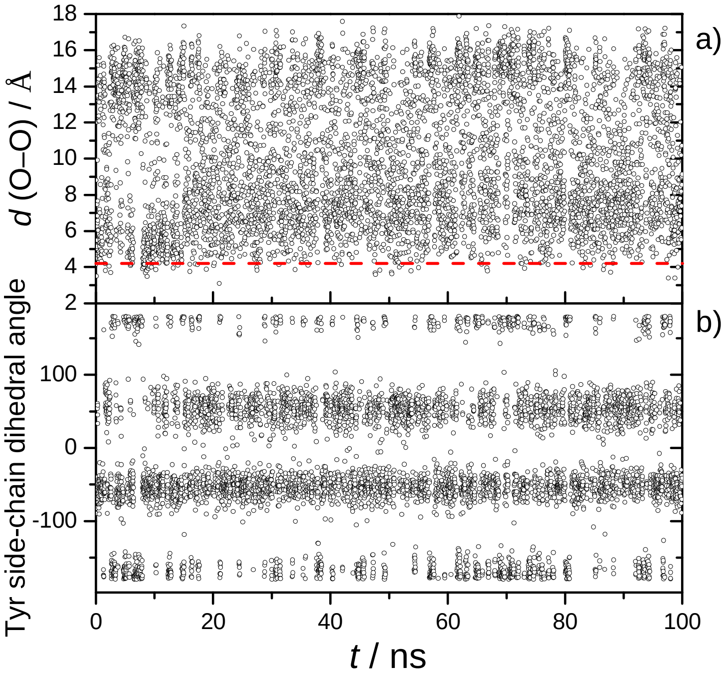

Figure 3.4-10 Long-time molecular-dynamics simulations for **CB-Met-Tyr** (implicit-solvent model for ACN); a) time variation of the inter-side-chain distance *d*(O–O) between the Tyr hydroxylic oxygen atom and the CB carbonyl oxygen atom; b) time variation of the Tyr side-chain dihedral angle.

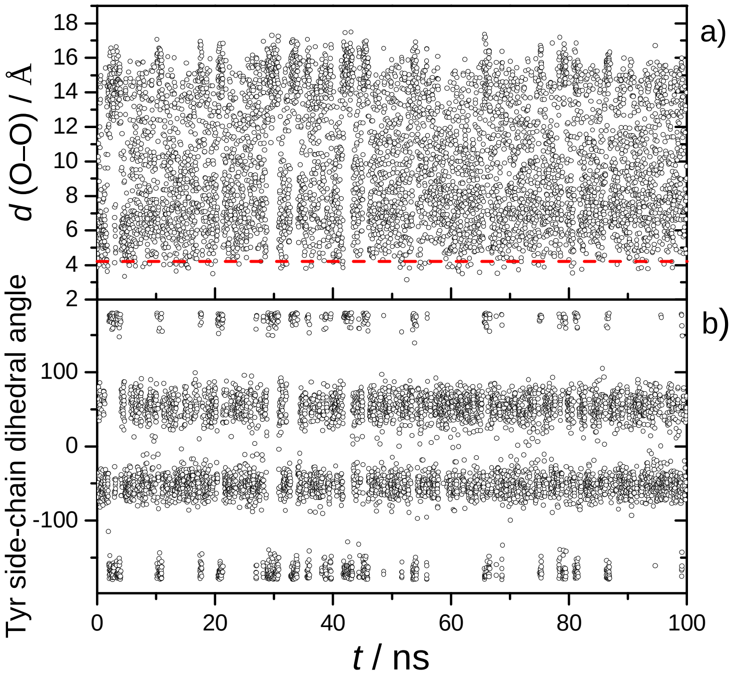

Figure 3.4-11 Long-time molecular-dynamics simulations for **CB-Leu-Tyr** (implicit-solvent model for ACN); a) time variation of the inter-side-chain distance *d*(O–O) between the Tyr hydroxylic oxygen atom and the CB carbonyl oxygen atom; b) time variation of the Tyr side-chain dihedral angle.

Figure 3.4-10a and Figure 3.4-11a show the changes in the distance *d*(O–O) between the Tyr hydroxylic oxygen atom and the CB carbonyl oxygen atom. Clearly, conformations with larger O–O distances (up to 17 Å) prevail. However, the results also unambiguously show that both trichromophores **CB-Met-Tyr** and **CB-Leu-Tyr** can, nevertheless, form conformations within the 4 Å range (dotted line in Figure 3.4-10a and Figure 3.4-11a) which allow for close contacts, as found in the DFT calculations and, see below, the pair-distribution functions. An important result from this analysis was that MD-derived populations of the Tyr side-chain rotamers showed no difference between the two investigated trichromophores. That result indicates that replacement of the leucine group by a methionine residue did not affect the dynamics of the tyrosine moieties and the possibility of the formation of conformations with close contacts between the reactive moieties. This conclusion is of importance for understanding not only the high intramolecular reactivity toward HAT in the two triads but also the experimental finding that both triads had the same value for their intramolecular HAT rate constants, $k_{H.}$

In addition, the pair-distribution functions of the carbonyl/hydroxylic group distance *d*(O–O), calculated based on the data from the MD simulations for **CB-Met-**

Tyr and **CB-Leu-Tyr**, provided further evidence for the lack of a difference between the two distance *d*(O–O) distributions of the two triads (Figure 3.4-12). The results confirm that both triads were capable of forming rotamers with close-contacts, starting with 3.5 Å between the hydroxylic group and carbonyl oxygen.

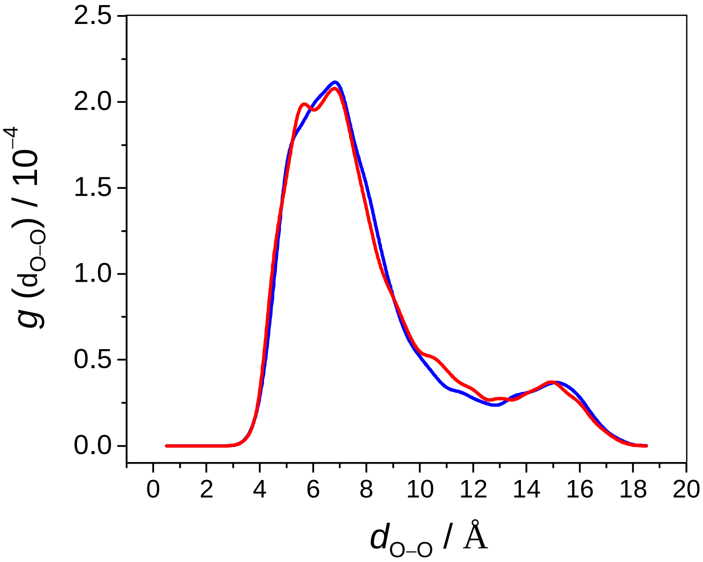

Figure 3.4-12 Pair-distribution functions of carbonyl/hydroxylic group distance *d*(O–O), obtained from molecular-dynamics simulation for **CB-Met-Tyr** – (blue), **CB-Leu-Tyr** – (red).

In the case of **CB-Met-Tyr**, the excited triplet state could also be quenched by electron transfer from methionine moieties, but surprisingly this was not observed in ACN. So, it was of interest to calculate also the pair-distribution function for the carbonyl oxygen/sulfur distance *d*(S–O) (Figure 3.4-13). The presence of a rigid amide bond in the para-position in the benzophenone-methionine connection in **CB-Met-Tyr** confined the accessible space of the remote groups in a way that close contacts between the carbonyl oxygen and the sulfur were completely inhibited. The pair-distribution function of the carbonyl/sulfur distance *d*(S–O) in the triad **CB-Met-Tyr** is significantly shifted to longer distances compared to the *d*(S–O) pair distribution functions in the very reactive benzophenone-methionine dyads discussed in Chapter 3.3. Methionine in **CB-Met-Tyr** was found to be completely inert in the intramolecular quenching of its triplet state in ACN. Based on the MD-simulation, this inertness can be attributed to the limitation in flexibility of the linkage between the interacting groups, expressed by *d*(S–O).

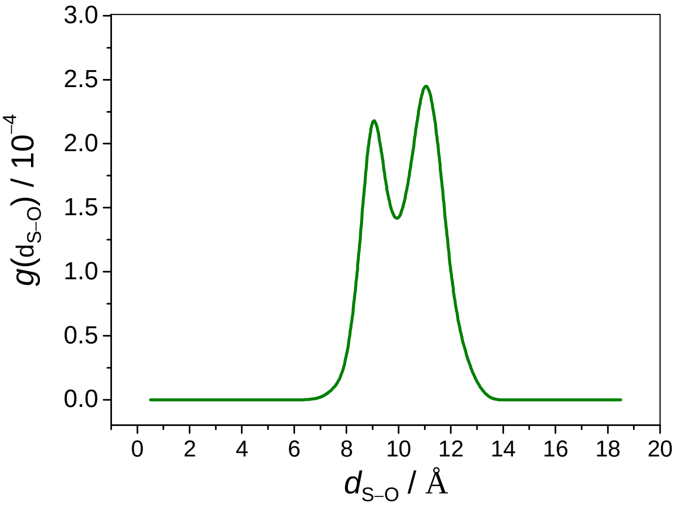

Figure 3.4-13 Pair-distribution functions of the carbonyl/sulfur group distance *d*(S–O), obtained from molecular-dynamics simulation in ACN for **CB-Met-Tyr**.

3.4.4 **Discussion**

Flash photolysis and theoretical calculations were used to investigate structural and solvent effects concerning the efficiencies of the triplet excited state quenching pathways for the two trichromophores: **CB-Met-Tyr** and **CB-Leu-Tyr**. First of all, both of the investigated compounds showed high reactivity toward intramolecular HAT. The high intramolecular reactivity of the triads was attributed to the high flexibility of the Tyr side-chain. More interestingly, the intramolecular HAT rate constants k_H of the two triads in ACN were found to be equal, within experimental error. MD simulations for an implicit solvent provided evidence that not only close contacts of the reactive moieties is possible for both triads but also the calculated pair-distribution functions of the carbonyl/hydroxylic group distance *d*(O–O) were the same for **CB-Met-Tyr** and **CB-Leu-Tyr**. This means that substitution of leucine by methionine did not influence the dynamics of the tyrosine side-chain or its reactivity toward intramolecular HAT.

Methionine moieties were found to be completely inert toward triplet quenching in ACN, which, together with the same reactivity of the Tyr side for both triads, made the behavior of **CB-Met-Tyr** and **CB-Leu-Tyr** in flash photolysis experiments indistinguishable in this solvent.

In contrast to the behavior in a non-protic solvent, the flash photolysis studies in TFE and ACN-H_2O (1:1 v/v) revealed significant differences between the **CB-Met-Tyr** and **CB-Leu-Tyr**. For both compounds, the triplet lifetimes were significantly reduced to such an extent that the triplet lifetimes were shorter than the detection limit of the nanosecond flash photolysis systems employed. However, in the case of **CB-Met-Tyr**, the methionine residue also participated in the triplet quenching as opposed to the triplet quenching results for **CB-Met-Tyr** in ACN. The presence of the $CB^{\bullet-}$ was observed only for one triad: **CB-Met-Tyr** in the protic solvents. This indicated that intramolecular electron transfer from methionine is one of the quenching pathways for the **CB-Met-Tyr** triplet state in protic solvents. The reactivity of excited **CB-Met-Tyr** was greatly enhanced in protic solvents. Similar conclusions were drawn from studies of **(S,R)-BP-DKP-Tyr** (Chapter 3.2.2.1) and **(S,R)-BP-DKP-Met** (Chapter 3.3.2.1) where dramatic activating solvent effects were observed. In addition, the efficient one-electron oxidation of anisole by triplet-excited benzophenone was observed only in protic solvents (Chapter 3.6). So, it appeared highly probable that the solvent-driven enhancement of the reactivity described here is a more general phenomenon.

It is an important result that the intramolecular-quenching paths (H-atom transfer from the tyrosine side-chain and electron transfer from the methionine side-chain) were reversible reactions and did not lead to stable products. Efficient back-electron transfer and lack of substrate disappearance for the **CB-Met-Tyr** in TFE were in contrast to the significant substrate consumption for the cyclic BP-Met dyads (Chapter 3.3.2.2). These results imply special structural requirements for the reactions to be reversible.

In summary, the presented experimental and theoretical work implied that efficiencies of excited triplet-state quenching paths (H-atom transfer from tyrosine and electron transfer from methionine) strongly depend on: (1) the flexibility of the linkers between the reactive moieties and (2) on the nature of the solvent. The rigid amide bond between BP and Met in **CB-Met-Tyr** limited completely the methionine reactivity in ACN. However, fairly efficient electron transfer from methionine was shown to occur in protic solvents.

3.5 Solvent effect studies with related compounds

3.5.1 Methoxybenzene analogues of benzophenone-tyrosine dyads

As pointed out in Chapter 2.5.5. it was necessary for a quantitative assessment of the intramolecular H-atom transfer rate constants, k_H, to know the natural triplet lifetimes of the compounds in the respective solvents. These triplet lifetimes were obtained by employing reference compounds of known properties. Due to the relatively low rate constants (~10^6 M^{-1} s^{-1}) and the lack of transient intermediates in the quenching of carbonyl triplets by anisole, O-methylated, anisole-type phenolic derivatives of BP/Tyr (BP-AN) were thought to be the most suitable compounds that could provide information on the intrinsic triplet-state properties of the bichromophores: benzophenone-tyrosine. Corresponding methoxy analogues of the phenolic dyads have, in fact, also been successfully applied by other research groups as reference compounds to account for non-HAT triplet-decay pathways.[46, 48, 51, 54]

3.5.1.1 Nanosecond flash photolysis: spectral and kinetic analysis

Laser-flash photolysis experiments on the intramolecular H-atom transfer reactions in triplet-excited benzophenone-tyrosine dyads in different solvents were followed by the experiments with O-methylated phenolic derivatives which should provide information on the intrinsic triplet-state properties of the dyads. Initially only non-protic solvents were investigated. The transient spectra, recorded upon 355 nm excitation of **(S,R)-BP-DKP-TyrOMe**, **(R,R)-BP-DKP-TyrOMe** and **(R,S)-BP-TyrOMe** in non-protic solvents (ACN, DCM, $CHCl_3$, DCE, EtOAc, C_6H_5CN) were dominated by strong absorptions at 325 nm (not shown) and 525 nm (see Figure 3.5-1). The spectra obtained at short times after the laser pulse matched those previously reported for the benzophenone triplet state. The transient absorption spectra exhibited no spectral evolution during the decay of the triplet in most of the solvents. Just in chlorohydrocarbon solvents, there was a small tendency of the triplet state to abstract H-atoms from the solvent, evidenced by some ketyl-radical formation (Figure 3.5-1b).

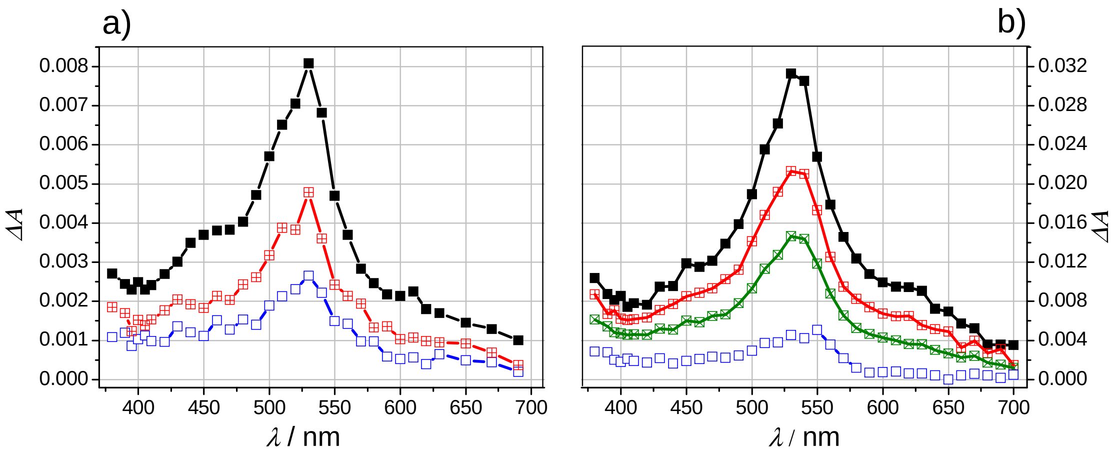

Figure 3.5-1 Transient absorption spectra obtained during laser flash photolysis at 355 nm of deoxygenated solutions of **(S,R)-BP-DKP-TyrOMe** in a) ACN: time delays after flash: 0.2, 3, 5 μs; b) DCM: time delays after flash: 0.1, 0.5, 1, 3 μs.

The values of the natural triplet lifetimes were extracted from mono-exponential fits to the experimental decay profiles at 630 nm. The triplet lifetimes in non-protic solvents were found to be in the range from 6 μs in ACN to 1.3 μs in DCM. The measured values were in accord with the triplet lifetimes of pure benzophenone in the respective solvents.[76]

The results of the LFP of the BP-AN compounds in protic solvents were in striking contrast to the data obtained in non-protic solvents in the sense that the transient absorption spectra in TFE and HFIP showed significant spectral evolution (Figure 3.5-2a, b). Transient products had previously not been observed in the BP-triplet quenching by anisole, even in the very polar ACN-H_2O (4:1 v/v) mixture.[108]

The triplet lifetimes of the methoxy analogues of the BP-Tyr dyads in the protic solvents were also much shorter than the triplet lifetime reported for pure benzophenone. The measured triplet lifetimes of the reference compound **(S,R)-BP-DKP-TyrOMe** in TFE and HFIP were equal to 220 ns and 50 ns, respectively. In general, the triplet lifetimes of the methoxy analogues of the BP-Tyr dyads were reduced dramatically on going from non-protic to protic solvents. The results in non-protic solvents were compatible with unproductive (no products) quenching *via* a charge-transfer state, whereas the generally fast quenching in protic solvents was accompanied by efficient formation of intermediates.

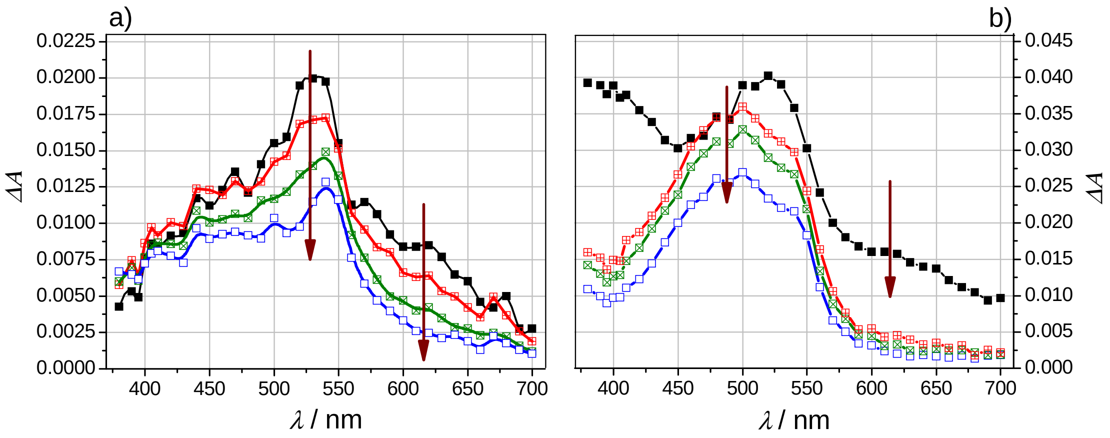

Figure 3.5-2 Transient absorption spectra obtained during laser flash photolysis at 355 nm of deoxygenated solutions of a) **(S,R)-BP-DKP-TyrOMe** in TFE; time delays after flash: 80, 150, 250, 350 ns; b) **(R,R)-BP-DKP-TyrOMe** in HFIP; time delays after flash: 80 (black symbols), 240, 280, 360 ns.

Since the methoxy analogues of the BP-Tyr dyads were not inert toward triplet quenching in protic solvents, they could not be used as reference compounds to estimate the natural triplet lifetimes of the benzophenone-tyrosine dyads.

3.5.2 **Benzophenone–diketopiperazine**

Because of the unexpectedly high reactivity of the initially employed reference compounds (the methoxy analogues of the BP/Tyr dyads) in protic solvents, ultimately benzophenone derivatives bearing only the diketopiperazine ring were chosen as the reference compounds to provide a reliable indication of the natural triplet decay of the respective BP-DKP-Tyr dyads.

3.5.2.1 **Nanosecond flash photolysis: spectral and kinetic analysis**

BP-DKP was studied by means of LFP in the same 12 solvents and solvents mixtures as the BP-DKP-Tyr dyads in order to provide the natural triplet-decay rate constants in the respective solvents. In particular, these experiments were conducted to determine the k_T required for calculating the intramolecular HAT, k_H (see Chapter 2.5.5). In all solvents the triplet state was identified as the dominate intermediate in the early spectra by its characteristic absorption maxima at 325 nm (not shown) and 520 nm, in addition to a long-wavelength absorption above 600 nm (Figure 3.5-2). The triplet state spectra of **BP-DKP** and pure BP were found to be indistinguishable from each other and showed only little variation with the change of solvent. Exceptional behavior was noted during the LFP of **BP-DKP** in HFIP solution, where an additional absorption band became evident at 400 nm. In addition, in TFE solutions, higher absorbance was also observed around 400 nm in comparison to other solvents (Figure 3.5-3b). The transient decays for the compound were not connected with any significant spectral evolutions with the exception of the solvents that can act as H-atom donor to the BP triplet. In MeOH, transient spectra revealed that the triplet decays of BP were connected with efficient ketyl-radical formation. In DCM, the efficiency of the ketyl-radical formation was small (Figure 3.5-3a) whereas in ACN, the solvent was virtually inert towards the BP triplet state.

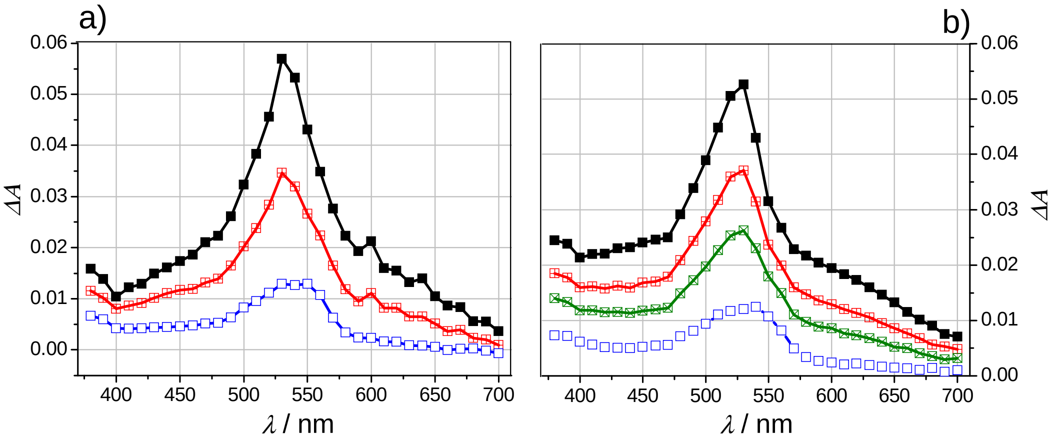

Figure 3.5-3 Transient absorption spectra obtained during laser flash photolysis at 337 nm of deoxygenated solutions of **BP-DKP** in a) DCM: time delays after flash: 0.1, 1, 3 μs; b) TFE: time delays after flash: 0.5, 4, 8, 20 μs.

Triplet lifetimes of **BP-DKP** in the respective solvents were obtained from monoexponential fits to the transient decays at 630 and from mono- or biexponential fits to the transient decays at 520 nm. The biexponential decay at 520 nm in the H-donor solvents is due to an overlap of the absorptions of ^{3}BP and the ketyl radical, BPH$^{\bullet}$. Long lifetimes of the triplet state in the microsecond range were observed irrespective of the solvents used (protic, non-protic). The triplet lifetimes measured in all solvents for **BP-DKP** were in agreement with the data obtained for pure benzophenone, indicating that the diketopiperazine ring did not affect the natural triplet decays in the respective solvents. Values for natural triplet rates constants, k_T, obtained by experiments with the reference compound, are summarized in Table 3.5-1. The range of values from < 10^5 s^{-1} in ACN-H_2O mixtures to 4.4 × 10^6 s^{-1} in MeOH mainly reflects the ability of the solvent to act as an H-atom donor to the BP triplet (Table 3.5-1). The k_T data from Table

3.5-1 were used in the evaluation of the intramolecular HAT transfer rate constants of the benzophenone-tyrosine dyads according to the procedure described in Chapter 2.5.5.

Table 3.5-1 Summary of natural triplet decay rate constants of **BP-DKP** in the investigated solvents.

	Solvent	**k_T (10^5 s^{-1})^a**
1	chloroform	6.8
2	dichloromethane	7.5
3	1,2-dichloroethane	4.9
4	acetonitrile	1.7
5	benzonitrile	7.3
6	ethyl acetate	2.3
7	trifluoroethanol	1.3
8	methanol	43.5
9	HFIP	2.0
10a	ACN/ H_2O (9:1 v/v)	< 1.0
10b	ACN/ H_2O (4:1 v/v)	< 1.0
10c	ACN/ H_2O (2:1 v/v)	< 1.0

[a] experimental error ≤ 5 %.

3.5.3 Discussion

Based on reports in the literature on (1) unproductive quenching of the triplet state of BP by anisole *via* a charge-transfer state[107, 108] and (2) the small quenching rate constants,[107-110] O-methylated phenolic derivatives of benzophenone-tyrosine dyads were initially thought to be the most suitable reference compounds for the purpose of estimating the natural triplet decay of the BP/Tyr bichromophores.

The concept of using these methoxy analogues as reference compounds worked well in all nonprotic solvents, that is, the BP triplet showed long lifetimes, owing to the weak affinity between anisole and BP. However, the reactivities of triplet-excited BP in the BP-AN derivatives were dramatically dependent on the nature of the solvent. In particular, the reactivities of the systems were dramatically enhanced in protic solvents. Triplet lifetimes were shortened so much in protic solvents that they were even comparable with the triplet lifetimes of the corresponding benzophenone-tyrosine dyads. Moreover, the presence of metastable intermediates was observed in the transient absorption spectra of these reference compounds in protic solvents. This unexpected activation of the BP-AN systems in protic solvents was the reason for their failure to serve as appropriate reference compounds for the purpose of estimating the natural triplet lifetimes of the benzophenone-tyrosine dyads. Thus, instead of these methoxy compounds, the benzophenone chromophore linked to the diketopiperazine ring was used as the reference compound.

The enhanced reactivity of methoxy compounds in protic solvents might be a significant parameter though for studies which, prompted by the low-reactivity of the anisole derivatives, considered the use of methoxy analogues of the phenolic dyads as reference systems for the chemistry of phenols.[46, 48, 51, 54]

The above finding of the high reactivity of the BP towards anisole, in conjunction with the formation of intermediates in these systems, appeared to be unprecedented in the previous literature on this topic; the same comment applies to other triplet sensitizers as well. There is only one single report, which noted the production of anisole radical cations following triplet quenching of an anthraquinone derivative, notably in aqueous solution.[172] The results, described above, raised the natural questions: (1) what is the nature of the reaction mechanism and (2) what is the correspondence between the BP reactivity toward anisole and the solvent character? Since the obviously solvent-dependent intramolecular reactions in the methoxy analogues of the benzophenone-tyrosine dyads were necessarily complicated by the intramolecular dynamics, a study of the bimolecular reaction between the two chromophores (benzophenone and anisole) appeared to be a more reasonable system to study in order to understand, in detail, the mechanism of the BP triplet quenching by anisole and to identify the role of the solvent in the activation of the observed enhanced reactivity. This will be dealt with in the following chapter.

3.6 Bimolecular quenching of triplet-excited benzophenones by anisole

The initial step in the quenching of triplet-excited BP by anisole in non-protic solvents has charge-transfer character and is fairly slow. This conclusion had been drawn earlier by a number of workers.[107-109] No transient products of the BP-triplet quenching by anisole have ever been observed, even in the very polar solvent ACN or in ACN/water mixtures. However, the results on the BP-anisole derivatives in TFE and HFIP discussed in Chapter 3.5.1.1 were not in accord with the literature data. Therefore, an extended study was undertaken on the bimolecular quenching of the triplet state of benzophenone by anisole in order to establish a quantitative picture of the quenching process in protic solvents.[18] This system was chosen since it was deemed to be much simpler to understand compared to the intramolecular quenching in the O-methylated phenolic derivatives of the BP-Tyr dyads. The dynamics of the bimolecular quenching of triplet-excited benzophenone by anisole were investigated by nanosecond flash photolysis. A detailed study of the solvent dependence of the reaction rates and efficiencies in a number of protic and non-protic solvents was carried out in order to verify that the strong activation of the reactivity is a general phenomenon and not limited only to fluorinated alcohols. These studies were augmented by theoretical modelling and experimental investigation of solute/solvent interactions in the triplet-excited state and in the ground state.

3.6.1 Hydrogen-bonding of the BP chromophore in the ground and in the triplet-excited state

Based on the results on the BP-AN derivatives (Chapter 3.5.1.1), the hydrogen-bond (HB) donating capability of the solvents was identified as an important parameter that can influence the rates and the mechanism of BP-triplet quenching by anisole. Thus, spectroscopic studies and theoretical calculations were performed to confirm the presence of the HB interaction between benzophenone and the protic additives (HS). The ultraviolet absorption spectra of benzophenone were measured to determine the ground-state properties of BP in solvents of different hydrogen-bonding abilities. The absorption of the $\pi\rightarrow\pi^*$ band around 250 nm showed a continuously increasing red shift with an increase of the HB-donating abilities of the solvents (here defined in terms of

Kamlet's HB acidity α_{Kamlet})[173] on going from ACN (α_{Kamlet} = 0.3), ACN-H_2O (4:1 v/v) (α_{Kamlet} = 0.89), TFE (α_{Kamlet} = 1.51) to HFIP (α_{Kamlet} = 1.96) (Figure 3.6-1).

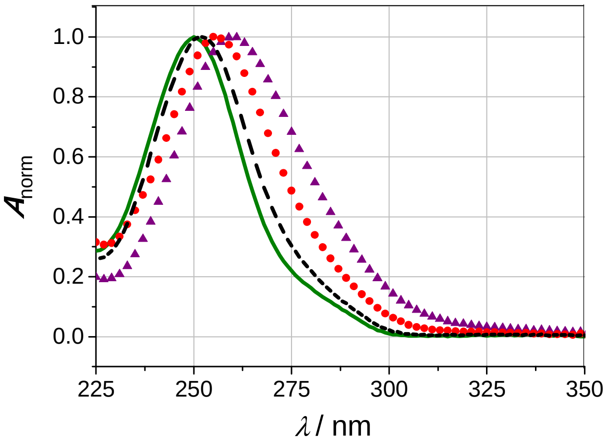

Figure 3.6-1 The $\pi\rightarrow\pi^*$ band in the UV absorption spectrum of benzophenone in ACN (green solid line), ACN-H_2O (4:1 v/v) (– – –), TFE (●), HFIP (▲).

Although HFIP has the smallest dielectric constant ε among the investigated solvents it exerts the strongest effect on the BP absorption with a maximum at 260 nm in comparison with 252 nm in an ACN-H_2O (4:1 v/v) mixture. The most important contribution to the observed solvatochromic effect, therefore, is due to specific solute-solvent interactions resulting from the formation of hydrogen bonding between the solute molecule and the protic solvent. These conclusions are fully in accord with early studies on BP solvation, which attributed the spectral red shift of the $\pi\rightarrow\pi^*$ absorption to (relatively weaker) effects of the permittivity and (relatively stronger) effects of the HB to the solvent; that is, to unspecific and specific solvation, respectively.[141, 174, 175]

In order to characterize the hydrogen bonding of solvent molecules with benzophenone in a quantitative manner, the equilibrium constants K for the formation of 1:1 hydrogen bonded solvent-solute complexes were extracted from the effects of protic additives to BP solutions in DCM on the $n\rightarrow\pi^*$ band of BP around 340 nm. Absorption spectra of BP in dilute DCM solution were measured in the presence of varying amounts of TFE (Figure 3.6-2b) and HFIP. They exhibited a typical blue shift of the $n\rightarrow\pi^*$ absorption band in HB media. The evaluation followed the procedures invented by Mataga and Tsuno[39, 176] which is summarized in Eq 3.6-1

$$\frac{\left[1-\frac{A_0}{A}\right]}{c_0} = -K + \left(\frac{\varepsilon_c}{\varepsilon}\right) K \frac{A_0}{A} \qquad \text{Eq 3.6-1}$$

Herein, ε_c and ε denote the molar absorption coefficients of the complex and the free molecules, respectively, whereas A_0 and A denote the measured absorbance at a given wavelength in the absence and presence of the HB-additive, and c_o is the total concentration of the HB additive, which has to be much greater than the concentration of BP.

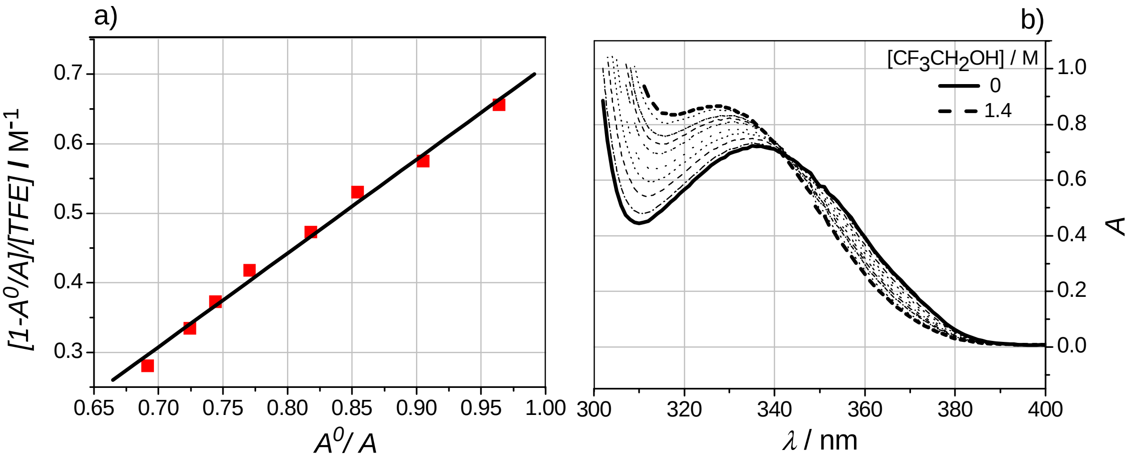

Figure 3.6-2 Effect of the addition of trifluoroethanol on the absorption spectra of benzophenone in dichloromethane (3×10^{-3} M); a) plot of absorbance data at 320 nm, according to Eq 3.6-1 b) UV spectra.

Plots of the absorption data in terms of Eq 3.6-1 for TFE (Figure 3.6-2a) and HFIP were linear. Based on this result, the conclusion was drawn that benzophenone and the protic additives TFE and HFIP form 1:1 ground-state complexes in DCM. From the intercept of the plot in Figure 3.6-2a, an equilibrium constant $K = 0.65 \pm 0.08$ M^{-1} was obtained for H-bonding with TFE in DCM. As expected, the formally stronger HB-acid HFIP gave a larger equilibrium constant of $K = 2.5 \pm 0.3$ M^{-1}. Both values are comparable with the data obtained by Linschitz *et al.* for the HB of fluorenone with TFE and HFIP in DCM.[39]

This experimental evidence for the formation of hydrogen bonded BP-solvent complexes applied only to the ground state of benzophenone. In order to supplement this information, DFT calculations were used to characterize the HB-complexes between benzophenone and a solvent molecule, both in the ground state and in the excited triplet state. The hydrogen-bond energy (E_{HB}) was calculated for different distances between the hydrogen-bond donor (a single molecule of TFE) and the hydrogen-bond acceptor (the carbonyl oxygen of BP). Separate calculations were made for the ground state and the triplet state. The detailes of the procedure can be found in Chapter 2.3.1. The plots, depicted in Figure 3.6-3, show the dependence of E_{HB} (calculated hydrogen-bond energy) for these two BP–TFE complexes.

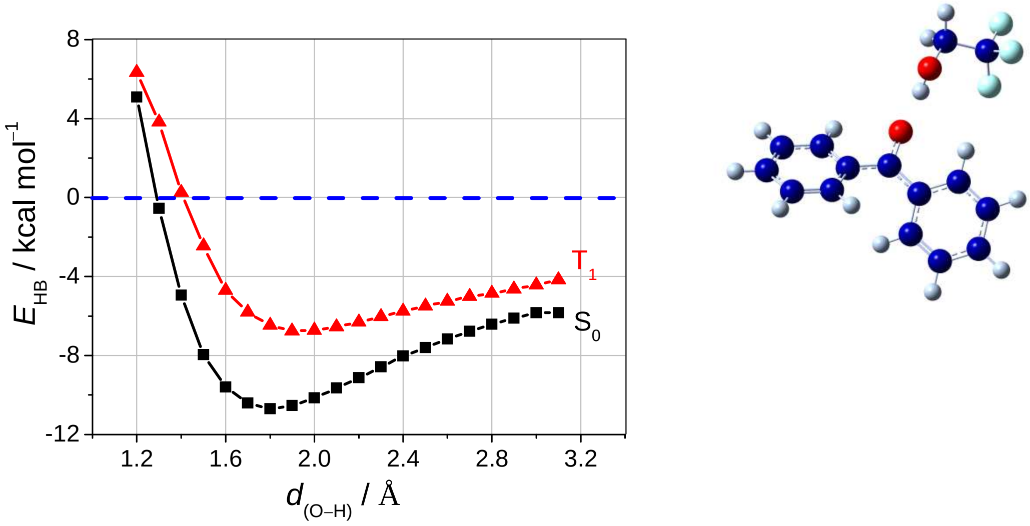

Figure 3.6-3 Calculated hydrogen-bond energies (stabilization energy, kcal/mol) of a 1:1 BP–TFE complex as a function of the O–H distance (Å) for the ground state (■) and the triplet state (▲); the point of zero energy (dotted line) denotes the two components of the complexes at infinite separation. Structural arrangement of the complex at the right.

The calculations show that the hydrogen bond is weakened when going from the ground state to the triplet state. This is reasonable due to the diminished n-electron density in the lowest BP triplet state which is of n,π^* character. However, even in the triplet state the stabilization energy was 6.7 kcal/mol at the minimum, which was calculated to occur at a distance of 1.9 Å. Thus, the presence of hydrogen-bonding interactions between benzophenone and TFE was confirmed both by experiments and theoretical calculations. It was shown that, in protic solvents, the BP is complexed to the solvent both prior and after excitation.

3.6.2 **Triplet quenching by anisole: kinetics**

In order to determine the bimolecular quenching rate constants k_q, the decay of the triplet state of benzophenone was monitored at 630 nm in the presence of increasing concentrations of anisole. Under the experimental conditions, all the time profiles were fit to first-order exponential decay functions with a reciprocal lifetime equal to k_{obs}.

Plots of these pseudo-first order rate constants, k_{obs}, against the anisole concentration were linear in all cases. Some illustrative examples are given in Figure 3.6-4. Notably, larger donor concentrations (up to 1 M) did not give rise to any significant deviation from linearity. In particular, no saturation was observed in the Stern-Volmer plots, as had been reported in some chemically related systems.[53, 177]

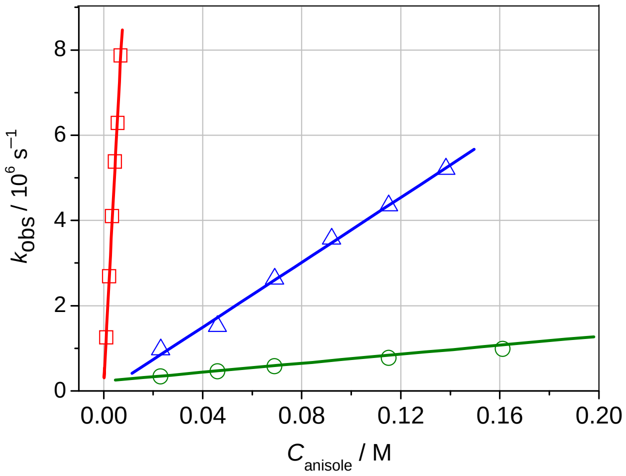

Figure 3.6-4 Concentration dependence of the pseudo-first order triplet-decay rate constants k_{obs} for benzophenone quenched by anisole in HFIP (red), acetic acid (blue), and ACN (green); [BP] = 5×10^{-3} M.

The bimolecular quenching rate constants, k_q, obtained from the Stern-Volmer type plots (see Chapter 2.5.4) for quenching of the triplet state of benzophenone by anisole in different solvents are summarized in Table 3.6-1. The data obtained in the nonprotic solvents are well in accord with the data previously reported.[107, 108]

Table 3.6-1 Summary of solvent parameters and rate constants for triplet quenching of ^{3}BP by anisole.

Solvent	ε^a	α_{Kamlet}	k_q [$M^{-1}s^{-1}$]
ACN	35.9	0.3	4.5×10^6
ACN-H_2O (4:1 v/v)	≈ 45^b	≈ 0.89	1.5×10^7
acetic acid	6.2	1.12	3.8×10^7
TFE	27.7	1.51	2.4×10^8
HFIP	16.7	1.96	1.1×10^9

[a] At 25 ºC. CRC Handbook of Chemistry and Physics, CRC Press, Boca Raton, 76th Ed., 1995.
[b] interpolated from literature data.[178]

A comparison of the kinetic data in Table 3.6-1 shows that triplet quenching by anisole is dramatically dependent on the nature of the solvent. The bimolecular rate constants cover a range of three orders of magnitude, with the highest being consistently found in protic solvents. Such significant differences between quenching rate constants, k_q, suggest that the quenching mechanism may vary among the investigated solvents. It should be noted that only a two-fold increase in the triplet-quenching rate constants was reported on changing solvents from benzene ($\varepsilon = 2.3$) to acetonitrile ($\varepsilon = 35.9$).[107, 109]

As can be deduced from the data in Table 3.6-1, there certainly exists no unifying correlation of k_q with the permittivity of the solvent. On the other hand, it can be noted that larger k_q values are found in solvents which are characterized by higher Taft's and Kamlet's[173] H-bond acidity α_{Kamlet}.[18] This parameter, alpha, describes the ability of the solvent to donate a hydrogen-atom in a solvent-to-solute hydrogen bond. The important aspect of this finding is that the strength of hydrogen bonding apparently is able to substantially enhance the reactivity in the BP/anisole system. Such significant differences between the triplet-quenching rate constants, k_q, in non-protic and protic solvents were discussed above in a chemically related system, in particular, for the intramolecular H-atom transfer between phenols and BP in triplet excited **(S,R)-BP-DKP-Tyr** (Chapter 3.2.2.1). The same observation was also reported by Hörner *et al.* for two related benzophenone-tyrosine dyads.[76, 162] In these cited works, the solvent effects were attributed to a change in the reaction mechanism to an electron-transfer initiated process in protic solvents.[76, 162]

A number of workers[107-109] associated the decay rates with the extent of charge-transfer interactions between the BP triplet and the anisole, with the former being the acceptor and the latter being the donor. An involvement of a charge-transfer interaction requires correlation between the reaction rate constants and the thermodynamic factors such as ionization potentials or oxidation-reduction potentials of the participating species. Thus, the electronic properties of the BP were varied by introducing different substituents. The quenching of benzophenone and its derivatives: 4,4'-dimethoxybenzophenone (DMBP), 4-methylbenzophenone (MBP), 4-trifluoromethylbenzophenone (TMBP) and decafluorobenzophenone (DFBP), by anisole in ACN strongly depended on the character of the substituent group. The observed rate constants covered a range of four orders of magnitude from 3.1×10^5 $M^{-1}s^{-1}$ in DMBP to 4.4×10^9 $M^{-1}s^{-1}$ in DFBP. Higher rates were attributable to the facilitation of CT complex formation when electron-withdrawing groups were present in the compound that could stabilize the incipient negative partial charge on the acceptor by delocalization. An opposite influence is observed when the electron-donating methoxy group was present. An involvement of a charge-transfer interaction in the reaction was further corroborated by the good correlation between the reaction rate constants and the formal Gibbs energy of the electron transfer. In Figure 3.6-5, the data of log k_q for several BP derivatives in ACN solution were plotted against the free energy term $-(E_T + e\,E_{red})$, which formally denotes the free-energy change associated with the one-electron reduction of the respective triplet-excited BP derivative. This plot gave a straight line with a slope of -5.2 ± 0.3 eV^{-1} ($r^2 = 0.992$).

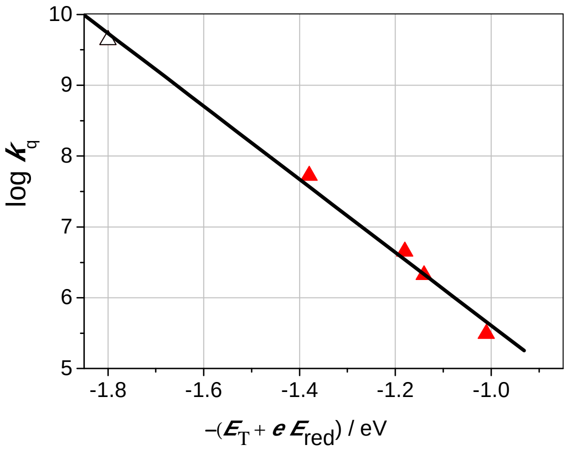

Figure 3.6-5 Correlation between the bimolecular triplet-quenching rate constants of benzophenone derivatives by anisole (in ACN) and the free-energy difference for reduction of the respective benzophenones' triplet state $-(E_T + e\,E_{red})$, filled symbols: from right to left data for DMBP, MBP, BP, TMBP, open symbol: DFBP, literature data.[40]

That slope is in good agreement with the complementary correlations of the rate constants of benzophenone triplet quenching with the oxidation potentials of substituted methoxybenzenes in acetonitrile described in Chapter 1.3.1.2.3.

3.6.3 Quenching in non-protic solvents *vs.* protic solvents: time resolved studies

Triplet quenching of BP triplets by anisole in ACN solution was not connected with any formation of free radical-ion products that would signify the occurrence of a full ET. The decay profiles obtained after nanosecond LFP at 355 nm nicely coincided, irrespective of the observation wavelength (Figure 3.6-6c). Concomitantly, the transient spectra, recorded on 355 nm excitation of BP in ACN or in an ACN-H_2O (4:1 v/v) mixture in the presence of anisole were dominated by strong absorptions at 325 nm (not shown) and 525 nm (see Figure 3.6-6a; in ACN). The spectra exhibited no spectral evolution during the decay and matched those previously reported for the BP triplet state.[37]

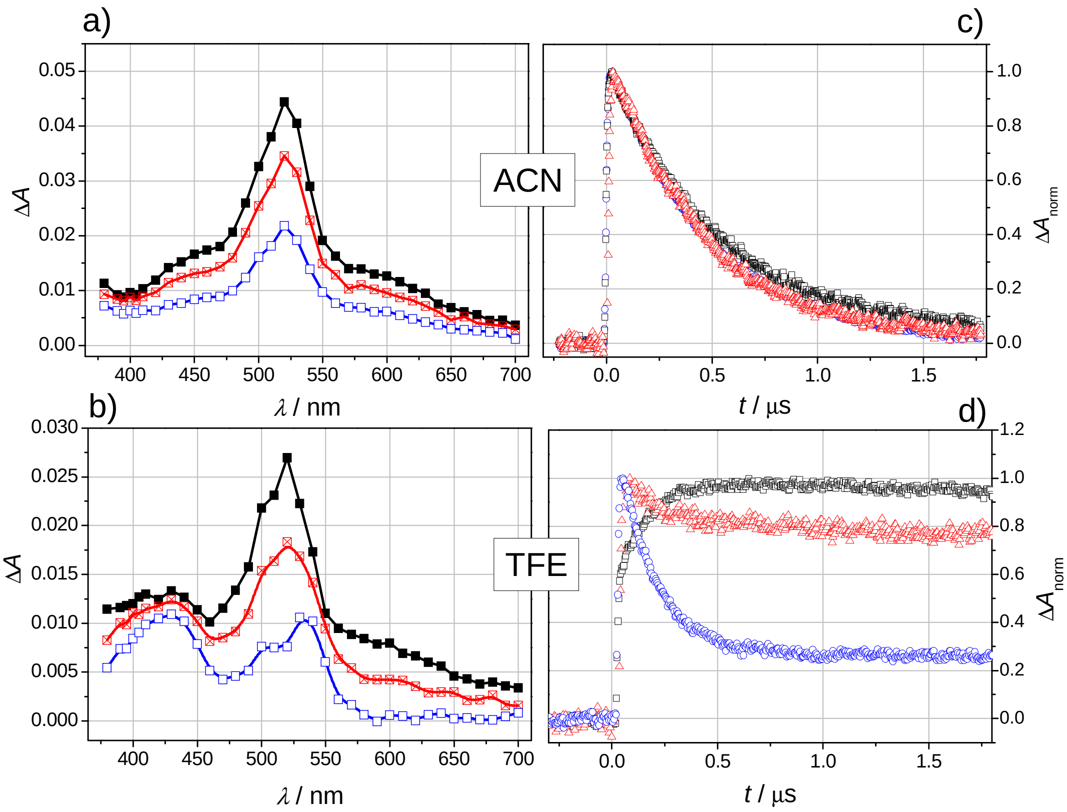

Figure 3.6-6 Transient absorption spectra obtained during laser flash photolysis at 355 nm of deoxygenated solutions of benzophenone (2.5×10^{-3} M) and anisole (2.3×10^{-2} M); a): ACN; time delays after flash (from top to bottom): 90, 200, 400 ns; b) TFE; time delays after flash (from top to bottom): 100, 200, 1000 ns; c), d): normalized decay profiles of the transient absorption monitored at 520 nm (blue), 330 nm (black), and 430 nm (red) for the quenching of BP (2.5×10^{-3} M) by anisole; c) in ACN (0.575 M anisole) and d) in TFE (2.3×10^{-2} M anisole).

As opposed to the behavior in ACN solutions, the quenching of triplet-excited BP derivatives in TFE gave rise to generally increased rate constants (Table 3.6-1) and was accompanied by significant formation of free radicals. Thus, the quenching of the benzophenone triplet in TFE by anisole gave rise to strongly different, wavelength-dependent kinetic profiles (Figure 3.6-6d) and was accompanied by a spectral evolution (Figure 3.6-6b). This finding was not limited to TFE as a solvent but appeared to be a common feature in protic solvents. Similar time evolution of the transient absorption spectra was observed for quenching of the BP triplet by anisole in HFIP, acetic acid and ACN-H_2O mixtures with water volume more than 50 %.

With time, the T-T absorption of BP decreased in intensity according to first-order kinetics, resulting in significant residual absorption bands with peaks at 540 and 430 nm after 1 µs. The transients can be assigned to the anisole cation radical (λ_{max} = 430 nm)[179] and the BP ketyl radical (λ_{max} = 540 nm).[180] The residual absorption of the 430-nm transient was not significantly affected by the presence of oxygen (Figure 3.6-7a). The inertness towards oxygen and the high sensitivity of this transient towards the presence of added nucleophiles (here, NaOH) (Figure 3.6-7b) are in agreement with previous findings from the pulse radiolysis of anisole[172, 181] and strongly suggest that transient to be the cation radical of anisole. In particular, the low oxygen sensitivity of the oxidized anisole intermediates rules out the presence of carbon-centered radicals formed *via* H-abstraction from the methoxy group or *via* adiabatic proton transfer within a primary radical-ion pair, as it has been reported for the system BP/dimethylaniline.[182] The spectral assignment of the BP-based transient to the C-centered BP ketyl radical, on the other hand, could be verified by experiments in the presence of oxygen, that revealed selective quenching of the underlying 540-nm transient (Figure 3.6-7a).

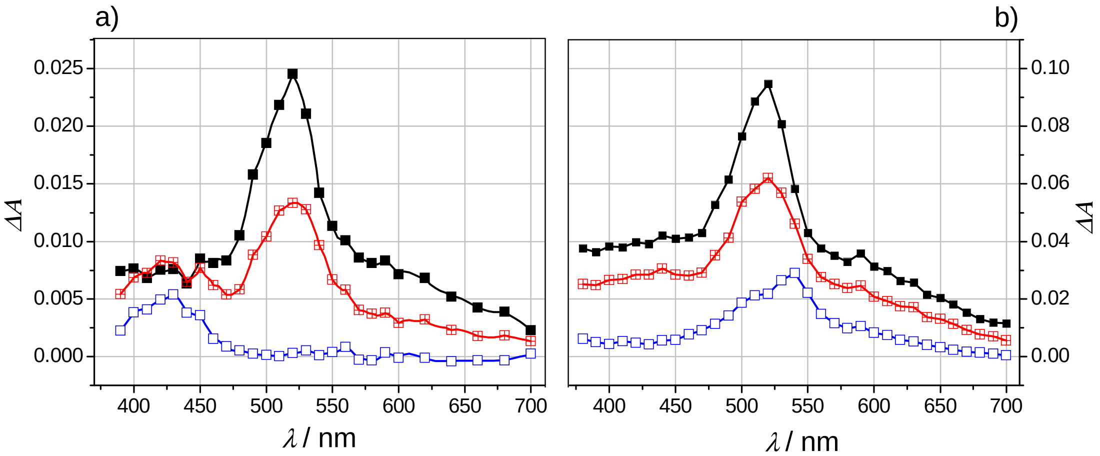

Figure 3.6-7 Transient absorption spectra obtained during laser flash photolysis at 355 nm of solutions of benzophenone (2.5 × 10^{-3} M) and anisole (2.3 × 10^{-2} M) in TFE a): without deoxygenating; b) in the presence of added nucleophile OH^-; time delays after flash (from top to bottom): 100, 200, 1000 ns.

The predominance of the BP ketyl radicals in the transient spectra points to an ET reaction from the anisole to the BP triplet which is followed by the protonation of the BP$^{\bullet-}$ by a proton donor SH. This finding is in agreement with results obtained for the system BP/diethylaniline in TFE, where the solvent was the source of the transferred protons.[34] The spectral dominance of the $BPH^{\bullet}$ ketyl radical can therefore be ascribed to fast protonation of the primarily formed benzophenone radical anion by the solvent. The stepwise nature of the BP ketyl formation was corroborated by experiments at large water concentrations, where the contribution of the $BP^{\bullet-}$ radical anion became prominent. It was possible to see this development in the water/ACN mixtures because the protonation reaction was slower than in the TFE. As already stated above, experiments in ACN-H_2O (4:1 v/v) mixture did not lead to any spectral evolution (Figure 3.6-8a), and the decay profiles coincided, irrespective of the wavelengths (Figure 3.6-8c). That result was in agreement with the data reported by Shizuka and co-workers.[108] However, by increasing the water content, the quenching rate constants and the quantum yields of the radical formation were changed significantly. LFP for BP in ACN-H_2O (1:4 v/v) was performed in basic solution (pH = 11) to avoid fast secondary protonation of the radical anion which was observed in the acidic fluoroalcohol TFE and in aqueous solution at low pH values. The rapid triplet-state quenching was actually accompanied by efficient formation of the direct ET product, as can be seen from the characteristic absorption of the respective ketyl-radical anions at λ_{max} = 600 nm (Figure 3.6-8b,d, blue curves). The anisole radical cation with the absorption at 430 nm was quenched efficiently by the nucleophile OH^-, but the radical cation was observed together with ketyl radical in an analogue experiment at lower pH. These experiments gave direct evidence that quenching occurred *via* full electron transfer in protic solvents.

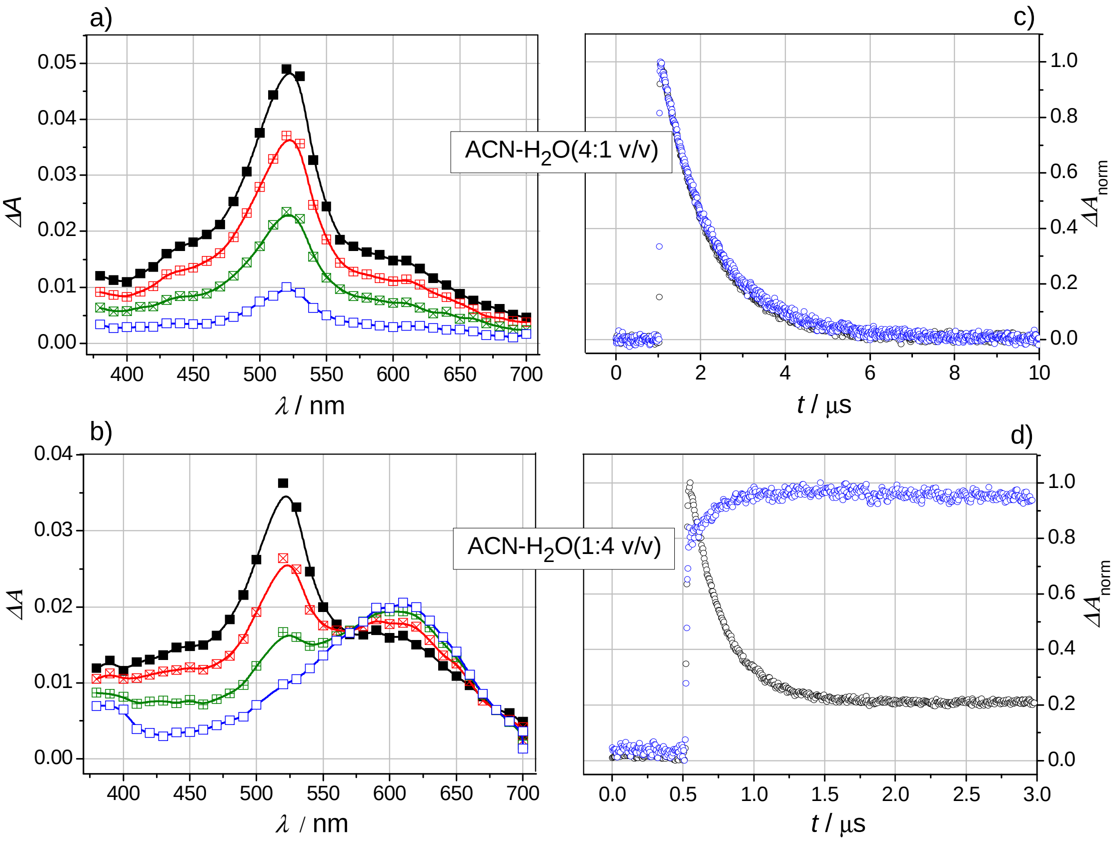

Figure 3.6-8 Transient absorption spectra obtained during laser flash photolysis at 355 nm of deoxygenated solutions of benzophenone (2.5×10^{-3} M) and anisole a): ACN-H$_2$O (4:1 v/v); time delays after flash (from top to bottom): 90, 200, 400 ns; b) ACN-H$_2$O (1:4 v/v) at pH = 11; time delays after flash (from top to bottom): 100, 200, 400 1000 ns; c), d): normalized decay profiles of the transient absorption monitored at 520 nm (black), 600 nm (blue) for the quenching of BP (2.5×10^{-3} M) by anisole c) in ACN-H$_2$O (4:1 v/v); (0.027 M anisole) and d) in ACN-H$_2$O (1:4 v/v) (4.6×10^{-3} M anisole).

A comprehensive study was made of the reaction kinetics and product ratios observed during the quenching of four BP-derivatives in solvent mixtures of ACN with water. The solvent dependence of the triplet-quenching rate constants in the BP/anisole system was studied using four different BP-derivatives: BP, CB, 4-carboxybenzophenone-*N*-methylamide (CBCONHMe), and DFBP. The solvent compositions employed varied from 0.0 to 0.9 volumetric ratio with respect to H$_2$O (except for DFBP, where the solubility limits the range only up to 0.5). Detailed analyses of these results are actually beyond the scope of this thesis, but the main important findings of this work will be discussed in brief since they are relevant to the data presented for **(S,R)-BP-DKP-Tyr** (Chapter 3.2.2.3) and **(S,R)-BP-DKP-Met** (Chapter 3.3.2). The quenching rate constants for all four derivatives increased significantly with increasing water content, e.g. for BP the k_q varied from 4.5×10^6 M^{-1}

s^{-1} in ACN to 1.7×10^9 M^{-1} s^{-1} in ACN-H_2O (1:9 v/v). In addition to the impact on the quenching rates, the water content was found to exert another important effect on the nature of the triplet quenching in the BP/anisole system. Thus, the quenching mechanism appeared to change on going from pure ACN to mixtures with large water content. This became evident from the water-content driven increase in the amount of free radicals that were present after complete triplet decay. For all four BP derivatives in pure ACN, no free radicals were detected. However, already in ACN-H_2O (1:1 v/v), the quantum yields of radical formation for BP, CBCONHMe, CB and DFBP were equal to 0.04, 0.3, 0.64 and 1.0, respectively. Free radicals were formed with moderate to high efficiencies within the systems of BPs/anisole in protic solvents. By the action of the hydrogen-bonding additives, the undesired charge recombination in the electron transfer process in the benzophenones/anisole systems was found to be largely suppressed.

3.6.4 **Steady-state irradiation**

Steady-state experiments, finally, provided clear evidence that the radical-producing pathways of BP-triplet quenching by anisole in protic solvents are largely reversible. Solutions of BP (2.5×10^{-3} M) and anisole (2.5×10^{-3} M) in TFE were irradiated with an argon ion laser at 351 nm. Each identically prepared sample was irradiated for 2, 5, 9 and 14 minutes, respectively, to keep the solute consumption below 20 %. The quantum yields of disappearance of the substrates, as studied by means of HPLC analysis of the reaction mixtures, were 0.07 and < 0.01 for benzophenone and anisole, respectively. Blank experiments in the absence of anisole, gave the same disappearance quantum yield of the BP, which was attributed to H-abstraction from the solvent. Actually, small amounts of ketyl radicals were also observed in the transient absorption spectra of **BP-DKP** in TFE (Figure 3.5-3b). GC-MS analysis was performed in order to identify the stable products of the steady-state irradiations. All stable products observed carry benzophenone moieties but no anisole moieties; that is, benzopinacol, tetraphenyloxirane, and 2-(trifluoromethyl)-1,1-diphenyl-1,2-ethanediol. These products arise from reactions with TFE which is in agreement with the conclusion that H-abstraction from the solvent is the only quenching pathway leading to the stable products.

These data indicate that the ketyl radical and the anisole radical cation formed in the quenching of the triplet BP by anisole in TFE react to regenerate the starting materials. The reversibility is in agreement with the observations during LFP, where the kinetic traces at 540 nm and 430 nm show a second-order decay with identical rate constants of $2.3 \times 10^9\ \mathrm{M^{-1}\ s^{-1}}$ and $2.1 \times 10^9\ \mathrm{M^{-1}\ s^{-1}}$, respectively.

3.6.5 **Discussion**

The experimental results presented above strongly suggest that protic solvents harbor conditions favorable for fast BP triplet quenching as well as for efficient radical formation due to a full electron transfer from anisole. The experimental findings are somewhat similar to the mechanism reported by Fessenden *et al.* in the photoreduction of BP by *N*,*N*-diethylaniline (DEA) in TFE.[34] In their nanosecond experiments a fast decay of the BP radical anion, as the primary ET product, was observed, concomitant with ketyl-radical formation. They ascribed the protonation reaction to PT from solvent alcohol molecules. In contrast to their study, the strong enhancements in the radical-producing quenching for the system BP/anisole were limited to protic solvents, but no dependence on the permittivity of the medium was found (Table 3.6-1). Even the highly polar solvent ACN did not allow the formation of free ET products. The strong acceleration of the triplet quenching that was observed in protic solvents points to a similar impact of the specific solvation on the activation barriers as was observed in the intramolecular quenching of **(S,R)-BP-DKP-Tyr** (Chapter 3.2.2.3) or **(S,R)-BP-DKP-Met** (Chapter 3.3.2.1).

The expressed influence of the solvent nature on the reaction rates is attributable to the energetics of the electron-transfer quenching that is addressed in terms of the Marcus theory of adiabatic electron transfer (see Chapter 1.3.1.2.1.1). This shows, in fact, that the acceleration of the ET reaction between anisole and ^{3}BP in protic solvents is mainly due to an increase in the driving force of the ET. Figure 3.6-9a,b presents potential energy surface descriptions of the ET between anisole and ^{3}BP in ACN and TFE solutions. The energy terms (triplet energy, E_T, and free energy of ET between ground-state reactants, $e(E_\mathrm{ox} - E_\mathrm{red})$) for ACN solution are based on literature data.[28, 183] Respective data for TFE solution are estimated to be close to the data that have been reported for aqueous solution.[41, 184]

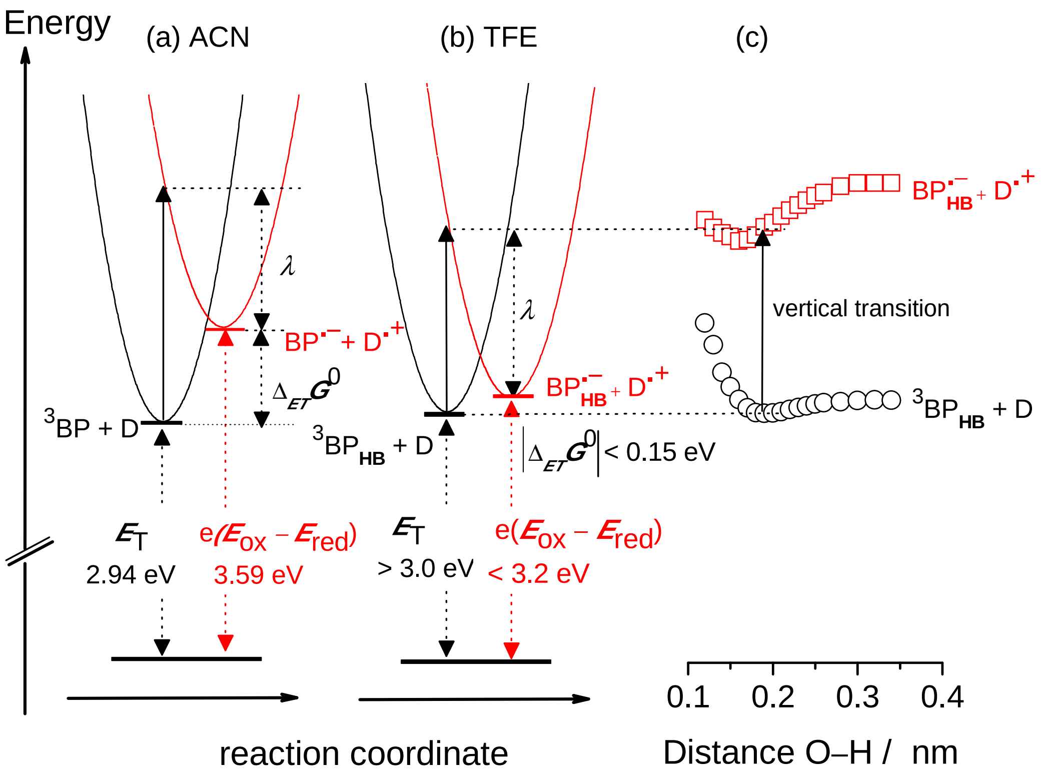

Figure 3.6-9 Semi-quantitative energy diagrams for the reduction of triplet-excited BP by anisole (D) in a) ACN and b) in TFE; for details see text. c) DFT calculations of the electronic energies of the isolated reactants (in black) and the isolated products (in red) as a function of the O–H distance between the BP moiety and TFE. At each O–H distance, the reactants' nuclear configuration was optimized, and the electronic energy of the products was also calculated at that same frozen nuclear configuration. An ACN continuum was employed in the final step of each calculation.

Evidently, the relative positions of the reactant and ET-product energy surfaces are strongly dependent on the nature of the solvent. The reaction free energy of the ET, $\Delta_{ET}G^{o}$, is close to zero in the presence of an H-bonding solvent like TFE as opposed to being distinctly positive in ACN. This change in $\Delta_{ET}G^{o}$ on changing the solvent from ACN to TFE can be traced to two distinct sources of specific solvation: shifts in redox potentials and level shifts in excited states. Specific solvation is well established to affect strongly the reduction potentials of aromatic ketones. Anodic shifts by up to 300 mV in protic solvents have been attributed to the strong stabilization of the radical anions being formed on reduction.[28, 146, 185-188] In addition, also the oxidation potential of anisole is lowered in a protic environment.[184, 189] These cooperative redox-potential shifts strongly favor the ET step thermodynamically. As discussed above, specific solvation of the triplet-excited BP also became evident during this study. Whereas this leads to a further increase in the driving force of the ET, the solvation-induced increase in the triplet energies appears to be of minor importance (ΔE_T < 0.1 eV),[190] when compared to the effects on the redox potentials.

As expected, the solvent-driven increase of the thermodynamic driving force of the ET is found to be connected with a solvent-induced decrease of the free energy of activation $\Delta G^{\neq}$ (see Eq 1.3-4), of the ET step. Based on Eq 1.3-4, it can be seen that the free energy of activation can be calculated when the sum $(\Delta_{ET}G^{o} + \lambda)$ is known. The vertical energy $(\Delta_{ET}G^{o} + \lambda)$ is the energy needed to excite the reactants to the products' energy surface with the nuclear configuration frozen to that of the reactants having their nuclei fully relaxed in the field of the initial electronic configuration (see bold arrows in Figure 3.6-9a-c). These energies have been accessed with DFT calculations.

To depict the energy levels of the excited state and benzophenone radical anion, vertical excitation energies were calculated at the PBE1PBE optimized geometries with the 6-31+G(d) basis set and the SCRF method with the IEFPCM model. The vertical energies $(\Delta_{ET}G^{o} + \lambda)$ were obtained by minimizing the electronic energy for the two isolated reactants ^{3}BP and anisole. Single-point calculations were done in this optimized nuclear configuration with a continuum model for the solvent acetonitrile. The computation of the vertical-energy differences in the presence of specifically solvated ^{3}BP followed the same procedure with a continuum model for the solvent acetonitrile and one TFE molecule being attached to the BP. Computations gave the respective vertical energy distances as a function of the O–H distance of the hydrogen-bonded complex ^{3}BP---HO(TFE) (Figure 3.6-9c). The results displayed in Figure 3.6-9a apply to unspecific solvation in an ACN continuum, whereas the data in Figure 3.6-9b denote the vertical energy within an energetically minimized ^{3}BP····TFE complex in an ACN continuum. The respective dependence of the vertical energy on the HB distance in the ^{3}BP····TFE complex is shown in Figure 3.6-9c. The vertical energies amount to 1.55 eV and 1.38 eV for ACN and TFE, respectively. Although the errors in the determination of these vertical-energy differences are on the order of 0.2 – 0.3 eV, the values are meaningful because of a cancellation of errors when these differences are being compared. This assumption appears to be justified because exactly the same computational methods were successfully applied on very similar systems. The validity of the approach was further corroborated by the excellent agreement of the obtained reorganization energies $\lambda \approx 0.8$ eV and 1.1 eV for ACN and TFE solutions, respectively with the values that have recently been reported for a related structure, namely benzoquinone ($\lambda \approx 0.8$ eV and 1.0 eV for ACN and MeOH solutions, respectively).[191] Afterwards, free energies of activation $\Delta G^{\neq}$ were calculated. They were found to be $\Delta G^{\neq} \approx (0.67 \pm 0.03)$ eV and $\Delta G^{\neq} \approx (0.39 \pm 0.05)$ eV for ACN and TFE solution, respectively (the errors in $\Delta G^{\neq}$ were calculated based on the error propagation formula associated with the error in the vertical energies). In terms of Eq 1.3-5, these values imply an acceleration of the rate constants of the ET in TFE by a factor of 10^5. Despite the simplified approach, the computed results are compatible with the experimental findings discussed above.

In summary, laser-flash photolysis was used to investigate the photoreduction of benzophenones by anisole in a number of non-protic and protic solvents and solvent mixtures. In agreement with literature data, the quenching in non-protic solvents was inefficient with respect to free-radical formation in the case of BP and some BP derivatives with electron-withdrawing and electron-donating substituents. The findings were compatible with the implications of quenching within an encounter complex with partial charge-transfer character. However, it was shown that the reactivity of an electronically excited molecule can be greatly enhanced by changes in the solvent nature i.e. free radicals were formed with moderate to high efficiencies within the system of BP/anisole in protic solvents. In this study specific solvent-solute interactions were identified as a major factor of the PET efficiency that extends the utility towards solvents of medium polarity. It is noteworthy that also the reactivity of the dyad **(S,R)-BP-DKP-Tyr** toward intramolecular HAT was found to be controlled by effects of specific solvation. In addition, it appears highly probable that the solvent-driven photoinduced electron transfer enhancement described here can be generalized to other PET systems also and that these findings thus provide a promising way to run PET reactions with efficient charge separation independently of the dielectric properties of the medium.

4 CONCLUSIVE SUMMARY

The motivation of this dissertation was (1) to explore, with a focus on methionine and tyrosine moieties, basic chemical information concerning reactions that can occur in natural biological systems, e.g in proteins, and (2) to contribute to an understanding of biological processes at the molecular level. Due to the outstanding biological significance of methionine and tyrosine, it was of general importance to carry out a detailed study of hydrogen, electron and proton transfer reactions that occur with these two amino acids. While *in-vivo* such processes are typically triggered by enzymatic action, any *in-vitro* investigation, particularly on molecular reactivities and mechanisms, usually relies on other means of free-radical and redox chemistry. A most convenient and informative tool in this respect has proven to be *Photochemistry*, particularly when complemented by appropriate theoretical calculations. This is the approach which has been chosen for the present study.

The reactions of ketone/tyrosine and ketone/methionine systems, specifically, are widely used as efficient and selective sources of biorelevant radical species like the tyrosyl radicals and the sulfur-centered radical cations. Their intramolecular variants with both functionalities in the same molecular structure in particular, can serve as model systems for providing detailed mechanistic insights into the underlying elementary reaction steps of biological relevance. Instead of working with complex and consequently more complicated biological systems though, specifically *de-novo* synthesized simple bichromophores, such as benzophenone-tyrosine and benzophenone-methionine as well as trichromophores such as carboxybenzophenone-methionine-tyrosine were employed.

One of the key elements of this study were parameters, which control the overall rates and efficiencies of the intramolecular hydrogen-abstraction and electron-transfer reactions. Especially the role of steric constraints on the reactivities was examined by changing the flexibility of the linkage between the interacting groups. In addition, the quantification of the photochemical reaction rates and efficiencies was extended toward a study of the effect of chiral-center configurations on the diastereo-selectivity of the triplet-quenching processes. Furthermore, the impact of the reaction media on the rates and the actual transfer mechanisms were addressed. Here, Ingold *et al.*'s concept of a kinetic solvent effect (KSE) in bimolecular H-atom transfer reactions was tested in the context of its applicability in interpreting solvent effects also in photoinduced intramolecular reactions. In particular, possible interrelations of structural and solvent effects on the intramolecular reactivity of benzophenone/tyrosine and benzophenone/methionine dyads were addressed.

Explicitly, mechanistic features of the overall UV-light-induced intramolecular reactions of hydrogen atom, electron and proton transfer reactions, i.e., transient lifetimes and quantum yields of the primary reactions were studied by nanosecond laser flash photolysis (LFP). In this manner, intramolecular quenching rate constants were obtained, while the efficiencies of irreversible reaction pathways were tested and quantified by steady-state UV photolysis. Vital contributions in the interpretation of the observed differences in the reactivity between the investigated compounds were provided by structural details of the respective quenching geometries. In addition, it was important to understand the correlation between intramolecular reactivity and the structural preferences that are reflected by the non-bonding distances of the interacting functional groups in the side chains. To provide insight into these aspects, the experimental studies were supplemented by extensive DFT calculations and MD simulations performed for each compound. This theoretical work involved studies of the ground-state structures and conformations which yielded quantitative information on the populations of the side-chain rotamers in the dyads' and triads' ground states and, in particular, furnished distributions of the sulfur to carbonyl-oxygen and the hydroxylic oxygen to carbonyl-oxygen distances.

The work presented in this thesis showed that the geometric constraints on intramolecular motions, tuned by different flexibility of the peptide linker connecting the reacting moieties, have, indeed, remarkable consequences for their intramolecular reactions. Both investigated open-chain dyads, **(S,S)-BP-Tyr** and **(R,S)-BP-Tyr**, were highly reactive toward intramolecular hydrogen-atom transfer (HAT). Notably, for both compounds the triplet-state quenching was faster by two orders of magnitude than in the case of the monochromophoric reference compound which did not contain the tyrosine moiety. In addition, although quantum yields for biradical formation ((BPH$^{\bullet}$–Tyr(O$^{\bullet}$)) were close to unity, the dyads **(S,S)-BP-Tyr** and **(R,S)-BP-Tyr** were very inert upon steady-state irradiation suggesting that these particular intramolecular HAT reactions were basically reversible. Such a reversibility constitutes, in turn, an efficient path for energy dissipation in the triplet-excited BP chromophore.

It is well established, that, in order to be successful, hydrogen-atom transfer reactions, initiated by triplet-excited ketones, require close contact between the H-atom donor and the accepting carbonyl moiety. Thus, the observed high intramolecular reactivity of the dyads consequentially reflects a large flexibility in the linkage between BP and Tyr, which allows for a close contact of the carbonyl oxygen and the hydroxylic oxygen. Indeed, DFT calculations (in the gas-phase) and MD simulations for an implicit solvent model provided evidence that, in both dyads, the close contact needed for intramolecular HAT can, indeed, occur between the reactive moieties.

Very similar observations to those for the open-chain BP-Tyr dyads were also made on both of the open-chain BP-Met dyads under study. Thus, **(S,S)-BP-Met** and **(R,S)-BP-Met** also showed a high efficiency of the triplet excited-state quenching but, in contrast to the BP-Tyr dyads, the BP-Met-based quenching in ACN as the solvent was not accompanied by directly detectable formation of any intermediates. However, based on the observed short triplet lifetimes and the analogy to the data on intermolecular triplet-state quenching by compounds containing a methionine group, in general, it was assumed that intramolecular electron transfer from the sulfur atom to the triplet state of the BP is, nevertheless, the primary photochemical step. Steady-state irradiations, on the other hand, revealed that secondary reactions, which could lead to stable products, occurred only with low efficiency (5-6 %.). Hence, the initially formed charge-transfer complex appears to decay irreversibly only to a minor extent and rather seems to involve most efficiently back electron transfer that regenerates the substrate.

The large conformational freedom of the linkage between BP and Met is expressed in the non-zero formation probabilities, as computed from MD simulations, of conformations with close contact between the reactive moieties. Thus, the observed significant intramolecular reactivity within **(S,S)-BP-Met** and **(R,S)-BP-Met** is in accord with a quenching mechanism which is dependent on the close contact of the BP and Met residues.

A further interesting, because to some extent initially unexpected, result was that the large intrinsic flexibility of the linker in the open-chain BP-Tyr and BP-Met dyads appeared to overshadow the stereoselectivity of the triplet quenching in the respective pairs of diastereomers. The highest stereoselectivity of the open-chain BP-Tyr dyads, expressed as the ratio of the rate constants for the respective intramolecular H-atom transfers, was obtained in MeOH, and was just equal to 3.5. As further example, the stereoselectivty of the open-chain BP-Met dyads, here expressed as the ratio of the triplet lifetimes in ACN, was even as low as 2.5. Thus in order to get deeper insights into the relations between the kinetic phenomenology and the molecular structure, the flexibility of the peptide linker was limited by introducing a rigid system, namely, a diketopiperazine (DKP) ring as a spacer between the reacting chromophores. Importantly, the structural differences between the diastereoisomers imposed by the DKP rings caused a marked influence on the photoreactivity of the compounds. The LFP results of dyads **(S,S)-BP-DKP-Tyr** and **(S,R)-BP-DKP-Tyr** in ACN showed a striking contrast between the two diastereomers with regard to their intramolecular H-atom transfer rate constants (k_H). The change in the configuration of just one chiral center produced already distinct changes in the intramolecular H-atom transfer rates. The highest stereoselectivity found in this work for the DKP-based BP-Tyr dyads was equal to 131 (in EtOAc as solvent). This value is about two orders of magnitude larger than for the flexible linker systems and much higher than any value ever reported in the literature for ketone/phenol dyads.

In order to explain the significant differences in the intramolecular H-atom transfer between **(S,S)-BP-DKP-Tyr** and **(S,R)-BP-DKP-Tyr**, the probabilities for the formation of the conformations with close contact of the reactive moieties were determined by MD simulations. It was found that only **(S,S)-BP-DKP-Tyr** was capable of forming conformations which allow for close contacts < 4.0 Å. On the other hand, **(S,R)-BP-DKP-Tyr**, wherein the two aromatic residues occupy opposite sides of the DKP rings, structures with close contacts < 4 Å of the reactive moieties do not appear at all during 100 ns simulation periods. Thus, the remarkable variations in the reaction rates of the isomeric BP-Tyr dyads can be attributed to differences in the distance distributions.

In view of the obvious close-contact requirement, as derived for the above systems from complementary experimental and theoretical data, it was then of interest to check whether this could, at least qualitatively, be rationalized solely on the grounds of MD simulations. However, in drawing any such conclusion, intramolecular reactivity of any compounds based on MD simulations requires insuring that any such calculated structural preferences are realistic. Thus, this work also addressed the question how reliable MD simulations were in regard to their representation of conformational preferences and distance distributions of the reacting moieties in benzophenone-tyrosine dyads. Having adopted a comprehensive MD/DFT combination of techniques, the MD-simulations were validated by comparing the theoretical values of the spin-spin coupling constants with the data obtained experimentally. Based on the observed agreement it can be concluded that MD simulations reflect quite well the conformational preferences of the cyclic DKP-based dyads. In summary, the successful validation of the MD-simulations, which addressed the pair-distance distribution between the reacting groups as a function of the molecular structure, identifies this technique indeed as a reliable tool for predicting *a priori*, i.e. before conducting any experiment, a qualitative order of the reactivity of other compounds toward intramolecular H-atom transfer.

Structural effects showed up not only in the intramolecular BP triplet state quenching by tyrosine in cyclic BP-Tyr dyads, but also in the quenching of the excited triplet state by the methionine residue in rigid BP-Met dyads. Again, some of the results were reasonably predictable while others had, at least at first glance, an element of surprise with respect to the absolute and relative reactivities. In contrast to BP-Met dyads linked by an open, flexibile chain which showed only small stereo effects, the quenching of the triplet state of the cyclic, i.e., rigid BP-Met dyads revealed significant chiral discrimination. Stereoselectivity, expressed as the ratio of the triplet lifetimes for the diastereoisomers **(S,R)-BP-DKP-Met** and **(S,S)-BP-DKP-Met** measured in ACN, was found to be 15, in comparison to only 2.5 obtained for the open chain BP-Met dyads. That significant difference in the reactivity between **(S,R)-BP-DKP-Met** and **(S,S)-BP-DKP-Met** indicated, that in these rigidly linked dyads, there must be some special structural constraints in operation on the BP-triplet-state quenching by the methionine residue. This distinct behavior could once again be attributed to the marked differences in the probability of forming rotamers with relatively close-contacts between the sulfur and carbonyl oxygen that were found in the MD simulations. **(S,S)-BP-DKP-Met** and **(R,S)-BP-DKP-Met** were, incidentally, the only compounds for which the triplet-state quenching process showed a high degree of irreversibility, indicating the existence of effective pathways to new reaction products. Interestingly, although the two compounds: one cyclic **(S,S)-BP-DKP-Met** and one open-chain **(R,S)-BP-Met** were found to undergo the triplet-state quenching with the same rate constants in ACN, their respective quantum yields of the substrate disappearance, differed by a factor of 7. This distinct discrepancy in efficiency of substrate consumption between the open-chain and cyclic BP-Met dyads indicates that beside the special structural constraints influencing the triplet-state quenching rate constants, there seem to be also further geometric factors in operation that control the efficiency of the secondary reactions that may lead to stable products.

Some mechanistic insight into the triplet-triggered product formation could be obtained from the analysis of the LFP results and the molecular structure of the stable product formed upon irradiation of **(S,S)-BP-DKP-Met**. This provided evidence that the triplet decay of this compound, in which both reactive moeities, BP and Met, occupy the same side of the DKP ring, can actually be attributed to an efficient H-atom transfer reaction. In more detail, the mechanism of the reaction appears to involve an initial electron-transfer that leads to an intramolecular radical-ion pair complex. This step is then followed by an intramolecular proton transfer involving exclusively a proton from the CH_3 carbon adjacent to the sulfur which finally results in a backbone-linked ketyl and α-thio-alkyl biradical. Subsequent intramolecular cross-linking of the biradical can then explain the observed annular product. Although this process was found to be strictly regioselective, involving only the (α-S)-positioned CH_3-carbon of the original Met side-chain, it does not exclude the possibility of a deprotonation from the also (α-S)-positioned CH_2-carbon in other peptide or protein substrates with different geometrical characteristics, e.g. higher flexibility.

Having established that hydrogen, electron and proton transfer reactions are decisively involved in the initial photochemical processes of the investigated compounds, a natural interest arose in how these processes may depend or, at least, are influenced by the surrounding environment.

In the next step of this work, special attention was, therefore, paid to the solvent effects with emphasis on the possible assist of the solvent in mediating the transport of H-atoms, protons and electrons. The most important finding was that, in contrast to the generally donor-specific kinetic solvent effects of bimolecular systems, the kinetic-solvent-effect phenomenology of intramolecular HAT reactions is highly correlated with structural features. The extensive work by Ingold had provided evidence that the solvent dependence of bimolecular-reaction rate constants may be quantified solely in terms of the H-bond ability of the H-atom donor and the H-bond acceptor ability of the solvent. In agreement with this, in the present work a plot of the kinetic data for the open-chain dyads **(R,S)-BP-Tyr** and **(S,S)-BP-Tyr** against the effective Abraham's H-bond acceptor ability, $\Sigma\beta_2^H$, of the solvents were found to follow a linear dependence on $\Sigma\beta_2^H$ with slopes of $b = -2.5$ and $b = -1.5$ for **(S,S)-BP-Tyr** and **(R,S)-BP-Tyr**, respectively. The results showed that this single-parameter approach actually sufficed to explain the solvent dependence of the intramolecular HAT in the two open-chain diastereomeric BP-Tyr dyads.

In contrast to the open-chain dyads, the two DKP-based structures exhibited, however, distinctly different solvent dependencies. The reaction rates for the dyad **(S,R)-BP-DKP-Tyr** were found to be strongly solvent dependent while for **(S,S)-BP-DKP-Tyr** the solvent was only of minor importance for the reaction rates. Such a contrasting solvent behavior toward intramolecular H-atom transfers, as observed for **(S,S)-BP-DKP-Tyr** and **(S,R)-BP-DKP-Tyr**, is quite unusual for a pair of diastereomers. In this regard, they can, therefore, be perceived as a unique pair of diastereomers with a unique solvent dependence of their stereoselectivity.

Further insight emerged from the details of the kinetic studies. Thus, non-protic and protic solvents exerted opposite effects on the rate constants, k_H, of **(S,R)-BP-DKP-Tyr**. These rate constants differed by two orders of magnitude. The compound **(S,R)-BP-DKP-Tyr** has its reactive moieties on opposite sides of its DKP ring and showed low reactivity toward intramolecular HAT in non-protic solvents. Quite unexpectedly though, in hexafluoro-2-propanol, a strongly protic solvent, it became even more reactive than **(S,S)-BP-DKP-Tyr**, wherein the benzophenone and tyrosine moieties occupy the same side of the DKP ring, i.e., exist in a configuration seemingly well suited for HAT. The rate-enhancing and rate-retarding effects of the solvents were attributed to specific solvent-solute interactions with both the hydrogen-donor and the hydrogen-acceptor. As a consequence, a single-parameter dependence of the intramolecular H-transfer reaction turned out to be not sufficient to explain the differences in the reaction rate constants of the cyclic dyad **(S,R)-BP-DKP-Tyr**. The sharp decrease of the reaction rates in non-protic solvents was quantified in terms of the KSE model and thus could be attributed to hydrogen bonding of the tyrosine to the solvent. HAT rates in non-protic solvents with weak effective H-bond donor abilities $\Sigma\alpha_2^H$ were actually found to follow a linear dependence on the H-bond acceptor parameter $\Sigma\beta_2^H$, with a slope $b = -3.1$. Importantly, dyads **(S,R)-BP-DKP-Tyr**, **(S,S)-BP-Tyr** and **(R,S)-BP-Tyr** are examples where the slopes of the logarithmic intramolecular HAT rate constants *vs*. $\Sigma\beta_2^H$ plots are individual characteristics for each dyad, but not the characteristic of each particular H-atom donor, in general, as may be expected from the theory of the KSE.

A sharp increase of the reaction rates with the solvents' hydrogen-bond donor ability was observed in protic solvents. Data for **(S,R)-BP-DKP-Tyr** plotted *vs.* the H-atom donor ability $\Sigma\alpha_2^H$ in this case also showed a linear correlation but with a positive slope of b = 2.3. These results on **(S,R)-BP-DKP-Tyr** show that, in contrast to the KSE phenomenology, which necessarily connects specific solvation with retarding effects, specific solvation can also accelerate the HAT reaction rates. This finding may, in fact, not only apply to the tyrosyl functionality but possibly to phenols, in general. The contrasting solvent dependencies of the H-atom transfer rate constants for dyad **(S,R)-BP-DKP-Tyr** in protic and non-protic solvents can thus be interpreted as being due to fundamentally different H-atom transfer mechanisms in the respective solvents.

It is further worth noting that, in sharp contrast to **(S,R)-BP-DKP-Tyr**, the complementary diastereomer **(S,S)-BP-DKP-Tyr** represents the first example for HAT reactions from a sterically unhindered phenol without any sizable dependence on specific-solvation effects. The observed reciprocal dependence of the HAT rates of **(S,S)-BP-DKP-Tyr** on the bulk viscosity could be interpreted as being solely due to intramolecular dynamics as the rate-determining step.

Importantly, acceleration of the intramolecular reactivity in protic solvents was not limited only to **(S,R)-BP-DKP-Tyr** but seems to be a more general phenomenon because it was also observed for **(S,R)-BP-DKP-Met** and **CB-Met-Tyr**. In the case of **(S,R)-BP-DKP-Met**, for example, the triplet lifetime was reduced by a factor of 10 on going from ACN to TFE as solvent. More surprisingly, it was noticed that fairly efficient electron transfer from methionine occured in protic solvents even though in ACN the rigid amide bond between BP and Met in **CB-Met-Tyr** completely suppressed any such methionine reactivity.

Moreover, the reactivities of triplet-excited BP in the anisole derivatives, BP-AN, were also dramatically enhanced in protic solvents. This large reactivity of BP towards anisole, in conjunction with the formation of intermediates in these O-methylated anisole-type phenolic derivatives of the BP-Tyr dyads, appears to be unprecedented in the previous literature on this topic. So, to clarify the respective solvent dependence and to identify the role of the solvent in the activation of the observed enhanced reactivity, additional studies were augmented on the methoxy analogues of the BP-Tyr dyads by results on a bimolecular system: benzophenone/anisole. Laser-flash photolysis was used to investigate the photoreduction of BP and its derivatives by anisole in a number of non-protic and protic solvents. While the results in non-protic solvents were compatible with „unproductive“ quenching *via* a charge-transfer state, which is in agreement with literature data, quenching in protic solvents, on the other hand, was accompanied by efficient formation of free-radical products. This finding was unexpected since this system has generally been found unable to harbor photoinduced electron transfer (PET) processes. The contrasting behavior was rationalized as a mechanistic switch from non-productive charge-transfer quenching in non-protic solvents to a full electron transfer (ET) in protic solvents, where the latter process is driven by specific solvation of the electron acceptor. Indeed, analysis of the solvent dependence in terms of Marcus‘ theory revealed the impact of specific solvation on benzophenone by protic solvents influencing the ET driving force and kinetics. Of crucial importance in this respect is a detailed knowledge of the factors that control PET processes, particularly those ones that affect the competition of the charge separation with undesired recombination. Thus, the finding that specific solvation interactions support efficient free radical-ion formation also in media of moderate and low polarity bears a meaningful message because it provides a promising way for the future to run PET reactions with efficient charge separation independent of the dielectric properties of the medium. In addition, it appears highly probable that the solvent-driven photoinduced electron-transfer enhancement described in this study can be generalized to other PET systems.

The results presented in this thesis very clearly demonstrate the complexity pertaining to intramolecular reactions even in relatively simple model compounds. Within this perspective, the comprehensive complementary experimental and theoretical study conducted in this work, specifically on intramolecular reactions between tyrosine/methionine and triplet-excited benzophenone, allows to make, in summary, the following general conclusions: (1) The rates of the intramolecular reactions are very sensitive to changing the flexibility of the linker connecting the reactive moieties. (2) The reactivity of an electronically excited molecule can be greatly enhanced by changes in the nature of the solvent. (3) Most interesting, as an extension to previous knowledge, the results imply that the kinetic effects that are imposed by the solvent and those that are due to the dyad structure are correlated with each other and cannot be understood if treated separately.

5 STRESZCZENIE PRACY

Badania nad reakcjami chemicznymi z udziałem związków zawierających metioninę i tyrozynę prowadzone są m.in. po to, by określić jak w naturalnych układach biologicznych, np. białkach, w wyniku działania promieniowania elektromagnetycznego może dojść do reakcji fotochemicznych. Powstające wówczas rodniki lub jonorodniki mogą w reakcjach z różnymi związkami organicznymi prowadzić do mutacji materiału biologicznego. W wyniku zainicjowanej fotochemicznie reakcji przeniesienia elektronu mogą powstać białka o bardzo podobnej strukturze do białka rdzennego, jednakże o innych właściwościach chemicznych. Utworzone w reakcji przeniesienia elektronu kationorodniki na atomie siarki (dla białek zawierających w swojej strukturze aminokwasy z atomami siarki) w procesie stresu oksydacyjnego włączają się we wczesny etap ataku oksydacyjnego, kojarzonego z procesami starzenia się oraz z patologiami takimi jak choroba Alzheimera.[8] Dodatkowo, wolne rodniki, anionorodniki oraz kationorodniki posiadające niesparowane elektrony głównie na atomie siarki, odgrywają jedyną w swoim rodzaju rolę w rozmaitych obszarach chemii, także w chemii organicznej. Przykładowo utlenianie leków białkowych zawierających metioninę, na które są one narażone podczas syntezy, oczyszczania, przechowywania może prowadzić do modyfikacji ich własności fizykochemicznych, a w konsekwencji do utraty ich aktywności biologicznej, niepożądanej reakcji układu immunologicznego organizmu, a także zmiany farmakokinetyki.[192] Rodnik tyrozylowy Tyr($O^{\bullet}$), utworzony w procesie przeniesienia atomu wodoru z fragmentu tyrozynowego (lub przeniesienia elektronu i dalszej reakcji przeniesienia protonu), także odgrywa niezmiernie ważną rolę w aktywności enzymów.[9, 12]

W świetle przedstawionej wyżej krótkiej argumentacji całkowicie uzasadnione jest podjęcie badań w celu szczegółowego poznania mechanizmu powstawania rodnika tyrozylowego Tyr($O^{\bullet}$) i kationorodnika $>S^{\bullet+}$ i ich dalszych reakcji wtórnych. Założeniem pracy było określenie stałych szybkości tworzenia się powyższych rodników niezależnie od procesu dyfuzji. Dlatego w badaniach skoncentrowano się na związkach, dla których możliwe są reakcje wewnątrzcząsteczkowego przeniesienia atomu wodoru, elektronu lub protonu. Ze względu na duży stopień skomplikowania układów biologicznych, do badań wybrano prostsze, modelowe cząsteczki zawierające układy bichromoforowe: benzofenon-tyrozyna i benzofenon-metionina jak i trichromoforowe: karboksybenzofenon-metionina-tyrozyna. Poznanie mechanizmów reakcji rodnikowych zachodzących *in vitro* w wybranych modelowych związkach może się przyczynić do zrozumienia procesów rodnikowych zachodzących *in vivo*.

Badania prowadzone dla podobnych układów wykazały, że fotoindukowane procesy wewnątrzcząsteczkowego przeniesienia atomu wodoru lub elektronu są procesami złożonymi i zależnymi od wielu czynników.[46, 65, 97, 100-102] Chociaż fotoindukowane procesy redukcji aromatycznego ketonu przez fenol lub związki zawierające atom siarki (II) są przedmiotem badań od wielu lat mechanizm reakcji nie jest nadal w pełni poznany. Dlatego zrozumienie mechanizmów reakcji rodnikowych i parametrów determinujących szybkość ich zachodzenia wymaga systematycznych badań nad grupą związków różniących się: rodzajem połączenia między donorem i akceptorem, chiralnością i możliwością oddziaływania elektronów π pierścieni aromatycznych.

W pracy tej zwrócono szczególną uwagę na te parametry układu, które mogą determinować szybkość zachodzenia badanych reakcji wewnątrzcząsteczkowych. W związku z tym określono wpływ geometrii badanych układów na stałą szybkości reakcji poprzez porównanie reaktywności związków o różnym typie połączenia (giętkim, sztywnym) między donorem i akceptorem. Ponieważ chiralność związku odgrywa istotną rolę w układach biologicznych, dlatego jednym z celów pracy było także określenie wpływu zmiany chiralności na węglu asymetrycznym (znajdującym się w łańcuchu peptydowym stanowiącym łącznik między donorem i akceptorem) na stałą szybkości reakcji, co zostało zrealizowane poprzez porównanie reaktywności odpowiednich diastereoizomerów. Jednym z dalszych etapów pracy było także scharakteryzowanie wpływu rozpuszczalnika na badane procesy wewnątrzcząsteczkowe. Intensywne badania Ingolda i Litwinienko[14-17] dotyczące kinetycznego efektu rozpuszczalnikowego w reakcjach międzycząsteczkowych wykazały, iż wpływ rozpuszczalnika można opisać poprawnie stosując zaledwie jeden parametr, ilustrujący zdolność danego medium to pełnienia roli akceptora wiązania wodorowego. Szczegółowe badania nad wpływem rozpuszczalnika pozwoliły zweryfikować poprawność opisu tego modelu do procesów wewnątrzcząsteczkowych dla bichromoforów benzfenon-tyrozyna stosowanych w pracy.

Głównym narzędziem badań była nanosekundowa fotoliza błyskowa (LFP). Zastosowanie lasera azotowego (337 nm) i Nd-YAG (trzecia i czwarta harmoniczna –

355 nm i 266 nm) o czasie błysku rzędu 8 ns umożliwiło pomiar absorpcji krótko żyjących produktów pośrednich, jak i absorpcji przejściowej cząsteczek w stanach wzbudzonych. Pomiar krzywych kinetycznych dla różnych długości fali pozwolił uzyskać widma absorpcji przejściowej badanych układów po różnych czasach opóźnienia po błysku lasera. Dalsze rozseparownie uzyskanych widm na składowe doprowadziło nie tylko do identyfikacji nietrwałych produktów przejściowych, ale także do określenia zmian ich stężeń w czasie. Istotną część pracy doktorskiej stanowiły obliczenia teoretyczne z zastosowaniem teorii funkcjonałów gęstości (DFT) przy użyciu pakietu Gaussian03, a także symulacje Dynamiki Molekularnej (MD) przy użyciu pakietu AMBER 10. Celem obliczeń teoretycznych było znalezienie zoptymalizowanych struktur w stanie gazowym dla stanu podstawowego badanych związków. Ponadto dla niektórych układów prowadzono obliczenia w obecności rozpuszczalnika dla stanu podstawowego i trypletowego. Symulacje MD pozwoliły dodatkowo określić prawdopodobieństwo występowania odpowiednich konformacji. Zadaniem obliczeń metodą DFT i symulacji MD było znalezienie czynników geometrycznych, takich jak odległość między donorem a tlenem karbonylowym, czy oddziaływanie elektronów π pierścieni aromatycznych, które wpływają na szybkość reakcji wewnątrzcząsteczkowego przeniesienia atomu wodoru lub elektronu.

Do badań wybrano otwartołańcuchowe bichromofory: benzofenon-tyrozyna (**(S,S)-BP-Tyr**, **(R,S)-BP-Tyr**) i benzofenon-metionina (**(S,S)-BP-Met**, **(R,S)-BP-Met**), w których oba chromofory połączone są giętkim łańcuchem peptydowym, o dużej swobodzie konformacyjnej. Drugą grupę związków stanowiły cykliczne bichromofory: benzofenon-tyrozyna (**(S,S)-BP-DKP-Tyr**, **(S,R)-BP-DKP-Tyr**) i benzofenon-metionina (**(S,S)-BP-DKP-Met**, **(S,R)-BP-DKP-Met**), w których oba chromofory połączone są sztywnym pierścieniem diketopiperazyny. Badania obejmowały łącznie cztery pary diastereoizomerów i skupiały się na porównaniu reaktywności w obrębie badanej pary diastereoizomerów, a także wpływie rodzaju łańcucha peptydowego łączącego chromofory na ich reaktywność. Badania zostały rozszerzone o układ trichromoforowy: karboksybenzofenon-metionina-tyrozyna (**CB-Met-Tyr**), dla którego uwzględnione były konkurencyjne procesy wygaszania stanu trypletowego karboksybenzofenonu przez oba aminokwasy. Wszystkie bichromofory, trichromofory i związki referencyjne stosowane w pracy zostały zsyntetyzowane przez doktorów F. Kaźmierczaka i G. Hörnera.

Pierwszym etapem prac było wykonanie widm absorpcji i fosforescencji wszystkich badanych związków, w celu sprawdzenia czy podstawienie cząsteczki benzofenonu nie zmienia właściwości spektroskopowych tego chromoforu. Widma fosforescencji dla badanych związków zostały wykonane w temperaturze 77 K w szkliwie dichlorometan-metanol (DCM-MeOH) (1:1 v/v). Znormalizowane widma fosforescencji wszystkich badanych bichromoforów i trichromoforów pokrywały się z widmami wykonanymi odpowiednio dla niepodstawionego benzofenonu i karboksybenzofenonu. Energie stanu trypletowego badanych związków obliczone na podstawie długości fali odpowiadającej pasmu 0-0 emisji znajdowały się w wąskim przedziale od 68.4 do 69.9 kcal/mol i zgadzały się z wartością wyznaczoną dla benzofenonu. Widma absorpcji każdego ze związków zostały wykonane w trzech rozpuszczalnikach w temperaturze pokojowej. Ponadto dla acetonitrylu (ACN) zostały wyznaczone molowe współczynniki absorpcji dla λ_{max} dwóch charakterystycznych dla benzofenonu pasm. Dla wszystkich związków zostało zaobserwowane charakterystyczne dla benzofenonu przejście $n \rightarrow \pi^*$ z maksimum przy $\lambda_{max} \approx 338$ nm, charakteryzujące się małym molowym współczynnikiem absorpcji w zakresie ok. 200 $\frac{dm^3}{mol \cdot cm}$ i bardziej intensywne przejście $\pi \rightarrow \pi^*$ z maksimum przy $\lambda_{max} \approx 259$ nm, z molowym współczynnikiem absorpcji rzędu 18000 $\frac{dm^3}{mol \cdot cm}$. Dodatkowo zaobserwowano przesunięcie się pasm $\pi \rightarrow \pi^*$ w stronę fal dłuższych ze wzrostem polarności i protyczności rozpuszczalnika, natomiast dla pasm $n \rightarrow \pi^*$ wraz ze wzrostem polarności i protyczności rozpuszczalnika następowało przesunięcie maksimum pasma w stronę fal krótszych. Podsumowując, na podstawie analizy widm absorpcji i fosforescencji stwierdzono, że struktura elektronowa badanych pochodnych benzofenonu nie uległa zmianie w stosunku do niepodstawionego benzofenonu.

Bichromofory: benzofenon-tyrozyna

Następny etap pracy stanowiły eksperymenty czasowo-rozdzielcze. Dla otwartołańcuchowych bichromoforów benzofenon-tyrozyna wykonano badania stosując nanosekundową fotolizę błyskową. Pomiary wykonano w 6 rozpuszczalnikach protycznych i nieprotycznych. Czasy życia stanu trypletowego wyznaczono z dopasowania funkcji monowykładniczej lub dwuwykładniczej do krzywych kinetycznych dla długości fali charakterystycznych dla absorpcji stanu trypletowego

(520 nm i 630 nm). Uzyskano wartości w zakresie od 10 ns do 80 ns dla **(S,S)-BP-Tyr** i od < 10 ns do 40 ns dla **(R,S)-BP-Tyr** w zależności od użytego rozpuszczalnika. We wszystkich eksperymentach stan trypletowy został zidentyfikowany jako dominujące indywiduum na widmie absorpcji przejściowej, po krótkich czasach opóźnienia w stosunku do błysku lasera (maksima absorpcji przy 325 nm i 525 nm oraz charakterystyczna absorpcja powyżej 600 nm). Na widmie absorpcji przejściowej dla dłuższych czasów opóźnienia widoczne jest przesunięcie maksimum absorpcji z 325 na 335 nm i z 520 nm na 540 nm oraz dodatkowo pojawienie się absorpcji przy 405 nm. Zaobserwowanie charakterystycznej absorpcji przejściowej dla rodnika ketylowego (λ_{max} = 540 nm) i rodnika tyrozylowego (λ_{max} = 405 nm) jest jednoznacznym, bezpośrednim dowodem na występowanie reakcji przeniesienia atomu wodoru w wygaszaniu stanu trypletowego benzofenonu. Krótkie czasy życia trypletu dla obu związków wykluczają reakcje dwucząsteczkową i wskazują na wewnątrzcząsteczkowy charakter wygaszania stanu trypletowego.

Następnym etapem prac było rozseparownie uzyskanych widm absorpcji przejściowej na składowe, co pozwoliło nie tylko na potwierdzenie identyfikacji nietrwałych produktów przejściowych, a także na określenie zmian ich stężeń w czasie. Bardzo dobre dopasowanie do danych eksperymentalnych otrzymanych w ACN uzyskano przy zastosowaniu widm referencyjnych dla trzech indywiduów: stanu trypletowego ^{3}BP, rodnika ketylowego BPH$^\bullet$ i rodnika tyrozylowego Tyr(O$^\bullet$), co jest dalszym potwierdzeniem występowania przeniesienia atomu wodoru w wygaszaniu stanu trypletowego. Wyznaczone z profili stężeniowych wydajności kwantowe tworzenia BPH$^\bullet$ i Tyr(O$^\bullet$) w ACN dla obu związków w granicy błędu były równe 1, co świadczy o bardzo wydajnym wygaszaniu stanu trypletowego w wyniku wewnątrzcząsteczkowego przeniesienia atomu wodoru.

Podsumowując, oba diastereoizomery wykazują wysoką reaktywność związaną z fotoindukowanym wewnątrzcząsteczkowym przeniesieniem atomu wodoru, a w oparciu o naświetlanie stacjonarne wykazano, iż reakcja ta jest całkowicie odwracalna. W zależności od struktury badanego związku i zastosowanego rozpuszczalnika stałe szybkości wewnątrzcząsteczkowego przeniesienia atomu wodoru, k_H, mieszczą się w zakresie od 7×10^6 s^{-1} do $1,3 \times 10^8$ s^{-1}. Wyznaczona stereoselektywność wyrażona jako stosunek stałych szybkości k_H dla pary diastereoizomerów znajduje się w przedziale od 1,2 do 3,5. Wysoka reaktywność obu bichromoforów niezależnie od użytego rozpuszczalnika jest powiązana z dużą swobodą konformacyjną łańcucha peptydowego łączącego benzofenon z tyrozyną. Wykonane zarówno obliczenia DFT dla stanu gazowego i symulacje MD o czasie trwania 100 ns dowiodły, że konfiguracje o bliskim kontakcie reagujących fragmentów są możliwe dla obu diastereoizomerów.

Istotnym wynikiem badań nad wpływem rozpuszczalnika na reaktywność związków **(S,S)-BP-Tyr** i **(R,S)-BP-Tyr** jest zaobserwowanie liniowej zależności log k_H od parametru $\Sigma\beta_2^H$, opisującego zdolność rozpuszczalnika do pełnienia roli akceptora w wiązaniu wodorowym. Nachylenia prostej wyznaczone z regresji liniowej wynoszą odpowiednio −2,5 i −1,5 dla **(S,S)-BP-Tyr** i **(R,S)-BP-Tyr**. Zmniejszenie stałej szybkości k_H wraz ze wzrostem parametru $\Sigma\beta_2^H$ rozpuszczalnika jest interpretowane jako związane ze zmniejszeniem stężenia wolnej części tyrozynowej niezwiązanej wiązaniem wodorowym z rozpuszczalnikiem. Zatem uzyskana korelacja jest zgodna z teorią kinetycznego efektu rozpuszczalnikowego - tylko donor atomu wodoru niezwiązany wiązaniem wodorowym z rozpuszczalnikiem może uczestniczyć w reakcji przeniesienia atomu wodoru.

Duża swoboda konformacyjna łańcucha peptydowego w otwartołańcuchowych bichromoforach ograniczyła możliwość dokładnej analizy zależności między reaktywnością związku a jego geometrią. Sztywność połączenia między chromoforami zwiększono poprzez zastosowanie pierścienia diketopiperazyny (DKP). Wprowadzenie pierścienia spowodowało wyraźnie różną orientację chromoforów względem DKP dla obu diastereoizomerów. W przypadku **(S,S)-BP-DKP-Tyr** zarówno benzofenon i tyrozyna znajdują się po tej samej stronie pierścienia DKP, natomiast związek **(S,R)-BP-DKP-Tyr** posiada reagujące chromofory po przeciwnych stronach pierścienia DKP. W celu zbadania jak zmiana chiralności na jednym węglu asymetrycznym w tak skonstruowanych diastereoizomerach wpłynie na ich reaktywność względem wewnątrzcząsteczkowego przeniesienia atomu wodoru wykonano pomiary metodą fotolizy błyskowej w 12 różnych rozpuszczalnikach protycznych i nieprotycznych.[147, 148]

Zaobserwowano dla badanych diastereoizomerów różny wpływ rozpuszczalnika na widma absorpcji przejściowej. Dla związku **(S,R)-BP-DKP-Tyr** widmo absorpcji przejściowej uzyskane w ACN po czasie 200 ns od błysku lasera odpowiada widmu stanu trypletowego benzofenonu (maksimum absorpcji 525 nm). Natomiast na widmie dla tego samego związku i po tym samym czasie opóźnienia otrzymanym podczas eksperymentu w mieszaninie ACN-H_2O (1:1 v/v) wyraźnie widoczne jest przesunięcie maksimum absorpcji z 520 nm na 540 nm oraz pojawienie się absorpcji przy 405 nm. Jednoznacznie wskazuje to na to, iż stan trypletowy ulega wygaszeniu w wyniku przeniesienia atomu wodoru, w efekcie czego powstają obserwowane na widmie rodnik ketylowy $BPH^{\bullet}$ i rodnik tyrozylowy $Tyr(O^{\bullet})$. Dla związku **(S,S)-BP-DKP-Tyr**, w przeciwieństwie do **(S,R)-BP-DKP-Tyr**, widma absorpcji przejściowej nie wykazują różnic ze zmianą rozpuszczalnika z nieprotycznego na protyczny i charakteryzują się wydajnym wygaszaniem stanu trypletowego w wyniku przeniesienia atomu wodoru niezależnie od użytego rozpuszczalnika.

Do rozkładu widm absorpcji przejściowej dla **(S,R)-BP-DKP-Tyr** w ACN niezbędne jest zastosowanie widm referencyjnych dla trzech indywiduów: stanu trypletowego ^3BP, rodnika ketylowego $BPH^{\bullet}$ i rodnika tyrozylowego $Tyr(O^{\bullet})$. Jednakże długi czas życia stanu trypletowego $\tau_T = 1\mu s$ i czasy życia rodnika ketylowego i rodnika tyrozylowego wynoszące dziesiątki mikrosekund wskazują na przeniesienie atomu wodoru w reakcji międzycząsteczkowej. Odmienna sytuacja występuje gdy dla **(S,R)-BP-DKP-Tyr** eksperyment jest przeprowadzony w mieszaninie ACN-H_2O (1:1 v/v), w tym przypadku do poprawnego rozseparowania widm niezbędne jest użycie ponadto widma wzorcowego anionorodnika $BP^{\bullet-}$. Dodatkowo czas życia trypletu jest skrócony dziesięciokrotnie w stosunku do ACN, a rodniki ketylowy i tyrozylowy zanikają z tą samą kinetyką z czasem życia 1μs. Obserwacje te świadczą, iż w rozpuszczalniku protycznym stan trypletowy związku **(S,R)-BP-DKP-Tyr** jest wygaszany w wyniku wewnątrzcząsteczkowego przeniesienia atomu wodoru, co zostało potwierdzone poprzez brak wpływu stężenia roztworu na czas życia trypletu. Warte podkreślenia jest to, że związek posiadający reagujące chromofory po przeciwnych stronach pierścienia diketopiperazyny może nie tylko ulegać reakcji wewnątrzcząsteczkowego przeniesienia atomu wodoru, ale co więcej wydajność tej reakcji może być bliska jedności.

Zdecydowanie różny wpływ rozpuszczalnika na reaktywność badanej pary diastereoizomerów monitorowany był także poprzez czasy życia trypletu. Dla bichromoforu **(S,S)-BP-DKP-Tyr**, w którym benzofenon i tyrozyna znajdują się po tej samej stronie pierścienia diketopiperazyny, krzywe zaniku przy długości fali charakterystycznej dla stanu trypletowego (630 nm) nakładają się na siebie niezależnie od badanego rozpuszczalnika. Świadczy to o niewielkim wpływie rozpuszczalnika na czas życia trypletu**.** Odmienne zachowanie obserwowane jest dla związku **(S,R)-BP-**

DKP-Tyr, dla którego czas życia trypletu jest silnie zależny od rozpuszczalnika i mieści się w zakresie od 50 ns w heksaflouroizopropanolu (HFIP) do > 1000 ns w ACN. Czas życia trypletu ulega zdecydowanemu skróceniu przy zmianie rozpuszczalnika z nieprotycznego na protyczny. Wyznaczone stałe szybkości wewnątrzcząsteczkowego przeniesienia atomu wodoru, k_H, dla związku **(S,R)-BP-DKP-Tyr** mieszczą się w przedziale od $< 1 \times 10^5$ s^{-1} w octanie etylu do 2×10^7 s^{-1} w heksafluoizopropanolu, podczas gdy dla związku **(S,S)-BP-DKP-Tyr** k_H zmienia się jedynie w zakresie od $8,2 \times 10^6$ s^{-1} w trifluoroetanolu (TFE) do $2,2 \times 10^7$ s^{-1} w ACN. Dla badanej pary diastereoizomerów zaobserwowano zupełnie odmienny wpływ rozpuszczalnika na stałą szybkości reakcji k_H. Zarówno brak zależności reaktywności od zastosowanego rozpuszczalnika dla **(S,S)-BP-DKP-Tyr** jaki i znaczący wzrost reaktywności w rozpuszczalnikach protycznych dla drugiego diastereoizomeru jest spostrzeżeniem unikatowym w literaturze przedmiotu. Odnotowane w publikacjach wartości stereoselektywności w przeniesieniu atomu wodoru dla diastereoizomerów keton-fenol mieściły się w przedziale od 2-10.[51, 54, 75] Natomiast dla omawianej pary cyklicznych diastereoizomerów stereoselektywność wyniosi aż 131 w octanie etylu. Niespodziewanie jednak stereoselektywność ta zmalała do 0,74 w HFIP. Oznacza to, iż związek **(S,R)-BP-DKP-Tyr** posiadający chromofory po przeciwnych stronach pierścienia DKP jest bardziej reaktywny w procesie wewnątrzcząsteczkowego przeniesienia atomu wodoru niż związek **(S,S)-BP-DKP-Tyr**, w którym benzofenon i tyrozyna znajdują się po tej samej stronie pierścienia DKP.

Badania eksperymentalne zostały uzupełnione szczegółowymi obliczeniami teoretycznymi i symulacjami Dynamiki Molekularnej (MD). Optymalizacja cząsteczek metodą DFT wykazała, iż oba związki mogą istnieć w konformacji umożliwiającej bliski kontakt tlenu karbonylowego i tlenu grupy hydroksylowej tyrozyny. Jednakże, gdy obliczenia zostały przeprowadzone w ACN tylko dla **(S,S)-BP-DKP-Tyr** konformacja typu „sandwich” o małej odległości d(O-O) była konformacją o najmniejszej energii. Wyniki z symulacji MD wykazały natomiast, iż tylko **(S,S)-BP-DKP-Tyr** w ciągu 100 ns symulacji przyjmuje konformacje o d(O-O) < 4 Å. Ponadto wyniki symulacji MD dla obu związków wykazały, iż odmienne konformacje są uprzywilejowane dla każdego z diastereoizomerów. Połączenie wyników z symulacji MD z dodatkowymi obliczeniami DFT pozwoliło na wyznaczenie stałych sprzężenia spinowo-spinowego $^3J(H^{\alpha}\text{-}H^{\beta(S/R)})$ dla **(S,S)-BP-DKP-Tyr** i **(S,R)-BP-DKP-Tyr**.

Obliczone teoretycznie wartości stałych sprzężeń są zgodne z wartościami wyznaczonymi eksperymentalnie z NMR i NOE. W ten sposób została zweryfikowana wiarygodność rezultatów zastosowanych symulacji MD. Otwiera to możliwość przewidywania stopnia reaktywności związków, w których zachodzą procesy zależne od odległości reagujących fragmentów np. wewnątrzcząsteczkowe przeniesienie atomu wodoru, za pomocą metod teoretycznych. Symulacje takie mogą stanowić wstępne jakościowe oszacowanie reaktywności związku i mogą być przydatne w planowaniu badań (wybór odpowiedniej struktury związków przed przeprowadzaniem drogich i czasochłonnych syntez).

Kluczowym spostrzeżeniem wynikającym z wyników fotolizy błyskowej dla cyklicznych bichromofórw: benzofenon-tyrozyna jest to, iż dla związku **(S,S)-BP-DKP-Tyr** obserwowano niewielką zależność stałej szybkości k_H od rozpuszczalnika, natomiast reaktywność związku **(S,R)-BP-DKP-Tyr** silnie zależała od użytego medium. Co najważniejsze zaobserwowano, iż stała szybkości reakcji k_{H} dla związku **(S,R)-BP-DKP-Tyr** w przeciwieństwie do bichromoforów otwartołańcuchowych nie może być poprawnie opisana przy użyciu jedynie jednego parametru rozpuszczalnika $\Sigma\beta_2^{\mathrm{H}}$. Reaktywność związku **(S,R)-BP-DKP-Tyr** jest natomiast skorelowana z dwoma parametrami rozpuszczalnika: parametrem $\Sigma\beta_2^{\mathrm{H}}$ i parametrem $\Sigma\alpha_2^{\mathrm{H}}$ opisującym zdolność rozpuszczalnika do pełnienia roli donora w wiązaniu wodorowym. Teoria Ingolda o kinetycznym efekcie rozpuszczalnikowym przewiduje, iż nachylenie prostej log k_{H} od $\Sigma\beta_2^{\mathrm{H}}$ jest cechą charakterystyczną donora atomu wodoru. Oznacza to, iż dla wszystkich badanych bichromoforów: benzofenon-tyrozyna nachylenie odpowiedniej prostej powinno być takie samo, gdyż wszystkie one posiadają ten sam donor atomu wodoru: tyrozynę. Jednakże, wyznaczone z regresji liniowej nachylenie prostej log k_{H} od $\Sigma\beta_2^{\mathrm{H}}$ dla **(S,R)-BP-DKP-Tyr** wynosi -3,1, co wraz z dwoma różnymi wartościami nachylenia odpowiednich prostych dla bichromoforów otwartołańcuchowych (-2,5, -1,5) wskazuje, że nachylenie prostej z logarytmu ze stałej szybkości wewnątrzcząsteczkowego przeniesienia atomu wodoru od parametru $\Sigma\beta_2^{\mathrm{H}}$ jest raczej cechą charakterystyczną każdego związku, a nie jedynie cechą donora atomu wodoru.

Wpływ obu parametrów rozpuszczalnika na reaktywność związku jest odwrotny, tj. większa wartość $\Sigma\beta_2^{\mathrm{H}}$ wpływa na zmniejszenie reaktywności, natomiast większa wartość $\Sigma\alpha_2^{\mathrm{H}}$ powoduje wzrost reaktywności badanego związku względem wewnątrzcząsteczkowego przeniesienia atomu wodoru. Wyniki te wskazują, że oddziaływanie specyficzne z rozpuszczalnikiem może również powodować wzrost reaktywności związku. Przeciwny wpływ rozpuszczalnika na stałą szybkości reakcji, k_H, związku **(S,R)-BP-DKP-Tyr** w rozpuszczalnikach protycznych i nieprotycznych może być interpretowany jako związany z fundamentalnie różnym mechanizmem przeniesienia adomu wodoru w odpowiednich rozpuszczalnikach. Za tym wyjaśnieniem przemawia po pierwsze wzrost stałej szybkości reakcji k_H o dwa rzędy wielkości przy przejściu z rozpuszczalnika nieprotycznego do protycznego, a także obserwacja na widmie absorpcji przejściowej w mieszaninie ACN-H_2O anionorodnika $BP^{\bullet-}$. Obserwacje te wskazują, iż wygaszanie stanu trypletowego w rozpuszczalnikach protycznych zachodzi według dwuetapowego mechanizmu składającego się z przeniesienia elektronu i następującego po nim przeniesienia protonu.

Stałe szybkości k_H dla różnych rozpuszczalników dla związku **(S,S)-BP-DKP-Tyr** wykreślone względem parametru $\Sigma\beta_2^\mathrm{H}$ czy $\Sigma\alpha_2^\mathrm{H}$ wykazują prawie zerowe nachylenie, co potwierdza brak wpływu rozpuszczalnika na reaktywność tego związku. Jedynym parametrem rozpuszczalnika, który wpływał na reaktywność związku **(S,S)-BP-DKP-Tyr** jest lepkość. Najdłuższy czas trypletu odnotowano dla tego związku w rozpuszczalniku o najwyższej lepkości, spośród użytych tj. w *tert*-butanolu. Sugeruje to, iż etapem determinującym szybkość zachodzenia reakcji jest wewnątrzcząsteczkowa dynamika ruchu cząsteczki. Sam etap przeniesienia atomu wodoru jest dużo szybszy od przekształcenia cząsteczki do geometrii właściwej do zajścia reakcji tj. geometrii o bliskim kontakcie reagujących fragmentów cząsteczki. Przy tym założeniu w oparciu o wyniki dynamiki molekularnej została wyznaczona stała szybkości tworzenia się konformacji o bliskim kontakcie między tlenami. Otrzymana wartość $k_\mathrm{OO} = 3 \times 10^7\ \mathrm{s}^{-1}$ jest w dobrej zgodności z wartościami stałej szybkości reakcji k_H zmierzonymi eksperymentalnie, co potwierdza słuszność założenia o wewnętrznej dynamice cząsteczki, jako etapu determinującego całkowitą stałą szybkości reakcji wewnątrzcząsteczkowego przeniesienia atomu wodoru.

Podsumowując, otrzymane wyniki wskazują, iż wpływ rozpuszczalnika na fotoindukowaną reaktywność związku względem wewnątrzcząsteczkowego przeniesienia atomu wodoru jest silnie skorelowany ze strukturą związki i oba te czynniki decydujące o stałej szybkości k_H nie mogę być rozpatrywane niezależnie.

Bichromofory: benzofenon-metionina

Kolejną grupę badanych związków stanowiły bichromofory analogiczne do układów benzofenon-tyrozyna, w których tyrozyna została zastąpiona metioniną. Dla obu diastereoizomerów otwartołańcuchowych **(S,S)-BP-Met** i **(R,S)-BP-Met** fotoliza błyskowa w ACN wykazała bardzo szybki zanik stanu trypletowego. Wyznaczone czasy życia trypletu w ACN wyniosły odpowiednio 56 ns i 22 ns dla **(S,S)-BP-Met** i **(R,S)-BP-Met**. Wartości te są ok. 100-krotnie mniejsze od czasu życia stanu trypletowego związku referencyjnego niezawierającego metioniny. Pomimo wyraźnego wpływu metioniny na wygaszanie stanu trypletowego w bichromoforach BP-Met nie zaobserwowano zmian widma absorpcji przejścowej z czasem opóźnienia, poza zanikiem absorpcji pochodzącej od stanu trypletowego. Szybkiemu zanikowi stanu trypletowego obu bichromoforów w ACN nie towarzyszyło tworzenie się spodziewanych jonorodników - produktów reakcji przeniesienia elektronu. Brak widocznych zmian na widmie absorpcji przejściowej towarzyszących zanikowi stanu trypletowego powoduje, iż analiza mechanizmu reakcji jest utrudnionona. Jednakże, pomimo braku bezpośredniej obserwacji produktów przejściowych, opierając się na zmierzonych krótkich czasach życia trypletu i danych literaturowych dotyczących dwucząsteczkowego wygaszania stanu trypletowego karboksybenzofenonu przez metioninę[2, 99, 100, 103] założono, że pierwotnym procesem fotochemicznym w układach **(S,S)-BP-Met** i **(R,S)-BP-Met** jest przeniesienie elektronu od atomu siarki do stanu trypletowego benzofenonu. Brak bezpośredniej obserwacji jonorodników może być spowodowany ich szybką dezaktywacją w wyniku powrotnego przeniesienia elektronu lub reakcji wtórnych prowadzących do trwałych produktów. W celu określenia udziału obu dróg wyznaczono wydajności tworzenia produktów trwałych poprzez naświetlanie stacjonarne związków **(S,S)-BP-Met** i **(R,S)-BP-Met**, dla stężenia $5 \times 10^{-5} \frac{mol}{dm^3}$ w ACN. Zastosowano stężenie rzędu $10^{-5} \frac{mol}{dm^3}$, aby ograniczyć ewentualny udział reakcji dwucząsteczkowej w wygaszaniu stanu trypletowego. Wyznaczone wartości wydajności kwantowej zaniku substratu wynoszą dla **(S,S)-BP-Met** i **(R,S)-BP-Met** odpowiednio 0,06 i 0,05. Relatywnie małe wartości wydajności kwantowej zaniku substratów wskazują, że reakcje wtórne nie konkurują z szybkim powrotnym przeniesieniem elektronu.

Fotolizę błyskową dla związków **(S,S)-BP-Met** i **(R,S)-BP-Met** przeprowadzono również w rozpuszczalniku protycznym: TFE. Dla obu związków zaobserwowano dwukrotne skrócenie czasu życia w stosunku do pomiarów w ACN. W przeciwieństwie do eksperymentu w ACN na widme absorpcji przejściowej wyraźnie widoczne jest przesunięcie maksimum absorpcji z 325 nm na 340 nm i z 520 nm na 540 nm, co wskazuje na obecność rodnika ketylowego. Poprzez analogię do dwucząsteczkowej reakcji 4-karboksybenzofenonu z metioniną zaproponowano mechanizm tworzenia się $BPH^{\bullet}$ w układach **(S,S)-BP-Met** i **(R,S)-BP-Met**. W wyniku przeniesienia elektronu powstaje para rodnikojonów, która może rozpadać się albo poprzez powrotne przeniesienie elektronu prowadzące do powstania substratów w stanie podstawowym (proces ten jest główny, gdy fotoreakcję prowadzi się w ACN) lub w obrębie powstałej pary rodnikojonów może nastąpić przeniesienie protonu z grupy αC (α w stosunku do siarki) do grupy karbonylowej anionorodnika. Powstaje wtedy rodnik ketylowy i rodnik α-tio-alkilowy.

Podsumowując, metionina w diastereoizomerach **(S,S)-BP-Met** i **(R,S)-BP-Met** wydajnie wygasza stan trypletowy chromoforu BP, jednakże w oparciu o naświetlanie stacjonarne w ACN wykazano, że w ok. 95 % proces ten jest odwracalny. Wysoka reaktywność obu bichromoforów **(S,S)-BP-Met** i **(R,S)-BP-Met** jest powiązana z dużą swobodą konformacyjną łańcucha peptydowego łączącego benzofenon z metioniną. Wykonane obliczenia DFT dla stanu gazowego i symulacje MD o czasie trwania 100 ns wykonane w ACN wykazały, że związki te nie mają jednej ściśle określonej uprzywilejowanej energetycznie konformacji. Jest to prawdopodobnie spowodowane brakiem możliwości dodatkowej stabilizacji określonej konformacji przez oddziaływnie pierścieni aromatycznych lub tworzenie wiązań wodorowych, co było obserwowane w bichromoforach BP-Tyr. Hörner wykazał, że wewnątrzcząsteczkowe wygaszanie stanu trypletowego BP przez metioninę jest całkowicie kontrolowane przez prawdopodobieństwo bliskiego kontaktu reagujących fragmentów.[164] Stąd duża swoboda konformacyjna związków **(S,S)-BP-Met** i **(R,S)-BP-Met**, której odbiciem jest znaczne prawdobpodobieństwo tworzenia się konformacji o bliskim kontakcie S–O, (wyznaczone z symulacji MD) tłumaczy obserwowane wydajne wewnątrzcząsteczkowe wygaszanie stanu trypletowego przez metioninę.

Duża giętkość łańcucha peptydowego w **(S,S)-BP-Met** i **(R,S)-BP-Met** z jednej strony powoduje wydajne wygaszenie stanu trypletowego przez metioninę, z drugiej jednak strony zaciera różnice w reaktywności między związkami związane ze zmianą chiralności, a także ogranicza możliwość badania wpływu rozpuszczalnika. Stereoselektywność dla otwartołańcuchowych bichromoforów BP-Met wyrażona, jako stosunek czasów życia trypletów znajdowała się w przedziale tylko od 2,3 w TFE do 2,5 w ACN. Stąd by móc przeprowadzić dokładniejszą analizę zależności między reaktywnością związku a jego geometrią, analogicznie jak w układach benzofenon-tyrozyna, połączenie między reagującymi fragmentami usztywniono poprzez wprowadzenie pierścienia diketopiperazyny.

W odróżnieniu od związków otwartołańcuchowych wykazujących jedynie subtelną stereoselektywność, zmiana chiralności na jednym stereocentrum dla cyklicznych układów BP-Met spowodowała wyraźnie różną reaktywność obu diastereoizomerów. Różnice w reaktywności **(S,S)-BP-DKP-Met** i **(S,R)-BP-DKP-Met** były obserwowane zarówno poprzez porównanie widm absorpcji przejściowej i profili kinetycznych zarejestrowanych podczas fotolizy błyskowej w ACN. Podczas gdy widmo absorpcji przejściowej dla **(S,S)-BP-DKP-Met** już po 22 ns od błysku lasera wykazywało znaczny udział rodnika ketylowego, widmo absorpcji przejściowej dla **(S,R)-BP-DKP-Met** po 500 ns od błysku lasera wciąż przypominało widmo stanu trypletowego. Widmo absorpcji przejściowej uzyskane dla **(S,R)-BP-DKP-Met** wykazywało jedynie subtelne zmiany w czasie, dostrzegalne dopiero bo nałożeniu znormalizowanych widm po różnych czasach opóźnienia, wskazując na tworzenie się indywiduum przejściowego.

Rozkład widm absorpcji przejściowej dla **(S,S)-BP-DKP-Met** w ACN wykazał po pierwsze, że czas życia trypletu wynosi zaledwie 21 ns, a po drugie proces wygaszania stanu trypletowego przebiega w wyniku wydajnego wewnątrzcząsteczkwego przeniesienia atomu wodoru, w efekcie którego tworzy się rodnik ketylowy. Zaproponowany mechanizm wewnątrzcząsteczkowego przeniesienia atomu wodoru jest dwuetapowy i polega na przeniesieniu elektronu z atomu siarki do stanu trypletowego benzofenonu, a następnie przeniesieniu protonu od grupy αCH_3 (α w stosunku do siarki) z utworzeniem rodnika ketylowego i rodnika α-tio-alkilowego. Dodatkowe dowody potwierdzające ten mechanizm pochodzą z badań stacjonarnych.

Czasy życia stanu trypletowego **(S,R)-BP-DKP-Met** wyznaczone z dopasowania funkcji monowykładniczej lub dwuwykładniczej do krzywych kinetycznych dla długości fali charakterystycznych dla absorpcji stanu trypletowego (520 nm i 630 nm) były zależne od zastosowanego stężenia. Uzyskane wartości czasów życia trypletu dla stężeń $1 \times 10^{-3}\,\frac{mol}{dm^3}$ i $2 \times 10^{-5}\,\frac{mol}{dm^3}$ wynoszą odpowiednio 230 ns i 330 ns. Zależność czasu życia od stężenia wynika z udziału procesu międzycząsteczkowego w wygaszaniu stanu trypletowego. Istotną obserwacją jest to, że czasy życia diastereoizomerów **(S,S)-BP-DKP-Met** i **(S,R)-BP-DKP-Met** w acetonitrylu dla stężenia $2 \times 10^{-5}\,\frac{mol}{dm^3}$ różniły się 15-krotnie. Analogicznie jak w przypadku cyklicznych bichromoforów BP-Tyr zmiana konfiguracji na jednym węglu chiralnym spowodowała wyraźnie różną reaktywność obu związków wskazując na to, że istnieją ściśle określone parametry strukturalne wpływające na stałą szybkości wygaszania stanu trypletowego także przez metioninę. Wyniki symulacji MD dla **(S,S)-BP-DKP-Met** i **(S,R)-BP-DKP-Met** wykazały zdecydowanie różne prawdopodobieństwo tworzenia konformacji o bliskim kontakcie siarki i tlenu karbonylowego pomiędzy tymi związkami. Dla **(S,R)-BP-DKP-Met** wyznaczone prawdopodobieństwo, iż odległość *d*(S-O) < 5,5 Å wynosi jedynie 0,09, natomiast dla **(S,S)-BP-DKP-Met** prawdobodobieństwo to jest równe 0,42. Tak znaczna różnica w rozkładzie odległości *d*(S-O) wyjaśnia obserwowaną różnicę w stałych szybkości wygaszania stanu trypletowego dla obu związków.

Dla **(S,R)-BP-DKP-Met** wykonano także fotolizę błyskową w TFE, której wyniki były znacząco odmienne od tych uzyskanych w ACN. Czas życia trypletu w stosunku do ACN został skrócony 10-krotnie, a na widmie absorpcji przejściowej wraz z zanikiem absorpcji pochodzącej od stanu trypletowego obserwowano przesunięcie maksimum absorpcji z 325 nm na 340 nm i z 520 nm na 540 nm, co wskazuje na obecność rodnika ketylowego. Wyniki te pokazują, że również stan trypletowy związku **(S,R)-BP-DKP-Met**, w którym benzofenon i metionina znajdują się po przeciwnych stronach pierścienia DKP może być wygaszany w wyniku wewnątrząsteczkowego przeniesienia atomu wodoru. Bichromofor **(S,R)-BP-DKP-Met** stanowi kolejny przykład związku, którego reaktywność może być znacząco zwiększona przez zmianę stosowanego rozpuszczalnika.

Dodatkowych informacji na temat mechanizmu wygaszania stanu trypletowego przez metioninę dla cyklicznych **(S,R)-BP-DKP-Met** i **(S,S)-BP-DKP-Met** dostarczyły wartości wydajności kwantowych zaniku substratu wyznaczone z naświetlań stacjonarnych w ACN, które wyniosły odpowiednio 0,18 i 0,35. Wartości te są znacznie większe niż te wyznaczone dla otwartołańcuchowych analogów wskazując, iż powrotne przeniesienie elektronu jest dla cyklicznych pochodnych mniej wydajne. Interesujące wydaje się być to, iż dwa związki **(R,S)-BP-Met** i **(S,S)-BP-DKP-Met** wykazujące bardzo podobne i krótkie czasy życia trypletu (ok. 20 ns) różnią się znacząco stopniem odwracalności reakcji. Wyraźnie różna wydajność zaniku substratu obu związków przy tej samej wartości stałej szybkości wygaszania stanu trypletowego wskazuje na to, że są specjalne czynniki geometryczne determinujące nie tylko stałą szybkości wygaszania stanu trypletowego, ale również wpływające na przebieg reakcji wtórnych.

W celu identyfikacji fotoproduktu tworzonego w procesie wygaszania stanu trypletowego **(S,S)-BP-DKP-Met** przez metioninę roztwór związku **(S,S)-BP-DKP-Met** naświetlano na skalę preparatywną w fotoreaktorze, a powstały produkt wyizolowano przy zastosowaniu chromatografii cienkowarstwowej. Widmo UV powstałego produktu potwierdziło redukcję benzofenonu, poprzez brak obecności na widmie charakterystycznego pasma z λ_{max}= 258 nm. Wysokorozdzielcze widma masowe produktu jak i substratu, wykonane techniką jonizacji strumieniem elektronów, zawierały jon molekularny przy m/z 382, co wskazuje na to iż oba związki są izomerami strukturalnymi. W oparciu o zebrane dane zaproponowano strukturę produktu, który powstaje w reakcji cyklizacji z utworzeniem trzeciorzędowego alkoholu. Struktura utworzonego produktu w pełni potwierdza zaproponowany mechanizm wygaszania stanu trypletowego **(S,S)-BP-DKP-Met** polegający na przeniesieniu elektronu od atomu siarki do stanu trypletowego a następnie przeniesieniu protonu od grupy αCH_3 (α w stosunku do siarki) na anionorodnik benzofenonu. Powstały w ten sposób dirodnik: ketylowy i α-tio-alikolowy rekombinuje poprzez utworzenie wiązania prowadzącego do cyklicznego produktu.

Trichromofory: karboksybenzofenon-metionina-tyrozyna, karboksybenzofenon-leucyna-metionina

Rozszerzeniem badań nad bichromoforami były prace nad fotoindukowanymi reakcjami zachodzącymi dla trichromoforu: karboksybenzofenon-metionina-tyrozyna. Zastosowano również drugi analogiczny związek, w którym metionina została zastąpiona leucyną: **CB-Leu-Tyr**. Fotoliza błyskowa w ACN wykazała, iż oba trichromofory wygaszają wydajnie stan trypletowy w wyniku wewnątrzcząsteczkowego przeniesienia atomu wodoru. Ponadto stałe szybkości k_H dla obu związków są sobie równe, co może być wytłumaczone w oparciu o wyniki symulacji MD. Wykazały one bowiem, że zamiana metioniny na leucynę nie wpływa na dynamikę części tyrozynowej cząsteczki, a tym samym na odległość *d*(O-O). W ACN nie zaobserwowano żadnych różnic między parą trichromoforów, co wskazuje na brak udziału metioniny w wygaszaniu stanu trypletowego. Jednakże, po raz kolejny zaobserwowano istotne zmiany w reaktywności związku przy zmianie rozpuszczalnika z nieprotycznego na protyczny. Na widmie absorpcji przejściowej otrzymanym podczas fotolizy błyskowej w TFE dla **CB-Met-Tyr**, oprócz rodnika ketylowego i tyrozylowego zaobserwowano anionorodnik $CB^{\bullet-}$, który nie występował dla drugiego trichromoforu **CB-Leu-Tyr**. Wydajności tworzenia rodnika ketylowego i anionorodnika dla **CB-Met-Tyr** w TFE wynoszą odpowiednio 0,61 i 0,33. Obserwacja ta dowodzi, że przeniesienie elektronu z metioniny, choć nieobserwowane w ACN, może być jednym z procesów wygaszających stan trypletowy w rozpuszczalniku protycznym. Przykład ten jest dalszym potwierdzeniem no to jak istotny może być wpływ rozpuszczalnika na fotoindukowaną reaktywność związku.

Układ dwucząsteczkowy: benzofenon/anizol

Do wyznaczenia stałej szybkości reakcji k_H niezbędna jest znajomość wszystkich stałych szybkości procesów dezaktywujących stan trypletowy, w tym również czasu życia trypletu w nieobecności wygaszacza w odpowiednim rozpuszczalniku. Do określenia czasu życia trypletu w nieobecności wygaszacza (donora atomu wodoru) wybrano związki referencyjne będące pochodnymi metoksy- wyjściowych bichromoforów benzofenon-tyrozyna. Wybór był podyktowany literaturowymi doniesieniami o małych stałych szybkości wygaszania benzofenonu przez anizol, a także brakiem obecności jakichkolwiek produktów przejściowych towarzyszących zanikowi stanu trypletowego. Czasy życia trypletu dla tych związków w rozpuszczalnikach nieprotycznych są zbliżone do tych zmierzonych dla niepodstawionego benzofenonu, a widma absorpcji przejściowej zgodnie z oczekiwaniami charakteryzuje brak ewolucji czasie. Niespodziewanie jednak w rozpuszczalnikach protycznych: TFE, HFIP czasy życia trypletów są znacząco krótsze i są one nawet porównywalne z czasami życia trypletów odpowiednich bichromoforów: benzofenon-tyrozyna. Co więcej zanikowi trypletu towarzyszą zmiany na widmie absorpcji przejściowej. W celu wyjaśnienia tej obserwacji zdecydowano się na kontynuowanie badań na prostszym układzie dwucząsteczkowym: benzofenon i anizol, dla którego interpretacja wyników nie jest utrudniona wewnętrzną dynamiką cząsteczki.[18] Systematyczne badania w licznych rozpuszczalnikach protycznych i nieprotycznych dla kilku podstawionych benzofenonów wykazały po raz pierwszy, iż wygaszanie stanu trypletowego benzofenonu przez anizol może zachodzić w wyniku pełnego przeniesienia elektronu, jednakże mechanizm ten jest ograniczony do rozpuszczalników protycznych. Wyniki te dowodzą raz jeszcze jak istotny jest wpływ rozpuszczalnika na badaną reakcję fotochemiczną. Przykładowo stała szybkości reakcji wygaszania stanu trypletowego benzofenonu przez anizol wzrosła o trzy rzędy wielkości przy zmianie rozpuszczalnika z ACN na ACN-H_2O (1:9 v/v), a wydajność tworzenia produktów przejściowych (kationorodnika anizolu i anionordnika $BP^{\bullet-}$) wzrosła od zera do 0,6. Aktywowanie mechanizmu przeniesienia elektronu zostało zinterpretowane w oparciu o teorię Marcusa i powiązane z obniżeniem energii aktywacji przeniesienia elektronu w rozpuszczalnikach protycznych.

Do tej pory uważano, iż pożądana separacja rodnikowej pary jonowej w reakcji fotoindukowanego przeniesienia elektronu jest ograniczona do rozpuszczalników polarnych. Zaobserwowany w pracy wzrost wydajności tworzenia rodników podczas fotoredukcji w układzie benzofenon/anizol w rozpuszczalnikach protycznych wydaje się być bardziej uniwersalnym zjawiskiem i otwiera nowe możliwości do prowadzenia wydajnych reakcji fotoindukowanego przeniesienia elektronu dla innych układów niezależnie od przenikalności elektrycznej użytego medium.

Podsumowując, przeprowadzone badania umożliwiły lepsze poznanie mechanizmów i czynników wpływających na szybkość reakcji wewnątrzcząsteczkowego przeniesienia atomu wodoru, elektronu i protonu w układach bichromoforowych BP-Tyr i BP-Met. Wykazano, że na reaktywność związku można wpłynąć poprzez zmianę swobody konformacyjnej łańcucha peptydowego łączącego reagujące chromofory BP-Tyr i BP-Met. Ponadto zmiana chiralności na jednym stereocentrum może wyraźnie ograniczyć wewnątrzcząsteczkową reaktywność związku, co zaobserwowano dla **(S,R)-BP-DKP-Tyr** i **(S,R)-BP-DKP-Met.** Szczegółowe badania nad wpływem rozpuszczalnika na przebieg reakcji wykazały jednoznacznie, że reaktywność związku silnie zależy od użytego medium, a teoria Ingolda dotycząca kinetycznego efektu rozpuszczalnikowego dla reakcji międzycząsteczkowych nie jest w stanie w pełni poprawnie opisać wpływu rozpuszczalnika na wewnątrzcząsteczkowe przeniesienie atomu wodoru. Poszerzeniem stanu wiedzy na temat reakcji wewnątrzcząsteczkowych i czynników determinujących ich stałe szybkości jest obserwacja, iż efekt rozpuszczalnika i struktura związku są ze sobą silnie skorelowane i oba te czynniki decydujące o stałej szybkości badanych fotoreakcji nie mogę być rozpatrywane niezależnie.

6 REFERENCES

1. P. Wisniowski, Ph. D thesis, 2001.
2. K. Bobrowski, G. L Hug, B. Marciniak, *J. Am. Chem. Soc.* 114, 10279 (1992).
3. E.R. Stadtman in *Free Radicals, Oxidative Stress, and Antioxidants*, Plenum Press, New York, 51 (1998).
4. E. R. Stadtman, H.V. Remmen, A. Richardson, N. B. Wehr, R.L. Levine, *Biochim. Biophys. Acta* 1703, 135 (2005).
5. C.B. Glaser, G. Yamin, V.N. Uversky, A.L. Fink, *Biochim. Biophys. Acta* 1703, 157 (2005).
6. D. A. Butterfield, D. Kimball-Boyd, *Biochim. Biophys. Acta* 1703, 149 (2005).
7. G.M. Martin, *Exp. Gerontol.* 35, 439 (2000).
8. C. Schöneich, *Biochim. Biophys. Acta* 1703, 111 (2005).
9. G.W. Burton, T. Doba, E. Gabe, L. Hughes, F.L. Lee, L. Prasad, K.U. Ingold, *J. Am. Chem. Soc.* 107, 7053 (1985).
10. M.C. Foti, *J. Pharm. Pharmacol.* 59, 1673 (2007).
11. C.W. Hoganson, C. Tommos, *Biochim. Biophys. Acta* 1655, 116 (2004).
12. J. Stubbe, W.A. van der Donk, *Chem. Rev.* 98, 705 (1998).
13. D.V. Avila, K.U. Ingold, J. Lusztyk, W.H. Green, D.R. Procopio, *J. Am. Chem. Soc.* 117, 2929 (1995).
14. G. Litwinienko, K.U. Ingold, *J. Org. Chem.* 68, 3433 (2003).
15. G. Litwinienko, K.U. Ingold, *J. Org. Chem.* 69, 5888 (2004).
16. G. Litwinienko, K.U. Ingold, *J. Org. Chem.* 70, 8982 (2005).
17. G. Litwinienko, K.U. Ingold, *Acc. Chem. Res.* 40, 222 (2007).
18. A. Lewandowska, G.L. Hug, G. Hörner, T. Pedzinski, P. Filipiak, B. Marciniak, *ChemPhysChem.* 11, 2108 (2010).
19. N. J. Turro, V. Ramamurth, J.C. Scaiano, *Modern Molecular Photochemistry of Organic Molecules*, University Science Books, Sausalito, CA, (2010).
20. B. Wardle, *Principles and Applications of Photochemistry*, A John Wiley & Sons, (2009).
21. P.M. Rantzepis, *Science* 169, 239 (1970).
22. J.C. Scaiano, *J. Photochem.* 2, 81 (1973).
23. P.J. Wagner, *Org. Photochem.* 11, 227 (1991).
24. L. Giering, M. Berger, C. Steel, *J. Am. Chem. Soc.* 96, 953 (1974).
25. P. J. Wagner, A. E. Puchalski, *J. Am. Chem. Soc.* 102, 7138 (1980).
26. J.C. Scaiano, *J. Am. Chem. Soc.* 102, 5399 (1980).
27. U. Pischel, D. Patra, A.L. Koner, W.M. Nau, *Photochem. Photobiol.* 82, 310 (2006).
28. P.J. Wagner, R.J. Truman, A.E. Puchalski, R. Wake, *J. Am. Chem. Soc.* 108, 7727 (1986).
29. S.G. Cohen, A. Parola, G.H. Parsons, *Chem. Rev.* 73, 141 (1973).
30. S. Inbar, H. Linschitz, S.G. Cohen, *J. Am. Chem. Soc.* 103, 7323 (1981).
31. W. M. Nau, U.Pischel in *Molecular and Supramolecular Photochemistry*, V. Ramamurthy, K. Schanze, Eds., FL, 75 (2006).
32. P.J. Wagner, R.J. Truman, J.C. Scaiano, *J. Am. Chem. Soc.* 107, 7093 (1985).
33. P. Aspari, N. Ghoneim, E. Haselbach, M.V. Raumer, P. Suppan, E. Vauthey, *J. Chem. Soc., Faraday Trans.* 92, 1689 (1996).
34. C. Devadoss, R.W. Fessenden, *J. Phys. Chem.* 95, 7253 (1991).
35. J.D. Simon, K.S. Peters, *J. Am. Chem. Soc.* 104, 6542 (1982).
36. P.K. Das, M.V. Encinas, J.C. Scaiano, *J. Am. Chem. Soc.* 103, 4154 (1981).
37. W.J. Leigh, E.C. Lathioor, M.J.S. Pierre, *J. Am. Chem. Soc.* 118, 12339 (1996).
38. P. J. Wagner, B.S. Park, *Org. Photochem.* 11, 227 (1991).
39. L. Biczok, T. Berces, H. Linschitz, *J. Am. Chem. Soc.* 119, 11071 (1997).
40. D.R. Boate, L. Johnston, J.C. Scaiano, *Can. J. Chem.* 67, 927 (1989).
41. S. Canonica, B. Hellrung, J. Wirz, *J. Phys. Chem. A* 104, 1226 (2000).
42. G. Cosa, J.C. Scaiano, *Org. Biomol. Chem.* 6, 4609 (2008).
43. R.E. Galian, L. Pastor-Perez, M.A. Miranda, J. Perez-Prieto, *Chem. Eur. J.* 11, 3443 (2005).
44. R.E. Galian, G. Litwinienko, J. Perez-Prieto, K.U. Ingold, *J. Am. Chem. Soc.* 129, 9280 (2007).
45. A.L. Koner, U. Pischel, W.M. Nau, *Org. Lett.* 9, 2899 (2007).
46. E.C. Lathioor, W.J. Leigh, *Can. J. Chem.* 79 (2001).
47. E.C. Lathioor, W.J. Leigh, *Photochem. Photobiol.* 82, 291 (2006).
48. E.C. Lathioor, W.J. Leigh, M.J.S. Pierre, *J. Am. Chem. Soc.* 121, 11984 (1999).
49. M. Wakasa, H. Hayashi, *J. Phys. Chem.* 99, 17074 (1995).
50. M. Yamaji, Y. Aoyama, T. Furukawa, S.T. T. Ito, *Chem. Phys. Lett.* 420, 187 (2006).

51. M.A. Miranda, A. Lahoz, R. Martınez-Manez, F. Bosca, J.V. Castell, J. Perez-Prieto, *J. Am. Chem. Soc.* 121, 11569 (1999).

52. J. Perez-Prieto, F. Bosca, R.E. Galian, A. Lahoz, L.R. Domingo, M.A. Miranda, *J. Org. Chem.* 68, 5104 (2003).

53. J. Perez-Prieto, R.E. Galian, M.C. Morant-Minana, M.A. Miranda, *Chem. Commun.*, 3180 (2005).

54. J. Perez-Prieto, A. Lahoz, F. Bosca, R. Martinez-Manez, M.A. Miranda, *J. Org. Chem.* 69, 374 (2004).

55. J. Perez-Prieto, S.E. Stiriba, F. Bosca, A. Lahoz, L.R. Domingo, F. Mourabit, S. Monti, M.A. Miranda, *J. Org. Chem.* 69, 8618 (2004).

56. U. Pischel, W.M. Nau, *Photochem. Photobiol. Sci.* 1, 141 (2002).

57. J.C. Scaiano, W.G. McGimpsey, W.J. Leigh, S. Jakobs, *J. Org. Chem.* 52, 4540 (1987).

58. M.R. Seyedsayamdost, S.Y. Reece, D.G. Nocera, J. Stubbe, *J. Am. Chem. Soc.* 128, 1569 (2006).

59. N.B. Sul´timova, P.P. Levin, O.N. Chaikovskayab, *Russ.Chem.Bull., Int.Ed.* 56, 1397 (2005).

60. M. Yamaji, J. Oshima, M. Hidaka, *Chem. Phys. Lett.* 475, 235 (2009).

61. M.C. Foti, C. Daquino, C. Geraci, *J. Org. Chem.* 69, 2309 (2004).

62. T. Irebo, S.Y. Reece, M. Sjödin, D.G. Nocera, L. Hammarström, *J. Am. Chem. Soc.* 129, 15462 (2007).

63. M. Sjödin, R. Ghnaem, T. Polivka, J. Pan, S. Styring, L. Sun, V. Sundström, L. Hammarström, *Phys. Chem. Chem. Phys.* 6, 4851 (2004).

64. W. M. Chan, C. Ma, W.M. Kwok., D. L. Phillips, *J. Phys. Chem. A.* 109, 3454 (2005).

65. G. Hörner, G.L. Hug, D. Pogocki, P. Filipiak, W. Bauer, A. Grohmann, A. Lämmermann, T. Pedzinski, B. Marciniak, *Chem. Eur. J.* 14, 7913 (2008).

66. S. Abad, F. Bosca, L.R. Domingo, S. Gil, U.Pischel, M.A. Miranda, *J. Am. Chem. Soc.* 129, 7407 (2007).

67. F. Bosca, I. Andreu, I.M. Morera, A. Samadi, M.A. Miranda, *Chem. Commun.*, 1592 (2003).

68. M.A. Miranda, L.A. Martínez, A. Samadi, F. Boscá, I.M. Morera, *Chem. Commun.*, 280 (2002).

69. J.T. Banks, K.U. Ingold, J. Lusztyk, *J. Am. Chem. Soc.* 118, 6790 (1996).

70. D.W. Snelgrove, J. Lusztyk, J.T. Banks, P. Mulder, K.U. Ingold, *J. Am. Chem. Soc.* 123, 469 (2001).

71. L. Valgimigli, J.T. Banks, K.U. Ingold, J. Lusztyk, *J. Am. Chem. Soc.* 117, 9966 (1995).

72. M.H. Abraham, *Chem. Soc. Rev* 22, 73 (1993).

73. M.H. Abraham, P.L. Grellier, D.V. Prior, J.J. Morris, P.J. Taylor, *J. Chem. Soc., Dalton Trans.* 20, 521 (1990).

74. N.J. Turro, R. Engel, *J. Am. Chem. Soc.* 91, 7113 (1969).

75. G. Hörner, G.L. Hug, A. Lewandowska, F. Kazmierczak, B. Marciniak, *Chem. Eur. J.* 15, 3061 (2009).

76. G. Hörner, A. Lewandowska, G.L. Hug, B. Marciniak, *J. Phys. Chem. C* 113, 11695 (2009).

77. G.L. Closs, J.R. Miller, *Science* 240, 440 (1988).

78. R.A. Marcus, *J. Chem. Phys.* 43, 679 (1965).

79. J.R. Miller, J.V. Beitz, R.K. Huddleston, *J. Am. Chem. Soc.* 106, 5057 (1984).

80. H. Oevering, M.N. Paddon-Row, M. Heppener, A.M. Oliver, E. Cotsaris, J.W. Verhoeven, N.S. Hush, *J. Am. Chem. Soc.* 109, 3258 (1987).

81. P. Pasman, G.F. Mes, N.W. Koper, J.W. Verhoeven, *J. Am. Chem. Soc.* 107, 5839 (1985).

82. D. Rehm, A. Weller, *Isr. J. Chem.* 8, 259 (1970).

83. F. Scandola, V. Balzani, G.B. Schuster, *J. Am. Chem. Soc.* 103, 2519 (1981).

84. N. Sutin, *Acc. Chem. Res.* 15, 275 (1982).

85. R.A. Marcus, *Annu. Rev. Phys. Chem.* 15, 155 (1964).

86. R.A. Marcus, *J. Chem. Phys.* 24 (1956).

87. R.A. Marcus, *Can. J. Chem.* 37 (1959).

88. J.R. Miller, L.T. Calcaterra, G.L. Closs, *J. Am. Chem. Soc.* 106 (1984).

89. D.M. Guldi, K.-D. Asmus, *J. Am. Chem. Soc.* 119, 5744 (1997).

90. K.-D. Asmus, M. Bonifačić in *S-Centered Radicals*, John Wiley & Sons, NY, 141 (1999).

91. W. Vogt, *Free Radical Bio Med* 18, 93 (1995).

92. B.M. Meyer J. D.; Ho, M. C. in *Rational Design of Stable Protein Formulations* (Ed. J. F. Carpenter, Manning M. C., Eds.; Kluwer), Carpenter, J. F., Manning M. C., Eds.; Kluwer, NY, 85 (2002).

93. E.R. Stadtman, *Free Radical Res.* 40, 1250 (2006).

94. Earl R. Stadtman, H. Van Remmen, A. Richardson, N.B. Wehr, R.L. Levine, *Biochim. Biophys. Acta* 1703, 135 (2005).

95. M.J. Hokenson, V.N. Uversky, J. Goers, G. Yamin, L.A. Munishkina, A.L. Fink, *Biochemistry* 43, 4621 (2004).

96. G. Ciccotosto, K. Barnham, R. Cherny, C. Masters, A. Bush, C. Curtain, R. Cappai, D. Tew, *Lett. Pept. Sci.* 10, 413 (2003).
97. K. Bobrowski, G.L. Hug, D. Pogocki, B. Marciniak, C. Schöneich, *J. Phys. Chem. B* 111, 9608 (2007).
98. R.S. Glass, G.L. Hug, C. Schöneich, G.S. Wilson, L. Kuznetsova, T.-M. Lee, M. Ammam, E. Lorance, T. Nauser, G.S. Nichol, T. Yamamoto, *J. Am. Chem. Soc.* 131, 13791 (2009).
99. G.L. Hug, K. Bobrowski, H. Kozubek, B. Marciniak, *Photochem. Photobiol.* 68, 785 (1998).
100. G.L. Hug, K. Bobrowski, H. Kozubek, B. Marciniak, *Photochem. Photobiol.* 72, 1 (2000).
101. G.L. Hug, K. Bobrowski, D. Pogocki, G. Hörner, B. Marciniak, *ChemPhysChem.* 8, 2202 (2007).
102. G.L. Hug, B. Marciniak, K. Bobrowski, *J. Photochem. Photobiol. A* 95, 81 (1996).
103. B. Marciniak, G.L. Hug, K. Bobrowski, H. Kozubek, *J. Phys. Chem.* 99, 13560 (1995).
104. B. Marciniak, G.L. Hug, J. Rozwadowski, K. Bobrowski, *J. Am. Chem. Soc.* 117, 127 (1995).
105. A. Wojcik, A. Lukaszewicz, O. Brede, B. Marciniak, *J. Photochem. Photobiol. A* 198, 111 (2008).
106. T. Nauser, M. Jacoby, W. H. Koppenol, T. C. Squier, C. Schöneich, *Chem. Commun.*, 587 (2005).
107. P.K. Das, K. Bobrowski, *J. Chem. Soc., Faraday Trans. 2* 77, 1009 (1981).
108. K. Okada, M. Yamaji, H. Shizuka, *J. Chem. Soc., Faraday Trans.* 94, 861 (1998).
109. M.W. Wolf, R.E. Brown, L.A. Singer, *J. Am. Chem. Soc.* 99, 526 (1977).
110. P. Jacques, X. Allonas, M.V. Raumer, P.Suppan, E. Haselbach, *J. Photochem. Photobiol. A* 111, 41 (1997).
111. K. Huvaere, K. Olsen, L.H. Skibsted, *J. Org. Chem.* 74, 7283 (2009).
112. Y.P. Tsentalovich, J.J. Lopez, P.J. Hore, R.Z. Sagdeev, *Spectrochim. Acta Part A* 58, 2043 (2002).
113. M. Ludwig, S.A. Asher, *J. Am. Chem. Soc.* 110, 1005 (1988).
114. T. Pedzinski, A. Markiewicz, B. Marciniak, *Res. Chem. Intermed.* 35, 497 (2009).
115. W. Kohn, L.J. Sham, *Phys. Rev.* 140, A1133 (1965).
116. P. Hohenberg, W. Kohn, *Phys. Rev.* 136, B864 (1964).
117. L. Piela, *Idee Chemii Kwantowej*, Wydawnictwo Naukowe PWN, Warszawa, (2005).
118. A.D. Becke, *J. Chem. Phys.* 98, 1372 (1993).
119. A.D. Becke, *J. Chem. Phys.* 98, 5648 (1993).
120. J.P. Perdew, M. Ernzerhof, K. Burke, *J. Phys. Chem.* 105, 9982 (1996).
121. M.J. Frisch, G.W. Trucks, H.B. Schlegel, G.E. Scuseria, M.A. Robb, J.R. Cheeseman, J.A. Montgomery, T.V. Jr., K.N. Kudin, J.C. Burant, J.M. Millam, S.S. Iyengar, J. Tomasi, V. Barone, B. Mennucci, M. Cossi, G. Scalmani, N. Rega, G.A. Petersson, H. Nakatsuji, M. Hada, M. Ehara, K. Toyota, R. Fukuda, J. Hasegawa, M. Ishida, T. Nakajima, Y. Honda, O. Kitao, H. Nakai, M. Klene, X. Li, J.E. Knox, H.P. Hratchian, J.B. Cross, V. Bakken, C. Adamo, J. Jaramillo, R. Gomperts, R.E. Stratmann, O. Yazyev, A.J. Austin, R. Cammi, C. Pomelli, J.W. Ochterski, P.Y. Ayala, K. Morokuma, G.A. Voth, P. Salvador, J.J. Dannenberg, V.G. Zakrzewski, S. Dapprich, A.D. Daniels, M.C. Strain, O. Farkas, D.K. Malick, A.D. Rabuck, K. Raghavachari, J.B. Foresman, Q.C. J. V. Ortiz, A.G. Baboul, S. Clifford, J. Cioslowski, B.B. Stefanov, G. Liu, A. Liashenko, P. Piskorz, I. Komaromi, R.L. Martin, D.J. Fox, T. Keith, M.A. Al-Laham, C.Y. Peng, A. Nanayakkara, M. Challacombe, P.M.W. Gill, B. Johnson, W. Chen, M.W. Wong, C. Gonzalez, J.A. Pople, *Gaussian 03, Revision C.02*, Gaussian, Inc., Pittsburgh, PA, (2003).
122. J.P. Perdew, K. Burke, M. Ernzerhof, *Phys. Rev. Lett.* 77, 3865 (1996).
123. J.P. Perdew, K. Burke, M. Ernzerhof, *Phys. Rev. Lett.* 78, 1396 (1997).
124. M.T. Cancès, B. Mennucci, J. Tomasi, *J. Chem. Phys.* 107, 3032 (1997).
125. B. Mennucci, J. Tomasi, *J. Phys. Chem* 106, 5151 (1997).
126. J. Wang, R. M. Wolf, J.W. Caldwell, P.A. Kollman, D.A. Case, *J. Comput. Chem.* 25, 1157 (2004).
127. D.A. Case, T.A. Darden, T.E. Cheatham, III, C.L. Simmerling, J. Wang, R.E. Duke, R. Luo, M. Crowley, R.C.Walker, W. Zhang, K.M. Merz, B.Wang, S. Hayik, A. Roitberg, G. Seabra, I.Kolossváry, K.F.Wong, F. Paesani, J. Vanicek, X.Wu, S.R. Brozell, T. Steinbrecher, H. Gohlke, L. Yang, C. Tan, J. Mongan, V. Hornak, G. Cui, D.H. Mathews, M.G. Seetin, C. Sagui, V. Babin, P.A. Kollman, *AMBER 10*, University of California, San Francisco, San Francisco, (2008).
128. M. Montalti, A. Credi, L. Prodi, M.T. Gandolfi, *Handbook of Photochemistry*, CRC Press, Boca Raton, 3rd Edition, (2006).
129. P.R. Bevington, *Data Reduction and Error Analysis for the Physical Sciences*, McGraw-Hill, NY, (1969).
130. G. Hug L., K. Bobrowski, D. Pogocki, B. Marciniak, C. Schöneich, G. Hörner, *Res. Chem. Intermed.* 35, 431 (2009).
131. P. Wisniowski, J.M. G. L. Hug, *DECOM2006*, Warsaw, (2006).
132. S. Baral-Tosh, S.K. Chattopadhyay, P.K. Das, *J. Phys. Chem.* 88, 1404 (1984).
133. E. Hayon, T. Ibata, N.N. Lichtin, M. Simic, *J. Phys. Chem.* 76, 2072 (1972).

134. S. Solar, W. Solar, N. Getoff, *J. Phys. Chem.* 88, 2091 (1984).
135. J. Feitelson, E. Hayon, *J. Phys.Chem* 77, 10 (1973).
136. B. Marciniak, K. Bobrowski, G. L. Hug, J. Rozwadowski, *J. Phys. Chem.* 98, 4854 (1992).
137. S.L. Murov, I. Carmichael, G.L. Hug, *Handbook of Photochemistry*, Marcel Dekker, NY, (1993).
138. G.D. Fasman, *Handbook of Biochemistry and Molecular Biology, Proteins*, CRC Press 3rd Ed., Clevelend, (1976).
139. H. Du, R. A. Fuh, J. Li, A. Corkan, J. S. Lindsey, *Photochem. Photobiol.* 68, 141 (1998).
140. G.J. Brealey, M. Kasha, *J. Am. Chem. Soc.* 77, 4462 (1955).
141. M. Ito, K. Inuzuka, S. Imanishi, *J. Am. Chem. Soc.* 82, 1317 (1960).
142. H. McConneIl, *J. Chem. Phys.* 20, 700 (1952).
143. M. Sheinblatt, *Int. J. Peptide Protein Res.* 38, 8 (1991).
144. P.J. Wagner, R. Pabon, B.S. Park, A.R. Zand, D.L. Ward, *J. Am. Chem. Soc.* 116, 589 (1994).
145. Hofmann R., Schleyer P. v. R., Shaefer III H. F., *Angew. Chem. Int. Ed* 47, 7164 (2008).
146. A.J.G. Barwise, A.A. Gorman, R.L. Leyland, P.G. Smith, M.A.J. Rodgers, *J. Am. Chem. Soc.* 100, 1814 (1978).
147. A. Lewandowska, G. L. Hug, G. Hörner, D. Pogocki, F. Kazmierczak, B. Marciniak, *Can. J. Chem.* 89, 266 (2011).
148. A. Lewandowska, G.L. Hug, G. Hörner, I. Carmichael, F. Kazmierczak, B. Marciniak, *Chem. Phys. Lett.* 473, 348 (2009).
149. M. North, *Tetrahedron* 48, 5509 (1992).
150. M. Sheinblatt, *J.Chem. Soc. Perkin. Trans. 2* 127 (1990).
151. T. Yamazaki, K. Nunami, M. Goldman, *Biopolymers* 31 (1991).
152. J. Ireta, J. Neugabauer, M. Scheffer, *J. Phys.Chem. A* 108 (2004).
153. M.A. El-Sayed, *Acc. Chem. Res.* 1, 8 (1968).
154. D. Pogocki, C. Schöneich, *Chem. Res. Toxicol.* 15, 408 (2002).
155. D. Chandler, *Introduction to Modern Statistical Mechanics*, Oxford University Press, Oxford, (1987).
156. R. Zwanzig, N.K. Ailawadi, *Phys. Rev.* 182, 280 (1989).
157. M. Karplus, *J. Chem. Phys.* 30, 11 (1959).
158. T. Helgaker, M. Watson, N.C. Handy, *J. Chem. Phys.* 113, 9402 (2000).
159. V. Sychrovsky, J. Gräfenstein, D. Cremer, *J. Chem. Phys.* 113, 3530 (2000).
160. F. Cloran, I. Carmichael, A.S. Serianni, *J. Am. Chem. Soc.* 121, 9843 (1999).
161. R. Stenutz, I. Carmichael, W. Goran, A.S. Serianni, *J. Org. Chem.* 67, 949 (2002).
162. G. Hörner, A. Lewandowska, G.L. Hug, S.E. Korchak, H.-M. Vieth, B. Marciniak, *unpublished results*.
163. M. Sakamoto, X. Cai, M. Fujitsuka, T. Majima, *J. Phys. Chem. A* 110, 11800 (2006).
164. G. Hörner, *unpublished results*.
165. A. Moretto, M. Crisma, F. Formaggio, L. A Huck, D. Mangion, W.J. Leigh, C. Toniolo, *Chem. Eur. J.* 15, 67 (2009).
166. F. Bernal, A.F. Tyler, S.J. Korsmeyer, L.D. Walensky, G.L. Verdine, *J. Am. Chem. Soc.* 129, 2456 (2007).
167. A.K. Boal, I. Guryanov, A. Moretto, M. Crisma, E.L. Lanni, C. Toniolo, R.H. Grubbs, D.J. O'Leary, *J. Am. Chem. Soc.* 129, 6986 (2007).
168. S. Cantel, A. Le Chevalier Isaad, M. Scrima, J.J. Levy, R.D. DiMarchi, P. Rovero, J.A. Halperin, A.M. D'Ursi, A.M. Papini, M. Chorev, *J. Org. Chem.* 73, 5663 (2008).
169. R. Hermann, G.R. Mahalaxmi, T. Jochum, S. Naumov, O. Brede, *J. Phys. Chem. A* 106, 2379 (2002).
170. K.S. Peters, J. Lee, *J.Phys.Chem* 97, 3761 (1993).
171. J. Dreyer, K.S. Peters, *J. Phys. Chem.* 100, 19412 (1996).
172. G. Grabner, W. Rauscher, J. Zechner, N. Getoff, *J.C.S. Chem. Comm.*, 222 (1980).
173. M.J. Kamlet, J.-L.M. Abboud, M.H. Abraham, R.W. Taft, *J. Org. Chem.* 48, 2877 (1983).
174. W. Dilling, *J. Org. Chem.* 31, 1045 (1966).
175. P. Suppan, *J. Photochem. Photobiol. A* 50, 293 (1990).
176. N. Mataga, S. Tsuno, *Bull. Chem. Soc. Jpn.* 30, 368 (1957).
177. S.M. Hubig, J.K. Kochi, *J. Am. Chem. Soc.* 121, 1688 (1999).
178. Y. Marcus, Y. Migron, *J. Phys. Chem.* 95, 400 (1991).
179. P. O'Neill, S. Steenken, D. Schulte-Frohlinde, *J. Phys. Chem.* 79, 2773 (1975).
180. R.V. Bensasson, J.-C. Gramain, *J. Chem. Soc., Faraday Trans.1* 76, 1801 (1980).
181. J. Holcman, K. Sehested, *J. Phys. Chem.* 80, 1642 (1976).
182. K.S. Peters, *Acc. Chem. Res.* 42, 89 (2009).

183. A. Zweig, W.G. Hodgson, W.H. Jura, *J. Am. Chem. Soc.* 86, 4124 (1964).
184. J.-L. Seris, G. Labat, B. Meunier, *Angew. Chem. Int. Ed.* 29, 1471 (1990).
185. D.H. Evans, *Chem. Rev.* 108, 2113 (2008).
186. N. Gupta, H. Linschitz, *J. Am. Chem. Soc.* 119, 6384 (1997).
187. B. Padusek-Kwiatek, M.K. Kalinowski, *Electrochim. Acta* 29, 1439 (1984).
188. S. Wang, P.S. Singh, D.H. Evans, *J. Phys. Chem. C* 113, 16686 (2009).
189. K. Fujimoto, Y. Tokuda, H. Mackawa, Y. Matsubara, T. Mizuno, I. Nishiguchi, *Tetrahedron* 52, 3889 (1996).
190. R. Rusakowicz, G.W. Byers, P.A. Leermakers, *J. Am. Chem. Soc.* 93, 3263 (1971).
191. J. VandeVondele, M. Sulpizi, M. Sprik, *Angew. Chem. Int. Ed* 45, 1936 (2006).
192. M. C Manning, K. Patel, R.T. Borchardt, *Pharm. Res.* 6, 903 (1989).

Praca doktorska jest oparta o wyniki nieopublikowane, a także prace opublikowane:

1. A.Lewandowska, G. L. Hug. G. Hörner, I. Carmichael, F. Kazmierczak, B. Marciniak, *Chiral discrimination in the hydrogen-atom transfer between tyrosine and benzophenone in rigid peptides*, Chem. Phys. Lett. 2009, 473, 348-353.

2. A.Lewandowska, G. L. Hug, G. Hörner, T. Pedzinski, P. Filipiak, B. Marciniak, *Efficient Photochemical Oxidation of Anisole in Protic Solvents. Electron Transfer driven by Specific Solvent-Solute Interactions*, ChemPhysChem. 2010, 11, 2108-2117.

3. A.Lewandowska, G. L. Hug, G. Hörner, D. Pogocki, F. Kazmierczak, B. Marciniak, *Intramolecular H-atom transfer reactions in rigid peptides. Correlated of solvent and structural effects*, Can. J. Chem, 2011, 89, 266-279.

Ponadto w interpretacji wyników pomocne były prace:

1. G. Hörner, G. L. Hug, A. Lewandowska, F. Kazmierczak, B. Marciniak, S*tereoselectivity of the Hydrogen-Atom Transfer in Benzophenone–Tyrosine Dyads: An Intramolecular Kinetic Solvent Effect*, Chem. Eur. J. 2009, 15, 3061-3064.

2. G. Hörner, G. L. Hug, A. Lewandowska, B. Marciniak, *Solvent Effects on the Intramolecular Hydrogen-Atom Transfer between Tyrosine and Benzophenone. Diverting Reaction Mechanisms in Protic and Nonprotic Media*, J. Phys. Chem. C, 2009, 113, 11695-11703.